FABRICATION AND CHARACTERIZATION OF NANOSTRUCTURED CERAMIC THIN FILMS FOR ELECTROCHEMICAL STUDIES

RABIA NAEEM

FACULTY OF SCIENCE
UNIVERSITY OF MALAYA
KUALA LUMPUR

2017

FABRICATION AND CHARACTERIZATION OF NANOSTRUCTURED CERAMIC THIN FILMS FOR ELECTROCHEMICAL STUDIES

RABIA NAEEM

THESIS SUBMITTED IN FULFILMENT OF THE REQUIREMENTS FOR THE DEGREE OF DOCTOR OF PHILOSOPHY

FACULTY OF SCIENCE
UNIVERSITY OF MALAYA
KUALA LUMPUR

2017

UNIVERSITY OF MALAYA

ORIGINAL LITERARY WORK DECLARATION

Name of Candidate: Rabia Naeem

Registration/Matric No: SHC120097

Name of Degree: Doctor of Philosophy

Title of Project Paper/Research Report/Dissertation/Thesis ("this Work"):

Fabrication and Characterization of Nanostructured Ceramic Thin Films for Electrochemical Studies.

Field of Study: Physical Chemistry

I do solemnly and sincerely declare that:

(1) I am the sole author/writer of this Work;
(2) This Work is original;
(3) Any use of any work in which copyright exists was done by way of fair dealing and for permitted purposes and any excerpt or extract from, or reference to or reproduction of any copyright work has been disclosed expressly and sufficiently and the title of the Work and its authorship have been acknowledged in this Work;
(4) I do not have any actual knowledge nor do I ought reasonably to know that the making of this work constitutes an infringement of any copyright work;
(5) I hereby assign all and every rights in the copyright to this Work to the University of Malaya ("UM"), who henceforth shall be owner of the copyright in this Work and that any reproduction or use in any form or by any means whatsoever is prohibited without the written consent of UM having been first had and obtained;
(6) I am fully aware that if in the course of making this Work I have infringed any copyright whether intentionally or otherwise, I may be subject to legal action or any other action as may be determined by UM.

Candidate's Signature Date:

Subscribed and solemnly declared before,

Witness's Signature Date:

Name:

Designation:

ABSTRACT

This work describes some general procedures for the synthesis and characterization of monometallic and heterobimetallic single source precursors $[Cu_2Ti_4(O)_2(OH)_4(TFA)_8(THF)_6]\cdot THF$ (**1**), $[Co_2Ti_4(\mu\text{-}O)_6(TFA)_8(THF)_6]\cdot THF$ **(2)**, $[Mg_2Ti_4(O)_2(OH)_4(TFA)_8(THF)_6]\cdot THF$ (**3**), $[Mn(dmae)_2(TFA)_4]$ (**4**) and $[Sn(dmae)(OAc)]_2$ **(5)** and their disposal for the growth of thin films for electrochemical applications. The complexes have been characterized by m.p, elemental analyses, FT-IR, TG/DTG and single crystal X-ray analysis. The precursors **(1)**, **(2)** and **(3)** were applied as a single source for the fabrication of $CuO\text{-}2TiO_2$ and $CoTiO_3\text{-}TiO_2$ composites and $MgTi_2O_5$ solid solution thin films, whereas film precursor **(4)** has been applied as a dual source along with Ag(I) acetate for the deposition of $Ag\text{-}Mn_2O_3$ composite thin film by aerosol assisted chemical vapour deposition (AACVD). The electric field directed aerosol assisted chemical vapor deposition technique (EFDAACVD) was used to make thin films of SnO_2, Mn_2O_3, Fe_2O_3, NiO, CuO, ZnO, CdO and PbO from precursor **(5)** and their respective acetates. Further $CuPbI_3$ was synthesized by heating co-precipitated mixture of copper(I) iodide and lead(II) iodide in an evacuated Pyrex ampule at 630 ^oC. The films of $CuPbI_3$ were decorated by electrophoretic deposition method. The phase purity, particle size and crystallinity of deposited thin films were examined by X-ray powder diffraction (XRPD) and Raman spectroscopy, while X-ray photoelectron spectroscopy (XPS), field emission scanning electron microscopy and energy dispersive X-ray spectroscopy (EDX) were used to investigate the oxidation states, electronic structure, surface morphology, shape and elemental composition of the involved elements. In the case of mesoporous nanostructure of SnO_2 microballs surface area 136 m^2g^{-1} was determined by BET. The optical band gaps of films were determined by UV-visible spectrophotometry and found to be were 1.8, 3.4, 3.8, 1.2, 2.2, 1.9,0.9,3.2, 2.2, 1.9 and

1.82 eV for Ag-Mn_2O_3, $MgTi_2O_5$, SnO_2, Mn_2O_3, Fe_2O_3, NiO, CuO, ZnO, CdO, PbO and $CuPbI_3$ films, respectively. The applicability of fabricated CuO-$2TiO_2$ and $CoTiO_3$–TiO_2 composite electrodes in electrochemical sensors has been investigated towards the sensitive and selective detection of NO_2^- ions and dopamine (DA), respectively. The CuO-$2TiO_2$ electrode showed the limit of detection (LoD) of 16.6 nM with the linear range of 10 to 200 μM at +1.0 V due to the oxidation of NO_2^- ions. The $CoTiO_3$–TiO_2 electrode showed good electrocatalytic activity for DA with the (LoD) of 0.083 μM and a linear range of 20 to 300 μM. The SnO_2 micro balls provide unique network pores that could be easily penetrated by the electrolyte to give high reversible recycling stability for application in lithium ion batteries. The photoelectrochemical activity (PEC) of Ag-Mn_2O_3, $MgTi_2O_5$, Mn_2O_3, Fe_2O_3, NiO, CuO, ZnO, CdO, PbO and $CuPbI_3$ thin films determined by the linear sweep voltammetry (LSV) show photocurrent densities of 3, 0.4, 1.2, 0.12, 0.23, 0.13, 0.23, 0.26, 0.20 and 0.25 $mAcm^{-2}$ at 0.7 V vs Ag/AgCl/3M KCl, respectively. The improved photoelectrochemical behaviour of Ag-Mn_2O_3, $MgTi_2O_5$, Mn_2O_3, Fe_2O_3, NiO, CuO, ZnO, CdO, PbO and $CuPbI_3$ electrodes was attributed to the increased photon absorption ability, increased surface area, and more efficient electron/hole transfer which were confirmed by LSV, Chronoamperometery, electrochemical impedance spectroscopy and Mott-Schottky plot.

ABSTRAK

Kerja ini menerangkan beberapa prosedur umum untuk sintesis dan pencirian prekursor monologam dan heterodwilogam $[Cu_2Ti_4(O)_2(OH)_4(TFA)_8(THF)_6]\cdot THF$ **(1)**, $[Co_2Ti_4(\mu\text{-}O)_6(TFA)_8(THF)_6]\bullet THF$ **(2)**, $[Mg_2Ti_4(O)_2(OH)_4(TFA)_8(THF)_6]\cdot THF$ **(3),** $[Mn(Dmae)_2(TFA)_4]$ (**4)** dan [Sn (Dmae)(OAc)]$_2$ **(5)** dan penggunaan precursor-prekursor ini untuk pertumbuhan filem nipis untuk aplikasi elektrokimia. kKompleks yang disintesis ini telah diciri melalui analisis takat lebur, unsur, FT-IR, TG / DTG dan sinar-X hablur tunggal. Prekursor **(1)**, **(2)** dan **(3)** digunakan sebagai sumber tunggal untuk fabrikasi komposit CuO-2TiO_2 dan $CoTiO_3$-TiO_2 dan filem nipis larutan pepejal $MgTi_2O_5$ melalui pemendakan wap kimia dibantu aerosol (AACVD) manakala prekursor **(5)** digunakan sebagai sumber dwi bersama-sama dengan Ag(I) asetat untuk pemendapan filem nipis komposit Ag-Mn_2O_3 oleh AACVD. Teknik pemendapan wap kimia dibantu aerosol diarah oleh medan elektrik (EFDAACVD) telah digunakan untuk fabrikasi filem nipis SnO_2, Mn_2O_3, Fe_2O_3, NiO, CuO, ZnO, CdO dan PbO, daripada asetat masing-masing dan precursor (4) telah digunakan untuk fabrikasi serbuk bebola nano SnO_2 dan filem nipisnya atas substrat kaca FTO. Seterusnya, $CuPbI_3$ telah disintesis melalui pemanasan campuran ko-mendakan plumbum(II) iodida dan kuprum(I) iodida dalam ampule pyrex tervakum pada 620^oC. Filem $CuPbI_3$ dihiasi dengan teknik pemendapan elektroforetik. Fasa ketulenan, saiz zarah dan penghabluran filem nipis termendap diuji dengan pembelauan sinar-X (XRD) dan spektroskopi Raman, manakala spektroskopi fotoelektron sinar-X (XPS), mikroskop elektron imbasan pemancaran medan dan spektroskopi tenaga serakan X-ray (EDX) digunakan untuk menyiasat keadaan pengoksidaan, struktur elektron, morfologi permukaan, saiz habluran, bentuk dan komposisi unsur bagi unsur-unsur yang terlibat. Dalam kes struktur nano bebola mikro SnO_2 yang berliang meso, luas permukaan yang ditentukan oleh BET didapati ialah 136 $m^2\ g^{-1}$. Jurang jalur optik bagi semua filem-filem yang difabrikasi diuji oleh

spektrofotometri UV dan didapati adalah 1.8, 3.4, 3.8, 1.2, 2.2, 1.9, 0.9 ,3.2, 2.2, 1.9 dan 1.82eV masing-masing bagi filem Ag-Mn_2O_3, $MgTi_2O_5$, SnO_2, Mn_2O_3, Fe_2O_3, NiO, CuO, ZnO, CdO, PbO dan $CuPbI_3$. Aplikasi elektrod komposit CuO-$2TiO_2$ dan $CoTiO_3$-TiO_2 yang difabrikasi dalam sensor elektrokimia telah disiasat terhadap pengesanan senstif dan terpilih masing-masing bagi ion NO_2 dan dopamin (DA). Elektrod CuO-$2TiO_2$ menunjukkan had pengesanan (LoD) sebanyak 16.6 μM dengan julat linear dari 10 hingga 200 μM pada +1.0 V disebabkan oleh pengoksidaan ion NO_2. Elektrod $CoTiO_3$–TiO_2 menunjukkan aktiviti electromangkinan yang baik untuk DA dengan (LoD) sebanyak.0.083 μM dan julat linear dari 20 hingga 300 μM. Bebola mikro SnO_2 menyediakan liang-liang rangkaian unik yang mudah ditembusi oleh elektrolit untuk memberi kestabilan kitaran semula berbalik yang tinggi untuk aplikasi dalam bateri ion litium. Aktiviti fotoelektrokimia (PEC) filem nipis Ag-Mn_2O_3, $MgTi_2O_5$, Mn_2O_3, Fe_2O_3, NiO, CuO, ZnO, CdO, PbO dan $CuPbI_3$ seperti ditentukan oleh voltammetri penyapuan linear (LSV) masing-masing menunjukkan ketumpatan arus foto sebanyak 3, 0.4, 1.2, 0.12, 0.23, 0.13, 0.23, 0.26, 0.20 dan 0.25 mA cm^{-2} pada 0.7 V vs Ag/AgCl/3M KCl. Peningkatan sifat fotoelektrokimia bagi elektrod Ag-Mn_2O_3, $MgTi_2O_5$, Mn_2O_3, Fe_2O_3, NiO, CuO, ZnO, CdO, PbO dan $CuPbI_3$ adalah disebabkan oleh peningkatan keupayaan penyerapan foto, peningkatan luas permukaan, dan pemindahan elektron/lubang yang lebih cekap yang telah disahkan oleh pengukuran voltammetri penyapuan linear, kronoamperometri, spektroskopi impedans elektrokimia dan plot Mott-Schottky.

DEDICATION

To

HAZRAT MUHAMMAD (PEACE BE UPON HIM)

WHO IS THE LAST MESSENGER OF ALLAH

To

LOVING PARENTS, WHOSE

UTMOST EFFORTS AND PRAYERS ARE ALWAYS WITH ME

To

RESPECTED TEACHERS, WHOSE

KIND GUIDANCE AND ENCOURAGEMENT HELPED ME TO REACH AT THIS STAGE

To

THOSE, WHO INSPIRED ME TO SEEK KNOWLEDGE FOR THE WELFARE OF MANKIND

ACKNOWLEDGEMENTS

All praises and graces to ***Almighty ALLAH*** who gave me knowledge, courage and strength to complete this work. All the respects for Prophet Muhammad (peace be upon him), who guided mankind to the path of rightness, who is the true source of wisdom, knowledge and whose love is the only way to reach ALLAH.

I express my sincere gratitude to my supervisor Professor Dr. Rosiyah Yahya for providing me support in analysis and for her unlimited moral and intellectual help at many steps in last three years.

I deem it my utmost pleasure to avail this opportunity to express the heartiest gratitude and deep sense of obligation to my supervisor Professor Dr. Muhammad Mazhar for his full support, expert guidance, constant encouragement, sincerity and enlightening discussions throughout the course of the completion of my research work.

My special thanks are also to the head of department and all professors of Chemistry department, especially Professor Misni Misran, Professor Zainudin Arrifin, Professor Wan Jeffery Basirun and their research group for providing me lab facilities. I am extremely thankful to Professor K.M. Lo and Dr. Hamid Khaledi for the determination of molecular structures by single crystal X-ray technique. Also, my sincere thanks to Dr. Huang Nay Ming for his support in photoelectrochemical and sensor studies which were vital for the success of my research project.

I am highly indebted to our foreign collaborators in UK, Professor Upul Wijayantha and Professor Vickie Mckee, Loughborough University for their excellent feedback, valuable discussions, immense help and cooperation for material characterization.

I have many thanks for my lab fellows and friends for cooperation and providing enjoyable moments throughout my research work. I gratefully acknowledge High Impact Research (HIR), University of Malaya Research (UMRG) and IPPP (PG111-2013A) grant that made my PhD work possible.

Finally, my deepest gratitude to my loving parents for their love, sacrifices, prayers and support throughout my life. Their prayers and thoughts gave me strength and motivation with positive energy to prosper myself in the life. Many thanks to my loving brother and sisters for their prayers and moral support. In the end, I also thank all my friends and well-wishers who remember me in their prayers.

Rabia Naeem

TABLE OF CONTENTS

LIST OF FIGURES

LIST OF TABLES

LIST OF SYMBOLS AND ABBREVIATION

μA		Microampere
μM		Micromolar
Å	:	Angstrom
AA	:	Ascorbic acid
AACVD	:	Aerosol assisted chemical vapor deposition
AP	:	Acetaminophen
APCVD	:	Atmospheric pressure chemical vapour deposition
BET	:	Brunauer–Emmett–Teller
BJH	:	Barrett-Joyner-Halenda
CB	:	Conduction band
CBM	:	Conduction band maxima
CHN	:	Carbon hydrogen nitrogen analysis
cm	:	Centimeter
cm^3	:	Cubic centimeter
CNTs		Carbon nanotubes
CPE	:	Carbon paste electrode
CV	:	Cyclic voltammetry
CVD	:	Chemical vapor deposition
DA	:	Dopamine
dmae	:	N,N-Dimethylaminoethanolate
dmaH	:	N,N-Dimethylaminoethanol
DMFC	:	Direct methanol fuel cell
DSSC	:	Dye sensitized solar cells
E	:	Energy
e.g	:	exempli gratia
ECSA	:	Electrochemical surface area
EDX	:	Energy dispersive X-ray
EFDAACVD	:	Electric field directed aerosol assisted chemical vapor deposition
EPD	:	Electrophoretic deposition
Eg	:	Bandgap
EIS	:	Electrochemical Impedance spectroscopic
EPD	:	Electrophoretic deposition
et al	:	et alia

Etc	:	et cetra
eV	:	Electron volt
FESEM	:	Field emission scanning electron microscopy
FIB		Focussed ion beam
f_{max}	:	Frequency peak maximum
FTIR	:	Fourier transform infrared
FTO	:	Fluorine doped tin oxide
g	:	Gram
GCE		Glassy carbon electrode
GO	:	Graphene oxide
H	:	Magnetic field
ICDD	:	International center for diffraction data
IR	:	Infrared
J	:	Photocurrent density
K	:	Kelvin
LACVD	:	Laser assisted chemical vapor deposition
LEDs	:	Light emitting diodes
LIBs	:	Lithium ion batteries
LoD	:	Limit of detection
LSV	:	Linear Scan voltammetry
mA	:	Milliampere
Me	:	Methyl
min	:	Minute
mL	:	Milliliter
MOCVD	:	Metal-organic chemical vapor deposition
MOD	:	Metal organic deposition
mol	:	Mole
mp	:	melting point
nm	:	Nanometer
nM	:	nanomolar
NMR	:	Nuclear magnetic resonance
OAc	:	Acetate
^{o}C	:	Degree centigrade
PEC	:	Photoelectrochemical
PECVD	:	Plasma enhanced Chemical vapor deposition

PEMFC	:	Polymer electrolyte membrane fuel cell
PZT	:	Lead zirconate titanate
Rct	:	Charge transfer resistance
RGO	:	Reduced graphene oxide
SOFCs	:	Solid oxide fuel cells
SPR	:	Surface plasmon resonance effect
SPT	:	Spray pyrolytic technique
SSP	:	Single source precursor
T_c	:	Curie temperature
TFA	:	Trifluoroacetato
TFAH	:	Trifluoroacetic acid
TGA	:	Thermogravimetric analysis
THF	:	Tetrahydrofuran
Trp	:	Tryptophan
Ttip	:	Titanium (IV) isopropoxide
UA	:	Uric acid
UV	:	Ultraviolet
V	:	Volume
VB	:	Valence band
VBM	:	Valence band minimum
Vis	:	Visible
XPS	:	X-ray photoelectron spectroscopy
XRD	:	X-ray diffraction
YSZ	:	Yittria stabilized zirconia

List of Appendices

PREFACE

The thesis entitled “Fabrication and Characterization of Ceramic thin films for Electrochemical Studies” is divided into five different chapters

The chapter 1 describes the scope of ceramic thin films for electrochemical applications in field of science and technology. The chapter 2 comprises of a detailed studies of background to ceramic materials, their properties and suitable techniques for the deposition of ceramic thin films. A detailed history of deposition techniques, characterization and electrochemical applications of thin films have been described. The materials used and method adopted for the synthesis of precursors and their utilization in the deposition of thin films by AACVD, EFDAACVD and EPD methods have been described in chapter 3.

The chapter 4 is further divided into seven sections. The first four sections deal with discussion on the chemistry of precursors and their conversion to composite oxide thin films by AACVD technique. The fifth and sixth sections elaborate the deposition of metal oxide thin films by EFDAACVD method. The last part describe the deposition of metal halide films by EPD technique. After a proper discussion on characterization each section ends with a brief discussion of electrochemical sensing, optical and photoelectrochemical results of films. At the end of the thesis, conclusions regarding this research work have been given in chapter 5.

CHAPTER 1: INTRODUCTION

Ceramic films deposited on substrates exhibit versatile properties and have revolutionized many technological areas specially the energy (Harrison, Levene, Rajeshwar, McConnell, & Licht, 2008) and environmental sectors (Jun Zhang, Bang, Tang, & Kamat, 2009). Micro and nano structured transition metal oxide/ halide materials with high surface area and controlled size, shape and morphology have found diverse applications in optical, optoelectronic, photovoltaic, supercapacitors, batteries and gas sensing devices (J. Chen, Xu, Li, & Gou, 2005; Clavero, 2014; Gao, Grätzel, & Nazeeruddin, 2014; Lang, Hirata, Fujita, & Chen, 2011). Such materials offer a unique combination of their structural, optical, electrical and photoelectrochemical properties. The photoactive materials have been designed and developed with the aim to fix the main photoelectrochemical problems such as proper conduction/valence band position, narrowing of the band gap to harness visible light, fast electron/hole pair separation/transportation (Baker & Kamat, 2009; Gonçalves, Leite, & Leite, 2012; Le Formal, Grätzel, & Sivula, 2010; Leung et al., 2010; G. Li et al., 2013; Momeni, Ghayeb, & Davarzadeh, 2015; Sivula et al., 2010; J. Su, Feng, Sloppy, Guo, & Grimes, 2010; M. Wang et al., 2013; Yan, Ye, Wang, Yu, & Zhou, 2012), however, these extensive studies could not find an individual material which can overcome all these issues at once. The main criteria for photocatalytic material is low cost, environment friendly and highly efficient.

Ceramic films are commonly nonselective, while some selectivity could be achieved by modifying the optical, electronic, electrochemical characteristics and the use of solid solution and composite materials (Lazar & Daoud, 2013). Diverse electroactive ceramic thin films of NiO, Fe_2O_3, Mn_3O_4, SnO_2 and Co_3O_4 have been broadly reported in literature. Some work has been done on their fabrication methods, structure, controlled surface morphology and electrochemical studies (Nakata & Fujishima, 2012; Park, Park,

Kim, & Choi, 2013; Rehman, Ullah, Butt, & Gohar, 2009). However photo activity can be improved by defect engineering, doping of non-metal, coupling with other semiconductor or metal oxides, deposition of noble metal nanoparticles (Jinlong Zhang, Wu, Xing, Leghari, & Sajjad, 2010). Defect engineering indicates inclusion of inherent defects, such as vacancies, interstitials, and antisites, while doping infers the addition of impurities into the crystal lattice (Djurisic, Leung, & Ching Ng, 2014). The recent work showed that coupling with other semiconductor or metal oxide (Dhanalakshmi, Pandikumar, Sujatha, & Gunasekaran, 2013) and deposition of noble metal nanoparticles (Pandikumar, Murugesan, & Ramaraj, 2010) results in enhances the charge transfer at the electrode electrolyte interface and minimization in the charge recombination. Therefore, the method of catalytic (Rossetti, 2013) and photocatalytic oxidation of organic molecules (Y. J. Kim et al., 2009) and water (Jiao et al., 2013) and application as anode materials for Li-ion batteries (S. Guo et al., 2015) can occur by transfer of an electron to the semiconductor surface (Shinde, Bhosale, & Rajpure, 2013).

The physical and chemical properties of metal oxide and metal halide solid solution thin films are intensely affected by the composition and microstructure of their particles, which depend on the research method used in their synthesis. A number of procedures are introduced for the fabrication of metal oxide and halide ceramic thin films (Babuji, Balasubramanian, Radhakrishnan, & Kasilingam, 1980; Corneille, He, & Goodman, 1995; C.-L. Huang, Wang, Chen, Li, & Lin, 2012; Korotcenkov, Brinzari, Schwank, DiBattista, & Vasiliev, 2001; M. Nirmala, 2010; Mondal, Bhattacharyya, & Mitra, 2013; Ozegowski, Meteva, Metev, & Sepold, 1999; Scott, 2008). Nevertheless, the reported methods have shortcomings of not distributing the precise stoichiometric composition and fail to provide phase purity of the materials (Mansoor, Ismail, et al., 2013; M. Veith, Haas, & Huch, 2004). Therefore, in order to use of chemical vapour deposition it is necessary to modify the physio-chemical properties of the complex to improve process parameters.

To attain this, the molecular structure design method is based on the selection of a proper molecular structure type and competing it with ligands providing the required donor atoms. The growth of materials with complexes composition in micro or nanometers can define the surface morphology and physical properties, which recently focus on single or dual source precursor comprising of molecules containing all required elements in the appropriate ratios and decompose in a controllable way under normal conditions.

The aim and objective of the work is to study the performance of electro ceramic materials and devices depends on the complex interplay between processing, chemistry, structure at many levels and device physics and so requires truly interdisciplinary effort by individuals from many fields. Topical areas cover a wide spectrum with recent active areas including sensors and actuators, electronic packaging, photonics solid state ionics, defect and grain boundary engineering, magnetic recording, non-volatile ferroelectric memories, wide band gap semiconductors, high Tc superconductors, integrated dielectric and nanotechnology. Improvements in the numerous categories of electroceramics have paralleled the development of new technologies.

The present research work focuses on the design and development of single and dual source molecular precursors that contain all the components of target material, for the deposition of metal/mixed metal oxides, composites and solid solution thin films by using the AACVD, EFDAACVD and EPD techniques. The deposited films were characterized by XRD, XPS, FESEM/EDX, Raman spectroscopy and UV-visible spectroscopy for their microstructure, morphology, stoichiometry, thickness, chemical sates of constituent metals and optical band gap. A further scope of these fabricated films electrodes towards electrochemical studies is investigated.

CHAPTER 2: LITERATURE REVIEW

2.1 Ceramic Materials

Ceramics consist of a wide range of synthetic materials based on inorganic non-metallic compounds, primarily oxides, sulphides, nitrides, carbides, silicides and silicates (Da Silva, 2016; Gryshkov et al., 2016; Lahcen et al., 2014; Y.-C. Liang, Wang, & Lo; H.-H. Lu & Chen, 2016; Secu, Secu, & Bartha, 2016; J. Wei et al., 2016; Y. Yang et al., 2015; Yeh et al., 2013). The essentially ionic, covalent, non-metallic compounds that constitute ceramics are compounds formed between metals and non-metals. The crystallinity of ceramic materials ranges from highly oriented to semi-crystalline, and not fully amorphous. The advantageous properties of these ceramics are hardness, rigidity, chemical inertness, toughness and nonconductors of heat and electricity. Ceramics in the form of thin films, powders, single crystals and composites, have showed important role in medical field, electronics, chemical, energy and manufacturing industries (Affatato, Ruggiero, & Merola, 2015; N. Choudhary & Kaur, 2016; Kose et al., 2016; Saji, Venkata Subbaiah, Tian, & Tiwari, 2016; Sommers et al., 2010; S. Zhang et al., 2015).

Ceramics can be classified into two main categories. Structural ceramics and functional ceramics. Structural ceramics have potential to tolerate mechanical and thermal loading exposed to aggressive, severe chemical and thermal environment. They combine the properties and benefits of ceramics like chemical inertness, high temperature capability and rigidity, high strength, toughness, stiffness, hard, corrosion and thermal shock resistance and long term durability (Booth et al., 2016). The lifetime of ceramics in several structural applications is sensitive to unusual measures including brittle failure during mechanical or thermal loading, pitting by corrosion, dielectric breakdown and fatigue crack initiation. Structural ceramics are also used to investigate for employment in many high performances applications including metal cutting and shaping tools.

Because of high temperature and corrosion resistant properties structural ceramics are mainly valuable to resolve a large number of today's material challenges in process industries, power generation, aerospace, transportation and military applications (M. Rahman, Haider, Akter, & Hashmi, 2014).

Functional ceramics have good electrical, magnetic, and optical properties and find vast application in the field of optics, optoelectronics, catalysis, photovoltaics, sensors, biomedical, biotechnological and environmental applications etc (Maglia, Tredici, & Anselmi-Tamburini, 2013; Treccani, Yvonne Klein, Meder, Pardun, & Rezwan, 2013). A variety of deposition techniques such as chemical vapor deposition, RF sputtering, Chemical bath deposition, electrodeposition and molecular beam epitaxial growth have been applied to synthesize functional ceramic thin films with preferred characteristics. Functional ceramics also attract attention of many researchers because they have ability to interact with the surrounding to detect, act upon and generate power. However, by reducing the dimension of the devices, development in terms of sensitivity, proficiency, and portability can be improved. For these reasons micro-electromechanical systems have been widely used in the field of science and technology. Lead zirconate titanate (LZT) a renowned functional ceramic displays a variety of composition and has been applied in a range of ultrasound, supercapacitors, batteries, transducers, actuators and sensor devices (Izyumskaya et al., 2007). Functional metal oxide and halide materials are the hot research topics due to their bonding and structures in the field of electrochemistry and photocatalysis.

As most of the metallic element are reactive towards oxygen, oxides exist in stable single or mixed phases. Oxides is the largest group of ceramic materials that have chemical inertness, good properties at high temperature and resistance to oxidation. As the oxygen is the most electronegative divalent element, most oxides have significant degree of ionic

bonding. As a result, they generally have the characteristics of ionic crystals, optical transparency, high electrical resistivity, low thermal conductivity, diamagnetism and chemical stability. There are some exceptions in which oxides of indium and tin are electrically conductive while others such as beryllium oxide have high thermal conductivity.

2.2 Properties of Ceramic Materials

The property of ceramic material is its characteristic features expressed in terms of the measured response to specific imposed stimulus. While ceramics have traditionally been admired for their mechanical and thermal stability, their unique electrical, optical and magnetic properties have become of increasing importance in many key technologies including communications, energy conversion and storage, electronics and automation. Such materials are now classified as electroceramics to distinguish them from other functional ceramics such as advanced functional ceramics.

2.2.1 Electrical Properties

The performance of electroceramic materials and devices depends on the complex interplay between processing, chemistry, structure at many level and device physics and so requires a truly interdisciplinary effort by individuals from many fields. Materials can be categorized in various ways on the basis of their capacity to conduct electricity. Depending upon their capacity to conduct electric current (an ease of flow of electron) ceramic have been classified as conductors, semiconductors and insulators. The borders between the three sets are somewhat adjustable and some overlap happens. There are, however, basic differences between the mechanism of conduction in metals semiconductors and insulators (Hensel, Slocombe, & Edwards, 2015). The electrical features of solid-state materials depend on their band structure. The highest filled electronic state at 0 K is called the Fermi energy E_f.

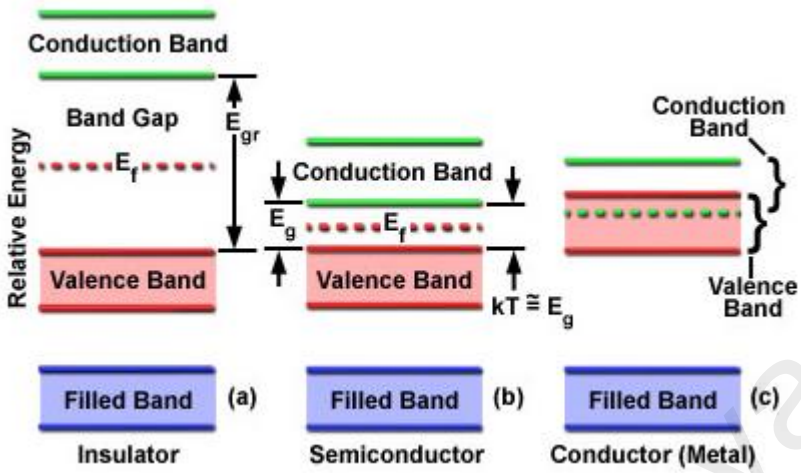

Figure 2.1: Energy level diagrams representing (a) insulators. (b) semiconductors and (c) conductors (Copyright permission from Hensel, et al., 2015)

Figure 2.1 shows that conductor such as copper, tungsten and silver which has a partially filled outermost band. Each copper atom has one 4s electron to make 4s band half filled. Electrons in this band are free to travel when an electric field is applied. However, in the case of magnesium, there is an overlap between the 3s and 3p band. On the other hand in insulators electrons are restricted within the valence band (VB) while conduction band (CB) is totally empty. The band gap, which is of some electron volts, makes it difficult to promote the electron from valence band to conduction band. For semiconductors a small gap splits the wholly filled valence band from an empty CB, because of which electrons can gain enough energy to promote into the empty CB.

Most of the structural ceramics are electric insulators, while some are electroceramics. Semiconducting functional ceramics can be either p-type or n-type depending on the access of number of holes or electrons. They mostly undergo redox reactions, i.e., oxidation-reduction reactions with surroundings and they are highly suitable for gas sensors. Developments in the various subdivisions of electroceramics along the growth of developing technologies. Dielectric materials are electrical insulators, used mainly in capacitors and electrical insulators. For practical uses, they have high electric strength,

able to endure high voltages without undergoing depletion and become electrical conductive as well as own low dielectric loss i.e., in an alternating electric field, the electrical energy loss in the form of heat should be lessened. When a potential difference is applied across a dielectric, polarization of charge within the material will take place, while long range movement of ions or electrons cannot occur (Figure 2.2). The polarization disappears as the voltage is removed. If a dielectric is placed between two plates of the capacitor, the total charge already stored in it will change which depends upon the polarizability of the material under an electric field. The change in charge storage is examined by the dielectric constant or permittivity of the ceramic material. High dielectric constants are necessary for high capacity applications.

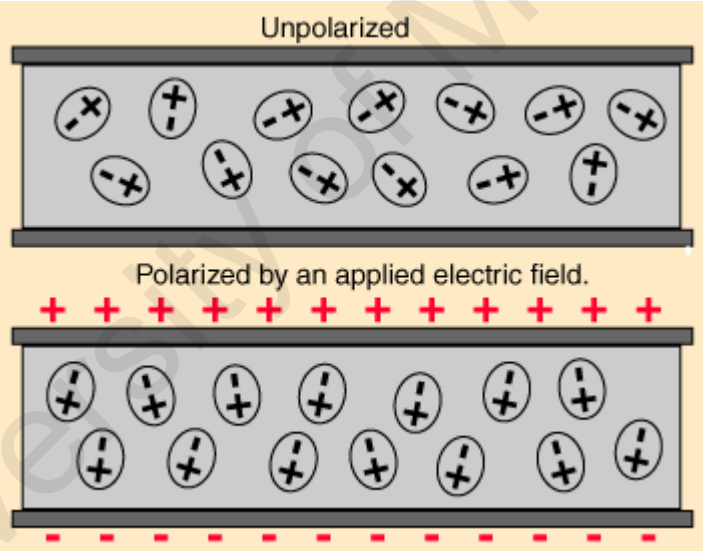

Figure 2.2: Plolatization of dielectric material by applying electric field

If a material contains polar molecules, they will generally be in random orientations when no electric field is applied. When the electric field is applied, the materials get polarized orienting the dipole moments of polar molecules. This decrease the effective electric field between the plates and will increase the capacitance of parallel plate structure. The dielectric must be a good electric insulator so as to minimize any DC leakage current through a capacitor.

2.2.2 Magnetic Properties

Magnetic materials are classified into five types by their response to externally applied magnetic fields as dimagnetism, paramagnetism, ferromagnetism, antiferromagnetism and ferrimagnetism. This classification based on magnetic properties such as ordering, sign, magnitude and temperature that influence magnetic susceptibility.

Diamagnetic materials have very weak negative susceptibility, typically of the order of -10^{-5} and relative permeability is less than one. These are the materials which do not have native magnetic moment but magnetic field (H) is applied show negative susceptibility and acquire magnetization. The orbital motion of electrons creates tiny atomic current loops, which produce magnetic fields. When an external magnetic field is applied to a material, these current loops will tend to align in such a way as to oppose the applied field (Figure 2.3). This may be observed as an atomic form of Lenz's law: induced magnetic fields tend to oppose the change which produced them.

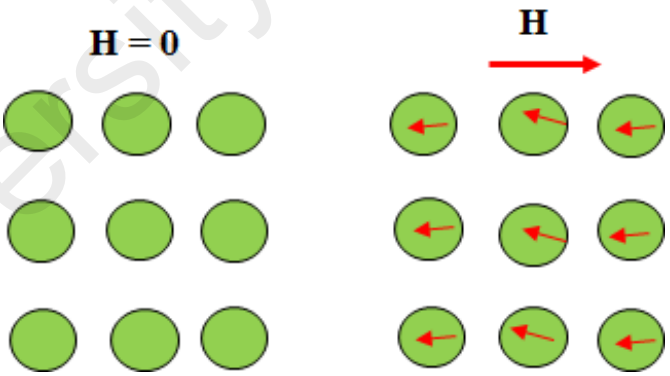

Figure 2.3: The atomic dipole orientation for a diamagnetic material in presence and absence of magnetic field.

Materials in which this effect is the only magnetic response are called diamagnetic. Diamagnetism is the residual magnetic behavior when materials are neither paramagnetic nor ferromagnetic. Ionic crystals and inert gas atoms are diamagnetic e.g. PbS, FeS_2.

Paramagnetic materials is class of materials, some of the atoms or ions in the material have a net magnetic moment due to unpaired electrons in partially filled orbitals. One of the most important atoms with unpaired electrons is iron. However, the individual magnetic moments do not interact magnetically, and like diamagnetism, the magnetization is zero when the field is removed. In the presence of a field, there is now a partial alignment of the atomic magnetic moments in the direction of the field, resulting in a net positive magnetization and positive susceptibility. The materials show a magnetization which is proportional to the applied magnetic field in which the material is placed. These materials are said to be paramagnetic. These materials show no net magnetic moment in the absence of an applied magnetic field. The presence of a permanent magnetic moment is often the result of unpaired electron spins. In such materials, the magnetic moment is non zero for each atom, but average to zero over many atoms. If a magnetic field is applied across the material and the atoms are free to oscillate, they will associate with the magnetic field, amplifying the strength (Figure 2.4). e.g. O_2 paramagnetic behavior. When a paramagnetic material is placed in a magnetic field, the magnetic moments experience a torque and they tend to orient themselves in the direction of magnetic field. At room temperature, paramagnetic susceptibilities are much less, typically about 10^{-5} barely exceeding the diamagnetic susceptibility.

Unlike paramagnetic materials, the atomic moments in these materials exhibit very strong interactions. These interactions are produced by electronic exchange forces and result in a parallel or antiparallel alignment of atomic moments. Exchange forces are very large, equivalent to a field. In addition, the efficiency of the field in aligning the moments is opposed by the randomizing effects of temperature. This results in a temperature dependent susceptibility, known as the Curie Law.

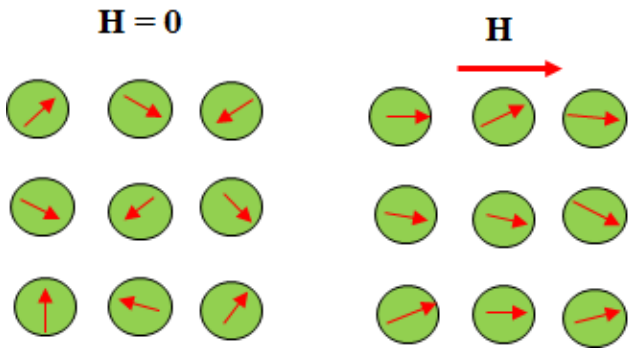

Figure 2.4: The atomic dipole orientation for a paramagnetic materials in the presence and absence of magnetic field.

At normal temperatures and in moderate fields, the paramagnetic susceptibility is small (but larger than the diamagnetic contribution). Unless the temperature is very low (<<100 K) or the field is very high paramagnetic susceptibility is independent of the applied field. Under these conditions, paramagnetic susceptibility is proportional to the total iron content. Many iron bearing minerals are paramagnetic at room temperature. The paramagnetism of the matrix minerals in natural samples can be significant if the concentration of magnetite is very small. In this case, a paramagnetic correction may be needed.

Ferromagnetic materials exhibit parallel alignment of moments resulting in large net magnetization even in the absence of a magnetic field (Figure 2.5). The elements Fe, Ni, and Co and many of their alloys are typical ferromagnetic materials. Two distinct characteristics of ferromagnetic materials are their (a) spontaneous magnetization and (b) magnetic ordering temperature.

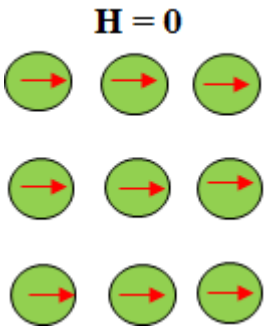

Figure 2.5: The atomic dipole orientation for a Ferromagnetic materials.

The *spontaneous magnetization* is the net magnetization that exists inside a uniformly magnetized microscopic volume in the absence of a field. The magnitude of this magnetization, at 0 K, is dependent on the spin magnetic moments of electrons. The saturation magnetization is the maximum induced magnetic moment that can be obtained in a magnetic field (H_{sat}); beyond this field no further increase in magnetization occurs. The difference between spontaneous magnetization and the saturation magnetization has to do with magnetic domains (more about domains later). Saturation magnetization is an intrinsic property, independent of particle size but dependent on temperature. There is a big difference between paramagnetic and ferromagnetic susceptibility. As compared to paramagnetic materials, the magnetization in ferromagnetic materials is saturated in moderate magnetic fields and at high (room-temperature) temperatures:

Even though electronic exchange forces in ferromagnetic materials are very large, thermal energy eventually overcomes the exchange and produces a randomizing effect. This occurs at a particular temperature called the *curie temperature* (T_c). Below the Curie temperature, the ferromagnetic is ordered and above it, disordered. The saturation magnetization goes to zero at the Curie temperature. In addition to the Curie temperature and saturation magnetization, ferromagnets can retain a memory of an applied field once it is removed. This behavior is called hysteresis and a plot of the variation of magnetization with magnetic field is called a hysteresis loop.

Another hysteresis property is the coercivity of remanence (Hr). This is the reverse field which, when applied and then removed, reduces the saturation remanence to zero. It is always larger than the coercive force. The initial susceptibility (χ_0) is the magnetization observed in low fields, on the order of the earth's field (50-100 μT) (Figure 2.6).

The various hysteresis parameters are not solely intrinsic properties but are dependent on grain size, domain state, stresses, and temperature. Because hysteresis parameters are dependent on grain size, they are useful for magnetic grain sizing of natural samples.

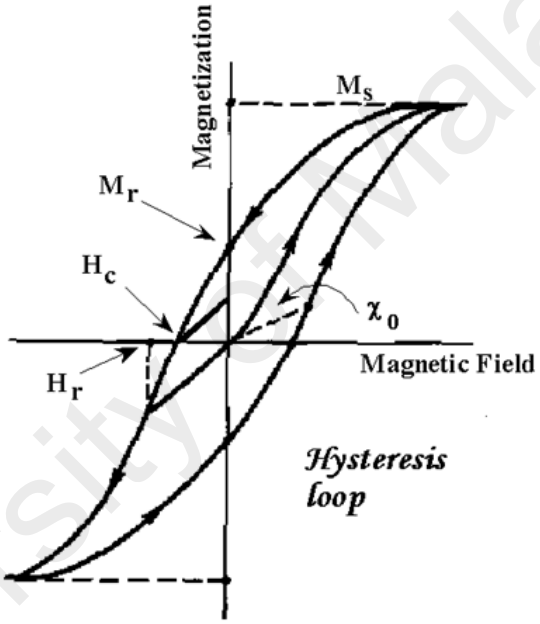

Figure 2.6: Hysteresis loop of a ferroelectric (Copyright permission from Shahid, 2009).

Antiferromagnetism involves materials in which atoms, ions, or molecules have permanent ferromagnetic materials. The crystals have domain structure, as in ferromagnetic materials, but alternating ions within a domain have their magnetic moments oriented in opposite directions, so the domain as a whole has zero magnetization, or zero magnetic susceptibility. An example of an antiferromagnetic material is manganese oxide, in which manganese ion has a magnetic moment. Such materials are generally antiferromagnetic at low temperatures. If the sublattice moments

are exactly equal but opposite, the net moment is zero. This type of magnetic ordering is called antiferromagnetism (Figure 2.7).

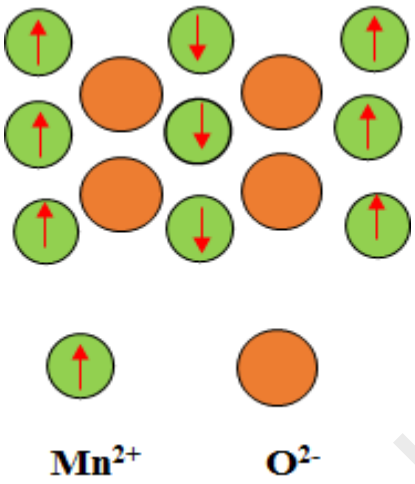

Figure 2.7: The atomic dipole orientation for antiferromagnetic manganese oxide.

In ionic compounds, such as oxides, more complex forms of magnetic ordering can occur as a result of the crystal structure (Muralt, 2000). One type of magnetic ordering is call *ferrimagnetism* (Damjanovic, 1998). A simple representation of the magnetic spins in a ferrimagnetic oxide is shown here. The magnetic structure is composed of two magnetic sublattices (called A and B) separated by oxygens. The exchange interactions are mediated by the oxygen anions. When this happens, the interactions are called indirect or super exchange interactions. The strongest super exchange interactions result in an antiparallel alignment of spins between the two sublattice. In ferrimagnets, the magnetic moments of the sublattices are not equal and result in a net magnetic moment. Ferrimagnetism is therefore similar to ferromagnetism. It exhibits all the hallmarks of ferromagnetic behavior- spontaneous magnetization, Curie temperatures, hysteresis, and remanence. However, ferro- and ferrimagnets have very different magnetic ordering. Like ferromagnetics and antiferromagnetics, there is a domain structure and like antiferromagnetic, alternate magnetic moments are pointing in opposite directions. However, this does not result in complete cancellation of the magnetization of a domain.

This often results if the alternating atoms or ions within domain are different species, with unequal magnetic moments. Magnetite (Fe_3O_4) is a well-known ferrimagnetic material. Indeed, magnetite was considered a ferrimagnet until Neel in the 1940's, provided the theoretical framework for understanding ferrimagnetism (Figure 2.8).

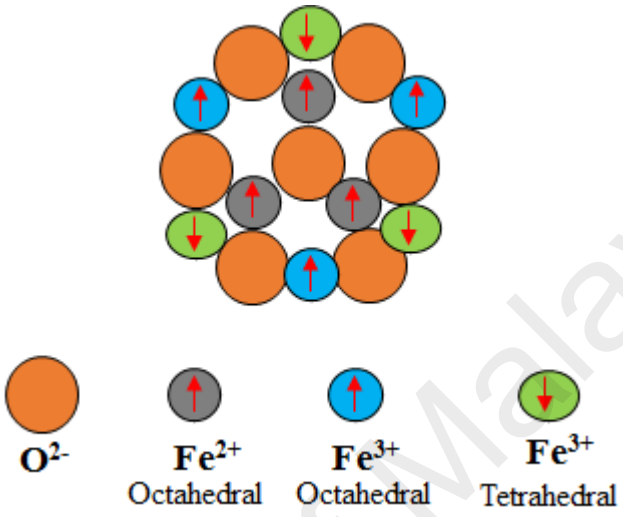

Figure 2.8: The atomic dipole orientation for a Fe (II) and Fe(III) ions in Fe_3O_4

2.2.3 Optical Properties

In a semiconductor, conductor, or insulator the valence electrons occupy the valence band, which is separated from the conductance band, by a forbidden gap of energy (band gap). In a conductor the two bands overlap resulting in the flow of electrons within the conduction band creating an electric current. Insulators have very large band gaps (> 5eV) and do not conduct electricity because electrons cannot be promoted from the VB to CB. However, an insulator can be made to conduct electricity if thermal energy or energy from an externally applied field contributes enough energy for the electrons in the filled valence band to jump to the conduction band. Semiconductors are elements or compounds with a small band gap (~1.4-5.0 eV) that can conduct electricity under some conditions (Figure 2.1). Therefore it is a good medium for the control of electrical current making it very attractive for applications in electronic devices. Additionally, metal oxides display optical

characteristics and their studies have directly showed the ground state electronic structures as well as numerous excitations of charge, spin, orbital, and lattice degrees of freedom. The optical features of metal oxides have broaden their field of technological applications including optical and optoelectronic devices by applying the optical responses, magneto-optical effect, photo-refractive effect and elasto-optic effect. Moreover, the conductivity of a semiconductor depends on the current or voltage applied to a control electrode or on the intensity of irradiation by infrared (IR), visible light, ultraviolet (UV) or X-ray.

2.3 Ceramic Thin Films

Thin film technology is the basis of astonishing development in solid state electronics (Kern, 2012). The utility of the optical properties of ceramic or semiconductor films, and scientific interest about the activity of two-dimensional solids has been responsible for the great interest in the area of science and technology of the thin films. Thin film studies depend on thickness, geometry, and structure of the film (Prellier, Singh, & Murugavel, 2005). The thickness of thin film ranges between tenths of nanometer (nm) and several micrometers (μm). So the properties of thin film particularly can be controlled by the thickness parameter. Thin films are especially suitable for applications in the field of microelectronics, optoelectronic, photonic, magnetic devices, integrated optics, IR detectors, interference filters, solar cells, polarizer's, temperature controller in satellite, superconducting films, anticorrosive and decorative coatings (Muralt, 2000). Amorphous and crystalline thin films have been produced mostly by deposition, either physical or chemical methods. The vast varieties of thin film materials, their deposition techniques and fabrication methods, spectroscopic characterization and optical characterization inquiries that are used to produce the devices (Niesen & De Guire, 2001). It is possible to categorize these techniques in two ways. (a) Physical method and (b) Chemical method.

Physical method includes the fabrication methods which depends on the evaporation or discharge of the material from a source such as evaporation and sputtering. Structure-property relationships are the important characteristics of such devices and basis of thin film technologies. Primarily the performance and economy of thin film depends on the deposition techniques in a specific chemical reaction. Thus chemical reactions may depend on thermal effects, as in vapour phase deposition and thermal growth. However, in all these cases a definite chemical reaction is required to get the final film. In order to classified deposition of films by *chemical methods* into two categories. The first of these category is concerned with the chemical formation of the film from medium involved are electroplating, chemical reduction plating and vapour phase deposition. While second one is that of production of thin film from the precursor ingredients like iodization, gaseous iodization (Hass, Francombe, & Hoffman, 2013), thermal growth, sputtering ion beam implantation (Windischmann, 1987), chemical vapour deposition (CVD) (Minegishi et al., 1997) and vacuum evaporation (Hass, et al., 2013). The techniques are summarized in table 2.1 are often capable of forming films. The films thickness of 1 μm or less are defined as thin films while thick films have thickness of 1 μm or more.

Furthermore, there are several techniques which are only able to produce thick films such as screen printing (Ito et al., 2007), glazing, electrophoretic deposition (EPD) (Kawachi et al., 2001), flame spraying and painting (Kawachi, et al., 2001). Controlled morphology and thickness of thin films can be used for optical and photoelectrochemical studies (Kawachi, et al., 2001; Hongkang Wang et al., 2014). Multiple layers of thin films can also enhance the optical efficiency (H. Wang, et al., 2014). Ceramic thin films extensively applied for solar cells (Chopra, Paulson, & Dutta, 2004; Poortmans & Arkhipov, 2006), photovoltaic devices (Izaki et al., 2007), Dye sensitizes solar cell (DSSC) (Chopra, et al., 2004; Mor, Shankar, Paulose, Varghese, & Grimes, 2006), gas sensor (Suchea, Christoulakis, Moschovis, Katsarakis, & Kiriakidis, 2006; Traversa, Gnappi, Montenero,

& Gusmano, 1996), fuel cells (Minh, 1993), supercapacitors (Yao et al., 2011) and in rechargeable batteries (Bates et al., 1993; Dudney, 2005). Semiconductor ceramic thin films are in the form of oxides, sulphides and nitrides have attract the attention of researchers in the last few decades (Suresh, 2013). These semiconducting films are highly important for electrochemical applications. Metal oxide and metal halide thin films are also used in making transparent transistors, which are of low cost, stable and environment and economic friendly. On behalf of phase separation, ceramic oxide thin films can be classified as:

i) Solid solution ceramic thin films

ii) Composite ceramic thin films.

2.3.1 Solid Solution Ceramic Thin Films

These ceramic thin films are mixture of two crystalline solid materials that exist together as a new crystalline solid, or crystal lattice. It can be done by mixing of two solids in their molten state at temperature higher than their melting point and then cooling that produce a new form of solid or by fabricating vapors of the precursor materials onto the substrates to deposit thin films. As compared to liquids solids have different criteria of mutual solubility, depending on their crystalline structure and chemical properties, which define how their atoms fix together in the combined crystal lattice. The combined lattice can be substitutional, in which the atoms of one crystal substitute those of the other, or interstitial, in which the atoms inhabit vacant position in the lattice other crystal. The solids may be soluble to some extent or entire range of relative concentrations, result a crystal with variable properties as compared to starting precursor (Handoko & Goh, 2013; Mansoor, Ehsan, et al., 2013). This offers a way to modify the properties of the solid solution for different applications. Solid solutions of ceramic semiconductors are of remarkable technological importance, as in the mixture of aluminum arsenide (AlAs),

gallium arsenide (GaAs) with gallium phosphide (GaP), or indium arsenide (InAs) (Askeland & Wright, 2015; Fulay & Lee, 2013; Voitsekhovskii, Drobyazko, & Mityurev, 1995). The properties of these solid solutions can be altered to final product by modifying the relative proportions of the starting materials; for example, the band gap for mixtures of InAs and GaAs can be adjusted in any range between the value for pure InAs (0.36 electron volt (eV) and that for pure GaAs (1.4 eV), depending on required electrical and optical properties of materials. This approach makes ceramic semiconducting solid solutions efficient towards optical and electronic devices, including solar cells, transistors, light-emitting diodes (LEDs), infrared detectors, and semiconductor lasers. Similar examples of solid solution ceramic thin films are PbS_xSe_{1-x}**,** $Cd_xZn_{1-x}S$**,** Bi-Sb**,** Cr-Me-Si**,** $MnCo_2O_4$ (K. J. Kim & Heo, 2012; Kud, Ieremenko, Likhoded, Uvarova, & Zyatkevich, 2012; Z. Liu et al., 2013; Noro, Sato, & Kagechika, 1993; Raviprakash, Bangera, & Shivakumar, 2009; Uusi-Esko, Rautama, Laitinen, Sajavaara, & Karppinen, 2010)**.**

2.3.2 Composites Ceramic Thin Films

These are materials prepared from two or more different materials with distinct physical or chemical properties, that when mixed, produce a material with properties changed from the isolated components (Ehsan, Naeem, Khaledi, Sohail, Saeed, et al., 2016; Ehsan, Naeem, McKee, et al., 2016). Each component remains dissimilar within the final product. Using this explanation, large number of engineering materials can be found in this class. For example when glass fibers are embedded in a polymer produces fiber glass sheet which is a composite.

Composite materials possess two phases. First one is the reinforcing phase like fibers, particles or sheets that are embedded in the second phase called the matrix phase. Both of the phases can be ceramic, metal or polymer. Mostly, matrix materials comprises of tough

or ductile materials whereas reinforcing are strong materials having low density. Some common composite thin films are TiO_2–Cu_2O used for superhydrophobic coatings (Aytug et al., 2014), Cu_2O–CoO composites employed for optical band gap. The incorporation of reduced graphene oxide (rGO) on a TiO_2 surface has been used for photoelectrochemical (PEC) studies (Aytug, et al., 2014) and ZnS–SiO_2 composite ceramics utilized thermal shock resistance materials (G.-S. Kim, Shin, Seo, & Do Kim, 2008).

2.4 Thin Film Deposition Techniques

Several fabrication techniques have been established over time as the concern in thin film formation has continued to build up (Hartnagel, Dawar, Jain, & Jagadish, 1995). In broad terms these techniques can be categorized as either physical or chemical deposition techniques (Humphreys et al., 1990; Mahan, 2000; R. Mane & Lokhande, 2000; Nair & Nair, 1991). The benefits and problems pertaining to these methodologies are summarized in Table 2.1.

Table 2.1: Classifications of thin films deposition techniques

Thin Films Deposition Techniques			
PHYSICAL		**CHEMICAL**	
Sputtering	**Evaporation**	**Gas Phase**	**Liquid Phase**
1) Glow discharge DC Sputtering	1) Vacuum evaporation	1) Chemical vapour deposition (CVD)	1) Electro-deposition
2) Triode Sputtering	2) Resistive heating evaporation	2) Atmospheric pressure CVD (APCVD)	2) Chemical bath deposition (CBD)
			3) Arrested precipitation technique (APT)
3) Getter Sputtering	3) Flash Evaporation	3) Low-pressure CVD (LPCVD)	4) Electroless deposition
4) Radio Frequency sputtering	4) Electron beam evaporation	4) Metal-organic CVD (MO-CVD)	5) Anodisation
5) Magnetron sputtering	5) Laser evaporation	5) Photo enhanced CVD (PHCVD)	6) Sol-gel
			7) Spin Coating
6) Ion beam sputtering	6) Reactive Evaporation	6) Laser induced CVD (PCVD)	8) Spray-pyrolysis technique (SPT)
7) A.C sputtering	7) Arc Evaporation	7) Electron enhanced CVD	9) Ultrasonic SPT
	8) Molecular beam epitaxy (MBE)		10) Polymer assisted deposition (PAD)

2.4.1 Electrophoretic Deposition (EPD)

The term ‘electrodeposition’ is often used to refer to either electroplating or electrophoretic deposition (EPD). It usually refers to the former term which exhibits the difference between the two processes deposition process (Santos et al., 2015). EPD is one of the colloidal method in semiconductor or ceramic formation and has benefits of less deposition time, require simple apparatus, slight limit on the shape of substrate, no need of binder burn out as the green coating do not contain organics. EPD also control the thickness and morphology of a deposited film through simple modification of the deposition time and applied potential. In EPD process, charged powder particles, dispersed or suspended in a liquid medium are attracted and deposited on a conductive substrate of opposite charge in the presence of electric field. There are two types of electrophoretic deposition depending on which electrode the deposition occurs. When the particles are positively charged, the deposition occurs on the cathode and the process is termed as *cathodic electrophoretic deposition* (Zhitomirsky, 1998). The deposition of negatively charged particles happens on an anode is named as *anodic electrophoretic deposition* (Hanaor et al., 2011) (Figure 2.9).

The EPD method has been used effectively for thick film of silica, nano size zeolite membrane (Shan et al., 2004), hydroxyapatite coating on metal substrate for biomedical applications (Pang & Zhitomirsky, 2005), luminescent materials, high-Tc superconducting films, gas diffusion electrodes and sensors (Hossein-Babaei & Taghibakhsh, 2000), multi-layer composites (Chang et al., 2010), glass and ceramic matrix composites by infiltration of ceramic particles onto fiber fabrics (A. R. Boccaccini, Kaya, & Chawla, 2001), oxide nanorods (Cao, 2004), carbon nanotube film (Aldo R. Boccaccini et al., 2006), functionally graded ceramics, layered ceramics, superconductors

and piezoelectric materials (Besra, Compson, & Liu, 2006; Besra, Zha, & Liu, 2006; Besra & Liu, 2007).

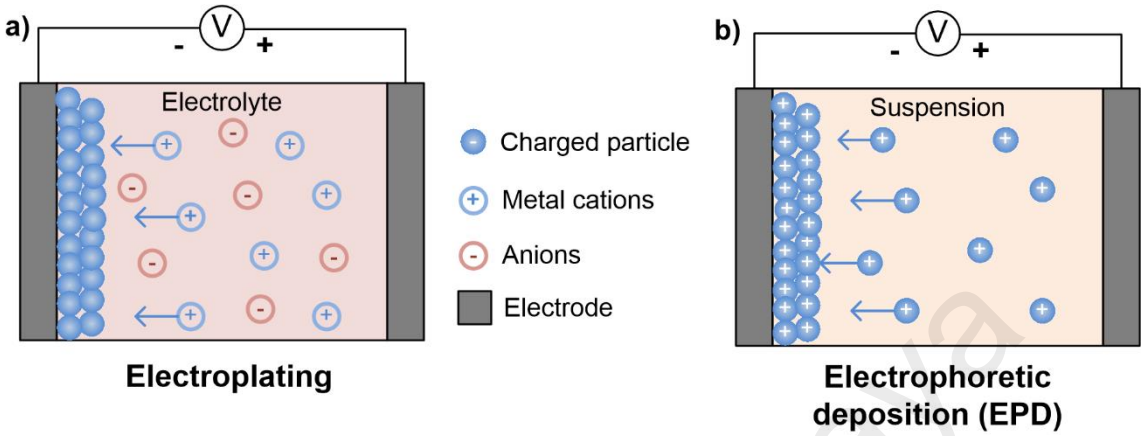

Figure 2.9: Schematic representation of the two types of cathodic electrodeposition processes: (a) electroplating and (b) electrophoretic deposition (EPD) (Copyright permission from Santos, et al., 2015).

2.4.1.1 Factors Influencing EPD

The EPD technique involve charged particles in a suspension being deposited on substrate in the presence of an applied electric field. Two groups of parameters define the features of this method related to; (i) the suspension, and (ii) the process including the physical factors such as nature of the electrodes and electrical conditions including voltage/intensity relationship, deposition time, etc.

(i) Effect of deposition time

Deposition rate for a fixed applied field decreases with increased or prolonged deposition time. A typical deposition characteristics of ZnO coating on copper electrode at different applied potentials, with increasing time of deposition (Wong & Searson, 1999). It is clearly evident that the deposition is linear during the initial time of deposition. But as more and more time is allowed, the deposition rate decreases and attains a plateau at very high deposition times. In a constant voltage EPD, this is expected because: while the potential difference between the electrodes is maintained constant, the electric field

influencing electrophoresis decreases with deposition time because of the formation of an insulating layer of ceramic particles on the electrode surface. But during the initial period of EPD, there is generally a linear relationship between deposition mass and time.

(ii) Applied voltage

For a higher applied field, which may cause turbulence in the suspension, the coating may be disturbed by flows in the surrounding medium, even during its deposition. In addition, particles can move so fast that they cannot find enough time to sit in their best positions to form a close-packed structure. Finally, in high field situations, lateral motion of the particles once deposited, also are restricted on the surface of the already deposited layer, because higher applied potential exerts more pressure on particle flux and movement, the applied field affects the deposition rate and the structure of the deposit. It is observed that the unstable current density effects the surface morphology of deposited films. It was found that quantity of YSZ deposition from the n-propanol increased with increasing applied voltage (Jia et al., 2006). However, the microstructures, texture and surface morphologies of the EPD deposited film were found to be smooth at low voltages and rough at high voltage.

(iii) Concentration of solid in suspension

The concentration of solid in the suspension play a significant part for multi-component EPD. In some cases, although each of the particle species have same sign of surface charge, they could deposit at different rates depending on the volume fraction of solids in the suspension. If the volume fraction of solids is high, the powders deposit at an equal rate. If however, the volume fraction of solids is low, the particles can deposit at rates proportional to their individual electrophoretic mobility.

(iv) Conductivity of substrate

The uniformity and conductivity of substrate electrode is an important parameter critical to the quality of the deposition of films by EPD. Peng and Liu (Peng & Liu, 2001) noticed that low conductivity of the $La_{0.9}Sr_{0.1}MnO_3$ (LSM) substrate deposit the non-uniform green films by EPD. Chen and Liu (F. Chen & Liu, 2001) observed that when LSM ($LaSrMnO_3$) or LSM–YSZ composite pellets have been used as conductive substrate for EPD, the deposition rate of non-uniform YSZ (yittria-stabilized zirconia) film was slow. Therefore, the green YSZ film obtained was of high quality.

2.4.2 Chemical Vapour Deposition (CVD)

2.4.2.1 Basic Principles of CVD

Chemical Vapour Deposition (CVD) is a main process that has found wide application in modern industry for the production of microelectronic devices, optical, decorative coatings, in order to produce a broad range of new materials, such as ceramic based thin films. The CVD process of creating a film has to be reproducible and controllable. As a result, the intrinsic properties such as the purity, composition, thickness, adhesion, microstructure and surface morphology have to be reproducible for the same reactor conditions.

Conventional CVD is an extensively-used method to growth of thin films of material of interest on substrate. The technique involves different steps including transfer of activated precursor by the inert carrier gas (argon/nitrogen/air/oxygen) to the reactor zone where the substrates are placed (Figure 2.10). Once the precursor approaches reactor zone it undergoes systematic reaction either in gaseous phase or onto the substrate surface. Both the possibilities of reactions result in the formation of thin film on the surface of substrate. Thus, CVD reactions can be homogenous or may be heterogeneous. Most CVD reactions are likely to be heterogeneous because they occur at the surface of substrate rather than gaseous or vapour phase. Homogenous process involves nucleation of particles in gaseous

phase resulting in powder coating that neither strongly adheres to substrate nor completely pure (Özgür et al., 2005).

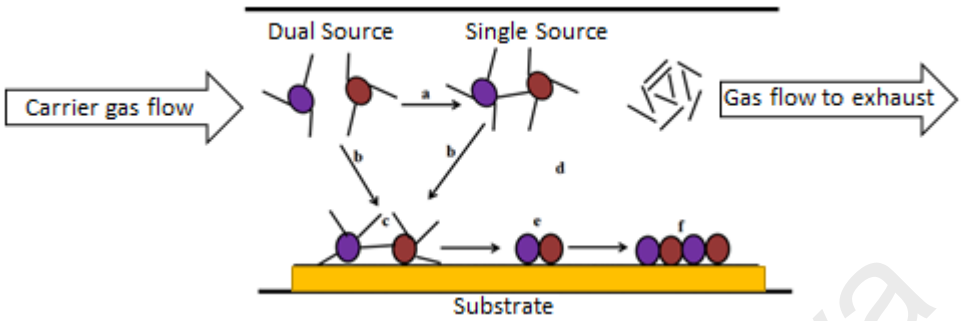

Figure 2.10: A representation of chemical vapour deposition (CVD) involving physical changes: [a] precursor reaction in vapour state; [b] diffusion of precursors on the surface of substrate; [c] precursor adsorptions and reaction on substarte; [d] elimination of volatile by-product; [e] adatoms get diffused on substrate sites; [f] nucleation and formation of thin film on substrate.

CVD technique is now considered as an important process in many industrial fields and solid-state microelectronics. Thin films of conductors (W, Mo, Al etc), semiconductors (Si, GaAs etc.) and insulators, dielectrics (oxides, silicates, and nitrides) are broadly used in the progress of solid state devices (Cahill, Goodson, & Majumdar, 2002). Most of these CVD reactions were used for the coating of the substrates at low pressure, often at high temperatures (Pierson, 1999). Recent developments emphasis on low or moderate temperature for deposition through CVD, such as plasma-CVD, and photo-CVD, MOCVD, and atomic layer deposition (ALD). These assisted techniques of chemical vapour deposition are widely applied in semiconductor industry, microelectronics, hard coatings corrosion and wear resistance applications at reduced fabrication temperatures thus facilitating utilization of substrates in a broader spectrum.

2.4.2.2 Variations of CVD

The improvement of CVD technique has developed in a many directions, leads to variety of variations of the process. The process selected for the deposition of any target material

is depending on the precursors used and type of thin film required. Some of the variations of CVD are plasma enhanced CVD (PECVD) (Hozumi & Takai, 1997), metal– organic CVD (MOCVD) (J. L. Yang, An, Park, Yi, & Choi, 2004), atmospheric pressure CVD (APCVD) (Manning, Parkin, Pemble, Sheel, & Vernardou, 2004), low pressure CVD (LPCVD) (X. Li et al., 2011), liquid injection CVD (Jones et al., 1998), laser Assisted CVD (LACVD) (Herman, 1989) and molecular beam epitaxy (Y. Chen et al., 1997). In this work we will through on two of significant variation of CVD known as Aerosol Assisted Chemical vapour deposition (AACVD) and electric field directed aerosol assisted chemical vapour deposition (EFDAACVD), are the latest modified assistance of CVD.

2.4.2.3 Aerosol-Assisted Chemical Vapour Deposition (AACVD)

Aerosol-assisted chemical vapour deposition (AACVD) is a liquid-phase variation of the conventional CVD process that involves first preparation of a clear soluble solution of precursor in some suitable volatile solvent from which an aerosol particles are formed by using ultrasonic humidifier (nebulizer), generating a mist of precursor solution, which is then transferred to a hot chamber of furnace (reactor), where the substrates are already placed, by a carrier gas. Once the aerosols approaches substrate in hot zone of reactor due to high temperature solvent gets evaporated and leaving behind the vapourized precursor in its gaseous state, followed by the deposition onto the substrate resulting in the formation of target material.

One main development of AACVD over conventional CVD techniques is any precursor that can be easily soluble in any volatile (preferably organic) solvent is required. The parameter for volatile precursor is excluded (Marchand, Hassan, Parkin, & Carmalt, 2013). However, inorganic molecular precursors are very stable and less sensitive towards air; possess less volatility, therefore require elevated temperatures and low pressure for

fabrication. Fabrication of gold films possess robust and strongly adhered by AACVD making it suitable to work at industrial scale (Hannon, Kodambaka, Ross, & Tromp, 2006). Hydrogen tetrachloroaurate, [$HAuCl_4$], was not suitable for conventional CVD due to its low decomposition temperature (175 °C) and poor volatility. However, [$HAuCl_4$] has revealed to be the best precursor in the growth of gold films via AACVD (Palgrave & Parkin, 2007). Another important advantage of AACVD arises from use of an ultrasonic humidifier to produce aerosol particles of precursor solution rather than focusing on the evaporation of precursors to transport it to the reaction chamber. This makes it simple to transport the precursor, thus becomes economical promising deposition method. Another favorable feature of AACVD is the utilization of carrier gas to deliver the precursor droplets to CVD reactor which requires adequate pressure to deliver the aerosols. For this purpose, the optimum gas flow rate during the process has to be established enabling increased the deposition rate due to the higher mass transfer of precursor on to the substrate. In a nutshell, AACVD is a versatile method to create thin films of a multicomponent material with controlled stoichiometry by chemical reaction of precursor on the substrate surface.

2.4.2.4 Deposition Conditions and their Influence on Morphology

The deposition conditions or parameters employed in a system during deposition are important to produce thin films with the required architecture and morphology. During an AACVD, the structure and morphology of the deposited thin films can be changed depends upon a variation in certain factors/conditions, for example the use of precursor, temperature, solvent and substrate. Field emission scanning electron microscopy (FE-SEM) is an important technique for defining the morphology of thin films by changing these factors. There are some main highlighted variables from which and how we can determine the variation in morphology.

a) Precursor

The selection of a precursor or complex plays a vital part in the deposition of thin film. It has been revealed that when different precursor were used for the fabrication of zinc oxide (ZnO) thin films via AACVD process, different topography, architectures and surface morphologies were obtained as shown in Figure 2.11. Walters et al. used Zn $(acac)_2$ as basic precursor for the growth of ZnO thin films (Walters & Parkin, 2009). They reported that the surface morphology of pristine ZnO films formed at 450 ^oC was round shape. However, hexagonal shaped nanoparticles (Figure 2.11a,b) could have been the subsequent growth of ZnO crystallites from the round shaped particles. In spite of using a normal precursor, Hamid et al. effectively fabricated ZnO films by using a zinc complex, $Zn_6(OAc)_8(\mu\text{-}OH)_2(dmae)_2(dmaeH)_2$ (OAc = acetate and dmaeH = *N,N′*-dimethylaminoethanol) at a temperature of 350 °C via AACVD process (Hamid et al., 2008).

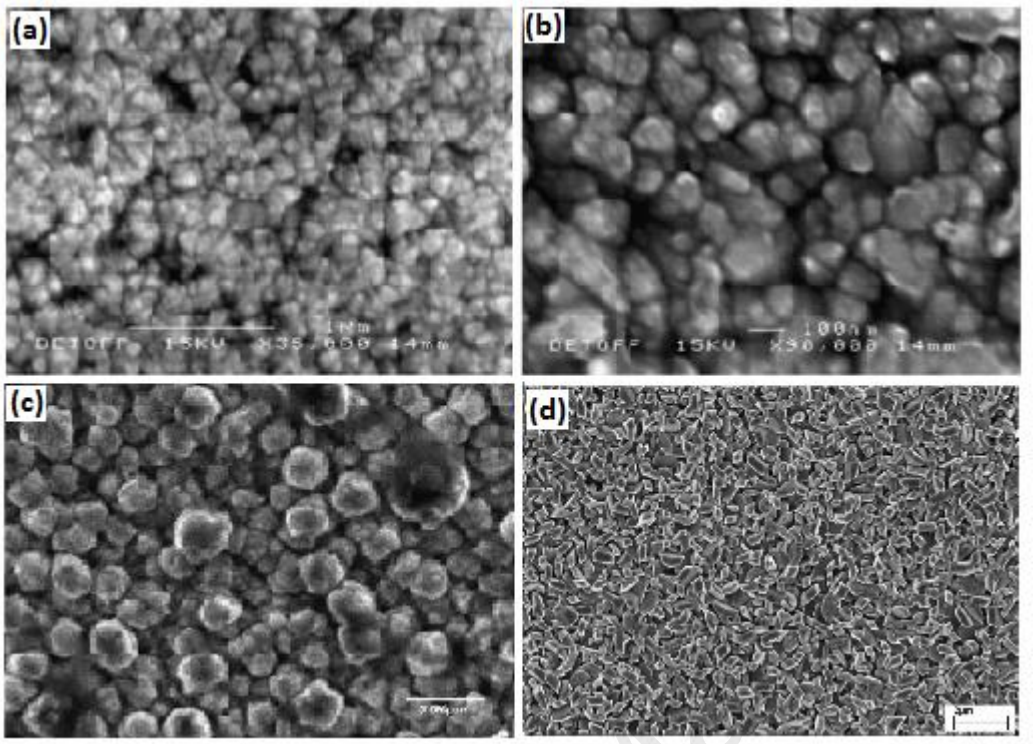

Figure 2.11: (a) SEM images of thin ZnO thin films fabricated by using different precursors (a,b) zinc acetate at 450 ^{o}C (Copyright permission from Walters & Parkin, 2009), (c) $Zn_6(OAc)_8(\mu\text{-}OH)_2(dmae)_2(dmaeH)_2$ at 350 ^{o}C (Hamid, et al., 2008) and (d) Zn_6 $(OAc)_8(\mu\text{-}O)_2(dmae)_4$ (OAc) at 400 ^{o}C (Copyright permission from M. Shahid, et al., 2012) by AACVD on FTO sunbstrate.

b) Deposition Temperature

The temperature can influence the texture of a film fabricated by AACVD. For example, Shahid et al. reported that when ZnO films were fabricated at various temperatures different morphologies had been experienced (M. Shahid, et al., 2012). Films fabricated at 250 °C had small, poorly defined individual grains in the range of 0.1–0.3 μm, while relatively large individual grains size of 0.2–0.7 μm were observed for the films fabricated at 475 °C. At temperatures of 325 and 400 °C, the films were more dense and flatter, with uniformly discrete grains as shown in Figure 2.12. The sphere-shaped particles had a good orientation and definite grain boundaries. . The various morphologies can be observed for the ZnO thin films, as shown in Figure 2.11 c, and it is establish that the zinc oxide thin film had a dense, compact, continuous, and smooth morphology. The spherical shaped particles have good orientation and clear well-defined grain boundaries.

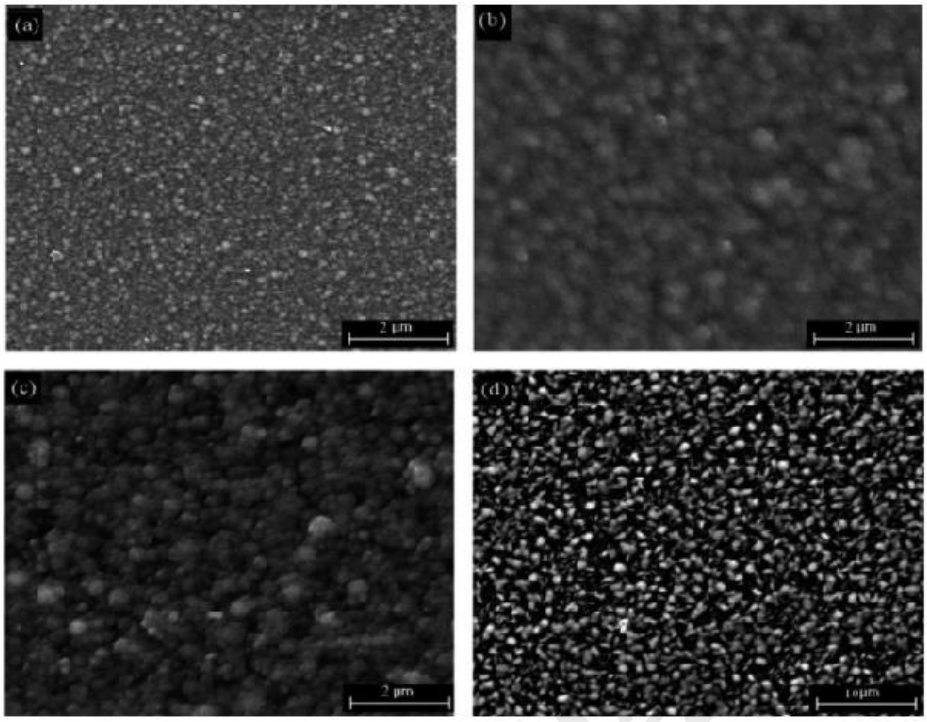

Figure 2.12: Surface morphology of ZnO thin films deposited from Zinc precursor at (a) 250, (b) 325, (c) 400 and (d) 475 ºC on glass substrate (Copyright permission from M. Shahid, et al., 2012).

Furthermore, Shahid et al. also used a novel hexanuclear zinc complex, Zn_6 $(OAc)_8(\mu\text{-}O)_2(dmae)_4$ (1) (OAc = acetato, dmae = N,N-dimethyl aminoethanolato) for the growth of ZnO films (M. Shahid et al., 2012). They stated that the ZnO film exhibited a more regular look, as compactly packed rectangular-shaped particles that were uniformly distributed, as shown in Figure 2.11d. They also reported that the production of well-developed isolated crystalline particles was due to the homogeneous decomposition pathway in AACVD approach. The formation of a well-defined ZnO nanostructure rather than the aggregation of nanoparticles is also well supported by the deposition of ZnO thin films using single source precursors (SSP) (AzadáMalik, 1994; Ying Wang, Li, Zhou, Zu, & Deng, 2011). These interpretations showed that the morphology of the semiconductor thin film significantly depend upon the choice of the precursors

c) Solvent

The effect of solvents on the morphologies of films grown by AACVD can be important and depending on the precursor. Titanium dioxide (TiO_2) thin films deposited by a AACVD using titanium (IV) isopropoxide (TTIP) with various solvents (hexane, ethanol, methanol, isopropanol and dichloromethane) which were used to deposit on glass and steel substrates at 550 °C as shown in Figure 2.13 (Edusi, Sankar, & Parkin, 2012).

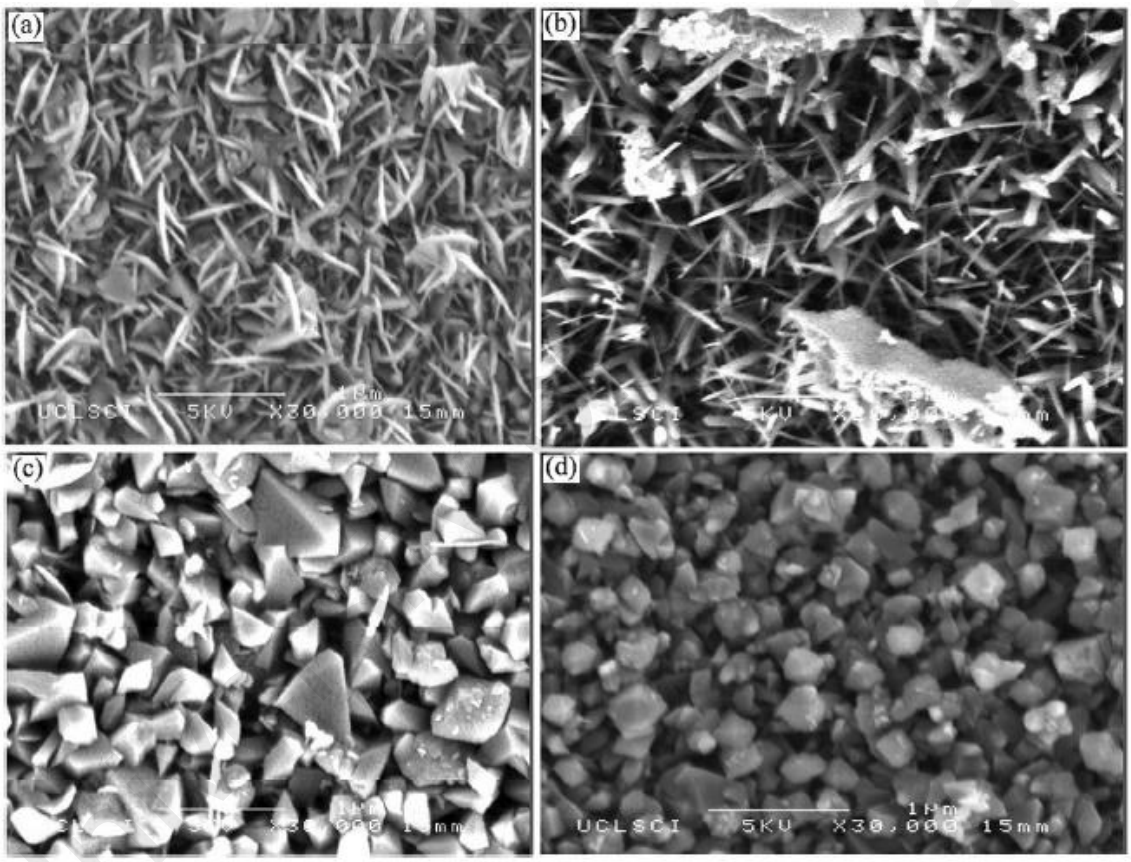

Figure 2.13: Different morphologies of TiO_2 thin films fabricated by using **(a)** 100% ethanol, **(b)** 100% methanol, **(c)** 10% methanol and 90% ethanol, and **(d)** 25% methanol and 75% ethanol from (a) chloroform and (b) chloroform/toluene (1:1) on steel via AACVD Copyright permission from (Edusi, et al., 2012).

Edusi, et al. reported that the solvent effected the phase of the fabricated TiO_2 film, it display either an anatase or rutile phase, or a combination of the two phases. As demonstrated in Figure 2.13, the influence of solvents on the phase of TiO_2 phase has been explained via AACVD. In case of methanol solvents under same conditions titania

films produce the rutile phase, while the other solvents only produced the anatase phase. More surprisingly, a mixture of ethanol and methanol as the solvent produced only the rutile phase at a mixture as low as 90% ethanol and 10% methanol as shown in Figure 2.13. This displays that the methanol has a directing influence on the formation of the rutile phase. They also exhibited that the TiO_2 films grown on steel substrates are photochemical active, and the rutile phase is less active than the anatase phase. Moreover, Panjawi et al. described the AACVD deposited titania thin films on gas-sensor substrates at 450 °C by using solution of titanium isopropoxide in toluene (N. Panjawi, A. Naik, M. E. Warwick, G. Hyett, & R. Binions, 2012).

d) Effect of Electric Field on AACCVD

Previous studies already reported the effect of an electric field during CVD, with crystallographic orientation, microstructure, and functional properties being the most influenced features (Naik et al., 2013; N. Panjawi, A. Naik, M. E. A. Warwick, G. Hyett, & R. Binions, 2012; Shaw, Parkin, Pratt, & Williams, 2005). This effect was also observed for titania thin films (Romero & Binions, 2013). These changes in morphology are thought to be a result of the interaction between a permanent or induced dipole in the CVD precursor species (or partially decomposed gas phase and/or surface species (Romero & Binions, 2013)) and the applied electric field and the application of EFDAACVD reactions (Crane, Warwick, Smith, Furlan, & Binions, 2011). It has previously been observed that there has been an enhancement of growth rate due to the introduction of an electric field in the deposition process. This has been attributed to the increase of kinetic energy of aerosol droplets which, in turn, increases the likelihood of nucleation on the substrate, or through bond activation due to the molecule being stretched along the direction of its dipole (Naik, et al., 2013), however in this instance it is unlikely that there is a strong interaction between the electric field and gas-phase species as the

TTIP precursor does not have a permanent dipole, as such gas-phase effects are not expected to dominate in this work.

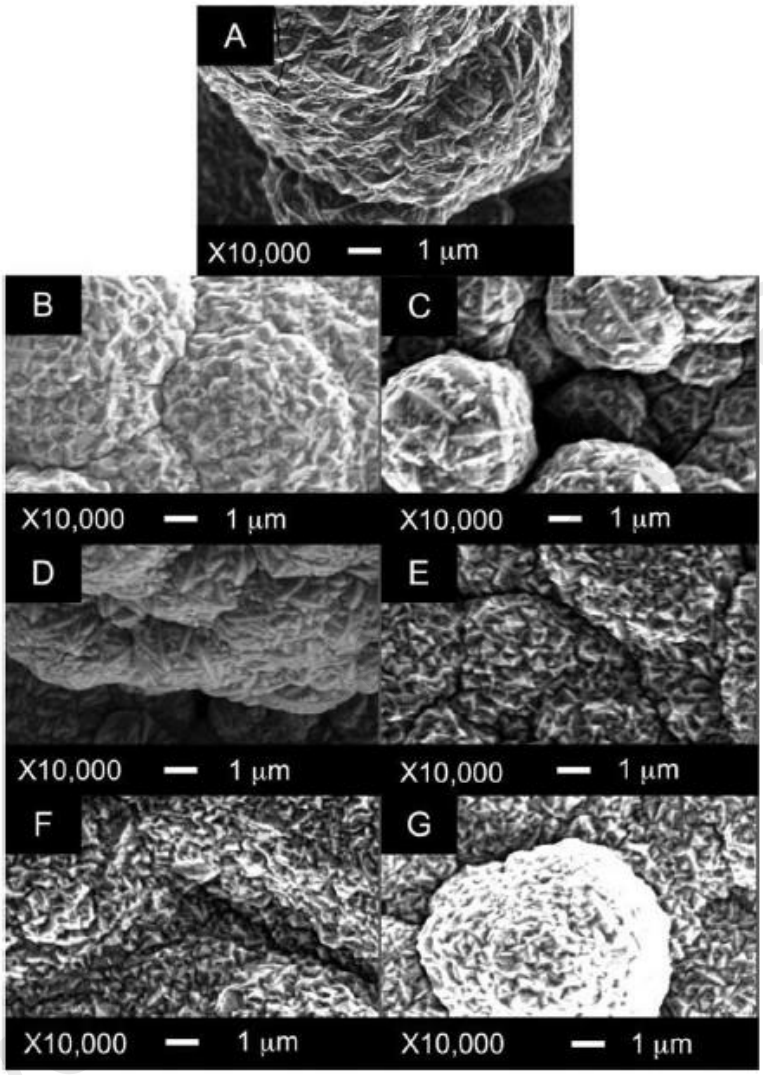

Figure 2.14: FE-SEM of TiO_2 films fabricated via EFD-AACVD of $Ti(O^iPr)_4$ solution in toluene at 450 °C by applying an electric field: **A)** no field. **B)** 1.11×10^4,**C)** 2.22×10^4, **D)** 1.11×10^5, **E)** 2.22×10^5, **F)** 4.44×10^5 and **G)** $6.67 \times 10^5 Vm^{-1}$ (Copyright permission from Panjawi, et al., 2012)

It is possible that the aerosol droplet may be charged: As the droplet approaches the heated substrate surface, the solvent evaporates and interaction with the electric field ceases. It is more likely, however, that the film growth is dominated by the interaction of the electric field with species on the substrate, most likely through the formation of surface dipoles, which direct the crystal growth via a strong localized electric field (Panjawi, et al., 2012; Romero et al., 2015). In this work, they examined the effect of the potential difference on

the architecture and surface morphology of the fabricated films. The electric field applied across the electrodes led to some differences in the morphology of the deposited films (Figure. 2.14B–G). Increasing the potential between 1.11×10^4 and 2.22×10^4 Vm^{-1} (Figure 2.14B and C) shows small 5 μm diameter of the sphere-shaped aggregates. The size of octahedral shaped particles was also uniformly decreased. By increasing the electric field strength (Figure 2.14C–G) larger aggregates are formed, and separate agglomerates were difficult to distinguish in the thick film.

2.5 Precursors for Ceramic Thin Films

The precursors can be widely categorized into three types.

i) The inorganic precursors, which do not contain carbon.

ii) The metal-organic precursors which contain organic ligands, but do not have metal-carbon bonds

iii) The organometallic precursors, which contain both organic ligands and metal-carbon bonds.

These kinds of precursors contain one or more atoms or group of atoms that are components of the target material. Target materials are produced by decomposition of precursor during synthesis process. Metal-organic and organometallic precursors have brought a great attention due to their ability to improve the structure, stoichiometry and the ligand framework, e.g. if a same metal of interest is surrounded by different types of hydrocarbons will finally change the chemical reactivity as well as physical properties of the different precursors for the same target material. Thus controlling these parameters is important for good precursor engineering.

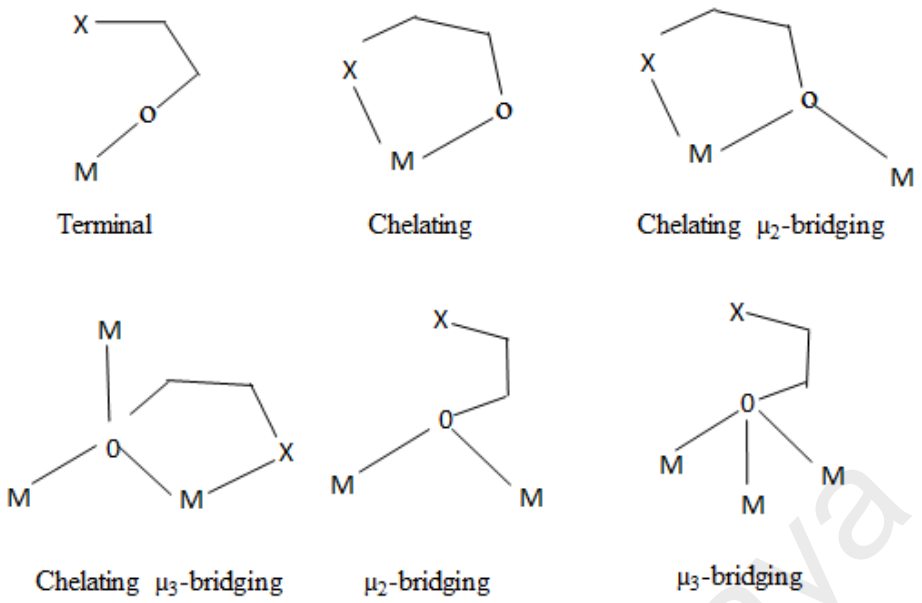

Figure 2.15: Coordination modes of alkoxide ligands

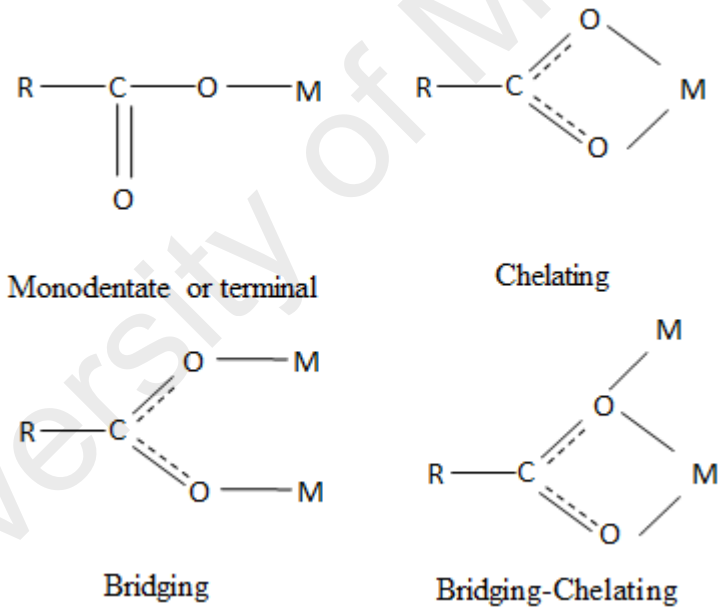

Figure 2.16: Coordination modes of carboxylate ligands.

Coordination modes of metal with alkoxide and carboxylate ligands are described in Figure 2.15 and Figure 2.16. Inorganic molecular precursors include binary hydrides or halides, owe chemical simplicity but they do not give similar degrees of freedom as in case of organo-metallic precursors. These inorganic precursors can also leave some halide contaminations in the target material at normal temperature of deposition.

2.5.1 Precursor Requirements for CVD

The struggle to prepare precursors is considered important that have a combination of exact characteristics which make them suitable for the basic of ceramic thin film deposition. Achievement of a precursor for adsorption and deposition depends on the grade of these characteristics and potential. However, the problem starts when the precursor preferably starts to react in vapour phase rather than on the surface of substrate during thin film fabrication by AACVD. This difficulty can be diminished by lessening the precursor concentration in a reaction chamber. Furthermore, the droplets that are created by reaction in vapour phase can contaminate the thin film. So it is compulsory to use precursor that preferably reacts or decomposes on substrate surface rather than in gaseous state during AACVD technique. For these types of systems precursor must be able to tolerate high temperature for short period of time before reaching the tube furnace for decomposition. So the necessary requirements for precursor design to fabricate the ceramic thin films have to meet the following properties.

Solubility: For film fabrication by CVD the first and primary demand for a precursor is to soluble in some appropriate, less dense and low boiling solvent. Which can allow the solution in making aerosol droplets to travel in the reactor region. The precursors should also have good volatility and easily travelled to the reactor zone.

Stability: A suitable precursor is the one which is stable in air and can be stored under normal conditions. Thus, it minimize the need of any inert or special conditions during film deposition. The precursor must be chemically and thermally stable during thermal decomposition to avoid premature decomposition and inimitable film growth.

Toxicity: Precursors with non-toxic or less toxic nature is always favored, if not then special storage and safety will be required during CVD.

Precursor Purity: One of the important demand is to synthesize pure precursor to improve fabrication of thin film that is free from residual impurities. Then it should be purified through suitable purification methods during the preparation of precursors. The decomposition of precursor should be clean, thus no residual contaminations can be incorporated in the ceramic thin film.

Precursor Reactivity: A suitable precursor for CVD is the one which decomposes on the substrate surface rather than in gaseous form. For good deposition it is necessary to heat the substrate before precursor decomposition in the tube furnace.

Synthesis in bulk: If a precursor is appropriate for CVD of thin film then it must also be easy to synthesize it in large amount without facing main difficulties.

Environment and cost effective: The precursor should be non-toxic, non-pyrophyric, non-flammable and non-explosive It should also be recyclable and its decomposition is either free from carbon dioxide (CO_2) emission or with very less quantity which can be controlled from environmental pollution. At the same time the CVD precursor must be easy to synthesize at low cost with high yield and stability in both air and moisture environment.

2.6 Characterization Techniques

2.6.1 Characterization of Precursors

2.6.1.1 Microanalysis

Microanalysis or elemental analysis is the qualitative and quantitative identification of chemical elements (atoms or ions) in a specimen. Results of elemental analysis face difficulties in determining the exact of stoichiometry heterometallic complexes due to the alteration in ratio of metals and ligands. However, by the help of atomic absorption analysis of metallic elements, the CHN results may become helpful to obtain the

composition of the heterometallic compounds. The validation of these results are further confirmed by single crystal X-ray analysis.

2.6.1.2 Infrared Spectroscopy

Infrared (IR) spectroscopy is a useful method for the determination of organic and inorganic moieties present in a sample. The IR spectrum is recorded by passing IR radiation through a sample and measured the absorption frequencies that correspond with the structural properties of molecules. The different functional groups attached to a molecule produce characteristics absorption in IR spectrum. The IR spectroscopy is known technique for the structural determination in the samples. The IR spectrum ranges from 14,000 cm^{-1} to 10 cm^{-1}. The region of most consideration for chemical interpretation is the mid-infrared regions (4000-400cm^{-1}). Which determines changes in vibrational energies within the molecules. The far-infrared region (400-10cm^{-1}) esteemed for molecules including inorganic compounds but needs somewhat particular laboratory techniques. IR spectra represents valuable data for the compounds with functionalized ligands, which face difficulties in structural determination of heterometallic schemes because of the screening of significant bands. The IR spectra becomes very complex because of crowded ligand climate and definite absorption band could not easily determined. The O-H group nature either bonded with central metal or may be a part of ligand can be known by the absorption frequency. The coordination performance of carboxylate to metal can be planned by identifying the factor $\Delta\nu$ = ($\nu(COO)_{asym}$ and $\nu(COO^{-})_{sym}$ by IR spectroscopy, if $\Delta\nu$ is less than 200 cm^{-1} the carboxylate behave as a bridging ligand. This technique also has been used to find out the presence of numerous alkoxy groups as every metal ligand bond produces a characteristic absorption such as ν_{OMe} = 1185, ν_{OEt} = 1020, ν_{OPr} = 839,1124 and 1158 cm^{-1}, respectively in different mixed metal alkoxides. The terminal and bridging alkoxy groups in various heterobimetallic

species may be determined on the behalf of IR absorption bands present in the area around 1022-1181 and 939-1072 cm^{-1}, respectively. Heterometallic diketonates shows two absorption bands around 1565-1573 due to C=O and 1510-1514 cm^{-1} due to C=O stretching vibrations. The presence of the absorption frequency due to bonded "dmae" bridging moiety appeared between 1070-1075 cm^{-1} varied from those reported for free "DmaeH" at 1040 cm^{-1}. A band identified in the region less than 550 cm^{-1} may be relate to M-O stretching vibrational band for the samples.

In case of inorganic compounds IR spectroscopy is very useful technique to determining the nature, and added impurities both in powder and thin films. FTIR was also useful for the evaluation of Hydrogen (H) and moisture contents on deposited films. The IR spectroscopy has verified to be a helpful analytical method for industrial and environmental areas.

2.6.1.3 Thermogravimetric Analysis (TGA)

Thermogravimetric analysis (TGA) is an analytical method used to approach the thermal stability of the materials. It also helps to obtain the components by observing the weight changes that occur when a sample is heated. Thermogravimetric measurements are generally carried out in air or an inert atmosphere (He, Ar and N_2) and weight loss is calculated as a function of raising temperature. Furthermore, differential scanning calorimetry (DSC) instrument can also record the temperature differences or heat flow between the sample and reference pans. DSC can be used to calculate the melting point, enthalpy, energy released or absorbed through chemical reaction during heating process. During TG analysis, when materials are heated they can lose weight whether by a sample drying process. In this study TGA analysis is performed to examine the pyrolysis temperature of the complex to give stable metal oxide or halide end product.

2.6.1.4 X-ray Crystallography

X-ray crystallography is a device that can see inside of crystals to determine their atomic and molecular structure. Which allow us to completely identify their structures, geometries and unit cell size. Based on the diffraction pattern obtained from X-ray scattering off the orderly arranged atoms or molecules in the crystal, the electron density map can be refined to generate valuable information about their atomic positions, bond length and angles and disorder and various other information. In single crystal X-ray diffraction the crystalline atoms cause a beam of incident X-rays to diffract into many specific directions, construct a diffraction pattern of spots called reflection. Each reflection relates to one set of planes within the crystal and the density of electrons is obtained from position and brightness of the several reflections collected as the crystal is gradually rotated in X-ray beam. For single crystals with a sufficient purity and uniformity, X-ray diffraction data can evaluate the mean of bond angle and bond length in few thousands of an angstrom and within a few tenth of a degree, respectively. X-ray crystallography is useful in determining identified materials, analyzing novel materials and differentiating materials that appear alike by other experiments. The single X-ray crystallography technique includes three steps to model the crystal structure. First step is to develop an appropriate crystal of the material under investigation. The crystal should be effectively large, stoichiometry pure, regular structure and free of defects like cracks. In second step rising of crystal in an intense beam of monochromatic X-ray, produce the arrangement of reflections. The third step is refinement of the thousands of the reflection intensities composed by the full reflection of the crystal. The reflection data are collected computationally with analogous chemical details to develop and refine a model of the location of atoms with in the crystal structure.

2.6.2 Characterization of Thin Films

2.6.2.1 X-ray Powder Diffractions

X-ray powder diffraction is a rapid technique primarily to identify crystalline phase and degree of crystallinity of thin films and powder. The diffraction pattern allows the detection of phase composition and texture of the film, favored orientation and size of crystallites and existence of film stress. By scanning the sample through a range of 2θ angles, all possible diffraction directions of the lattice should be achieved due to the random orientation of the thin films. It is difficult to identify the crystal structure for the high symmetry crystals. A large library of spectra of famous compounds is available at JCPDS (Joint Committie for Powder Diffraction Standards) files. When the powder pattern of the sample are collected and miler indices, d-spacing and lines intensity are displayed, these can be matched with the standard reference pattern of identified compounds in the library.

2.6.2.2 Raman Spectroscopy

Raman spectroscopy is an efficient and non-destructive spectroscopic technique based on the scattering of monochromatic light. Photons of the monochromatic light are absorbed by the samples and then remitted. Frequency of reemitted photons is shifted up and down in comparison with the original monochromatic frequency called a raman shift. This shift provides information about vibrational, rotational and other low frequency modes in the molecules. Raman shift in wavelength of the scattered radiation that provides the chemical and structural information. Raman shifted photons can be of either higher or lower energy, depending upon the vibrational state of the molecule under study.

2.6.2.3 X-ray Photoelectron Spectroscopy

X-ray photoelectron spectroscopy (XPS) is an important and widely used surface and subsurface analysis technique in a many fields of study in physics and chemistry such as microelectronics, heterogeneous catalysis, environmental geochemistry etc. XPS investigates the energy distribution of electrons removed from the solids by irradiation of X-ray and the photoelectric effect: the electrons contain information about chemical oxidation state, electronic structure, binding energy and elemental composition of the compounds being studied. Thus, surface composition as well as the electronic environment can be determined. Since the photoelectrons examined come only from the topmost atomic layer of the solid surface being analyzed, the method is powerful tool for studying the interfacial phenomena at the solid-solid and solid-gas boundaries. XPS is usually accomplished by exciting the surface with mono-energetic Al *kα* x-rays causing photoelectrons to be escaped from the sample surface. An electron energy analyzer is used to measure the energy of the ejected photoelectrons. From the binding energy and intensity of a photoelectron peak, the elemental identity, chemical state, and quantity of a detected element can be identified. A typical XPS spectrum is a plot of the number of electrons detected versus the binding energy of the electrons identified. Each element produces a characteristic set of XPS peaks at specific binding energy values that directly find each element that exists in or on the surface of the material being studied. The XPS data explains about surface layers or thin film structures is important for many industrial and research applications where surface or thin film composition plays an important part in performance including: nanomaterials, photovoltaics, catalysis, corrosion, adhesion, electronic devices and packaging, magnetic media, display technology, surface treatments and thin film coatings used for several applications.

2.6.2.4 BET Analysis

Brunauer–Emmett–Teller (BET) study provides a detailed specific surface area estimation of materials by nitrogen multilayer adsorption measured as a function of relative pressure using a fully automated analyzer. The technique includes external area and pore area evaluations to investigate the total specific surface area in m^2/g yielding important information to study the effects of surface porosity and particle size in many applications. While Barrett-Joyner-Halenda (BJH) analysis can also be used to find out the pore area and specific pore volume using adsorption and desorption method. This method characterizes pore size distribution independent of external area due to particle size of the sample.

2.6.2.5 Field Emission Scanning Electron Microscope (FE-SEM) and Energy Dispersive X-ray Analysis (EDX)

Field emission scanning electron microscope (FE-SEM) uses a focused electron analysis to extract structural chemical data from required area in a thin film. The high resolution spectra of FE-SEM make it a useful tool to characterize a broad range of materials at several nm and µm. FESEM offers high magnification with greater depth then optical microscopes. FESEM images may be distorted by the surface potential which improves an insulator level defects at sharp contours. Nonconductive samples are decorated by conductive layer of Au, Pt or carbon to disperse the surface charge. FE-SEM images at high magnification describe the surface morphology or architecture and film thickness.

The most usual extension to the FE-SEM is the energy dispersive x-ray spectrometer (EDX). The energy level for EDX systems is from 1.0 to 220 KeV, which detects the elemental composition or chemical characterization in the composite thin films. When EDX detectors with thin protective layers functioned in high vaccum systems, allow the

analysis of the lighter elements down to B. The analysis depth depending on the path length of the X-ray not on the primary electron beam. As a results EDX signals may arise from the depth of 0.5 μm or more. Due to pulse counting mode of EDX system, it has ability to detect the characteristic X-ray of all elements above F in the periodic table. However, EDX takes a lesser time to scan the complete spectrum as compared to wavelength dispersive X-ray analyzer. The simultaneous development of the high-brightness, high beam current thermal field emission gun-SEM has provided an electron-optical platform that ideally matches the performance of the silicon drift detector (SDD-EDS).

2.7 Electrochemical Applications of Ceramic Thin Films

Micro and nanostructured thin films of metal oxides and metal halides for electrochemical applications has been recognized recently, but the number of studies is increasing suddenly. The recent importance of renewable energy sources has sparked research on very fundamental and applied levels. The most prominent applications in Li-ion batteries, fuel cells, gas sensors and photovoltaic devices. The most important drawback is the material, which is either very expensive noble metal or lacking in performance and stability. It is therefore one of the main future task to identify a material which is cost effective, stable and environment friendly. Ceramic thin films deposited by AACVD, EFDAACVD and EPD are therefore the potential candidate to test their activity and stability for application in electrochemical devices, some of these are discussed below.

2.7.1 Batteries and Supercapacitors

Many chemically deposited metal oxide thin films including ruthenium oxide, iridium oxide, manganese oxide, cobalt oxide, nickel oxide, tin oxide, iron oxide, pervoskites, ferrites, etc. have been applied in supercapacitors.(Fujimoto, Kuwata, Matsuda,

Kawamura, & Kang, 2015; C. D. Lokhande, D. P. Dubal, & O.-S. Joo, 2011) The thin film deposition methods involving the growth from solution are called as chemical methods. Depending on applications, one would prefer thin films which have a special texture, low grain boundary density, or smooth surfaces. Amongst the numerous metal oxide materials, only RuO_2, MnO_2, NiO and Co_3O_4 thin film based systems have gained more attention due to superior electrochemical capacitor response. Apart from the scientific quest for high capacitance of metal oxide thin films, the long-term cycling stability of these electrodes is a technological issue that must be addressed to evaluate the commercial development of metal oxide thin film based aqueous supercapacitors. Other issues such as self-discharge, corrosion of the current collector, low temperature performance etc should also be studied. Considering that metal oxide thin film based supercapacitor technology is still in its beginning, future research and development should ultimately yield high-performance, low cost, and safe energy storage devices. Synthesis of phase-pure SnO_2 hierarchical structures with different morphologies such as nanorods, nanosheets, and nanospheres, as well as their modifications by doping and compositing with other materials. They studied the design of SnO_2-based nanostructures with improved performance in the field of lithium-ion batteries (LIBs), supercapacitors and energy conversion performance (J. S. Chen & Lou, 2013; Q. Zhao, Ma, Zhang, Wang, & Xu, 2015). SnO_2-based nanostructures, such as anode materials, demonstrate superior cycle performance of lithium storage by doping (J. S. Chen & Lou, 2013). In the supercapacitors, the prepared SnO_2-based nanostructures provide fast ion and electron transfer, which led to a prominent supercapacitor performance. Therefore, SnO_2-based nanostructures with a proper design can possess advanced physical and chemical properties, which are vital for a variety of energy and environment applications.

Nanostructured V_2O_5 has potential application in the fields of lithium-ion batteries, the as-prepared vanadium hollow microspheres can be calcined into crystalline V_2O_5 without

changing their morphologies. These V_2O_5 products exhibit improved electrochemical properties when they are used as cathode material in lithium-ion batteries and show good application potential. The prepared V_2O_5 exhibits desirable electrochemical properties such as high capacity and remarkable reversibility when it is used as cathode material in a lithium-ion battery (A. M. Cao, Hu, Liang, & Wan, 2005). Mesoporous Co_3O_4 nanowire arrays (Y. Li, Tan, & Wu, 2008), Mn_3O_4−graphene hybrid (Hailiang Wang et al., 2010), Fe_3O_4-based Cu nano-architecture (Taberna, Mitra, Poizot, Simon, & Tarascon, 2006), reduced graphene oxide/Fe_3O_4 (Guangmin Zhou et al., 2010; X. Zhu, Zhu, Murali, Stoller, & Ruoff, 2011) electrode nanocomposites were employed as a high-capacity and rate capability anode material for lithium ion batteries applications.

2.7.2 Fuel Cells

Fuel cells, due to their high efficiency and low environmental effect, have been paid more attention in these years. The fuel cell is the most potential tool for automotive, portable, and stationary applications. Although hydrogen is an ideal fuel for polymer electrolyte membrane fuel cells (PEMFC), it is very dangerous to store it under high pressure. The hydrogen production is still challenging. To avoid these drawbacks, the direct methanol fuel cell (DMFC) has been developed with a simplified structural system, using aqueous methanol as the fuel. It is widely established that carbon monoxide (CO) species produced in the process of methanol electro-oxidation are the main poisoning intermediate that slows down the oxidation kinetics and rate of reaction. To resolve this issue, Pt-based binary catalysts (PtRu (Koper, Lukkien, Jansen, & van Santen, 1999) and (Q. Lu, Yang, Zhuang, & Lu, 2005), PtMo (Russell, Ball, Maniguet, & Thompsett, 2007) , PtSn (Y. Guo, Zheng, & Huang, 2008), etc.) and ternary catalyst (PtRuNi (Moreno, Chinarro, Pérez, & Jurado, 2007)) have been established to enhance the catalytic activity of Pt through bifunctional mechanism. Besides this, it has been found that Pt with metal oxides

like (Rolison, Hagans, Swider, & Long, 1999) TiO_2 (Song, Qiu, Guo, & Li, 2008), Al_2O_3, ZrO_2 (Ribeiro, Mendes, Perez, Souza, & Schmal, 2008), MoO_2 (Ioroi et al., 2006), etc. can efficiently improve the electro-oxidation of methanol and reduce the CO poisoning. Firstly, metal oxides stabilize Pt particle dispersion, which increase the surface area of the catalyst. Secondly, metal oxide have a good ability for storing and releasing oxygen, which plays a vital role in CO_{ads} (adsorbed CO) methanol oxidation. At the same time, the low cost and the abundance of metal oxides can help to reduce the price of DMFC. Therefore, metal oxides are suitable additives for Pt catalysts. Direct methanol fuel cells (DMFCs) have some benefits such as high energy density, low temperature operation and convenient operation (Y. Huang et al., 2014), thus they have been considered as a potential candidate for power generation in portable electronic devices and hybrid electric vehicles.

After the hydrothermal reaction, (graphene oxide) GO sheets evolved into (reduced graphene oxide) RGO sheets and well-crystallized Mn_3O_4 nanoparticles uniformly distribute on RGO sheets, followed by the spontaneous deposition of Pt on Mn_3O_4/RGO surface via the galvanic replacement process between Mn_3O_4 and $PtCl_4^{2-}$ (Y. Huang, et al., 2014). By combining the advantages from the small-sized and well-dispersed Pt nanoparticles, the possible synergetic effect from the ternary components, and the strong metal-support interaction, the Pt/Mn_3O_4/RGO catalyst exhibited higher electrochemical surface area (ECSA), better tolerance toward CO and outstanding electrocatalytic activity than the Pt/RGO catalyst, and long-time stability than the conventional Pt/C catalyst. Thus, this work supplied an important and efficient way to build up various two-dimensional sandwich-like nanomaterials that provide an important platform for many advanced industrial fields, such as electrocatalysis, photocatalysis and sensors. Moreover, metal oxides (CeO_2, TiO_2 and SnO_2) and Pt nanoparticles were successively decorated on carbon nanotubes (CNT). The effect of metal oxides on the catalytic behaviour of Pt for

electro-oxidation of methanol has been studied by cyclic voltammetry (CV), chronoamperometry (CA) and electrochemical impedance spectroscopy (EIS) methods, purpose to establish the most suitable catalyst for fuel cells. Different $Pt/MO_2/CNT$ catalysts (M = Ce, Ti, Sn) were synthesized and the electrocatalytic activity in respect to the electro-oxidation of methanol in H_2SO_4 solution were examined. The CV revealed that the current density of the oxidation peak increases for $Pt/CeO_2/CNT$ as compared to Pt/CNT catalysts, showed the highest catalytic activity. The kinetics of methanol oxidation, rate of reaction, maximum frequency, charge recombination life time were studied by using electrochemical impedance spectroscopy. It was establish that metal oxides can promote the electro-oxidation of CO_{ads}, which was verified by a decrease of the charge-transfer resistance at a low potential region. The accumulation process of CO_{ads} was not observed as it was on the Pt/CNT electrode. In addition, the decreased rate of charge-transfer resistance was determined by the metal oxides added, which indicated different reaction activity of CO_{ads} oxidation with hydroxyl groups on various metal oxides (Yuan, Guo, Qiu, Zhu, & Chen, 2009). In the present investigation, the potential of formation of solid electrolyte thin film on ceramic substrates has been demonstrated using spray pyrolysis technique (SPT). Analysis of (gadolinia-doped ceria/ galdolinium-doped ceria) GDC/GDC structure revealed that electrolyte-grade substrates could be coated with ultra-thin protective layer using SPT to avoid the interfacial reactions. Besides, the studies on GDC films deposited on NiO–GDC substrate depicted that the electrolyte-grade GDC films could also be deposited using SPT. However, some modification, as mentioned, should be employed in the process. Further, the choice of material for solid electrolyte film i.e. GDC and NiO–GDC as substrate (precursor composite ceramic anode) would enable to utilize the prepared structure (GDC/NiO–GDC) for fabrication half-cell in low temperature solid oxide fuel cells (SOFCs). Electrical characterization of GDC/NiO–GDC structure showed that there is only a

nominal decrease in overall ionic conduction of the structure over the bare substrate, indicating good quality film/substrate interface. Such synthesized structures along with a layer of suitable cathode material, could find promising application in low temperature SOFCs (Myung, Ko, Lee, Lee, & Hyun, 2012). In practical application of direct methanol fuel cells (DMFC), methanol concentration plays a vital role. In this regard effect of methanol concentration was studied by varying the concentration of methanol in the presence of CuO–1.5ZrO_2 composite oxide film modified Pt electrode deposited by AACVD at a scan rate of 50 mV s^{-1} in the presence of 0.1 M KOH can be noticed that anodic peak current increases and the anodic peak potential have a slightly shifted to positive potential while increase in the methanol content due to the saturation of active catalytic sites at the CuO–1.5ZrO_2 composite oxide film modified Pt electrode surface.

2.7.3 Electrochemical Sensor

Electrocatalysts are occasionally employed in the development of electrochemical sensors. It has recently been shown that composite electrodes of transition-metal oxides are electrocatalytically active for range of different analytes. Lead (IV) oxide is a noted electrocatalyst and is characterized with good electrical conductivity, mechanical stability and chemical inertness, and high oxygen evolution overpotential. Lead dioxide electrodes are particularly attractive since they do not require voltage pretreatment to attain their electrocatalytic activity (Biljana Šljukić, Craig E. Banks, Alison Crossley, & Richard G. Compton, 2007). These properties suggest applications in a variety of fields, particularly the generation of oxygen (Ho, Filho, Simpraga, & Conway, 1994) and ozone (Feng, Johnson, Lowery, & Carey, 1994) and electro-oxidation of organic compounds, both for their synthesis (Amadelli, De Battisti, Girenko, Kovalyov, & Velichenko, 2000; Treimer, Feng, Scholten, Johnson, & Davenport, 2001) and degradation of organic contaminants

in water (Grimm, Bessarabov, Maier, Storck, & Sanderson, 1998; Hyde, Jacobs, & Compton, 2004; Saterlay et al., 2001).

Transition metals have attracted the attention of researchers due to their multiple oxidation which make them suitable candidates for electron-transfer processes (El Khatib & Abdel Hameed, 2011; Rafiee & Fakhari, 2013). Because transition metallic nanoparticles (NPs) increase their surface area, enhance mass transport and hold good biocompatibility, the metallic nanoparticles can be used as modification for sensors and biosensors (Lin, Lin, & Chen, 2013). Especially, transition metal oxides combine physical with chemical properties, which make them become the promising electrode materials (Azaceta et al., 2012). Nanomaterials are gaining increasing interest in the development of several research fields. Among various nanomaterials, nickel oxide (NiO) and copper oxide (CuO) are attractive electro-catalysts in electrochemical different catalytic application (Arredondo Valdez, García Jiménez, Gutiérrez Granados, & Ponce de León, 2012; Ripolles-Sanchis, Guerrero, Azaceta, Tena-Zaera, & Garcia-Belmonte, 2013). Due to relatively low cost and high catalytic activity, NiO and CuO can be ideal modifying agent. Some effort have been made on determination of glucose (Lin, et al., 2013) and (X. Wang, Liu, & Zhang, 2014), H_2O_2 (Gao & Liu, 2015) and other biomolecules (S. Zhou et al., 2013) by using nanostructured NiO and CuO materials (B. Liu et al., 2016). CuO–2TiO_2 electrode in electrochemical sensor was investigated towards the detection of NO_2^- ions and the electrode showed the limit of detection (LoD) of 0.0166 μM with linear range of 10 to 200 μM. Beyond this, present sensor electrode is more selective towards NO_2^- ions in the presence of other common interfering species. This CuO–2TiO_2 electrode is more ideal candidate for the selective and sensitive detection of toxic NO_2^- ions from environmental remediation aspect (Ehsan, Naeem, McKee, et al., 2016).

Furthermore, Pt-based GO modified nano-catalysts not only maximize the availability of nano-sized electro-active surface area for electron transfer but also provide better mass transport of reactants to the electro-catalyst and sensors for dopamine (DA), ascorbic acid (AA), uric acid (UA), catecholamines and acetaminophen (AP) (Alothman, Bukhari, Wabaidur, & Haider, 2010; Atta, El-Kady, & Galal, 2010; S. A. Kumar, Tang, & Chen, 2008; B. Liu, et al., 2016). The NiO–CuO/Graphene/Glassy carbon electrode enhanced the oxidation peak currents towards DA, acetaminophen (AP) and tryptophan (Trp) and the negative shift of the oxidation peak potentials, which were attributed to the incorporation of transition metal oxides providing larger specific surface and electro-catalytic activity (B. Liu, et al., 2016). This modified electrode exhibited that the linear response ranges for detecting DA, AC and Trp were 0.5–20 μM, 4–400 μM and 0.3–40 μM, respectively, and the detection limits were 0.17 μM, 1.33 μM and 0.1 μM (*S*/*N*=3). The proposed method for GO–La/CPE electrode provides an effective linear calibration ranges of 0.01–0.1 μM and 0.1–400.0 μM, low detection limit of 0.32 nM, good repeatability and stability. Thus, the developed GO–La/CPE sensor presents good potential application in the selective detection of DA (F. Ye et al., 2015). $CoTiO_3$–TiO_2 electrode in electrochemical sensors has been investigated towards the detection of DA. The results indicate that the $CoTiO_3$–TiO_2 electrode showed good electrocatalytic activity for DA with the limit of detection (LoD) of 0.083 μM and a linear range of 20 to 300 μM (Ehsan, Naeem, Khaledi, Sohail, Hakeem Saeed, et al., 2016). The improvement of various nanostructured metal-oxide such as ZnO, CuO, CuO_2, MnO_2, Mn_2O_3, TiO_2, CeO_2, SiO_2, ZrO_2 have been used as glucose biosensors (M. M. Rahman, Ahammad, Jin, Ahn, & Lee, 2010).The study on H_2O_2 detection is of practical significance for both academic and industrial purposes. Electrochemistry can offer simple, rapid, sensitive, and cost effective means since H_2O_2 is an electroactive molecule (W. Chen, Cai, Ren, Wen, & Zhao, 2012).

2.7.4 Photoelectrochemical (PEC) performance of ceramic thin films

Now a days the progress of clean energy has become a main attention among the scientists. Water using sunlight has attracted attention as a new renewable energy source to generate hydrogen gas with negligible pollution. Because the other energy sources such as fossil fuel, coal, oil and natural gas is quickly being reduced. Hydrogen gas has developed as a new alternate energy supply that offers several benefits as compared to other fuels, including a decrease in global warming carbon dioxide (CO_2) emissions, developments in air quality and the capability to reduce the energy crises. On one hand, the wide use of fossil fuel leads to a decline in natural resources. While on the other hand, the energy requirements have enormous effect on society include financial troubles and environmental pollution. Since climate alertness has raised in society, the hydrogen generation has suffered difficulties in the form of greenhouse effect and global warming issues. Hydrogen is secondary and alternate energy carrier that allows the normal energies such as coal, oil, gas and nuclear fission to join the clean sustainable energies. Furthermore, hydrogen has distinct properties that make it a potential candidate for future clean energy, which are described below:

i. It is recyclable and can be efficiently converted into electricity
ii. Abundantly available water is a raw material for hydrogen generation.
iii. It can be kept as a liquid, gas, or solid in the form of metal hydrides.
iv. It can be easily carried through large distances by using pipelines or by other ways.
v. It can be transformed into other energy forms than any other fuel.
vi. As an energy carrier, hydrogen is environment friendly and economical.

The quest to split water into oxygen and hydrogen has explored a huge variety of nano/micro photcatalyst materials and solar energy techniques that can actively perform this ambitious goal (Shi et al., 2015; Hisatomi, Kubota, & Domen, 2014). However,

highly efficient hydrogen production by photocatalytic water splitting is limited by many factors such as non-ideal photocatalyst materials, complex thermodynamics of the reactions and ambiguous mechanisms and therefore is still far from industrialization levels (Ma et al., 2014; Martin et al., 2015). Continuous efforts are being made to resolve these problems and to make solar photocatalytic hydrogen production feasible. A variety of photoactive materials have been designed and developed with the aim to fix the main PEC obstacles such as proper conduction/valence band position, narrowing of the band gap to harness visible light, fast electron/hole pair separation/transportation (Baker & Kamat, 2009; Gonçalves, et al., 2012; Le Formal, et al., 2010; Leung, et al., 2010; G. Li, et al., 2013; Momeni, et al., 2015; Sivula, et al., 2010; J. Su, et al., 2010; M. Wang, et al., 2013; Yan, et al., 2012), however, these extensive studies could not find an individual material which can overcome all these issues at once. The main criteria for photocatalyst material is low cost, environmentally friendly, high efficiency and stability under visible light irradiation (Serpone & Emeline, 2012; Walter et al., 2010). TiO_2 is a strong candidate due to its high stability in aqueous solutions and high photovoltaic and photocatalytic activity (Nowotny, Bak, Nowotny, & Sheppard, 2007; Fujishima, Zhang, & Tryk, 2008) but it is restricted to work under UV light due to its large a band gap (3-3.2 eV) limitations.

Photoelectrochemical water splitting cells require semiconductor materials with following characteristics:

i. An ideal optical band gap.
ii. Holes diffusion length should be small
iii. Able to support rapid charge transfer at a semiconductor/electrolyte interface
iv. Show stability to photocorrosion
v. Space-charge layer should be relatively large.

In the photoelectrochemical mechanism, when light is absorbed by the semiconductors metal oxide electron hole pairs are generated as a result photolysis of water take place and oxidation reduction reaction occurs at anode and cathode for the production of hydrogen and oxygen.

$$H_2O \xrightarrow{h\nu} H_2 + 1/2O_2 \tag{2.1}$$

$$2h\nu \rightarrow 2e^- + 2h^+ \tag{2.2}$$

$$2h^+ + H_2O \rightarrow 1/2O_{2(g)} + 2H^+ \tag{2.3}$$

The electron and holes get separated due to potential produced at interface of the semiconductor-electrolyte due to band bending. The holes migrate to the interface and reacts with the water to produce oxygen.

$$2e^- + 2H^+ \rightarrow H_{2(g)} \tag{2.4}$$

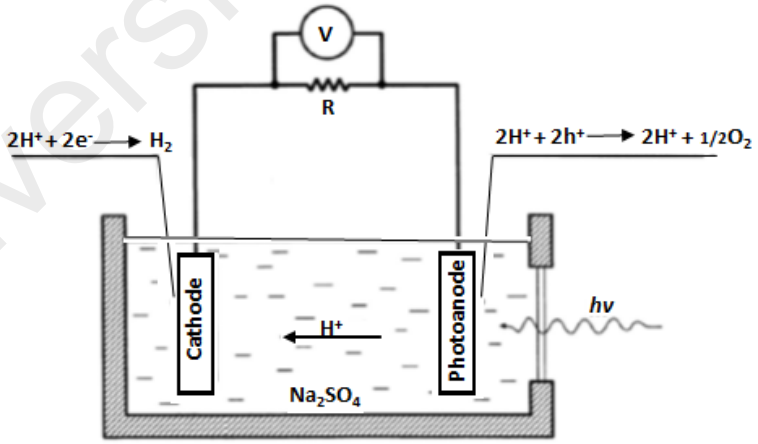

Figure 2.17: Illustration of a photoelectrochemical cell that consists of a semiconducting photoanode.

The electron move to an external circuit and arrive at interface between counter electrode and electrolyte, where hydrogen ion is reduced to hydrogen as gas. These overall photo-

induced charge separation obtained for the semiconductor in the photoelectrochemical cells are schematically shown in Figure 2.17.

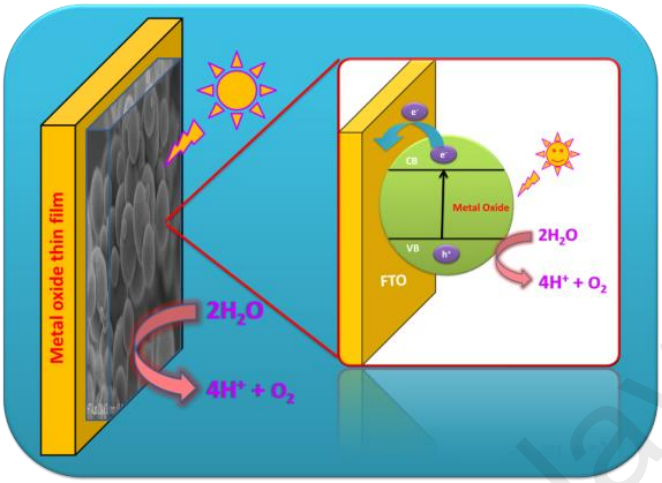

Figure 2.18: Schematic representation for the photo induced charge-separation process at metal oxide thin film in a photoelectrochemical cell (Copyright permission from Naeem et al., 2015).

Overall photoelectrochemical decomposition of water is shown in Figure 2.18. Numerous PEC cells using thin film electrodes have been established especially for the cleavage of water. But suitable electrodes with ideal band gap and stable towards photocorrosion are still under research.

An optical band gap is the energy gap, usually apply to the energy difference (in electron volts) between the top of the valence band (VB) and the bottom of the conduction band (CB) in semiconductors and insulators. The optical band gap describes that which part of the solar spectrum a photovoltaic cell absorbs. In case of semiconductors, there band gap is always one of two types, a *direct band gap* or an *indirect band gap*. The band gap is called "direct" if the momentum of electrons and holes is the same in both the CB and the VB; an electron can directly emit a photon (Figure 2.19). In case of "indirect" gap, a photon cannot be emitted because the electron must travel through an intermediate state and transfer momentum to the crystal lattice (phonon).

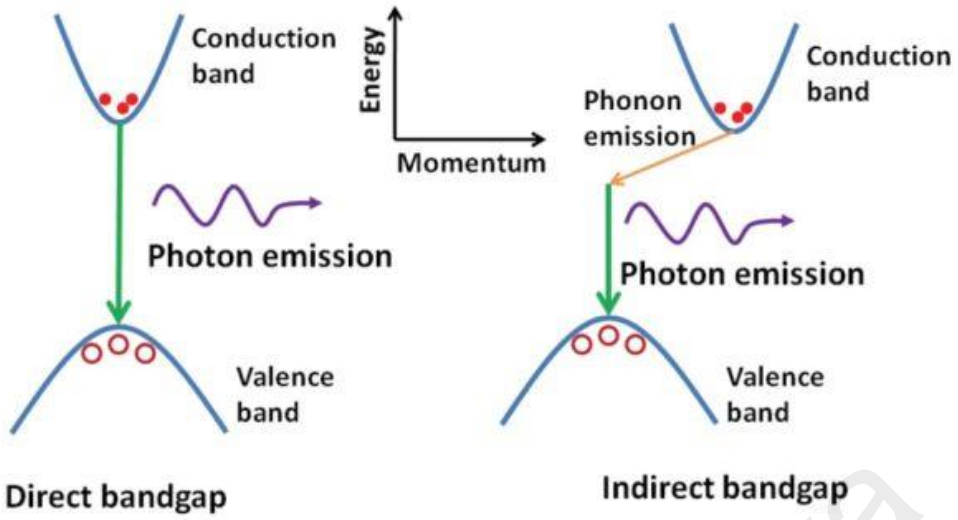

Figure 2.19: Optical transitions in semiconductors with a direct and an indirect bandgap. The indirect transition requires assistance of a phonon with energy h*v* (Copyright permission from Seo & Hoffmann, 1999).

The optical band gap of thin films can be examined by the Tauc equation, if the top of the VB and bottom of the CB are expected to have a parabolic shape. The Tauc's equation is

$$\alpha = A(h\nu - E_g)^{\gamma}/h\nu$$

where, α is the linear absorption coefficient of the material, hν is the energy of photon, A is a proportionality constant and γ is a constant depending on the band-gap nature; γ= 1/2 for direct band gap and γ = 2 for indirect band gap (Seo & Hoffmann, 1999).

The water splitting potential is 1.23 V (G = +237.7 KJ/mol). Which relates to photon below about 1000 nm and covers a large part of spectrum. For water splitting reaction to be thermodynamically favorable, the band gap of the semiconductor phorocatalyst should have these reduction potentials. The conduction band should have higher energy (more negative potential) than the hydrogen evolution potential (H_2/H^+) and the valence band should be lower in energy (more positive potential than the oxygen evolution potential (H_2O/O_2). So electrons can lower their energy being transferred to hydrogen ions in solution and holes lower their energy being transferred to water molecules through a short circuited reaction and balancing the charges transferred to the solution. The final results

are H_2 and O_2 molecules. If the position of valance and conduction band energy state is not achieved an external bias has to be applied in order to promote the photo-oxidation process. Figure 2.20 shows band levels of various semiconductor materials to fulfil the requirement for the PEC cell. This means the photocatalytic materials have a very strong water splitting ability to enhance the photoelestrochemical performance.

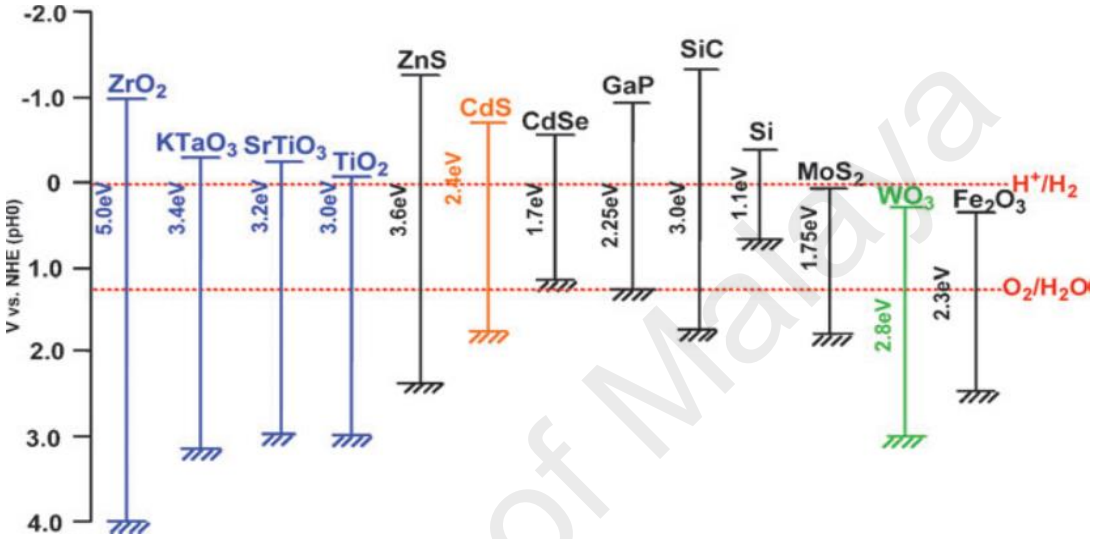

Figure 2.20: Relationship between band structure of semiconductor and redox potentials of water splitting (Copyright permission from S. Choudhary et al., 2012).

Furthermore, photocatalytic behavior under visible light could be attained by defect engineering, doping of non-metal, combining with other semiconductor (Dhanalakshmi, et al., 2013) and decoration of noble metal nanoparticles (Pandikumar, et al., 2010; Jinlong Zhang, et al., 2010) results in better interfacial charge transfer, thus reducing the charge recombination and decrease in band gap. Defect engineering indicates controlled introduction of innate defects, such as vacancies, interstitials, and antisites, while doping implies controlled introduction of impurities into the crystal lattice (Djurisic, et al., 2014). Therefore, the photocatalysis process takes place by moving of an electron from noble metal to semiconductor due to surface plasmon resonance effect (SPR) (Figure: 2.21).

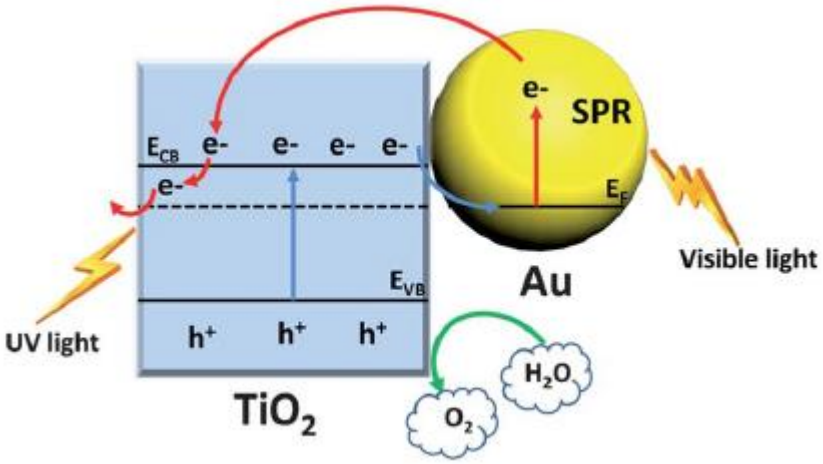

Figure 2.21: Charge transfer mechanism between Au nanoparticles and TiO_2 in visble and UV light (Copyright permission from F. Su et al., 2013).

The performance of electro ceramic materials and devices depends on the complex interplay between processing, chemistry, structure at many levels and device physics and so requires truly interdisciplinary effort by individuals from many fields.

CHAPTER 3: MATERIALS AND METHODS

3.1 General Consideration

All the manipulations were carried out under an inert atmosphere of dry argon, using Schlenk tubes and vacuum line attached to a RZ 6 ROTARY VANE PUMP (Model: 698132). All flasks are evacuated and then purged with argon at least three times prior to use, with external heat applied where considered necessary. Liquid air sensitive reagents were transferred to Schlenk tube by using cannula filter. Most of the chemicals and reagents used such as $SnCl_2$(anhydrous), $Y(OAc)_3$. xH_2O, $Mn(OAc)_2$, $Co(OAc)_2.4H_2O$, $Zn(OAc)_2.2H_2O$, $Cd(OAc)_2.2H_2O$, $Pb(OAc)_4$, $Ti(OPro)_4$, $Mg(OAc)_2.4H_2O$, Ag(OAc), $Cu(OAc)_2.2H_2O$, $Ni(OAc)_2.2H_2O$, $Fe(OAc)_2$, CuI, $Pb(NO_3)_2$, KI, Triethylamine, N,N-Dimethylaminoethanol (dmaeH), Trifluoroacetic acid (TFAH) and sodium were purchased from Sigma Aldrich. The solvents like tetrahydrofuran (THF) and toluene were rigorously dried on sodium benzophenoate and distilled immediately before use. N,N-Dimethylaminoethanol (dmaeH) was purified by refluxing over K_2CO_3 for 10 hrs and distilled immediately before use. The melting point was determined in a capillary tube using an electrothermal melting point apparatus; model MP.D Mitamura Riken Kogyo (Japan). The elemental analysis were performed using Leco CHNS 932. FT-IR spectra were recorded on an attenuated total reflectance (ATR) instrument (4000–400 cm^{-1}, resolution 4 cm^{-1}). The controlled thermal analysis was investigated using a METTLER TOLEDO TGA/ SDTA 851e Thermogravimetric Analyzer with a computer interface. The ^1H -NMR were recorded by JEOL DELTA2 NMR Spectrometer at field strength of 400 MHz using deuterated chloroform ($CDCl_3$) and dimethyl sulfoxide (DMSO-d6) as solvent. The thermal measurements were carried out in an alumina crucible under an atmosphere of flowing nitrogen gas (25 cm^3 min^{-1}) with a heating rate of 10 ^oC min^{-1}.

The surface morphology and cross-sectional view of thin films were determined by using a field-emission gun scanning electron microscope (FESEM, FEI Quanta 400) coupled with Energy Dispersive X-ray spectrometer EDX INCA Energy 200 (Oxford Inst.) at an accelerating voltage of 10-20 kV and a working distance of 3-9 mm. The phase purity and crystallanity were characterized using X-ray diffraction (XRD) on a D8 Advance X-Ray Diffractometer- Bruker AXS using Cu-Kα radiation (λ = 1.542 Å) at a voltage of 40 kV and current of 40 mA at ambient temperature). Raman spectra of the thin films were acquired using a Renishaw inVia Raman microscope with green laser excitation (532 nm). The UV-visible spectrum of the thin film was measured on a Lambda 35 Perkin-Elmer UV-visible spectrophotometer in the wavelength range of 300-900 nm and the film thickness was also obtained by using profilometer KLA Tencore P-6 surface profiler. The PEC studies of thin film electrodes were recorded by using a electrochemical workstation with a conventional three-electrode system. The thin films were used as a working electrode, platinum as a counter and Ag/AgCl as a reference electrode. For photocurrent measurement, the metal oxide thin films were dipped into the supporting electrolyte (0.1 M Na_2SO_4 and 1M NaOH) and irradiated with a 150-W xenon arc lamp (Newport, Model 69907) containing a simulated AM 1.5G filter. The effective area of the film was adjusted to 1 × 1 cm. Frequency response analysis (FRA) software was used in the EIS experimental and simulation experiments while general purpose electrochemical software (GPES) was used in the linear scan voltammetry (LSV) by Autolab PGSTAT-302N. The scan rate for LSV was 50 mV s^{-1} between -0.2 V to 1V while the EIS measurements were carried out at a frequency range of 100 kHz-10 mHz.

3.2 Syntheses

3.2.1 Synthesis of $[Cu_2Ti_4(O)_2(OH)_4(TFA)_8(THF)_6]\cdot THF$ (1)

Complex (**1**) was prepared by mixing stoichiometric amounts of 0.50g (2.50 mmol) of $Cu(CH_3COO)_2\cdot H_2O$ and 1.49mL (5.03mmol) of $Ti(OCH(CH_3)_2)_4$ followed by the addition of 1.14mL (10.05mmol) of CF_3COOH in 25mL of THF in a 50mL Schlenk tube. The reaction mixture was stirred for 4h and solvent was evacuated under vacuum to obtain a green powder which was dissolved in THF. The resulting transparent clear green solution was cannula-filtered and placed at room temperature for overnight to obtain green block shaped crystals of precursor (**1**) in 70% yield. Mp: 225 °C (decomposition). Elemental analysis, (Found: C, 27.96; H, 2.87. $C_{44}H_{58}F_{24}O_{29}Cu_2Ti_4$ requires C, 28.89; H, 3.17 %). IR: ν_{max}/cm^{-1} 3290br, 1715s, 1671s, 1544m, 1471s, 1442w, 1197s, 1146s, 1054w, 1025s, 891s, 797s, 722s, 682w, 623w, 581w, 522s. TGA: 51-134 °C (11.1% wt. loss); 139-240 °C (25.8% wt. loss); 241-277 °C (14.0% wt. loss), 280-500 °C (22.3% wt. loss) (Residual mass of 26.80%); (Cal. for $CuO\text{-}2TiO_2$ 26.18%).

3.2.2 Synthesis of $[Co_2Ti_4(\mu\text{-}O)_6(TFA)_8(THF)_6]\cdot THF$ (2)

Complex (**2**) was prepared by mixing stoichiometric amounts of 0.50 g (2.0 mmol) of $Co(CH_3COO)_2\cdot 4(H_2O)$ and 1.19 mL (4.0 mmol) of $Ti(OCH(CH_3)_2)_4$ followed by the addition of 1.21 mL (16.0 mmol) of CF_3COOH in 25 mL of THF in a 50mL Schlenk tube. The reaction mixture was stirred for 4h and solvent was evacuated under vacuum to obtain a red powder which was again dissolved in THF. The resulting transparent clear red solution was cannula-filtered and placed at room temperature for 2 days to obtain the red block shaped crystals of complex (**2**) in 75% yield. Mp: 195 °C (decomposition). Elemental analysis, (Found: C, 26.98; H, 2.17. $C_{44}H_{54}F_{24}O_{29}Co_2Ti_4$ requires C, 28.89; H, 2.97 %). IR: ν_{max}/cm^{-1} 2989w,

2904w, 1717s, 1681s, 1469s, 1388w, 1329w, 1198s, 1148s, 1025w, 1038w, 899w, 792s, 722s, 681w, 654w, 618s, 585w, 493s, 474s. TGA: 50-95 °C (1.53% wt. loss); 100-180 °C (7.2% wt. loss); 181-225 °C (23.6% wt. loss), 250-500 °C (40.17% wt. loss) (Residual mass of 27.50%); (Cal. for $CoTiO_3$-TiO_2 25.80%).

3.2.3 Synthesis of $[Mg_2Ti_4(O)_2(OH)_4(TFA)_8(THF)_6]\cdot THF$ (3)

Complex (**3**) was isolated by mixing stoichiometric amounts of 0.50g (2.33 mmol) of $Mg(OAc)_2\cdot 4H_2O$ and 1.38mL (4.66mmol) of $Ti(^iPro)_4$ followed by the addition of 0.70mL (9.36 mmol) of TFAH in 25mL of THF in a 50mL Schlenk tube. The reaction mixture was stirred for 4 hours and solvent was evacuated under vacuum to obtain a white powder which was re-dissolved in THF. The resulting transparent solution was cannula-filtered and placed at room temperature overnight to obtain colourless block shape crystals of complex (**3**) in 75% yield. Mp: 220 °C (decomposition). Elemental analysis, (Found: C, 27.06; H, 2.77. $C_{44}H_{58}F_{24}O_{29}Mg_2Ti_4$ requires C, 28.89; H, 3.17 %. IR: ν_{max}/cm^{-1} 3318br, 2988w, 1721w, 1636s, 1453s, 1192s, 1143s, 1034s, 845s, 797s, 722s, 619s, 509w, 480w. TGA: 73-130 °C (3.6 % wt. loss); 135-235 °C (19.0 % wt. loss); 238-575 °C (56.5 % wt. loss), (Residual mass of 20.9 %); (Cal. for $MgTi_2O_5$ 20.6%).

3.2.4 Synthesis of $[Mn(dmae)_2(TFA)_4]$ (4)

0.40 g (2.31 mmol) of $Mn(CH_3COO)_2$ and 0.5ml (6.2mmol) of trifluoroacetic acid were added to 50ml Schlenk tube containing 20ml of THF under argon atmosphere. The mixture was stirred for 6 h to obtain a clear solution. The solvent was then evaporated under vacuum to obtain a powder which was re-dissolved in 5 ml of THF followed by the addition of 0.228mL (2.28 mmol) N, N-dimethyl-2-aminoethanol in a 50mL Schlenk tube. The resulting transparent solution was cannula-filtered and placed at -10 ^oC for one

week to obtain the transparent crystals of complex **(4)** in 70% yield. Crystals suitable for single crystal X-ray analysis were grown from THF solution. m.p: 83 °C (decomposition). Elemental analysis: % calculated (found) for $[Mn(dmae)_2(TFA)_4]$ C, 21.11 (20.83), H, 1.77 (1.69), N, 2.05 (1.95). IR (cm^{-1}): 1728(s), 1635(s), 1444(m), 1420(s), 1391(w), 1177(s), 1130(s), 1074(s), 1048(m), 986(s), 852(m), 727(s), 600(m), 502(m). TGA: 179-260°C (72.77% wt. loss) and 260-550 °C (7.06% wt. loss); (Residual mass of 20.40%); (Cal. for Mn_2O_3 23.10%).

3.2.5 Synthesis of $[Sn(dmae)(OAc)]_2$ (5)

A solution of 0.97g (0.40 mmol) of bis(dimethylaminoethanolato)tin(II), $Sn(dmae)_2$, (Wakeshima & Kijima, 1972) prepared as reported earlier,(Wakeshima & Kijima, 1972) in 10 mL of toluene was transferred to a suspension of 0.10 g $Y(OAc)_3$. xH_2O in 10 mL of toluene. The reaction mixture was then stirred at room temperature for 6 h for the completion of the reaction. Filtration through a cannula gave a clear white solution which was evaporated to dryness under vacuum, and the solid residue was re-dissolved in 5 mL of toluene to give a 65% yield of white crystals after 5 days at -10°C. mp: 147°C. Micro analysis for [Sn((dmae) OAc)]2: Calculated (found) % C, 27.10 (27.28); H, 4.90 (5.04); N, 5.28(5.12). Selected FT-IR absorption (cm^{-1}): 2810w, (NCH_3); 1615s, (C= 0); 593s, (Sn- O); H1NMR: (SI Figure 3) 1.9 (3H, s, Me), 2.3 (6H, s, NMe), 2.6 (2H,b, CH_2N), 3.4 (2H, b, CH_2O). TGA: 177-258 ^{0}C (51.46 wt % loss) (Residue = 48.53 %).

3.2.6 Synthesis of $CuPbI_3$

0.50 g (2.62 mmol) copper(I) iodide was suspended in 20 mL distilled water in a 100 mL beaker. 0.87 g (2.64 mmol) lead(II) nitrate solution in 10 mL of distilled water was added drop by drop to the suspension of copper(I) iodide with constant stirring for 1 h. 0.87 g (5.28 mmol) potassium iodide dissolved in 10 mL of distilled water was added very

slowly to the vigorously stirred mixture for 2 h. The obtained yellow-brown precipitates were filtered and washed several times with distilled water until free from lead, nitrate and iodide ions. Finally, the precipitates were washed with ethyl alcohol and dried in air. The obtained yellow-brown powder was charged in a 5 mL Pyrex glass ampule and evacuated for several hours. The ampule was sealed under vacuum and heated at 620 ^{o}C for 72 h in a tube furnace (Titilayo A. Kuku & Salau, 1987). The furnace was allowed to cool to room temperature before the ampule was taken out. The ampule was opened carefully and mustard colour solid was carefully scratched from the ampule and ground to fine powder in an agate pestle mortar. The finely ground powder of copper lead iodide was washed with several 5 mL portions of DMF to remove excess of unreacted lead(II) iodide to give crystals of $CuPbI_3$ (m.p. 307 ^{o}C).

3.3 Crystallography and Structure Refinement

The data of complex **(1)** were collected at 150(2)K on a Bruker-Nonius Apex II CCD diffractometer using MoK_α radiation (α = 0.71073Å) and were corrected for Lorentz-polarisation effects and absorption (SADABS) (Krause, Herbst-Irmer, Sheldrick, & Stalke, 2015). The structure was solved by dual space methods (SHELXT) (Sheldrick, 2015) and refined on F^2 using all the reflections (SHELXL-2014) (Sheldrick, 2015). The central section, comprising most of the molecule is disordered and was modelled with 50% occupancy of two positions related by a center of symmetry (reduction of the space group symmetry did not reduce the disorder). The data for complex **(2)** collected on a Agilent Supernova diffractometer equipped with a MoKα Microfocus X-ray source (λ = 0.71073 Å). The Agilent CrysAlisPro software was used for data collection, cell refinement, data reduction and absorption collections. Molecular graphics were drawn by using the XSEED and Mercury software were collected at 150(2)K on a Bruker Apex II CCD diffractometer using MoK_α radiation (λ = 0.71073Å). The structure was solved

by direct methods (SIR-2004) and refined on F^2 using all the reflections (SHELX) (Sheldrick, 2015). All the non-hydrogen atoms were refined using anisotropic atomic displacement parameters and hydrogen atoms were inserted at calculated positions using a riding model.

Diffraction data for the crystal **(3)** were collected on an Agilent SuperNova Dual diffractometer with an Atlas detector (graphite-monochromatized Mo-*K*α radiation, λ = 0.71073 Å) at 100(2) K. The data were processed using CrysAlisPro, Agilent Technologies, Version 1.171.37.34 (release 22-05-2014 CrysAlis171.NET) and empirical absorption correction using spherical harmonics implemented in SCALE3 ABSPACK scaling algorithm. The structure was solved using the program SHELXT and was refined by the full matrix least-squares method on F^2 with SHELXL-2014/7 (Sheldrick, 2008). All the non-hydrogen atoms were refined anisotropically. All the hydrogen atoms were placed at calculated positions and were treated as riding on their parent atoms. The structure exhibits a whole molecule disorder with the two components being related by a pseudo-inversion center. The occupancy of the main component refined to 0.640(2). The structure was also refined as a racemic twin with the twin parameter of 0.46(4). Drawing of the molecule was produced with *Mercury* (Macrae et al., 2006). Crystal data: $C_{44}H_{56}Co_2F_{24}O_{29}Ti_4$, M_r = 1814.34, pink block, 0.49 × 0.28 × 0.26 mm^3, orthorhombic, *Pca*2$_1$, *a* = 19.2672(4), *b* = 20.5759(5), *c* = 17.2453(4) Å, *V* = 6836.7(3) Å^3, *Z* = 4, D_c = 1.763 Mg/m^3, 135126 measured reflections, 19480 unique reflections (R_{int} = 0.0517), 14499 observed reflections [(I > 2σ(I)], final *R* indices [(I > 2σ(I)]: R_1 = 0.0858, wR_2 = 0.2091. CCDC No. 1453304.

Diffraction data for the crystal **(4)** were collected on an Agilent SuperNova Dual diffractometer with an Atlas detector (graphite-monochromatized Mo-*K*α radiation, λ = 0.71073 Å) at 100(2) K. The data were processed using CrysAlisPro, Agilent

Technologies, Version 1.171.37.34 (release 22-05-2014 CrysAlis171.NET) and empirical absorption correction using spherical harmonics implemented in SCALE3 ABSPACK scaling algorithm. The structure was solved using the program SHELXT and was refined by the full matrix least-squares method on F^2 with SHELXL-2014/7.The data of crystal **(5)** were collected at 150(2)K on a Bruker-Nonius Apex II CCD diffractometer using MoK_α radiation (λ = 0.71073Å) and were corrected for Lorentz-polarisation effects and absorption (SADABS) (Krause, Herbst-Irmer, Sheldrick, & Stalke, 2015). The structure was solved by dual space methods (SHELXT) (Sheldrick, 2015) and refined on F^2 using all the reflections (SHELXL-2014) (Sheldrick, 2015).

3.4 Thin Film Deposition Techniques

The semiconducting solid solution and composite thin films were developed by using the precursor **(1-5)**. The thin films of precursor **(1-4)** were tailored on commercially available FTO-coated glass substrates using a self-designed AACVD assembly. Precursor **(5)** and metal acetates of (Mn, Fe, Cu, Ni, Zn, Cd and Pb) were fabricated on FTO substrate by an in house built EFDAACVD method. $CuPbI_3$ films were deposited by EDP technique. The general procedure of all these methods are described below:

3.4.1 Aerosol Assisted Chemical Vapor Deposition

The FTO-coated glass substrates purchased from Sigma Aldrich were cut to the dimension of 25.4 x 12.7 x 2.2 mm (L x W x D) and then prepared by ultrasonically washing with distilled water, acetone and then ethyl alcohol. Finally, they were washed with distilled water, kept in ethanol and dried in air before use. Substrate slides of the dimension of 25.2 mm × 12.7 mm were placed inside a tube furnace chamber and then heated up to the deposition temperature for 10 min before carrying out the deposition. The aerosol of the precursor solution was formed by keeping the round-bottom flask in a

water bath above the piezoelectric modulator of an ultrasonic humidifier. The aerosol particles generated by the complexes were transferred into the hot wall region of the reactor by the carrier gas, whose flow rate was measured by a LIX linear flow meter and adjusted at 120 mL/min (Figure 3.1). In the last step of deposition, the aerosol assembly was turned off and a carrier gas was streamed over the substrates till the chamber cools down to normal temperature before they were removed for analysis.

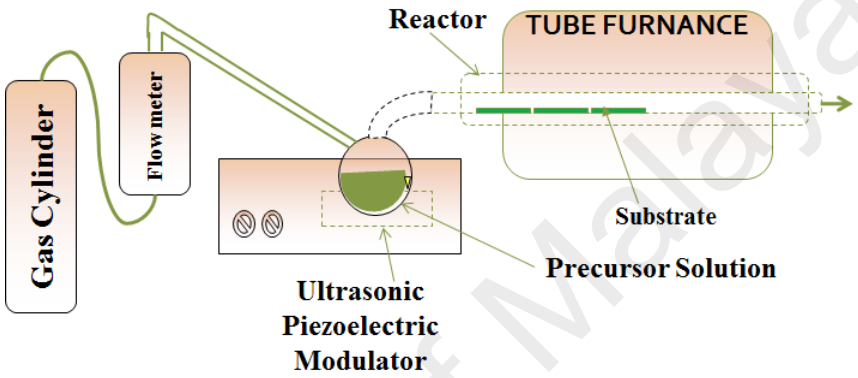

Figure 3.1: Schematic diagram of Aerosol-Assisted Chemical Vapour Deposition.

3.4.2 Electric Field Directed Aerosol Assisted Chemical Vapor Deposition

The deposition of thin films on the commercially available fluorine-doped tin oxide (FTO) substrate dimension of 25.2 mm × 12.7 mm were carried out using an in-house built EFDAACVD technique as shown in Figure 3.2. Prior to the deposition, the FTO substrates were cleaned ultrasonically by washing with distilled water, acetone and ethyl alcohol. Finally, they were washed with distilled water, stored in ethanol and dried in air before use. The aerosol of the metal precursor was generated by keeping the reaction mixture in a two necked round bottom flask in a water bath above the piezoelectric modulator of an ultrasonic humidifier. The generated aerosol droplets of the precursor were transferred through an injection needle anode that was connected to a power supply. The distance between the edge of the needle (anode) and the substrate was kept at 6 inches

and the substrate connected to the cathode was placed on the heater. Argon gas was passed through the aerosol mist at a flow rate of 200 mL/min to carry the aerosol droplets.

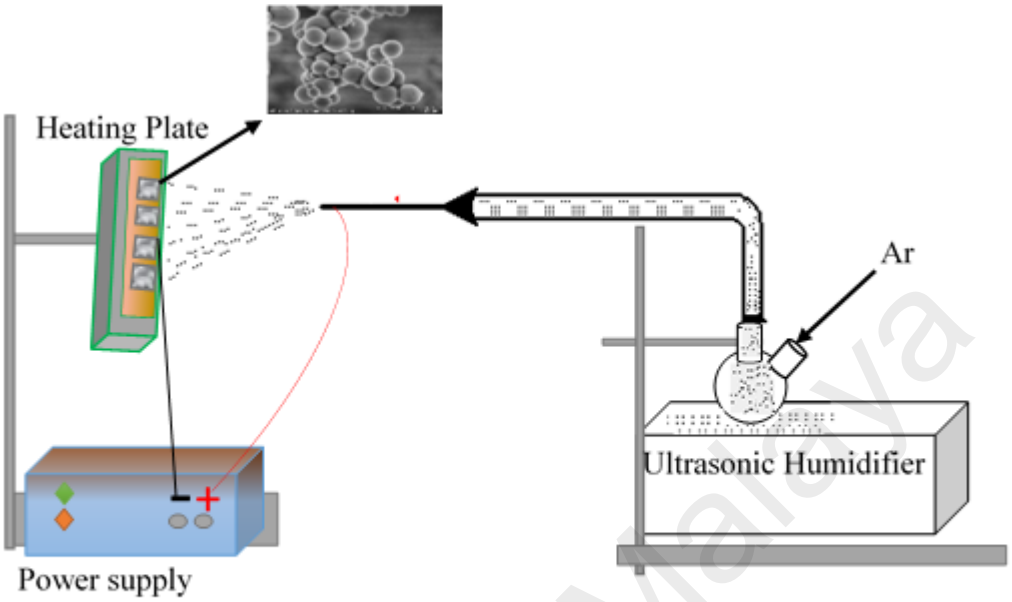

Figure 3.2: An in-house built experimental set up the orientation of the spray-needle was directed horizontally orthogonal to the plane of the substrate for Electric Field-Directed Aerosol-Assisted Chemical Vapour Deposition.

A potential of 9.5 kV was applied across the terminals while the aerosol was flowing through the needle and the deposition were conducted at 400 ˚C for 45 min. The power supply and the ultrasonic humidifier were switched off and the aerosol line was closed. The substrate was then coolled down to room temperature before it was removed from the heating plate to obtain thin films. As the coated area and the deposition rate are strongly dependent on the angle of the needle tip to the substrate, the aerosol spray-needle must be mounted in a horizontal position and perpendicular to the substrate surface at a suitable distance. It was observed that a relatively shorter distance between needle and substrate reduces the spinning time of the aerosol to yield a higher deposition rate and small coated areas having irregular particle shape. The increase in voltage and adjustment of distance between the needle tip and the substrate resulted in an evenly distributed thin film of precursor particles.

3.4.3 Electrophoretic Deposition

$CuPbI_3$ modified FTO electrodes were prepared by adopting EPD technique as reported in the literature (Tajabadi et al., 2015) (Figure 3.3). In a typical experiment a two milligrams of the as-synthesized $CuPbI_3$ powder was dispersed in 40 mL of 0.025 M $Mg(NO_3)_2$ in isopropanol.

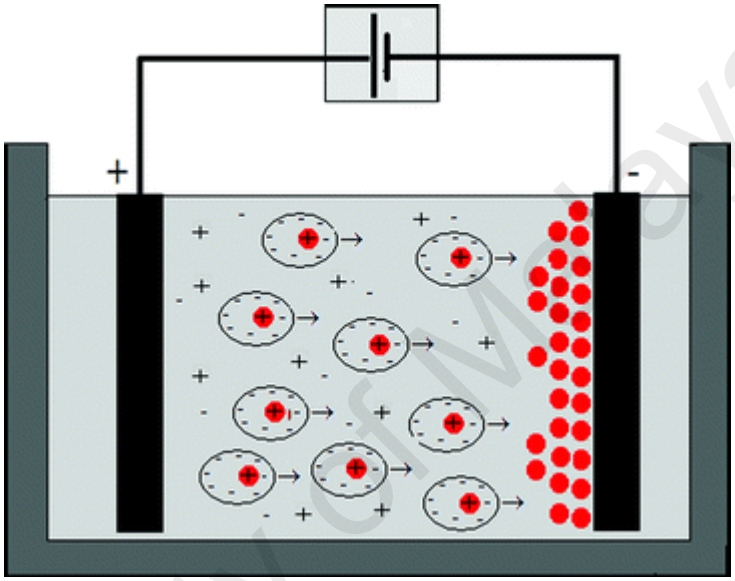

Figure 3.3: Schematic diagram of electrophoretic deposition of charged particles on the anode of an EPD cell with planar electrodes.

The mixture was sonicated for 30 min to obtain a homogeneous suspension containing 0.05 mgL^{-1} of $CuPbI_3$. The pH of the suspension was adjusted at 3 by utilizing 1 M HCl solution before carrying out EPD experiment. The FTO glass substrates with an area of 10 mm × 20 mm were immersed in a 5% HF solution for a few minutes to remove the native oxide layer followed by washing in acetone and distilled water prior to being vertically immersed into the suspension. The linear distance between the electrodes was maintained at 10 mm and the DC potential and deposition time were adjusted to 80 V and 5 min, respectively. The coated film was dried at 50 °C in a vacuum oven to remove the excess solvent from the EPD process.

3.5 Photoelectrochemical Behavior

Photoelectrochemical activities of semiconducting metal oxides and metal halide films were examined by the use of three electrode system fitted with quartz window. Three electrode electrochemical cell consist of metal oxide/halide thin film as working, Ag/AgCl/3M KCl used as reference and Pt wire as counter electrode respectively. 0.1M Na_2SO_4 and 1M NaOH were used as electrolyte solution to evaluate the PEC behavior of particular photoelectrodes. The surface of FTO substrate of working electrode was employed as a mean for electrical contact, connected to crocodile clip coated with gold and kept beyond the electrolyte surface. A potentiostat (Eco Chemie micro-Autolab type III) was used to set the potential to photoelectrode in range of -0.2 to 1.2 V, while the cells were illuminated by an AM 1.5 Class A solar simulator (Solar Light 16S-300 solar simulator), at 100 mW cm^{-2} light intensity from 150 W xenon arc lamp, adjusted by a silicon pyrometer (Solar Light Co., PMA2144 Class II). The active area of the film was arranged to 1 × 1 cm. The light enters the electrochemical cell through quartz window. Generally working electrode is irradiated for two minutes before the cell is turned ON so that electrons can travel to the conduction band.

3.6 Electrochemical Sensor Studies

Sensor studies of semiconducting bimetallic oxide thin films were performed in a single compartment three–electrode cell at room temperature using a PAR-VersaSTAT-3 Electrochemical workstation. The $CoTiO_3$-TiO_2 composite thin film and a platinum wire were used as working and counter electrodes, respectively. Silver/silver chloride (Ag/AgCl) electrode was used as a reference electrode. All studies for DA were carried out at pH 7.0 using a phosphate buffer solution. All solutions for electrochemical experiments were prepared with Millipore water having a resistivity of 18.2 M (Purelab Classic Corp., USA).

Table 3.1: Parameters for the fabrication of thin films from their respective precursors.

Precursors	Solvent	Deposition Temperature	Method	Carrier Gas	Deposition Time	Composition of Fabricated Thin Films
		ºC		**mL/min**	**min**	
$[Cu_2Ti_4(O)_2(OH)_4(TFA)_8(THF)_6]\cdot THF$ (**1**)	Methanol, Ethanol	550	AACVD	Air/150	40	$CuO\text{-}2TiO_2$
$[Co_2Ti_4(\mu\text{-}O)_6(TFA)_8(THF)_6].THF$ **(2)**	Methanol, Ethanol	500, 550, 600	AACVD	Air/150	40	$CoTiO_3\text{-}TiO_2$
$[Mg_2Ti_4(O)_2(OH)_4(TFA)_8(THF)_6]\cdot THF$ **(3)**	Methanol, Ethanol	500, 550, 600	AACVD	Air/150	40	$MgTi_2O_5$
$[Mn(dmae)_2(TFA)_4]$ **(4)** + Ag(OAc)	Methanol	450	AACVD	Ar/120	45	Mn_2O_3, $Ag\text{-}Mn_2O_3$
$[Sn(dmae)(OAc)]_2$ **(5)**	Toluene	400	EFDAACVD	Ar/200	30	SnO_2
$Mn(OAc)_2$	THF	400	EFDAACVD	Ar/200	45	Mn_2O_3
$Fe(OAc)_2..2H_2O$	THF	400	EFDAACVD	Ar/200	45	Fe_2O_3
$Cu(OAc)_2..2H_2O$	THF	400	EFDAACVD	Ar/200	45	CuO
$Ni(OAc)_2..H_2O$	THF	400	EFDAACVD	Ar/200	45	NiO
$Zn(OAc)_2.2H_2O$	THF	400	EFDAACVD	Ar/200	45	ZnO
$Cd(OAc)_2.2H_2O$	THF	400	EFDAACVD	Ar/200	45	CdO
$Pb(OAc)_2.4H_2O$	THF	400	EFDAACVD	Ar/200	45	PbO
$CuPbI_3$	Isopropyl alcohol	50	EPD	Air	5	$CuPbI_3$

3.7 Attempted Reactions

Some chemical reactions that might not produce the desired products were tried. The common method utilized in the attempted reactions is as follows: In a stirred mixture of Tin dimethhylamino ethanol $Sn(dmae)_2$ and metal alkoxide/carboxylate in dry Toluene was added few drops of triflouroacetic acid to result a clear solution after several hours, which was evaporated under vaccum to a dry solid. The solid was dissolved in 2-3 mL Tolune to give a clear solution which was filtered by cannula and kept for crystallization at -10 ^oC as well as room temperature.

The quantities of reactants used are given below

i) Reaction between $Sn(dmae)_2$ and Titanium isopropoxide

4.4 g (0.34 mmol) bis (dimethylaminoethanolato)tin (II) ; 0.093 mL (0.34 mmol) Titanium isopropoxide; 20 mL Toluene.

ii) Reaction between $Sn(dmae)_2$ and Iron (II) acetate

4.4 g (0.34 mmol) bis (dimethylaminoethanolato)tin (II); 0.06g (0.34 mmol) Iron (II) acetate (anhydrous); 20 mL Toluene.

iii) Reaction between $Sn(dmae)_2$ and Manganese (II) acetate

4.4 g (0.34 mmol) bis (dimethylaminoethanolato)tin (II); 0.058g (0.34 mmol) Manganese (II) acetate (anhydrous); 20 mL Toluene.

iv) Reaction between $Sn(dmae)_2$ and Zinc (II) acetate

4.4 g (0.34 mmol) bis (dimethylaminoethanolato)tin (II); 0.07g (0.34 mmol) Zinc (II) acetate dihydrtate; 20 mL Toluene.

v) Reaction between $Sn(dmae)_2$ and Nickle (II) acetate

4.4 g (0.34 mmol) bis (dimethylaminoethanolato)tin (II); 0.08g (0.34 mmol) Nickle (II) acetate tetrahydrate; 20 mL Toluene.

vi) Reaction between $Sn(dmae)_2$ and Silver (I) acetate

4.4 g (0.34 mmol) bis (dimethylaminoethanolato)tin (II); 0.056g (0.34 mmol) Silver (I) acetate (anhydrous); 15 mL Toluene.

vii) Reaction between $Sn(dmae)_2$ and Copper (II) acetate

4.4 g (0.34 mmol) bis (dimethylaminoethanolato)tin (II); 0.07g (0.34 mmol) Copper (II) acetate monohydrate; 20 mL Toluene.

viii) Reaction between $Sn(dmae)_2$ and Lead (IV) acetate

4.4 g (0.34 mmol) bis (dimethylaminoethanolato)tin (II); 0.15g (0.34 mmol) Lead (IV) acetate; 25 mL Toluene.

ix) Reaction between $Sn(dmae)_2$ and Iron (II) acetate

4.4 g (0.34 mmol) bis (dimethylaminoethanolato)tin (II); 0.06g (0.34 mmol) Iron (II) acetate (anhydrous); 20 mL Toluene.

x) Reaction between $Sn(dmae)_2$ and Cadmium (II) acetate

4.4 g (0.34 mmol) bis (dimethylaminoethanolato)tin (II); 0.07g (0.34 mmol) Cadmium (II) acetate dihydrate; 20 mL Toluene.

xi) Reaction between $Sn(dmae)_2$ and Cobalt (II) acetate

4.4 g (0.34 mmol) bis (dimethylaminoethanolato)tin (II); 0.08g (0.34 mmol) Cobalt (II) acetate tetrahydrate; 15 mL Toluene.

xii) Reaction between $Sn(dmae)_2$ and Cerium (III) acetylacetonate

4.4 g (0.34 mmol) bis (dimethylaminoethanolato)tin (II); 0.06g (0.34 mmol) Cerium (III) acetylacetonate; 25 mL Toluene.

xiii) Reaction between $Sn(dmae)_2$ and Chromium (III) acetylacetonate

4.4 g (0.34 mmol) bis (dimethylaminoethanolato)tin (II); 0.12g (0.34 mmol) chromium (III) acetylacetonate Iron (II) acetate (anhydrous); 20 mL Toluene.

CHAPTER 4: RESULTS AND DISCUSSION

Metal carboxylates with their unique properties of high volatility, suitable decomposition temperature and stability during transport in the gas phase make them versatile CVD precursors for the fabrication of thin layers of metal oxides for various technological applications (Joshi & Cole, 2000; Niederberger & Pinna, 2009). The different coordination modes (monodentate or terminal, chelating, bridging and bridging chelating) of the carboxylate ligand force the metal into strict molecular regimes that enhance their potential to perform as CVD precursor (Chandler, Roger, & Hampden-Smith, 1993; Hubert- Pfalzgraf, 1992; Norman, Perez, Schulz, & Waechtler, 2008). Metal oxide core covered by organic surrounding making the precursor soluble in suitable organic solvents (Chandler, et al., 1993; Hasenkox, Hoffmann, & Waser, 1998). Semiconducting nanostructured metal oxide/halide thin films have been fabricated by different chemical and physical techniques and studied widely for their material based applications (Jagadish & Pearton, 2011; C. Lokhande, D. Dubal, & O.-S. Joo, 2011; Ohring, 2001). These materials have been offer a significant role in field of telecommunication, microelectronics, optoelectronics, sensors, actuators, computer memories, optical wavelength guide, infrared detectors and fuel cell (Beckel et al., 2007; Hotovy, Huran, Spiess, Hascik, & Rehacek, 1999; Kessler, 2003). A variety of newly synthetic routes are now capable to yield desired products under mild conditions are known as the Soft chemistry approach (Graf et al., 2011; Kessler, 2003; Lepage, Michot, Liang, Gauthier, & Schougaard, 2011; Niederberger, Pinna, Polleux, & Antonietti, 2004). These techniques including non-hydrolytic Sol-Gel processing, Metal Organic Deposition (MOD) or Chemical Vapour Deposition (CVD) and others involve the utilization of metal-organic compounds or metal complexes. These metal complexes can be easily hydrolytically or thermally decomposed and are usually described as molecular

precursors. Single source precursors (SSP) are molecules containing all necessary elements required by the final material in proper ratio have proven extremely versatile as they often decompose cleanly under mild conditions and in a controllable manner.

Here, we report a deposition method of solid solution and composite metal oxide/halide thin films using the AACVD, EFDAACVD and EPD technique. Different metal oxide complexes such as $[Cu_2Ti_4(O)_2(OH)_4(TFA)_8(THF)_6]\cdot THF$ **(1),** $[Co_2Ti_4(\mu\text{-}O)_6(TFA)_8(THF)_6].THF$ **(2),** $[Mg_2Ti_4(O)_2(OH)_4(TFA)_8(THF)_6]\cdot THF$ **(3),** $[Mn(dmae)_2(TFA)_4]$ **(4)** and $[Sn(dmae)(OAc)]_2$ **(5)** were prepared using Lewis-acid base adduct methodology (Michael Veith et al., 2000), which is unique procedure for the design of mono and bimetallic oxides.

The syntheses of these precursors involves the reaction of matal alkoxides, carboxylates and β-diketonates in presence of more volatile and strongly bonding trifluoroacetic acid (TFAH) or dimethylaminoethanol (dmaeH) (Nicholas & Tuley, 2012). The replacement of alkoxides, carboxylates and β-diketonates by trifluoroacetato (TFA) and dimethylaminoethanolato (dmae) provides a stable mono and bimetal complex of that is soluble in various organic solvents and able to deliver a target material either as a single or dual source of respective metals in the form of a thin film on the FTO substrate without carbonaceous contamination.

The semiconducting photoactive thin films of $CuO\text{-}2TiO_2$, $CoTiO_3\text{-}TiO_2$ and $MgTi_2O_5$ were fabricated from single source precursors **(1)**, **(2)** and **(3)** respectively, whereas thin film of $Ag\text{-}Mn_2O_3$ were grown from dual source using **(4)** via AACVD. SnO_2, Mn_2O_3, Fe_2O_3, CuO, NiO, ZnO, CdO and PbO films were deposited from the precursor **(5)** and respective metal acetates (Mn, Fe, Cu, Ni, Zn, Cd and Pb) precursors by EFDAACVD technique. While metal halide $CuPbI_3$ deposited by EPD method. After possible characterizations, photoelectrochemical response of these thin films (except for CuO-

$2TiO_2$, $CoTiO_3$-TiO_2 and SnO_2) was investigated in order to evaluate their photocurrent and solar energy harvesting properties. CuO-$2TiO_2$ and $CoTiO_3$-TiO_2 thin films were tested for electrochemical sensing of NO_2^{-1} ion and dopamine (DA), whereas SnO_2 for lithium ion batteries.

4.1. Synthesis and Characterization of $[Cu_2Ti_4(O)_2(OH)_4(TFA)_8(THF)_6]\cdot THF$ (1)

The chemical interaction between diacetatocopper(II) and tetrakisisopropoxytitanium(IV) in the presence of trifluoroacetic acid yields a heterobimetallic complex $[Cu_2Ti_4(O)_2(OH)_4(TFA)_8(THF)_6]\cdot THF$ (**1**). The isopropoxo and acetato groups attached to titanium and copper centres are completely exchanged by the stronger trifluoroacetato ligands as the reaction progresses in forward direction. The complex (**1**) prepared in a good yield, has copper to titanium ratio of 1:2, is stable in air and finds high solubility in common organic solvents such as methanol, ethanol, acetonitrile and tetrahydrofuran. The overall reaction for the formation of (**1**) is shown below in equation 1.

Chemical equation 1

$$2Cu(CH_3COOH)_2.H_2O + 4Ti(OCH(CH_3)_2)_4 + 8CF_3COOH \xrightarrow{THF} [Cu_2Ti_4(O)_2(OH)_4(CF_3COO)_8(C_4H_8O)_6].C_4H_8O + 4CHCOOH + 16(CH_3)_2CHOH$$

The heterometallic architecture of the complex (**1**) has been framed on the basis of elemental analysis, FT-IR, and single crystal X-ray analyses as described in experimental section. The FT-IR spectrum of complex (**1**) shows the presence of characteristic vibrations of functional groups attached to the copper and titanium atoms. The typical symmetric and asymmetric ν(C=O) absorptions of trifluoroacetato ligand arose at 1671 and 1471 cm^{-1} respectively. The difference in value of 208 cm^{-1} between symmetric and asymmetric ν(C=O) absorption bands reveals the bidentate behaviour of the carboxylato

group of trifluoroacetato ligand that is bonded to different metal centres (Ehsan, Khaledi, Pandikumar, Rameshkumar, et al., 2015; Ehsan et al., 2011). Similarly, the peak at 1195 cm^{-1} confirms the presence of C–F bonds in complex (**1**) (Ehsan, Khaledi, Pandikumar, Rameshkumar, et al., 2015; Ehsan, et al., 2011).

4.1.1 Molecular Structure of Complex $[Cu_2Ti_4(O)_2(OH)_4(TFA)_8(THF)_6]\cdot THF$ (1)

The structure of (**1)** was solved in space group *Pbca* , and is disordered about the centre of symmetry. The core of the molecule consists of a tetrahedron of Ti(IV) ions (Figure 4.1). Each edge of the tetrahedron is bridged by an oxygen atom (O^{2-} or OH^-), generating a Ti_4O_6 adamantane-type cage. Four of the bridging species are hydroxo ions; the remaining two are oxo ions which are also coordinated to Cu(II) ions. The disorder arises from titanium ions occupying alternative sites, generating a second, overlapping adamantine with the oxygen atoms in the same positions. All the non-hydrogen atoms were refined using anisotropic atomic displacement parameters and hydrogen atoms were inserted at calculated positions using a riding model. Parameters for data collection and refinement are summarised in Table 4.1.

Table 4.1: Crystal data and refinement parameters for complex $[Cu_2Ti_4(O)_2(OH)_4(TFA)_8(THF)_6]\cdot THF$ (**1)**

$C_{40}H_{52}Cu_2F_{24}O_{28}Ti_4\cdot C_4H_8O$	V = 6863.3 (7) Å^3
M_r = 1827.60	Z = 4
Orthorhombic, *Pbca*	Mo *K*α radiation, λ = 0.71073 Å
a = 18.8071 (11) Å	μ = 1.20 mm^{-1}
b = 17.3656 (10) Å	*T* = 150 K
c = 21.0146 (12) Å	0.43 × 0.32 × 0.24 mm
$R[F^2 > 2\sigma(F^2)]$ = 0.067	59386 measured reflections
$wR(F^2)$ = 0.217	7057 independent reflections
S = 1.01	4097 reflections with $I > 2\sigma(I)$
$\Delta>_{max}$ = 0.65 e Å^{-3}	1810 restraints
$\Delta>_{min}$ = -0.67 e Å^{-3}	910 parameters

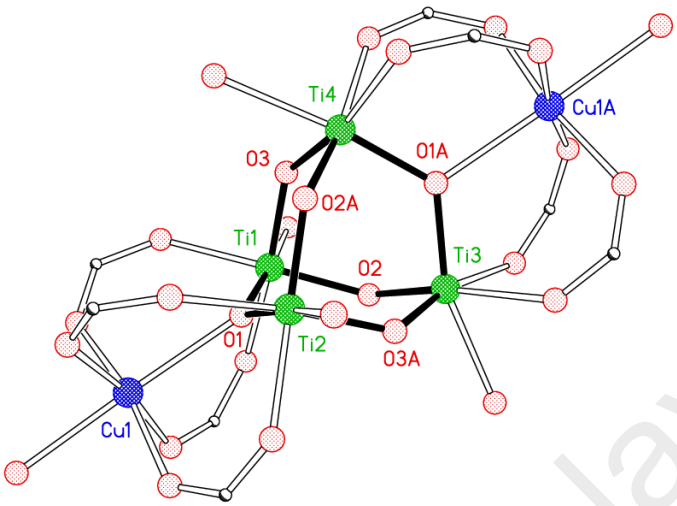

Figure 4.1: Perspective view of the core of (1). CF_3COO^- ions are represented by OCO links; terminal O atoms represent THF molecules, bold bonds highlight the $Ti_4O_2(OH)_4$ adamantane core. Atoms with suffix "A" generated by symmetry operation 1-x, 1-y, 1-z.

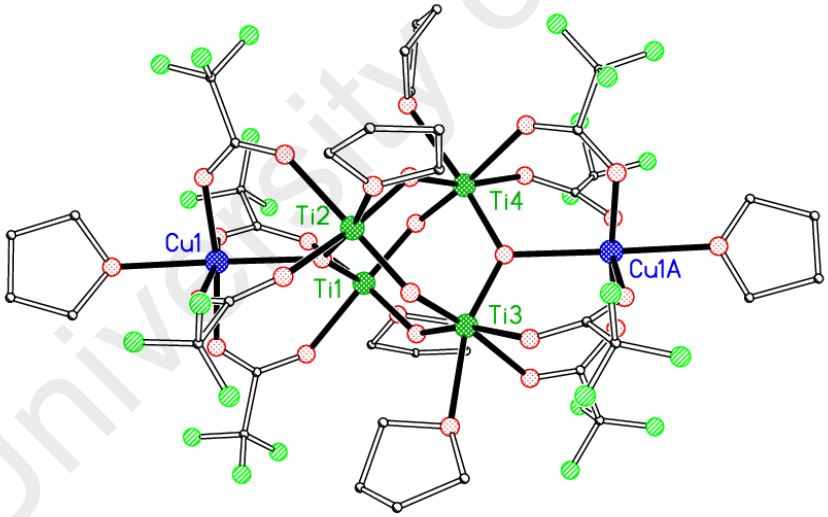

Figure 4.2: Perspective view of the $[Cu_2Ti_4(O)_2(OH)_4(CF_3COO)_8(THF)_6]$ (1) molecule. Bold bonds highlight the metal coordination spheres. Disorder and H atoms are omitted for clarity.

Four trifluoroacetate (CF_3COO^-) ions are bonded to each copper ion; each trifluoroacetate also bridges to a titanium ion. All of the metal ions are six-coordinate, the last binding

site being filled by one coordinated THF molecule for each metal ion (Figure 4.2). There is also a (disordered) non-coordinated THF solvate molecule in the lattice.

4.1.2 Thermal (TG/DTG) Analysis of Complex $[Cu_2Ti_4(O)_2(OH)_4(TFA)_8(THF)_6]\cdot THF$ (1)

The thermal decomposition behaviour of the complex (**1**) was studied by simultaneous thermogravimetric (TG) and derivative thermogravimetric (DTG) analysis under an inert dinitrogen atmosphere with a flowing rate of 25 cm^3 min^{-1} and a heating rate of 10 °C min^{-1} and the results are presented in Figure 4.3.

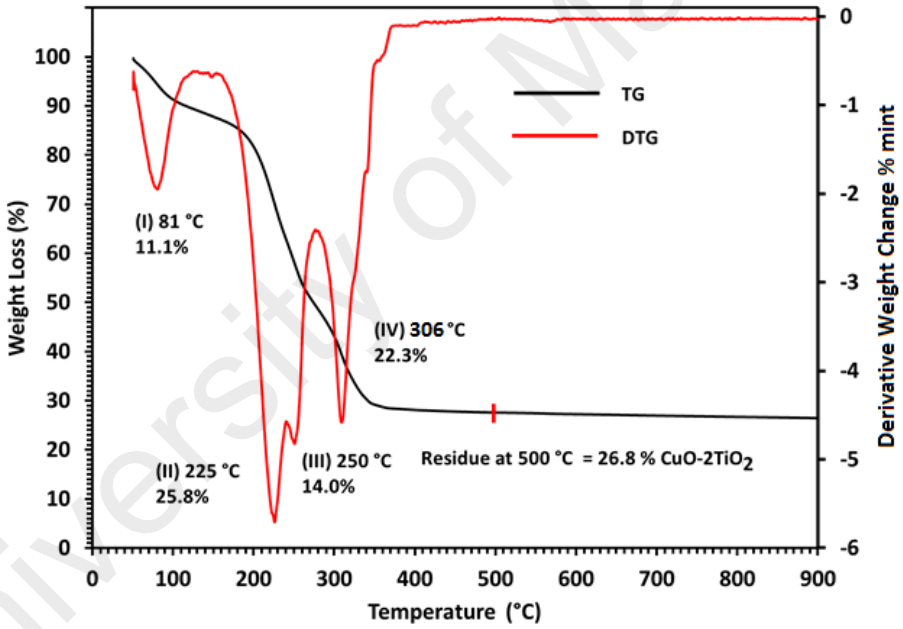

Figure 4.3: TG (black) and DTG (red) profiles representing thermal decomposition of complex (**1**) as a function of temperature.

The TG/DTG curves impart that thermal degradation of (**1**) completes in four continuous weight loss steps and maximum heat intakes sequentially occur at 81, 225, 250 and 306 °C giving weight loss of 11.1 %, 25.8%, 14.0%, and 22.3% respectively. The thermal decay process in (**1**) ends at 500 °C leaving an invariable residue that amounts to 26.80 % of its original mass. The weight of the residue (26.18%) reasonably accords with the formation of the expected 1:2 CuO: TiO_2

composite oxide material from (**1**). Further sintering of the observed residue to the higher temperature of 900 °C did not experience any change in weight, suggesting that (**1**) decomposes quantitatively to endow CuO-2TiO_2 as a stable final product. Based on TGA information, quantitative pyrolysis of (**1)** has been indicated in equation below:

Chemical equation 2:

$$[Cu_2Ti_4(O)_2(OH)_4(TFA)_8(THF)_6].THF \xrightarrow{500^{\circ}C} 2CuO - 2TiO_2 + Volatiles$$

4.1.3 Structural Analysis of CuO-2TiO_2

Thin films were developed via AACVD method on FTO glass substrate at temperature of 550 °C from 0.1M solution of precursor (**1**) in ethanol and methanol solvents respectively, using air as a carrier gas. The phase formation and degree of crystallinity of the deposited films were examined by XRD technique and X-ray diffractograms are comparatively overlapped in Figure 4.4. The XRD peak patterns seem identical in terms of their peak positions and 2θ values and both the diffractograms are dominated by the diffraction peak located at 2θ = 25.27° and 37.81°. XRD qualitative phase analysis was performed on each XRD pattern shown in Figure 4.4, which reveals the growth of tenorite CuO (ICSD 98-001-6025) (Åsbrink & Norrby, 1970) and a mixture of anatase (98-000-9853) (E.P. Meagher, 2002) and rutile (98-003-1321) (Mumme, Cranswick, & Chakoumakos, 2002) TiO_2 phases as crystalline end product in both the cases. The prepared CuO exists in a monoclinic crystal system with space group C12/c1 and produced characteristic peaks indicated by (Z) at 2θ = 32.58, 35.60, 48.84, 58.36, and 75.16˚ as observed by their Miller indices (110), (11-1), (20-2), (202) and (004) respectively. The emergence of peaks at 2θ = 25.27 (011), 37.80 (112), 48.0 (020)

70.39 (220) and 73.59˚ (017) denoted by (**X**) are well indexed to tetragonal anatase TiO_2.

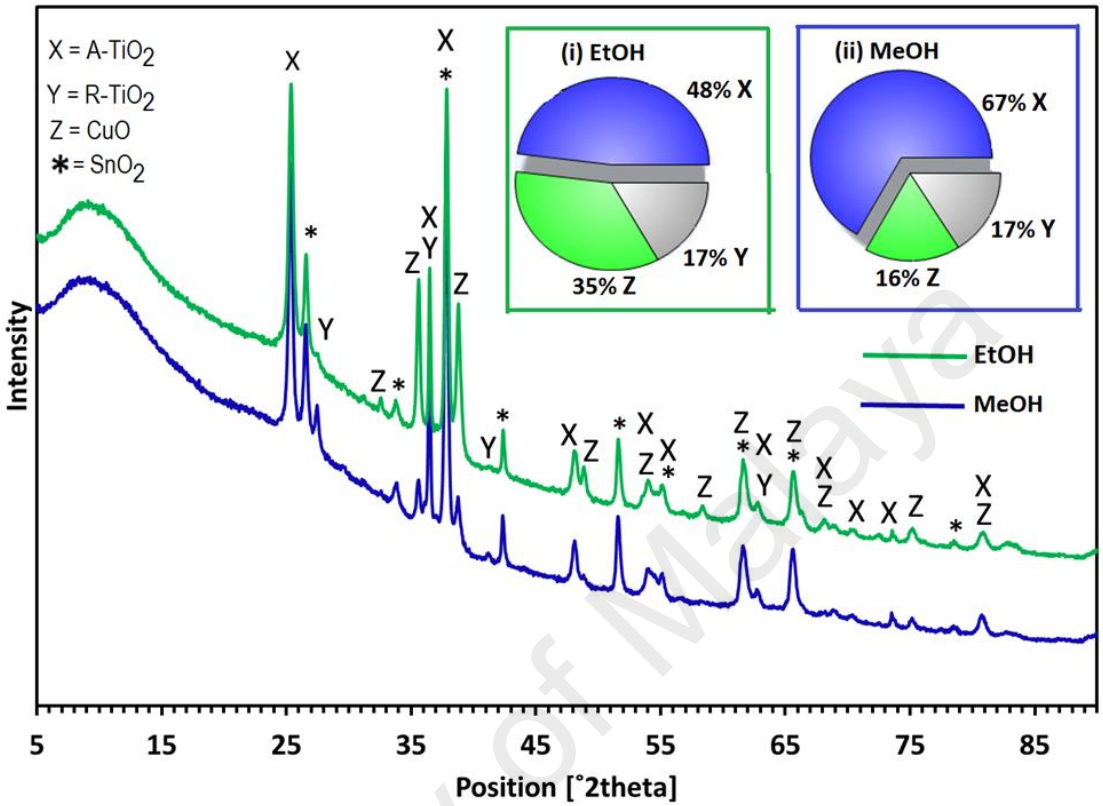

Figure 4.4: XRD patterns of the CuO-2TiO_2 composite thin films prepared from solutions of (1) in ethanol (green line), methanol (blue line), on FTO glass at 550 °C in air ambient; Inset shows the proportion of crystalline phases present in CuO-2TiO_2 composite films from (i) ethanol: 48% anatase TiO_2 (X), 17% rutile TiO_2 (Y), 35% tenorite TiO_2 (Z); (ii) methanol: 67% anatase TiO_2 (X), 17% rutile TiO_2, (Y) 16% tenorite CuO (Z).

Furthermore, the peaks marked by (**Y**) at 2θ = 27.46° (110), 36.0° (011) and 41.27° (111) are attributed to tetragonal rutile TiO_2. The X-ray diffractograms also demonstrate the overlapped peaks between CuO and anatase TiO_2 phases at 2θ values of 53.95°, 68.89° and 80.62˚. A few common reflections originating from both anatase and rutile TiO_2 phases appear at 2θ values of 36.45 and 62.75°. No possible crystalline impurities such as metallic copper or Cu_2O were detected from these XRD patterns.

The XRD qualitative phase analysis has established that both the copper oxide-titania composite films deposited from two different solvents are comprised of

similar crystalline phases including tenorite CuO and a mixture of anatase and rutile TiO_2. The proportion of crystallinity of each phase in the composite product was determined by XRD semi-quantification analysis. The crystalline composition of CuO-2TiO_2 deposit obtained from ethanol is poised at 48% anatase TiO_2 (**X**), 17% rutile TiO_2 (**Y**) and 35% tenorite CuO (**Z**), respectively (inset Figure 4.4(**i**)). The film deposited from methanol contains the crystalline contents of 67% anatase TiO_2 (**X**), 16% rutile TiO_2 (**Y**) and 17% tenorite CuO (**Z**), respectively (inset Figure 4.4(**ii**)).

The crystalline contents of the CuO-2TiO_2 films deposited from different solvents varies from each other which suggest that solvents play a vital role in decorating the crystalline phases of the films on substrate surface by AACVD and not just act as a transport medium. In aerosol deposition, solvents play an important role in the determination of the extent of a reaction. The precursor can react differently in various solvents in the gas phase which may lead to the formation of different intermediates and thus to different phases of the deposit. There have been similar reports whereby a variety of solvents have been used to alter the phase composition of titania using sol-gel approach, spray pyrolysis and AACVD (Edusi, et al., 2012),(Xiaoxin, Zhengguo, Shaojing, & Tao, 2005).

4.1.4 Raman Spectroscopy of CuO-2TiO_2

Further the structural analysis of CuO-2TiO_2 composites thin films deposited from two different solutions was carried out by Raman spectroscopy and results are displayed in Figure 4.5. The Raman scattering vibration modes detected at 151, 400, 519 and 630 cm^{-1}, corresponds to anatase TiO_2 phase (Nolan, Seery, & Pillai, 2011) and peaks located at 280 and 630 cm^{-1} signify the presence of CuO phase (Nguyen, Nguyen, Ung, & Nguyen, 2013). The characteristic peaks for rutile TiO_2

which are expected to appear at 246, 446 and 601 cm^{-1} are merged in the broad bands at 280, 400 and 630 cm^{-1} (Hardcastle, 2011). Hence the CuO and mixture of anatase and rutile TiO_2 phases determined from our XRD analysis are further validated from Raman spectroscopy.

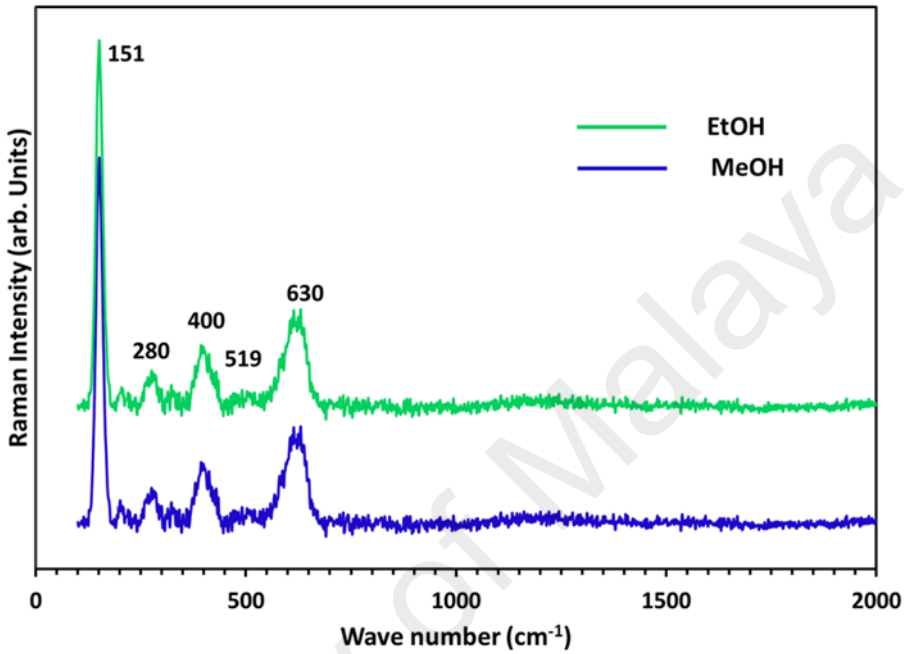

Figure 4.5: Raman spectra of the CuO-2TiO_2 composite thin films prepared from solutions of **(1)** in ethanol (green line), methanol (blue line), on FTO glass substrate at 550 °C in air ambient.

4.1.5 Micro-structural Properties of CuO-2TiO_2

The micro-structural properties of the films deposited from 0.1 M (20 mL) solution of precursor (**1**) in ethanol and methanol at 550 ˚C in air atmosphere were analysed by SEM.

Figure 4.6 depicts the surface and cross sectional SEM images of CuO-2TiO_2 composite films. Figure 4.6(a) shows the surface topography of the film, prepared from ethanol solution, is composed of interconnected spherical objects of heterogeneous design, shape and size which are developed in the vertical direction of substrate plane. One type of microspherical object attains donuts shape structure while

the other exists as round ball shaped entity of size range 0.5-1.3μm (Appendix 1(a2)). The low resolution surface SEM images (Appendix 1(a1)) reveal that these microspherical objects are homogenously distributed though out the film matrix.

The cross sectional view of CuO-2TiO_2 composite film of average thickness 4.0 μm, deposited from ethanol solution, displayed in Figure 4.6(b) and (Appendix 1. (b1)), show growth of small grains on the boundary layer of the FTO substrate. Figure 4.6 (b) shows that the surface architecture of the film obtained from methanol solution is made up of small and big sized spherical objects which are discretely grown in upward direction. The high resolution image (Appendix 1(c2)) demonstrates that the surface of these spherical bodies is fully covered with buds. The low resolution surface SEM image (Appendix 1. Figure 1(c1)) depicts that these objects are uniformly furnished on substrate surface however the surface of the substrate is not fully covered as observed in the film deposited from ethanol solution.

The shape of the thin-film cross sections is shown in Figure 4.6(d) and (Appendix 1 (d1)) and a layer of spheroid objects of thickness range 1.77-4.40 μm can be clearly seen on the surface of the FTO substrate.

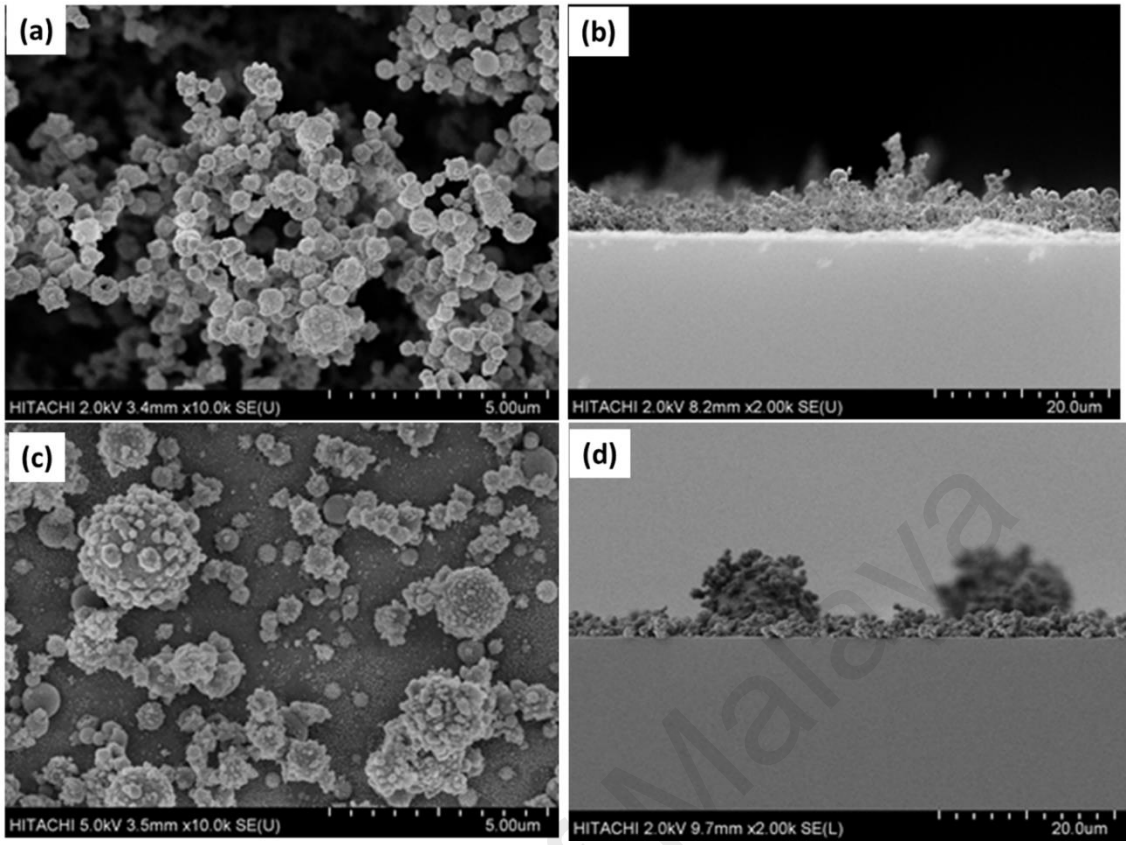

Figure 4.6: (a) and (c) show surface and (b) and (d) indicate the cross sectional SEM images of $CuO\text{-}2TiO_2$ composite thin films deposited on FTO glass substrate at 550 °C from solution of precursor (1) in (a, b) ethanol (c, d) methanol, respectively.

The elemental composition of $CuO–2TiO_2$ composite oxide thin films were analyzed by energy dispersive X-ray (EDX) analysis and spectra are presented in (Appendix 2(**i** & **ii**)). The EDX analysis performed on several randomly selected large regions revealed that the metallic ratio of Cu:Ti in the films is close to 1: 2 confirming the retention of the same metallic ratio in the films as found in complex (**1)**.

Further EDX map analysis was performed to establish the composite nature of the $CuO–2TiO_2$ films. The distribution of the constituent Cu, Ti and O atoms has been highlighted by using different color schemes as shown in Figure 4.7 (a & b) which reveals the even distribution of these atoms throughout the films matrix.

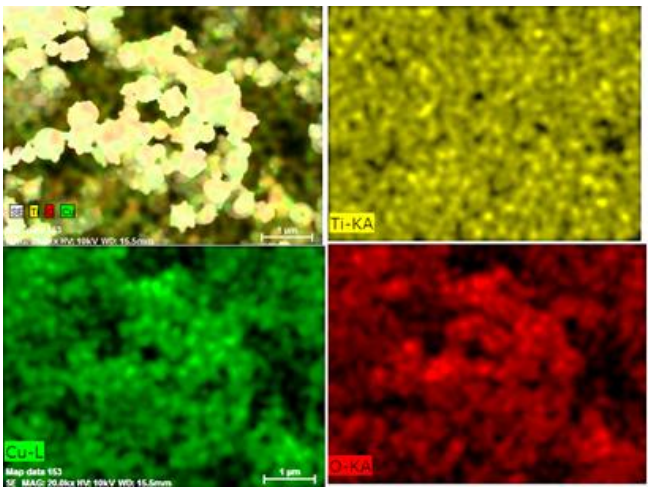

Figure 4.7a: : EDX Elemental map showing the distribution of Cu, Ti and O atoms in CuO–2TiO_2 composite thin film deposited from ethanol solution of precursor (**1**).

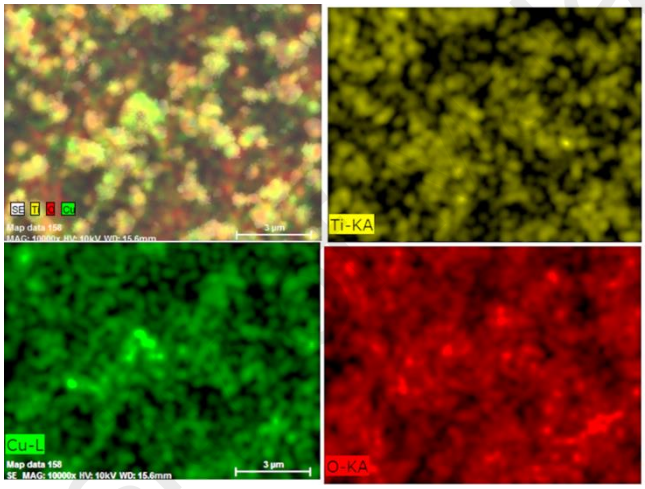

Figure 4.7b: EDX Elemental map showing distribution of Cu, Ti and O atoms in CuO–2TiO_2 composite thin film deposited from methanol solution of precursor (**1**).

4.1.6 XPS Analysis of CuO-2TiO_2

The XPS analysis was employed to determine the surface composition and chemical states of the Cu, Ti, and O elements in CuO-2TiO_2 composite oxide thin film prepared from ethanol solution of precursor (**1**) at 550 °C.

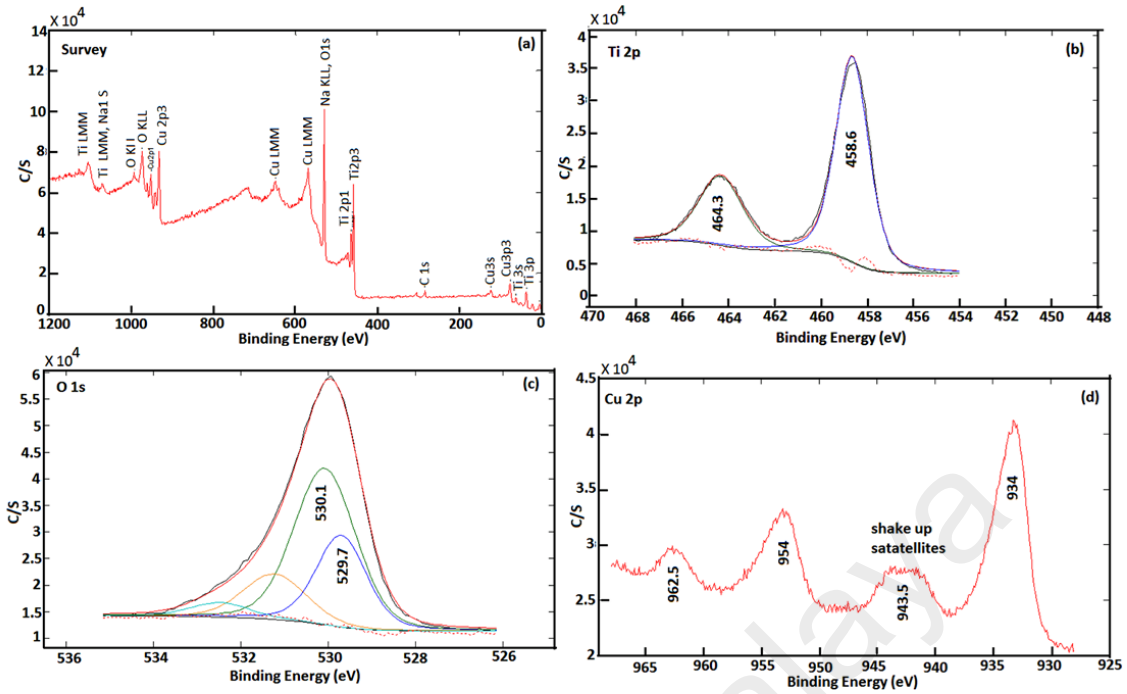

Figure 4.8: **(a)** Survey scan XPS spectrum of CuO-2TiO_2 composite thin films prepared from ethanol solution; High resolution spectra of CuO-2TiO_2 for **(b)** Ti 2p **(c)** O 1s **(d)** Cu 2p

The survey scan spectrum in Figure 4.8(a) shows the binding energy peaks at 458.4, 529.5 and 933.4 eV which are attributed to Ti 2p, O 1s and Cu 2p respectively. In the high resolution Ti 2p spectrum Figure 8(b), binding energies of 458.6 and 464.3 eV are indicative of Ti 2p3/2 and Ti 2p1/2 respectively which correspond to Ti^{4+} and matches well with the published data for TiO_2 (S. S. Lee, Bai, Liu, & Sun, 2013). Meanwhile, the peaks at 529.7 and 530.1 eV are evidence of O1s in CuO and TiO_2 Figure 4.8(c). The Cu 2p peak of the CuO-2TiO_2 is shown in Figure 4.8(d). The Cu 2p3/2 is allocated at 934 eV with a shakeup satellite peak at about 943.5eV and Cu 2p1/2 lies at 954 eV with a satellite peak at about 962.5eV, which is consistent with earlier reports (Dar, Nam, Kim, & Kim, 2010; D. Tahir & Tougaard, 2012). The presence of shakeup satellite features for Cu 2p rules out the possibility of presence of Cu_2O phase. The gap between Cu 2p1/2 and Cu 2p3/2 is 20eV, which is in agreement with the standard CuO spectrum (L. Zhu, Hong, & Ho, 2015).

4.1.7 Electrochemical Detection of Nitrite Ions by CuO-2TiO_2 Film Electrodes

The CuO–2TiO_2 composite film deposited from ethanol solution of (**1**) was used for the electrocatalysis and sensing of NO_2^- ions in 0.1 M phosphate buffer solution (PBS) (pH 7.2).

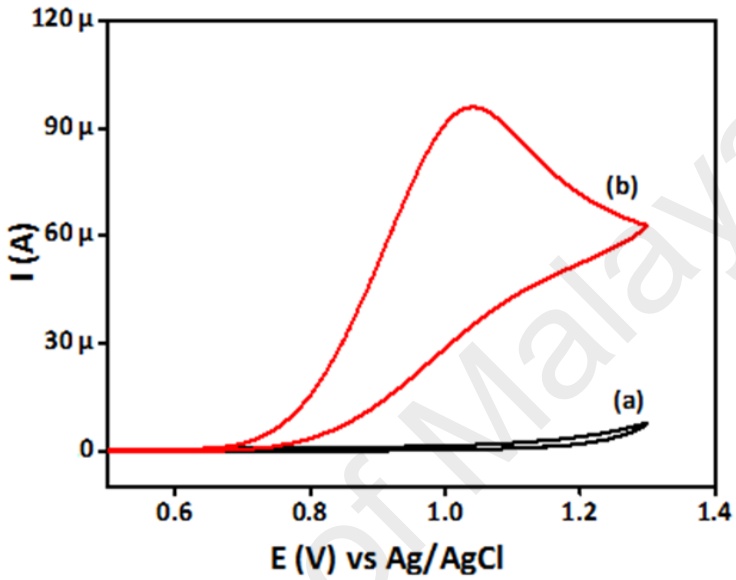

Figure 4.9: Cyclic voltammograms obtained for the CuO–2TiO_2 composite thin film in the (a) absence and (b) presence of 5 mM NO_2^- ions in 0.1 M PBS (pH 7.2) at a scan rate of 50 mV s^{-1}

The CuO–2TiO_2 composite electrode displayed an intense anodic peak current in the cyclic voltammogram for 5 mM NO_2^- at +1.0 V due to the electrocatalytic oxidation of NO_2^-, Figure 4.9(b), and did not show any voltammetric response in the absence of NO_2^-, Figure 4.9(a). During the electrocatalytic oxidation of NO_2^-, two electrons were transferred and thus to form NO_3^- as a product.(Guidelli, Pergola, & Raspi, 1972)·(Pandikumar, Yusoff, Huang, & Lim, 2014) Further, influence of the scan rate on the electrocatalytic oxidation peak potential (E_{pa}) and peak current for NO_2^- at the CuO–2TiO_2 film electrode in 0.1 M PBS (pH 7.2) were studied using CV, as shown in Figure 4.10(a).

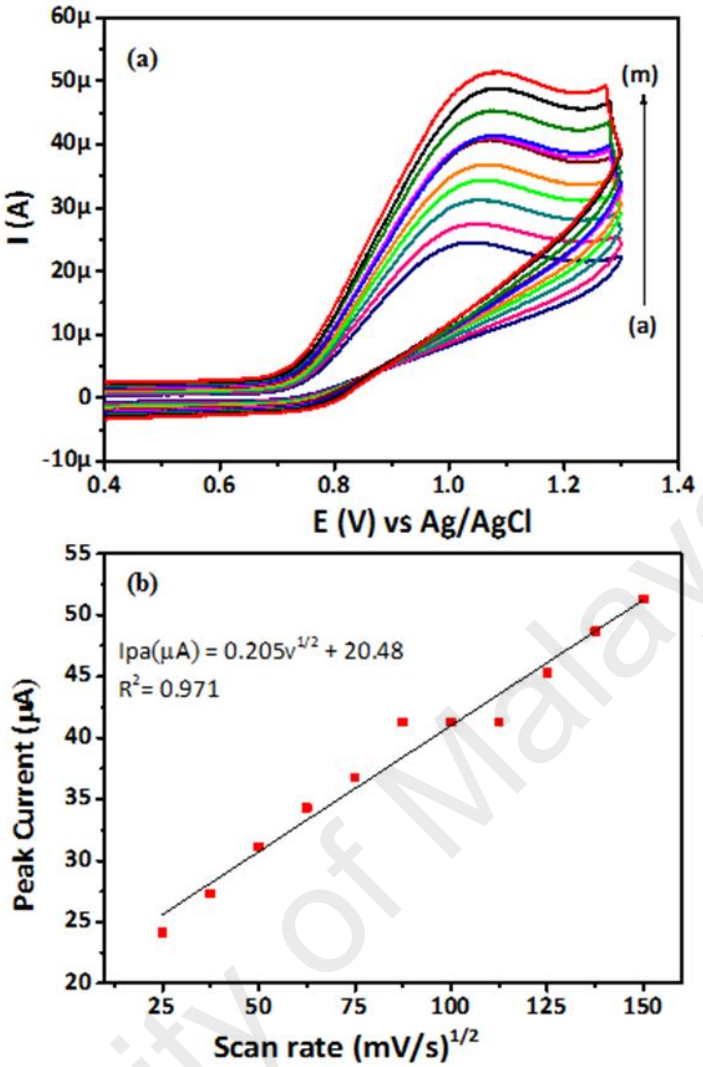

Figure 4.10: (a) Cyclic voltammograms recorded for the CuO–2TiO_2 electrode in the presence of 1 mM NO_2^- ions in 0.1 M PBS (pH 7.2) at various scan rates of ((a)–(m)) 10–300 mV s^{-1}. (b) Plot of anodic peak current vs square root of the scan rate obtained for the CuO–2TiO_2 electrode.

The current values were found to be increased with an increase in the scan rate from 10 to 300 mV s^{-1}, Figure 4.10(a). The linear relationship between the anodic peak currents and the square root of the scan rate is shown in Figure 10(b). As can be seen, the anodic peak current (I_{pa}) for the 1 mM NO_2^- varied linearly with the square root of the scan rate ($v^{1/2}$), with a linear regression equation of (I_{pa} (μA) = $0.205v^{1/2}$ + 20.48) and a correlation coefficient R^2 = 0.971. This result indicates that the electron transfer of the CuO–2TiO_2 composite film is mainly controlled by a diffusion-controlled electrochemical process (Ikhsan et al., 2015).

The sensitivity of the sensor under the optimized detection for NO_2^- conditions were tried, and a series of linear sweep voltammetry (LSV) curves were recorded in 0.1 M PBS (pH 7.2) with different NO_2^- concentrations at the CuO–2TiO_2 electrode as shown in Figure 4.11(a). It could be observed that the anodic peak current increased linearly with an increase in the concentration of NO_2^- in the range of 10 to 200 μM, with a linear regression equation of I_{pa} = 0.0415 M + 1.4336 μ (R^2 = 0.9994), Figure 4.11(b). The sensitivity is determined from the slope of the calibration plot. The Figure 4.11(b) shows the standard addition line, limit of detection (LoD) for NO_2^- was calculated as 16.6 nM (S/N = 3). It can be seen that this present detection limit is comparable as well as lower than detection limits obtained for other oxides by different electrochemical methods.

The sensing performance of the CuO–2TiO_2 composite film was compared with other previously reported sensor materials for the detection of NO_2^- and the results are summarized in Table 4.2 which indicates that the detection limit of the present sensor is better than the other oxide materials.

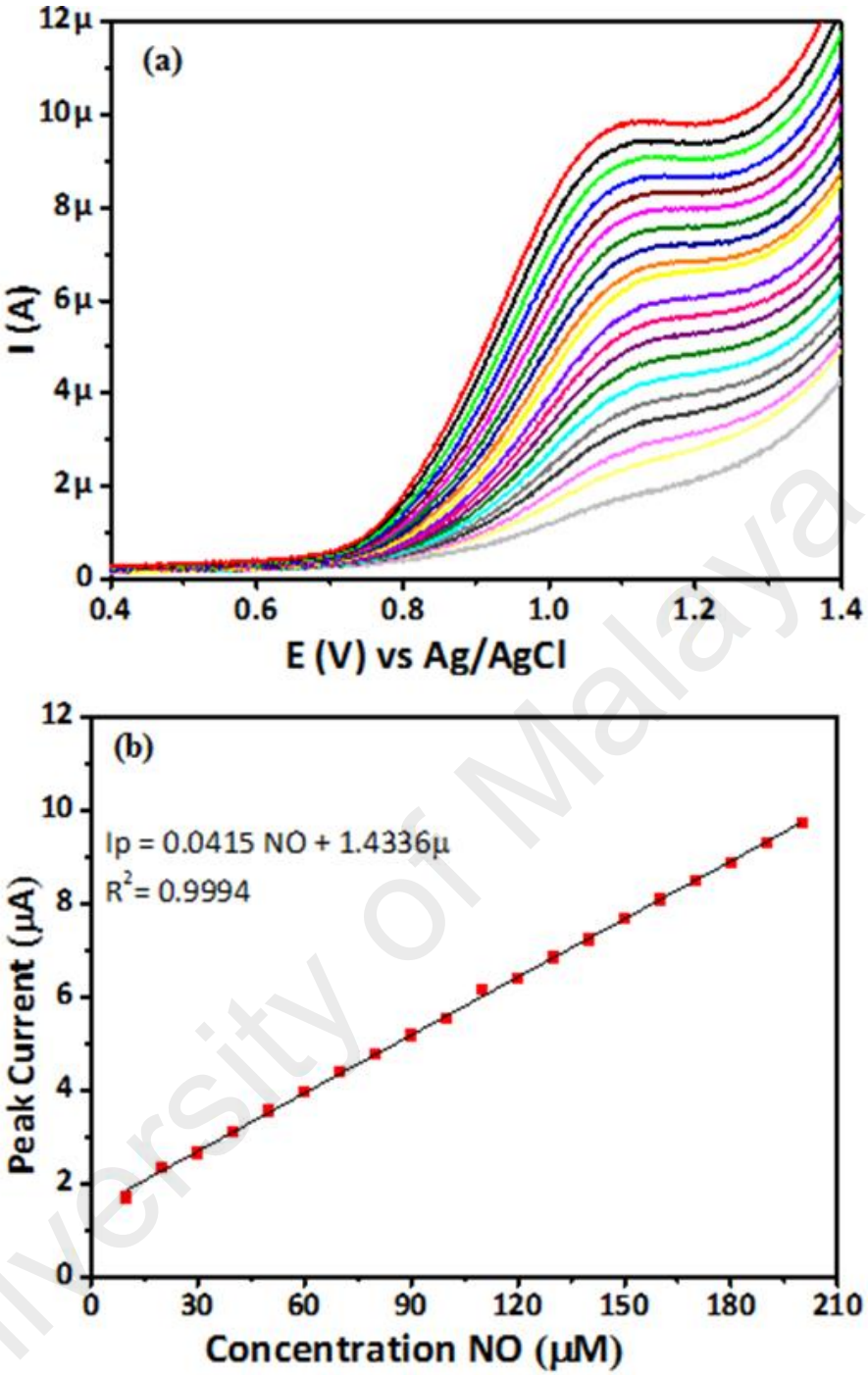

Figure 4. 11:(a) Linear sweep voltammograms (LSV) obtained for the CuO–2TiO_2 composite thin film for various concentration of NO_2^- ions in 0.1 M PBS (pH 7.2) at a scan rate of 50 mV s^{-1}. (b) Correlation between the concentration of NO_2^- and peak current for the CuO–2TiO_2 electrode.

Table 4.2: Comparison of analytical performance of various electrochemical sensors for nitrite (NO_2^-) detection.

Sensor material	Analytical technique	Limit of detection (LOD)	Ref.
MnO_2-CP-E	Linear sweep voltammetry	1.2μM	(Langley, ŠLJUKIC, Banks, & Compton, 2007)
Cobalt oxide	Cyclic voltammetry	20 mM	(Salimi, Hallaj, Mamkhezri, & Hosaini, 2008)
CuO–graphite	Cyclic voltammetry	0.6 μM	(Biljana Šljukić, Craig E Banks, Alison Crossley, & Richard G Compton, 2007)
PbO_2 –graphite	Cyclic voltammetry	0.9 μM	(Biljana Šljukić, Craig E Banks, Alison Crossley, & Richard G Compton, 2007)
f-ZnO@rFGO	Linear sweep voltammetry	33 μM	(Pandikumar, et al., 2014)
$ZnTiO_3$–TiO_2	Amperometry	3.98 μM	(Ehsan, Khaledi, Pandikumar, Rameshkumar, et al., 2015)
CuO–$2TiO_2$	Linear sweep voltammetry	16.6 nM	Present work

The selectivity of the CuO–$2TiO_2$ electrode for the determination of NO_2^- investigated by adding various possible interferents and observing the change in current (Figure 4.12). The LSV was continuously recorded for the addition of common interferents such as NaF, NH_4Cl, KCl, $NaNO_3$ and $MgSO_4$ in a homogeneously stirred of 0.1 M PBS (pH 7.2) and

there is no significant current response found due the interferents. Upon addition 100 µM NO_2^-, the electrode showed the response signal (Figure 4.12). This observation clearly demonstrates that the selective detection of NO_2^- even in the presence of common interferents is possible and the CuO–2TiO_2 composite possesses high selectivity toward NO_2^- over other common interferents.

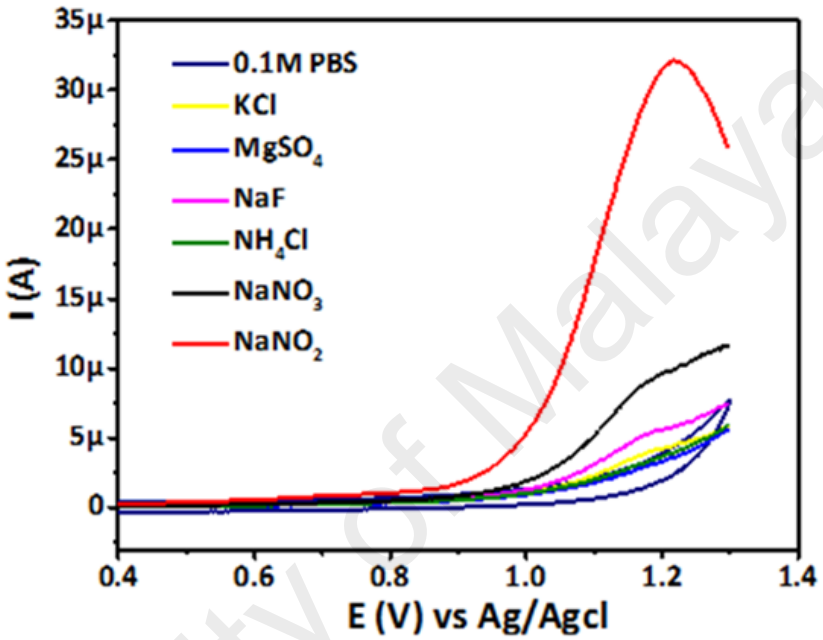

Figure 4.12: LSV response obtained for CuO–2TiO_2 composite thin film for the addition of and each 1000 µM addition of other interferences such as KCl, $MgSO_4$, NaF, NH_4Cl , $NaNO_3$ and 100 µM NO_2^- ions in 0.1 M PBS (pH 7.2) at scan rate of 50 mV s^{-1}.

4.2 Synthesis of Complex $[Co_2Ti_4(\mu\text{-}O)_6(TFA)_8(THF)_6]\cdot THF$ (2)

The synthetic protocol of heterobimetallic precursor $[Mg_2Ti_4(O)_2(OH)_4(TFA)_8(THF)_6]\cdot THF$ (**2**) involves the reaction of diacetatomagnesium(II) tetrahydrate with tetraisopropoxytitanium(IV) in presence of trifluoroacetic acid in THF. As the reaction progresses, the more labile isopropoxy ligands are exchanged by stronger chelating TFA groups which bind Mg and Ti atoms through its carboxylate oxygen atoms. The exchange of ligands and progress of the reaction can be observed by dissolution of salts to result in a clear solution. The transparent solution was then evaporated in vacuum to obtain a

white powder which was re-dissolved in 3 mL THF and kept at room temperature to grow the first 70% yield of translucent white crystals of the precursor (**2**). The overall reaction for the formation of (**2**) is shown below in equation .

Chemical equation 3

$$2Co(CH_3COOH)_2.4H_2O + 4Ti(OCH(CH_3)_2)_4 + 8CF_3COOH \xrightarrow{THF}$$
$$[Co_2Ti_4(\mu - O)_6(CF_3COO)_8(C_4H_8O)_6].C_4H_8O + 4CH_3COOH + 16(CH_3)_2CHOH$$

The substitution of carboxy with TFA groups not only aids binding of Mg and Ti atoms in one framework but also co-ordinatively saturates each metal centre, making the precursor more volatile as well as soluble in organic solvents such as chloroform, THF, methanol and ethanol, rendering it a suitable precursor to produce single phased $MgTi_2O_5$ thin films by the AACVD method. The stoichiometric composition of complex (**2**) was recognized by single crystal X-ray diffraction and further confirmed by FTIR and TG/DTG analysis. The FT-IR spectrum of Mg-Ti precursor showed strong absorption bands at 1654 and 1453 cm^{-1} due to the asymmetric and symmetric ν(C=O) vibrations of the 95carboxylate group of the TFA ligands respectively. The difference of value $\Delta\nu_{asy}$-$\Delta\nu_{sy}$ = 200 cm^{-1} is consistent with the bidentate bridging behavior of TFA ligand. Similarly, a sharp peak at 1192 cm^{-1} confirms the existence of C–F bonds in complex (**2).** The IR spectrum is closely related to those reported previously for similar heterobimetallic compounds.

4.2.1 Molecular Structure of Complex $[Co_2Ti_4(\mu\text{-}O)_6(TFA)_8(THF)_6]\cdot THF$ (2)

The molecular structure of the Co-Ti complex is depicted in Figure 4.13 and a schematic drawing for the molecule is given in Figure 4.14. The structure of the Co-Ti complex resembles those of the analogous Fe-Ti (Ehsan, et al., 2011), Cd-Ti (Ehsan, Khaledi,

Pandikumar, Huang, et al., 2015) and Zn-Ti (Ehsan, Khaledi, Pandikumar, Rameshkumar, et al., 2015) complexes, being isostructural with the latter two complexes.

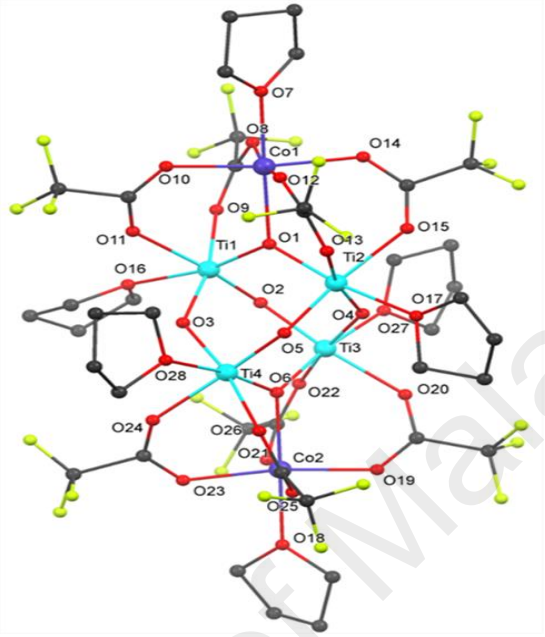

Figure 4.13: Crystal structure of complex $[Co_2Ti_4(\mu\text{-}O)_6(TFA)_8(THF)_6]\cdot THF$ (**2**). The minor component of disorder, hydrogen atoms, and the solvate THF molecule are not shown.

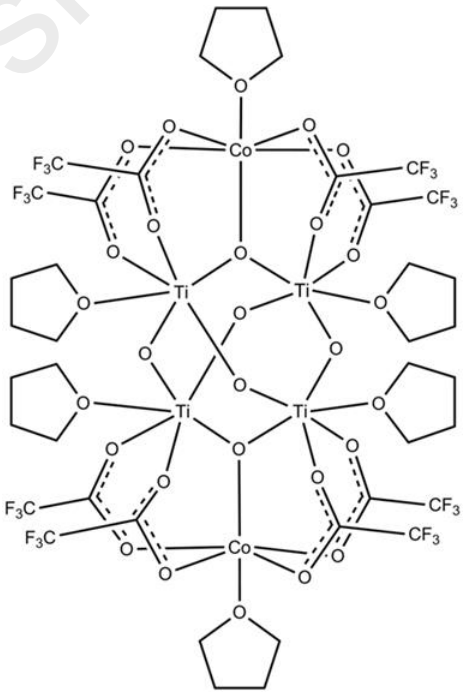

Figure 4.14: Schematic diagram of complex $[Co_2Ti_4(\mu\text{-}O)_6(TFA)_8(THF)_6]\cdot THF$ (**2**).

The molecule has a non-crystallographic D_2 point symmetry and consists of a Ti_4O_6 core arranged in an adamantane-like structure. Two of the core O atoms (O1, O6) are of the μ_3-type that bridge pairs of the tetrahedrally located Ti's to the two Co^{II} centers. The other four O atoms (O2, O3, O4, O5) link only pairs of the Ti atoms. Each metal center in the structure is in an octahedral coordination environment made of six O atoms from the Ti_4O_6 cage, TFA's and THF ligands. Table 4.3 lists the coordination bond lengths for the structure. The Ti-Ti separations are between 3.328-3.352 Å which are comparable to those in the analogous structures.

Table 4.3: Coordination bond lengths for $[Co_2Ti_4(\mu\text{-}O)_6(TFA)_8(THF)_6]\cdot$ THF **(2)**

Co(1)-O(1)	2.175(6)	Ti(2)-O(13)	2.080(12)
Co(1)-O(7)	2.111(7)	Ti(2)-O(15)	2.108(10)
Co(1)-O(8)	2.039(8)	Ti(2)-O(17)	2.168(9)
Co(1)-O(10)	2.064(7)	Ti(3)-O(2)	1.860(8)
Co(1)-O(12)	2.083(8)	Ti(3)-O(4)	1.744(8)
Co(1)-O(14)	2.079(8)	Ti(3)-O(6)	1.881(7)
Co(2)-O(6)	2.154(7)	Ti(3)-O(20)	2.079(13)
Co(2)-O(18)	2.108(6)	Ti(3)-O(22)	2.101(12)
Co(2)-O(19)	2.030(11)	Ti(3)-O(27)	2.179(8)
Co(2)-O(21)	2.035(8)	Ti(4)-O(3)	1.851(8)
Co(2)-O(25)	2.041(8)	Ti(4)-O(5)	1.782(8)
Co(2)-O(23)	2.046(8)	Ti(4)-O(6)	1.925(7)
Ti(1)-O(1)	1.853(7)	Ti(4)-O(24)	2.067(9)
Ti(1)-O(2)	1.809(8)	Ti(4)-O(26)	2.116(11)
Ti(1)-O(3)	1.792(8)	Ti(4)-O(28)	2.161(9)
Ti(1)-O(9)	2.092(13)	Ti(1)-Ti(2)	3.347(4)
Ti(1)-O(11)	2.085(10)	Ti(1)-Ti(3)	3.328(4)
Ti(1)-O(16)	2.155(10)	Ti(1)-Ti(4)	3.345(4)
Ti(2)-O(1)	1.938(7)	Ti(2)-Ti(3)	3.347(4)
Ti(2)-O(5)	1.813(8)	Ti(2)-Ti(4)	3.338(4)
Ti(2)-O(4)	1.870(8)	Ti(3)-Ti(4)	3.352(4)

4.2.2 Thermal (TG/DTG) of complex $[Co_2Ti_4(\mu\text{-}O)_6(TFA)_8(THF)_6]\cdot THF$ (2)

The thermal pyrolysis of complex (**2**) was investigated by thermogravimetric (TG) and derivative thermogravimetric (DTG) analysis in a flowing N_2 atmosphere at the rate of 25 cm^3 min^{-1} and a heating rate of 10 °C min^{-1} and results are displayed in Figure 4.15.

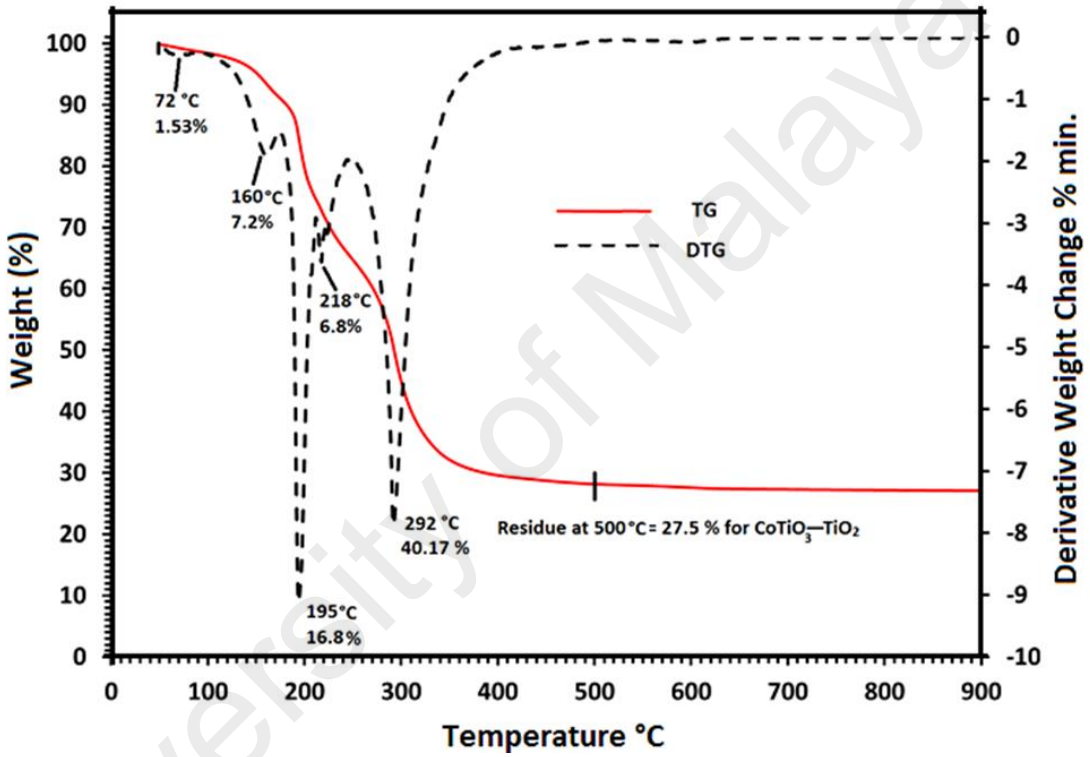

Figure 4.15: TG (red) and DTG (dotted black) traces of thermal decomposition of complex (**2**) as a function of temperature

The TG (red) and DTG (black) curves in Figure 4.15 indicate that complete thermal degradation of complex (**2**) occurs in five consecutive weight loss stages of 1.53, 7.2, 16.8, 6.8 and 40.17% which appear at maximum heat intake steps at 72, 160, 195, 218, and 292 ˚C respectively. The weight loss phases are completed at 500 °C yielding steady residues of 27.5 % of its original mass which is equitable with the formation of the expected 1:1 of $CoTiO_3$: TiO_2 (25.80%) composite oxide material from (**2**). Further sintering of the observed residue to the higher temperature of 900 °C did not produce any change

in weight, suggesting that complex (**2**) decomposes quantitatively to endow $CoTiO_3$–TiO_2 as a stable final product. Based on TGA information, quantitative pyrolysis of (**2)** has been indicated in equation below:

Chemical equation 4:

$$[Co_2Ti_4(\mu-O)_6(TFA)_8(THF)_6].THF \xrightarrow{500^{\circ}C} 2CoTiO_3 - TiO_2 + Volatiles$$

4.2.3 XRD Analysis of $CoTiO_3$-TiO_2 Thin Films

The ability of complex (**2**) to act as a single source precursor (SSP) for the formation of advanced composite oxides thin film was investigated by AACVD and film deposition experiments were carried out on FTO glass substrate at three different temperatures of 500, 550 and 600 ˚C using ethanolic solution of complex (**2**) in air ambient.

The structural characterization of crystalline deposit was made by XRD analysis and resultant patterns as function of substrate temperature are overlaid in Figure. 4.16. Each XRD pattern in Figure 4.16 was analyzed by qualitative phase analysis which indicates the presence of similar cobalt titanium oxide $CoTiO_3$ (ICSD 98-001-6548) (Newnham, Fang, & Santoro, 1964) and rutile TiO_2 (ICSD 98-001-6636) (Tomaszewski, 2002) phases in all the cases. In all films, the prepared $CoTiO_3$ exists in a hexagonal crystal system with space group R-3 and produced characteristic peaks indicated by (**X**) at 2θ = 23.9, 32.8, 35.4, 40.5, 49.0, 53.5, 61.9 and 63.6 ˚ as observed by their Miller indices (012), (104), (2-10), (2-13), (024), (116), (214) and (030), respectively. The emergence of peaks at 2θ = 27.4 (110), 36.0 (011), 41.3 (111), 44.0 (120) and 54.3˚ (121) denoted by (**Y**) are well indexed to tetragonal rutile TiO_2.

The X-ray diffractograms also demonstrate overlapped peaks between $CoTiO_3$ and rutile TiO_2 phases at 2θ values of 56.7, and 68.9˚. Peaks indicated by (*) are originated from

crystalline SnO_2 of the FTO substrate. Interestingly, all the XRD patterns show similar phases of ilmenite $CoTiO_3$ and rutile TiO_2 as end product prepared at different temperatures and no sign of phase transformation or growth of impurity phases such as CoO, Co_3O_4 and other titania varieties is perceived from these XRD results.

In comparison with recent literature, the cobalt titanate material is usually prepared at higher temperature of 600 ˚C and prolong heating is often required to improve the crystallinity of the product (Kapoor, Uma, Rodriguez, & Klabunde, 2005; G Zhou, Lee, Kim, Kim, & Kang, 2006; Chuang et al., 2010). This post sintering process deteriorates the phase purity of the product by generating various unwanted phases and undermines the worth of the material for technological applications.

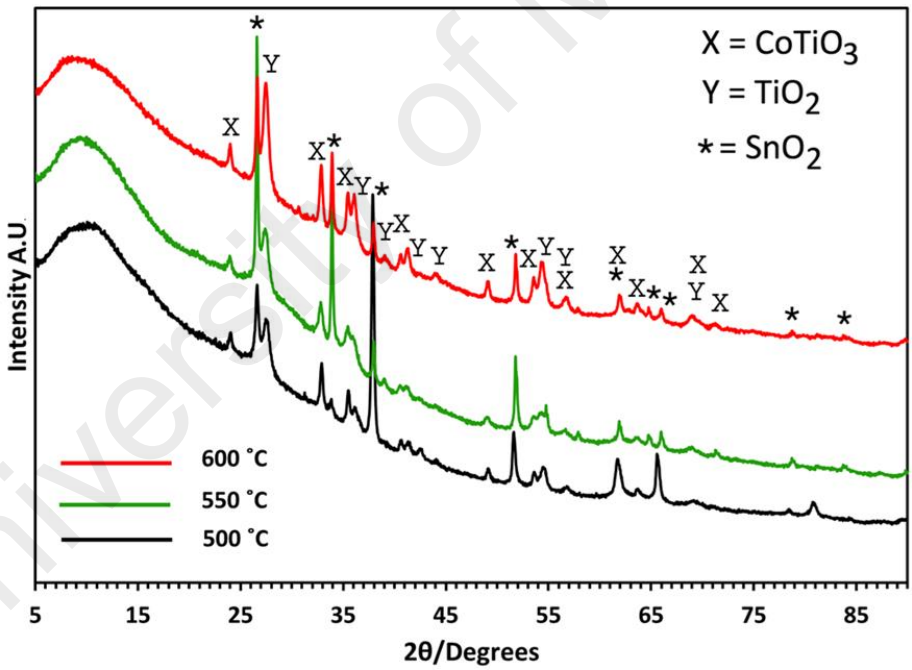

Figure 4.16: XRD patterns of $CoTiO_3$-TiO_2 composite films deposited on FTO glass substrate at different temperatures of 500 ˚C (black line), 550 ˚C (green line) and 600 ˚C (red line) from ethanolic solution of precursor (1). (X) indicates peaks originating from ilmenite-$CoTiO_3$ ((ICSD 98-001-6548)), (Y) specifies peaks related to rutile TiO_2 (ICSD 98-001-6636).

In comparison well crystallized $CoTiO_3$-TiO_2 composite oxide is formed at lower temperature of 500 ˚C and product remain pure and stable until 600 ˚C which is unique aspect of AACVD based SSP method.

4.2.4 Raman Spectroscopy of $CoTiO_3$-TiO_2 thin films

The chemical structure and identity of cobalt titanate and titanium dioxide phases in the composite films were further characterized from FT-Raman spectroscopy and the spectra of as-deposited films at different temperatures are comparatively shown in Figure 4.17.

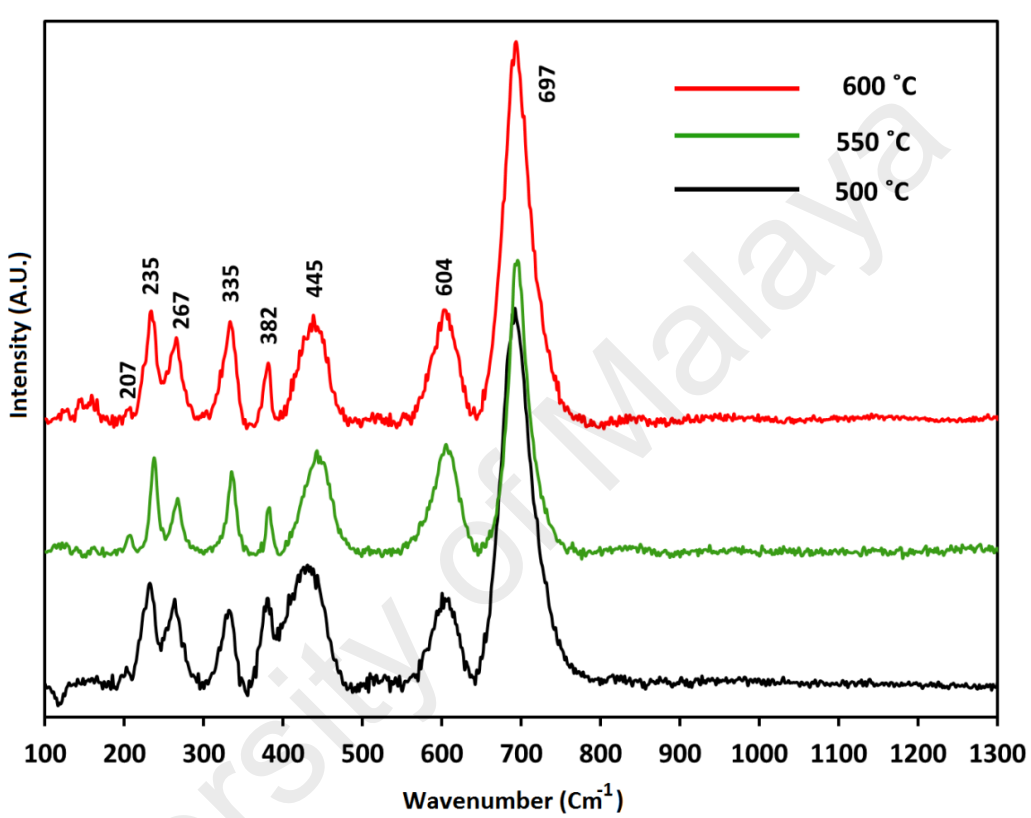

Figure 4.17: FT-Raman spectra of $CoTiO_3$-TiO_2 composite films deposited at different temperatures of 500 ˚C (black line), 550 ˚C (green line) and 600 ˚C (red line).

According to the literature, the Raman scattering modes appeared at 207, 235, 267, 335, 382, 604 and 696 cm^{-1} witness the presence of ilmenite $CoTiO_3$ phase in all cases (G Zhou, et al., 2006; Shilpy, Ehsan, Ali, Hamid, & Ali, 2015). The most typical feature of $CoTiO_3$ is the strong Raman mode observed near 700 cm^{-1}. This mode arises from the highest frequency vibrational mode of CoO6 octahedra that is the symmetric stretching mode (A_{1g} symmetry for regular Oh octahedral) (G Zhou, et al., 2006). The characteristic Raman active band for ruitle TiO_2 (Hardcastle, 2011; Nolan, et al., 2011) phase is observed at 447 cm^{-1}, while the other expected absorptions bands of 246 and 601 seem to

merge with the broad peaks of 235 and 604 of $CoTiO_3$. These results indicate formation of phase pure $CoTiO_3$ and rutile TiO_2 in all cobalt titanate-titania composite films prepared at different temperatures of 500, 550 and 600 ˚C.

4.2.5 Microstructural properties of $CoTiO_3$-TiO_2 thin films

The surface morphology, architectures and cross sectional views of $CoTiO_3$-TiO_2 composite films developed at 500, 550 and 600 °C from ethanol solutions of the precursor (**2**) are shown in Figure 4.18. Figure 4.18a shows that the surface topography of the $CoTiO_3$-TiO_2 film deposited at 500 ˚C is composed of spherical objects of two different types of microspheres which are grown in horizontal and vertical directions of the substrate surface and are in the size range of 0.3-0.9μm. The surface of one type of microsphere contains buds while others are relatively bare. The cross sectional view of $CoTiO_3$-TiO_2 composite film prepared at 500 ˚C is displayed in Figure 4.18(**b**) where small grains developed on the boundary layer of the FTO substrate can be clearly seen and film average thickness was measured to be 4.5 μm.

When the deposition temperature increases to 550 ˚C, the substrate surface is decorated with a new designs of $CoTiO_3$-TiO_2 spherical entities and Figure. 4.18 (c) displays that the surface of one kind of spherical object of size 1.12 μm contains tiny particles on its surface while the other type of microsphere of size 0.55 μm exhibits a smooth and plain texture. Figure 4.18(d) designates the cross sectional view of the $CoTiO_3$-TiO_2 composite film and it is observed that film thickness increases to 7.8 μm with the rise in temperature from 500 to 550 ˚C. Further increasing the deposition temperature to 600 °C results in formation of mixture of donuts and round shaped crystallites of $CoTiO_3$-TiO_2 as displayed in Figure 4.18 (e) and the shape of the thin-film cross sections is shown in Figure 4.18 (f) where

a layer of spheroid particles of thickness 18 µm is visibly displayed on the surface of the FTO substrate.

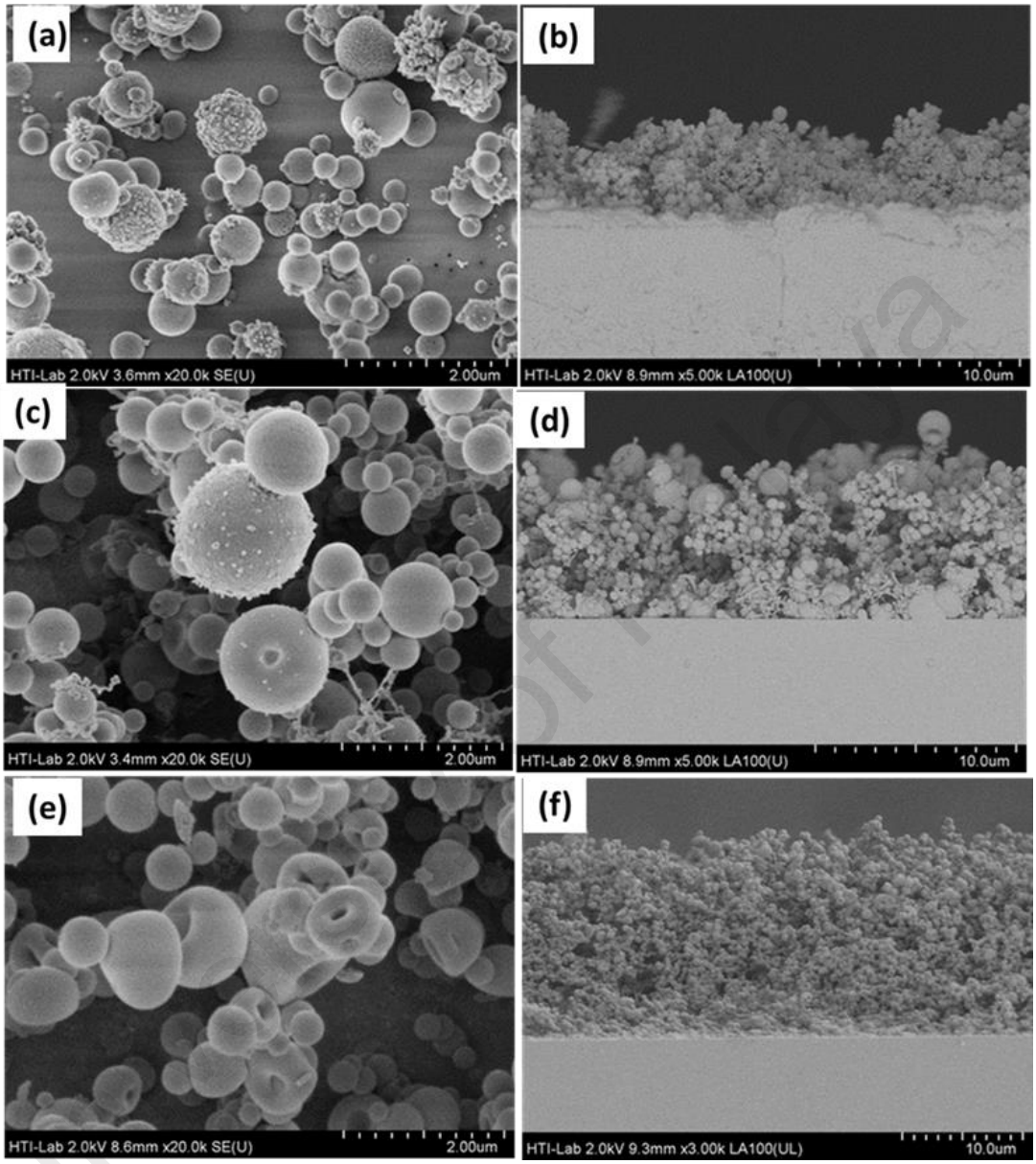

Figure 4.18: (a), (c) and I show surface and (b), (d) and (f) indicate the cross sectional SEM images of $CoTiO_3$-TiO_2 composite thin films deposited on FTO glass substrate from ethanolic solution of precursor (**2**) at temperatures (a, b) 500 ˚C (c, d) 550 ˚C and (e, f) 600 ˚C, respectively.

The surface compositions of all films were analysed by energy dispersive analysis (EDX) analysis. EDX spectra shown in (Appendix 3(i, ii and iii) were recorded at various arbitrary large areas of the films which revealed that the percent atomic ratio of Co: Ti in the films is almost 1: 2 which is in accordance with the expected 1: 2 elemental ratio present in precursor (**2)**. These results confirm that the films

grown at different temperatures 500, 550 and 600 ˚C retain the same metallic ratio as found in complex (**2)**.

Further the heterogeneity and distribution of cobalt, titanium and oxygen atoms in $CoTiO_3$-TiO_2 composite films was examined by EDX mapping and results are shown in Figure 4.19 (a- c) which reveal that these atoms are evenly distributed throughout the films matrix confirming the composite nature of all films prepared at different temperatures.

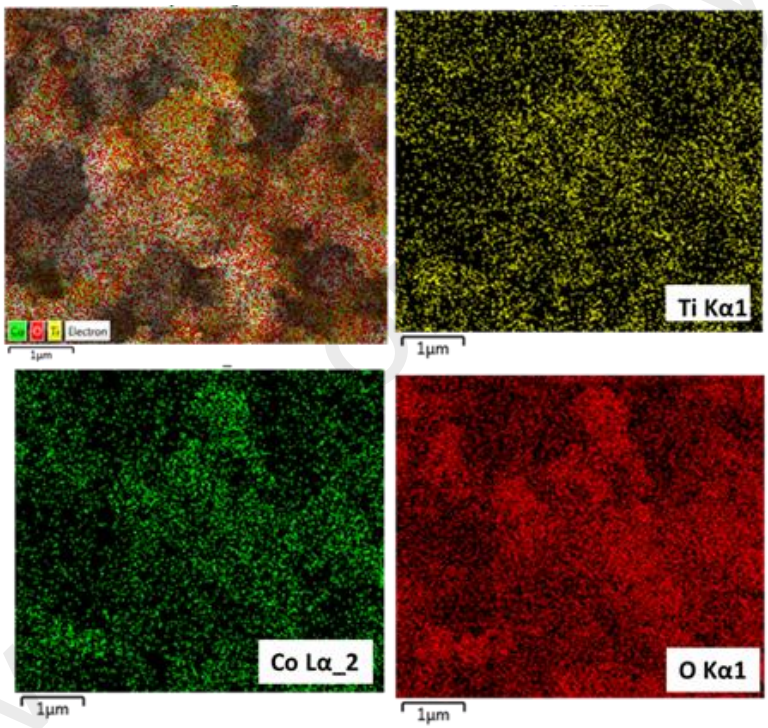

Figure 4.19a: Elemental Map showing the distribution of Co, Ti and O elements in $CoTiO_3$-TiO_2 composite film deposited at 500 ^oC

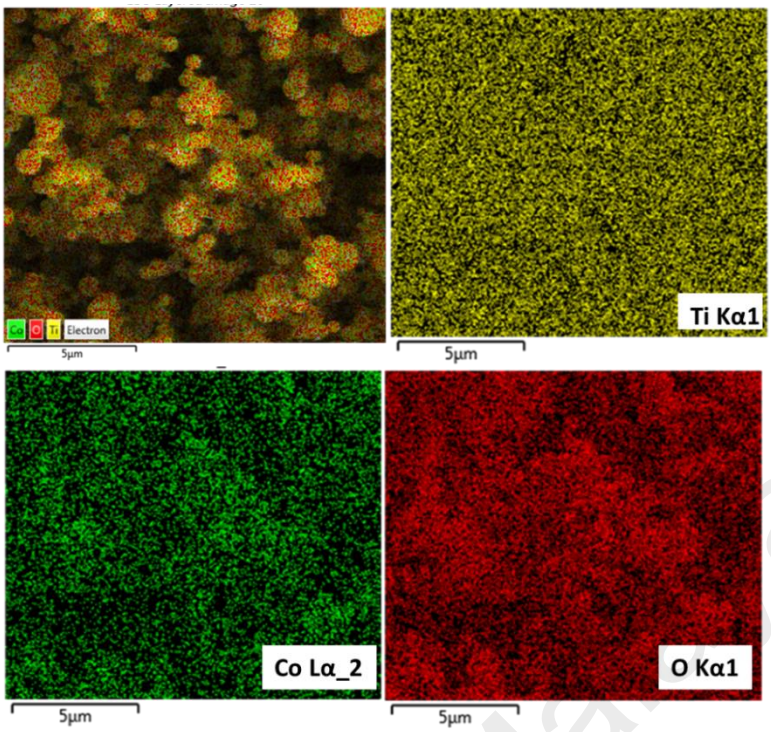

Figure 4.19b: Elemental Map showing the distribution of Co, Ti and O elements in $CoTiO_3$-TiO_2 composite film deposited at 550 ^oC

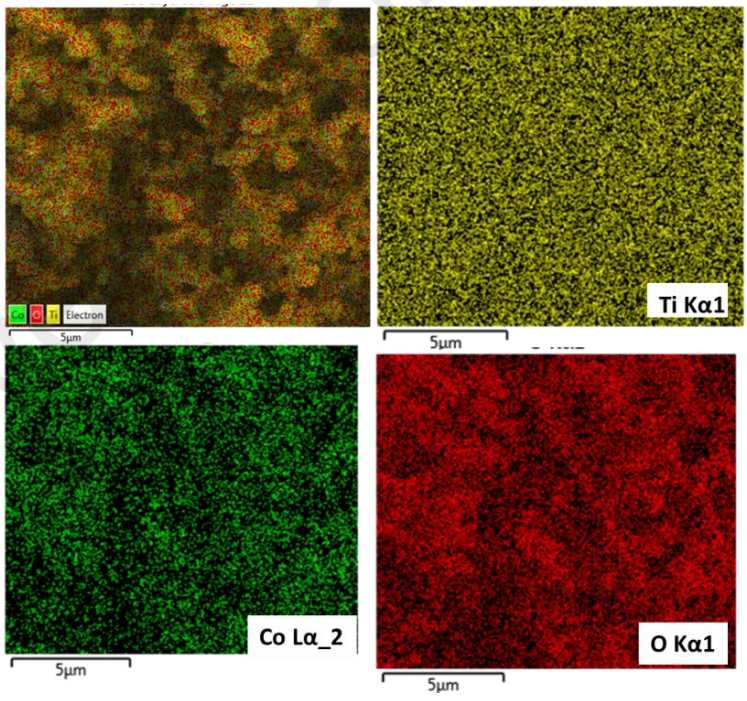

Figure 4.19c: Elemental Map showing the distribution of Co, Ti and O elements in $CoTiO_3$-TiO_2 composite film deposited at 550 ^oC

All $CoTiO_3$-TiO_2 films were translucent and light green in colour. The films deposited at lower temperature of 500 and 550 ˚C were robust and adhered strongly on the FTO substrate as verified by the ‘‘Scotch tape test’’ while the film prepared at 600 ˚C showed poor adhesive properties and was failed to qualify the adherence test.

4.2.6 XPS Analysis of $CoTiO_3$-TiO_2 thin films

The $CoTiO_3$-TiO_2 composite film prepared at 550 ˚C was further examined by X-ray photoelectron spectroscopy (XPS) and results are presented in Figure 4.20. The XPS survey scan spectrum in Figure 4.20 (a) indicates that cobalt, titanium, and oxygen are the major components at the surface of the film. After elements identification, their chemical and valence states were analyzed by narrow scans and results are shown in Figure 4.20 (b-d).

In the high resolution Ti 2p spectrum , Figure 4.20 (b), the binding energies of 458.7 and 464.4 eV are indicative of Ti 2p3/2 and Ti 2p1/2 respectively which correspond to Ti^{4+} and matches well with the published data for TiO_2 (G Zhou, et al., 2006; Chuang, et al., 2010). Figure 7(c), represents O1s spectra where a primary peak at 530 eV can be further divided into sub peaks centered at 529.7 and 530.2 eV attributing to Ti–O , Co–O in $CoTiO_3$, respectively (G Zhou, et al., 2006; Chuang, et al., 2010). Two peaks at 531.4 and 532.6 eV are assigned to the adsorbed oxygen and hydroxyl oxygen, respectively.

The high resolution Co 2p spectrum is shown in Figure 4.20(d). Two main peaks at binding energies of 781.5 and 797.3 eV correspond to Co $2p_{3/2}$ and Co $2p_{1/2}$. The difference (Δ) between Co 2p1/2 and Co 2p3/2 orbital is nearly 16 eV, which implies the fundamental oxidation state of high-spin Co^{2+}, and is very similar to those reported earlier for $CoTiO_3$ (Y. Liang et al., 2013; Shilpy, et al., 2015). Moreover, the splitting of the Co

2p1/2–Co 2p3/2 orbital components Δ is usually 15 eV for the low-spin Co^{3+} . Toward the left of each main peak is a satellite peak known as a shake-up line which occurs when Co (II) resides in a high spin state. Thus, the XPS results strongly suggest the formation of phase pure $CoTiO_3$-TiO_2 composite oxide films.

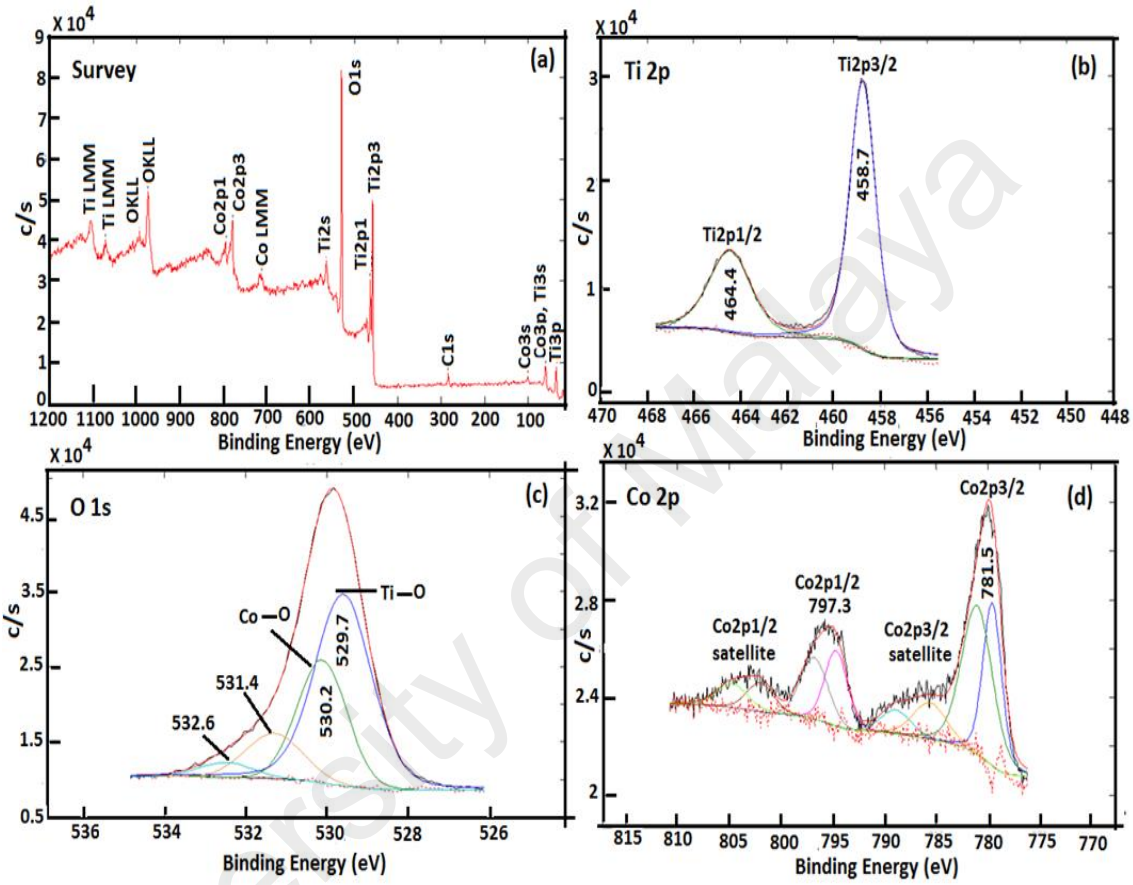

Figure 4.20: (a) XPS spectra of $CoTiO_3$-TiO_2 composite thin films prepared at 550 ˚C from ethanol solution of precursor (1) ; High resolution spectra $CoTiO_3$-TiO_2 for (b) Ti 2p **(c)** O 1s (d) Co 2p.

4.2.7 Electrochemical detection of dopamine (DA) by $CoTiO_3$-TiO_2 film electrode

4.2.7.1 CV behavior of DA

The $CoTiO_3$-TiO_2 composite film deposited at 550 ˚C was used for the electrocatalysis and sensing of dopamine (DA) in 0.1 M phosphate buffer solution (PBS) (pH 7.0). Figure 4.21 represents cyclic voltammograms (CVs) both in absence and presence of DA in a phosphate buffer solution, also containing 10 mM of Ascrobic acid (AA), a common interfering specie for DA.

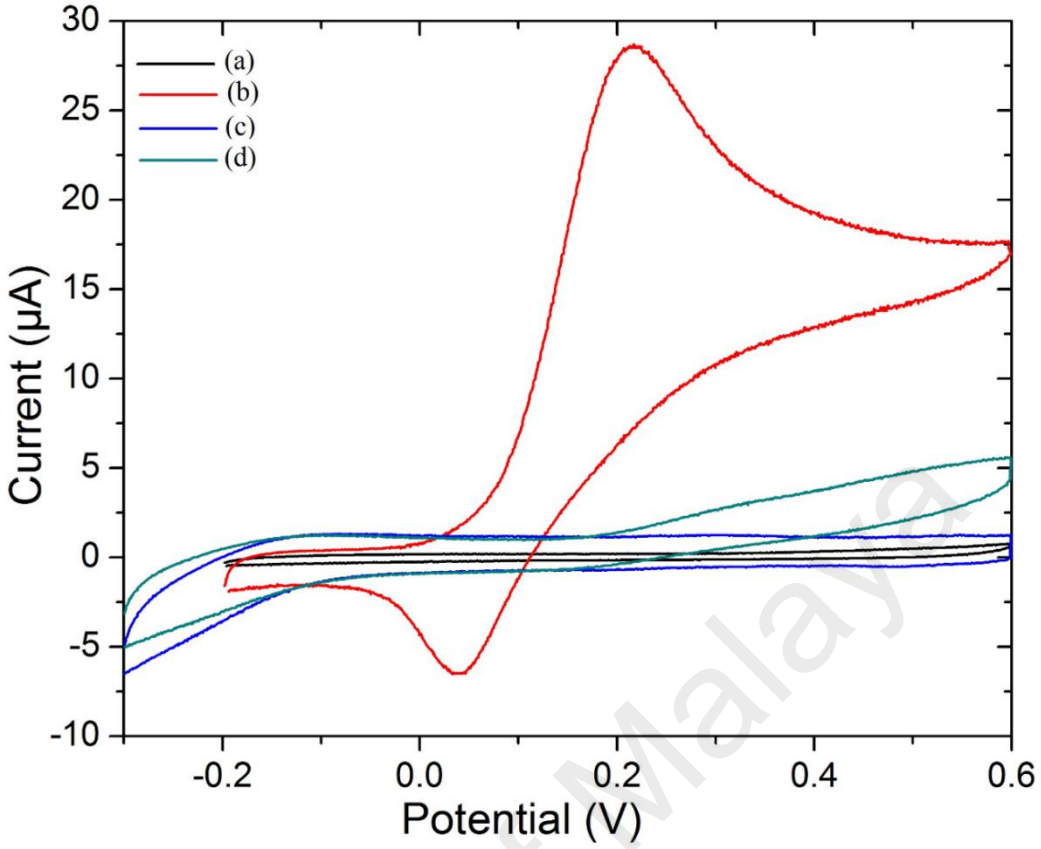

Figure 4.21: Cyclic voltammograms **(a)** absence, **(b)** presence of 15 μM DA obtained with the $CoTiO_3$-TiO_2 composite electrode; **(c)** absence and **(d)** presence of 50 μM DA recorded with the bare FTO electrode in the in 0.1 M PBS (pH 7.0) at a scan rate of 50 mV s^{-1}.

The potential was scanned between – 0.2 to + 0.6 V. It is evident from Figure 4.21(a) that no redox peaks were observed in the absence of DA, which also infers that AA was not electrochemically active in this potential window. Figure 4.21(b) represents that the $CoTiO_3$-TiO_2 composite electrode displayed an intense and sharp anodic peak current at +0.215 V due to the electrocatalytic oxidation of dopamine when 15 μM of DA was present in the buffer solution. The corresponding reduction peak appeared at +0.075 V but with much less current density representing the quasi-reversible redox behavior of DA. The sharp peak for DA oxidation at +0.215 V was also indicative of fast electrode kinetics for the DA oxidation (Ping, Wu, Wang, & Ying, 2012; L. Wu, Feng, Ren, & Qu, 2012). To observe contribution from FTO towards DA oxidation, CVs in presence and absence of DA were recorded with bare FTO electrode as shown in Figure 4.21(c,d). The voltamograms indicate that in the absence of DA no redox peaks were observed and background current was higher than the $CoTiO_3$-TiO_2

composite electrode. In the presence of 50 μM of DA and AA, only a slight increase in current was observed with a broad oxidation peak starting from approximately 0.22 V and extending up to 0.6 V. These results clearly indicate that the $CoTiO_3$-TiO_2 composite electrode is capable to catalytically oxidize DA with a sharp oxidation peak within the tested potential window.

4.2.7.2 Effect of scan rate on CV studies

Further, influence of the potential scan rate on the electrocatalytic activity of DA at the $CoTiO_3$-TiO_2 film electrode surface was studied in the PBS (pH = 7.0) using CV, as shown in Figure 4.22. Increase in scan rate from 25 to 200mV/s led to the increase in both DA oxidation and reduction peaks with a slight shift in the peak potential. The shift in peak potential was due to the quasi-reversible redox process (D. Wu et al., 2013). The linear relationship between the peak currents (I_p) and the square root of the scan rate was observed for both oxidation and reduction processes as shown in the inset of Figure 4.22. It is evident that, the anodic peak currents (I_{pa}) for the 10 μM DA varied linearly with the square root of the scan rate ($\nu^{1/2}$), with a linear regression equation, for anodic peak current I_{pa} (μA) = $0.0563\nu^{1/2}$ + 11.40 and a correlation coefficient R^2 = 0.985. This behavior suggests that the electrode kinetics is mainly diffusion controlled electrochemical reaction.

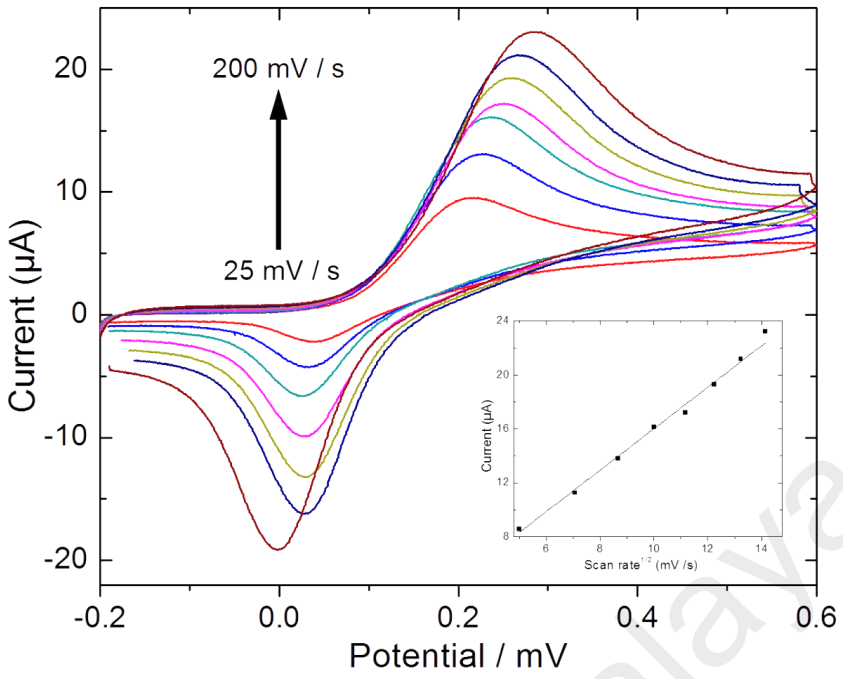

Figure 4.22: Cyclic voltammograms recorded for the $CoTiO_3$-TiO_2 electrode in the presence of 10 µM DA in 0.1 M PBS (pH 7.0) at various scan rates 25–200 mV s^{-1}. (Inset) Plot of anodic peak current vs. square root of the scan rate obtained with the $CoTiO_3$-TiO_2 electrode.

4.2.7.3 Effect of pH

pH plays a crucial role in the redox behavior of DA at the $CoTiO_3$-TiO_2 film electrode surface. In fact, in CV experiments, redox couple of DA shifted towards the negative direction upon increasing the pH from 5-9, Figure 4.23. This infers that electrocatlaytic behavior of DA is pH dependent. For practicality purposes, pH 7 was chosen for further analysis of DA with the $CoTiO_3$-TiO_2 composite electrode.

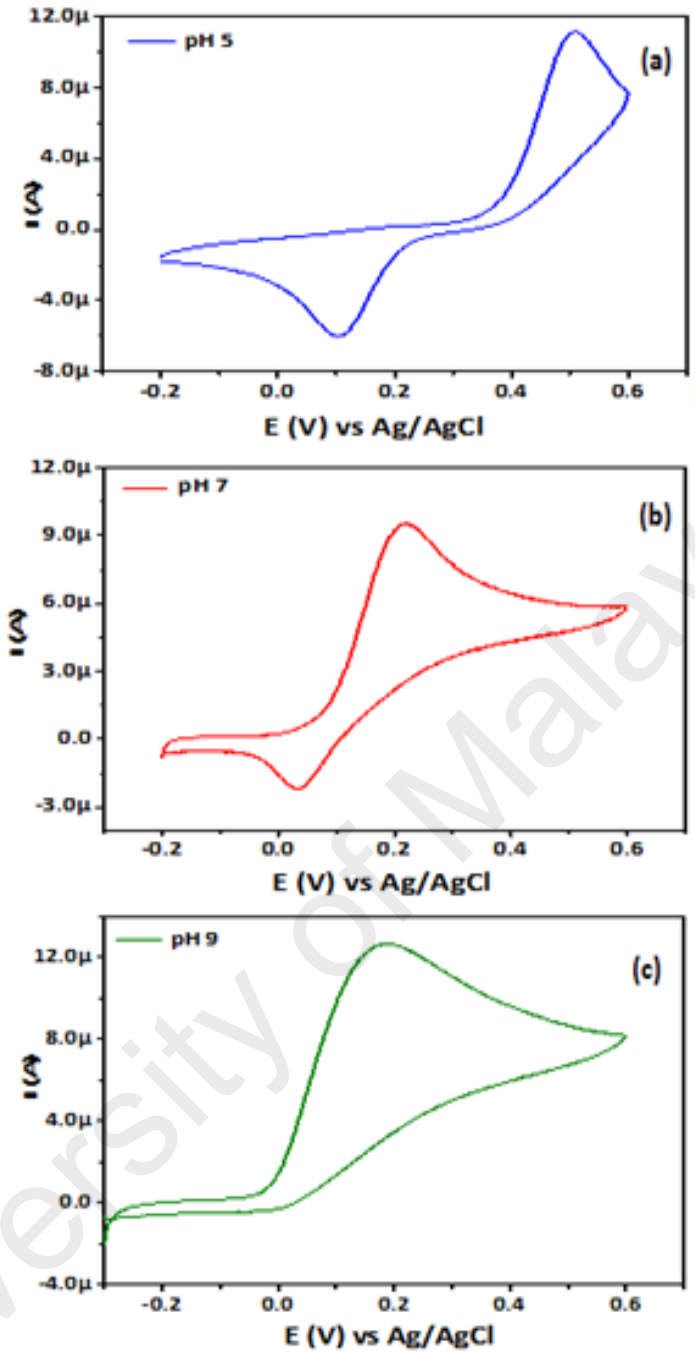

Figure 4.23: (a-c) Cyclic voltammograms recorded at $CoTiO_3$-TiO_2 electrode for 2 µM of DA in 0.1 M PBS with different pH values at scan rate of 50 mVs^{-1}.

4.2.7.4 Analytical utilization

A series of linear scan voltammetry (LSV) curves were recorded in 0.1 M PBS (pH = 7.0) with different DA concentrations at the $CoTiO_3$-TiO_2 composite as shown in Figure 4.24 (a). It could be observed that the anodic peak current increased linearly with an increase in the concentration of DA in the range of 20 to 300 µM, with R^2 = 0.993 (Figure 4.24b).

The sensitivity is determined from the slope of the calibration plot. The Figure 4.24 (b) shows the standard addition line with linear regression equation. The detection limit found was 0.083 μM (S/N = 6) by LSV. The sensitivity found from the slope was 0.325 μA. $\mu M^{-1}.cm^{2}$.

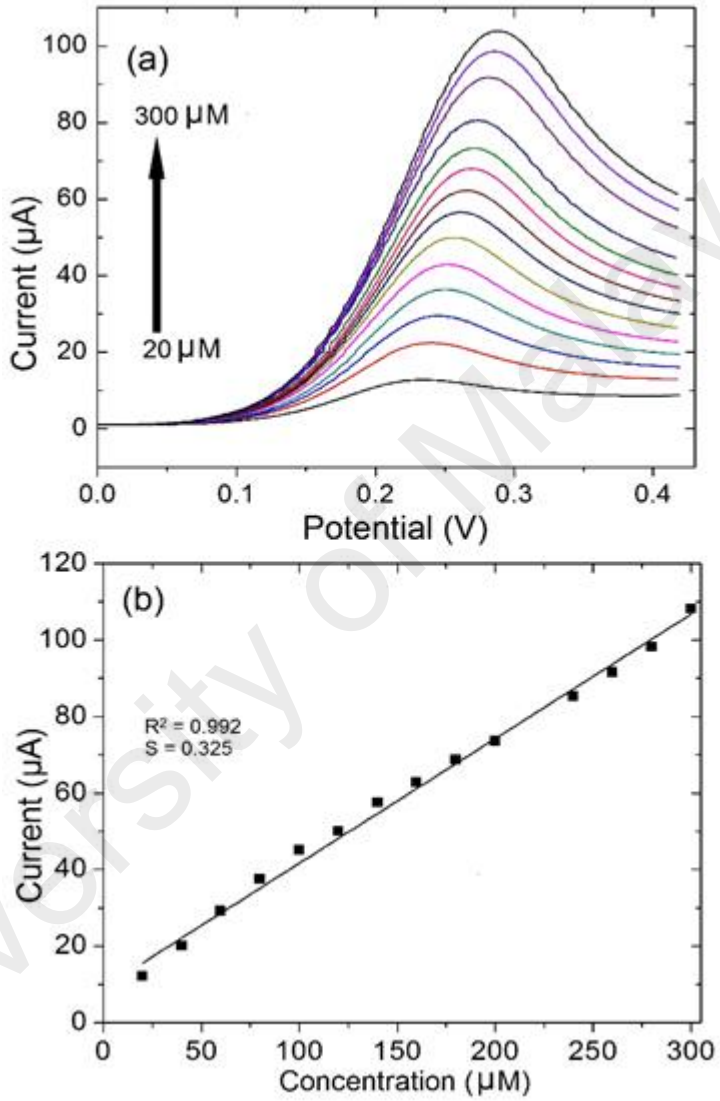

Figure 4.24: (a) LSV curves obtained with the $CoTiO_3$-TiO_2 composite electrode for various concentration of DA 0.1 M PBS (pH 7) at a scan rate of 50 mV s^{-1}. (b) Correlation between the concentration of DA and peak current for the $CoTiO_3$-TiO_2 electrode.

4.2.7.5 Selectivity and stability studies

The selectivity of the $CoTiO_3$-TiO_2 electrode towards DA oxidation was also investigated by LSV. Common interfering species AA, uric acid (UA), glucose, sulphate, nitrate and chloride were chosen and their effect on DA oxidation signal was evaluated as represented in Figure 4.25. It is evident that even when 100-fold higher concentration of an interference source is used in a homogeneously stirred of 0.1 M PBS (pH 7), there is no significant current response in the potential window used for DA analysis. This clearly suggested that DA oxidation at the fabricated $CoTiO_3$-TiO_2 composite was more selective and not affected in the presence of common interferences.

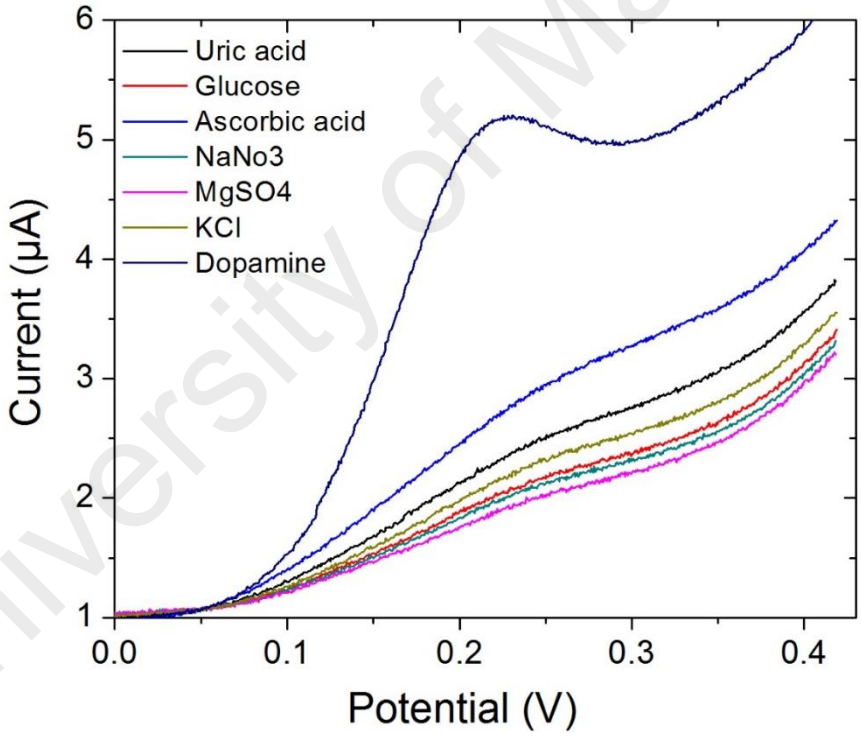

Figure 4.25: LSV response obtained with the $CoTiO_3$-TiO_2 composite electrode for 100 µM of each interferent and 10µM Dopamine in 0.1 M PBS (pH 7) at scan rate of 50 mV s^{-1}.

The stability of $CoTiO_3$-TiO_2 composite electrode was also monitored over the period of study. There was no significant loss observed in response for DA over 4 weeks with the standard deviation (RSD) of 3.4 %. Such a high stability of the $CoTiO_3$-TiO_2 composite

electrode can be accredited to inherent properties of metal oxides compared to electrodes modified with pure metallic gold or platinium nanoparticles (J. Li et al., 2012).

Table 4.4: Comparison of analytical performance of various electrochemical sensors for DA detection

Sensor Material	Analytical techniques	Limit of detection (LoD) (μM)	Ref.
Au-Pt/GO-ERGO	Cyclic voltammetry	0.02	(Y. Liu et al., 2015)
NiO–CuO/GR/GCE	Square Wave voltammetry	0.10	(B. Liu, et al., 2016)
GO–La/CPE	Differential pulse voltammetry	0.00032	(F. Ye, et al., 2015)
EPPGE-SWCNT–Fe_2O_3	Square Wave voltammetry	0.36	(Adekunle, Agboola, Pillay, & Ozoemena, 2010)
GO/SiO_2–MIPs/GCE	Amperometry	0.03	(Zeng, Zhou, Kong, Zhou, & Shi, 2013)
ZnO- GCE	Amperometry	0.06	(Xia, Wang, Wang, & Guo, 2010)
Graphene–AuNPs	Differential pulse voltammetry	1.86	(J. Li, et al., 2012)
$CoTiO_3$-TiO_2	Linear scanning voltammetry	0.083	Present work

ERGO = Electrochemically reduced graphene oxide, GCE = glassy carbon electrode, CPE = Carbon paste electrode

GO = graphene oxide , MIP = molecularly imprinted polymers, EPPGE = edge-plane pyrolytic graphite electrode

The sensing performance of the $CoTiO_3$-TiO_2 film electrode was compared with other previously reported sensor materials for the detection of DA and the results are

summarized in Table 4.4 which reveals that the present electrocatalyst performs equally good to the other bimetallic or metal oxide composite with carbon nanotubes (CNTs) and graphene oxide (GO) for the oxidation of DA.

It is very well known that the use of CNTs and GO provides large network for collecting electrons from oxidation process thereby assisting efficient current generation to improve the detection performance of electro catalyst. However, considering the prolong synthetic methods of these catalysts and high cost of Pt and Au metals, present catalyst prepared from AACVD technique is suitable alternative to Pt and Au free electrocatalyst for the DA oxidation with low cost and ease of fabrication.

4.3 Synthesis and Characterization of Complex $[Mg_2Ti_4(O)_2(OH)_4(TFA)_8(THF)_6]\cdot THF$ (3)

The synthetic protocol of heterobimetallic precursor $[Mg_2Ti_4(O)_2(OH)_4(TFA)_8(THF)_6]\cdot THF$ (**3**) involves the reaction of diacetatomagnesium(II) tetrahydrate with tetraisopropoxytitanium(IV) in presence of trifluoroacetic acid in THF. As the reaction progresses, the more labile isopropoxy ligands are exchanged by stronger chelating TFA groups which bind Mg and Ti atoms through its carboxylate oxygen atoms. The exchange of ligands and progress of the reaction can be observed by dissolution of salts to result in a clear solution. The transparent solution was then evaporated in vacuum to obtain a white powder which was re-dissolved in 3 mL THF and kept at room temperature to grow the first 70% yield of translucent white crystals of the precursor (**3**). The overall reaction for the formation of (**3**) is shown below in equation .

Chemical equation 5

$$2Mg(CH_3COOH)_2.4H_2O + 4Ti(OCH(CH_3)_2)_4 + 8CF_3COOH \xrightarrow{THF}$$
$$[Mg_2Ti_4(O)_2(OH)_4(CF_3COO)(C_4H_8O)_6].C_4H_8O + 4CH_3COOH + 16(CH_3)_2CHOH$$

The substitution of acetate with TFA groups not only aids binding of Mg and Ti atoms in one framework but also co-ordinatively saturates each metal center, making the precursor more volatile as well as soluble in organic solvents such as chloroform, THF, methanol and ethanol, rendering it a suitable precursor to produce single phased $MgTi_2O_5$ thin films by the AACVD method. The stoichiometric composition of (**3**) was recognized by single crystal X-ray diffraction and further confirmed by FTIR and TG/DTG analysis. The FT-IR spectrum of Mg-Ti precursor showed strong absorption bands at 1654 and 1453 cm^{-1} due to the asymmetric and symmetric ν(C=O) vibrations of the carboxylate group of the TFA ligands respectively. The difference of value $\Delta\nu_{asy}$- $\Delta\nu_{sy}$ = 200 cm^{-1} is consistent with the bidentate bridging behavior of TFA ligand. Similarly, a sharp peak at 1192 cm^{-1} confirms the existence of C–F bonds in (**3**)**.** The IR spectrum is closely related to those reported previously for similar heterobimetallic compounds.

4.3.1 Molecular Structure of Complex $[Mg_2Ti_4(O)_2(OH)_4(TF)_8(THF)_6]\cdot THF$ (3)

The structure of (**3**) is isomorphous with that of the copper analog $[Cu_2Ti_4(O)_2(OH)_4(CF_3COO)_8(THF)_6]\cdot THF$ and shows the same severe disorder. The structure was solved in space group *Pbca* , and is disordered about the centre of symmetry. The core of the molecule consists of a tetrahedron of Ti(II) ions (Figure 4.26). Each edge of the tetrahedron is bridged by an oxygen atom (O^{2-} or OH^-), generating a Ti_4O_6 adamantane-type cage. Four of the bridging species are hydroxo ions; the remaining two are oxo ions which are also coordinated to Mg (II) ions. The disorder arises from titanium ions occupying alternative sites, generating a second, overlapping adamantine with the oxygen atoms in the same positions. Four trifluoroacetate ions are bonded to each magnesium ion; each trifluoroacetate also bridges to a titanium ion. All of the metal ions

are six-coordinate, the last binding site being filled by one coordinated THF molecule in each case (Figure 4.27). There is also a non-coordinated THF solvate molecule in the lattice.

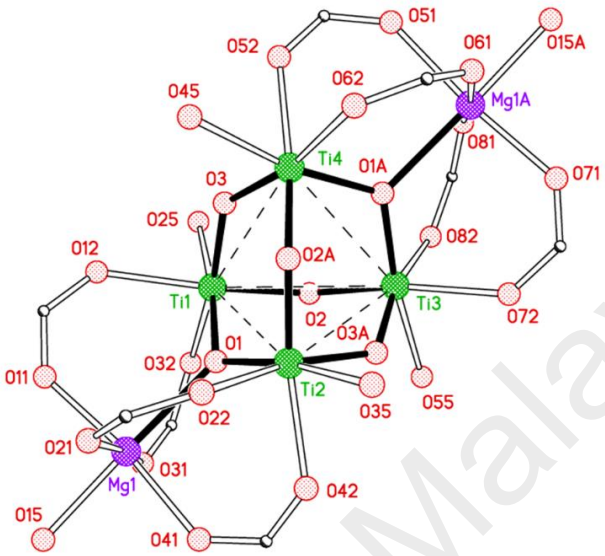

Figure 4.26: Perspective view of the core of (**3**). CF_3COO^- ions are represented by OCO links; terminal O atoms represent THF molecules, bold bonds highlight the $Ti_4O_2(OH)_4$ adamantane core. Atoms with suffix "A" generated by symmetry operation 1-x, 1-y, 1-z.

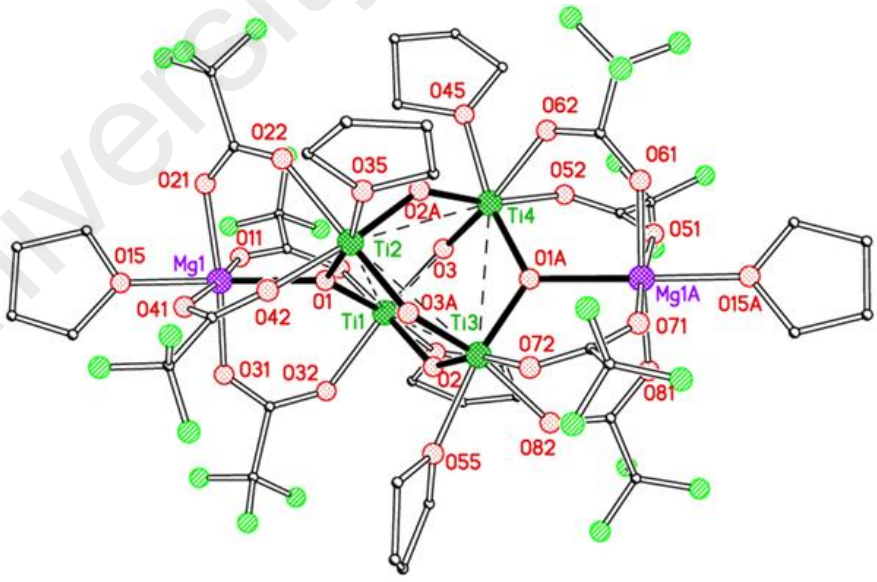

Figure 4.27: Perspective view of the $[Mg_2Ti_4(O)_2(OH)_4(CF_3COO)_8(THF)_6]$ (**3**) molecule. One component of the disorder and H atoms are omitted for clarity.

Table 4.5: Crystal data and refinement parameters for $[Mg_2Ti_4(O)_2(OH)_4(TF)_8(THF)_6]\cdot THF$ (**3)**

$C_{40}H_{52}F_{24}Mg_2O_{28}Ti_4\cdot C_4H_8O$	V = 6956.1 (4) Å^3
M_r = 1749.14	Z = 4
Orthorhombic, *Pbca*	Mo *K*α radiation, λ = 0.71073 Å
a = 19.2879 (7) Å	μ = 0.60 mm^{-1}
b = 17.3364 (6) Å	*T* = 150 K
c = 20.8027 (7) Å	0.28 × 0.26 × 0.23 mm
Data collection	
Bruker APEX 2 CCD diffractometer	8627 independent reflections
Absorption correction: multi-scan *SADABS* v2012/1, (Krause et al., 2015)	6572 reflections with $I > 2\sigma(I)$
T_{min} = 0.677, T_{max} = 0.746	R_{int} = 0.050
69548 measured reflections	
Refinement	
$R[F^2 > 2\sigma(F^2)]$ = 0.088	2012 restraints
$wR(F^2)$ = 0.230	H-atom parameters constrained
S = 1.09	$\Delta\rangle_{max}$ = 0.58 e Å^{-3}
8627 reflections	$\Delta\rangle_{min}$ = -0.68 e Å^{-3}
955 parameters	

4.3.2 Thermogravimetric Analysis of Precursor $[Mg_2Ti_4(O)_2(OH)_4(TFA)_8(THF)_6]\cdot THF$ (3)

Prior to thin film growth from precursor (**3**), thermogravimetric (TG) and derivative thermogravimetric (DTG) analysis were performed to study the step-by-step decomposition of the precursor compound and the evolution of the target material that may experience subtle phase changes during analysis. The optimal temperature suitable for the complete pyrolysis of the precursor was also probed and applied for the deposition of thin films.

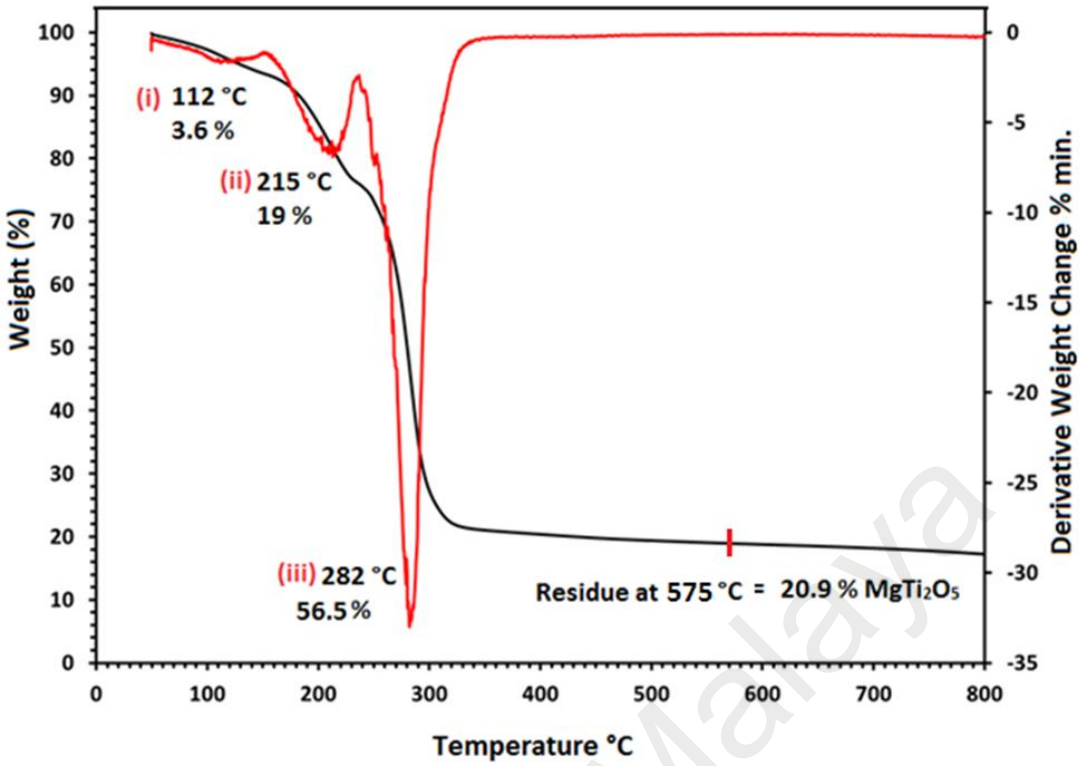

Figure 4.28: TG (black) and DTG (red) curves showing pyrolysis of precursor (3) as a function of temperature under an inert nitrogen ambient and heating rate of 10 ˚C min-[1]

TGA/DTG profiles (Figure 4.28) of precursor (**3**) displayed an unceasing three-step degradation process with a rapid weight loss of 3.6%, 19.0% and 56.5% at 112 °C, 215 °C and 282 °C, respectively. The weight of the remaining residue at 575 ˚C is 20.9%, which corresponds to $MgTi_2O_5$ (calculated percentage 20.6 %). Further sintering of the observed residue to the higher temperature of 800 °C did not bring any appreciable change in weight, suggesting that precursor (**3**) decomposes quantitatively to endow $MgTi_2O_5$ as a stable final product. Based on TGA information, quantitative pyrolysis of (**3)** has been indicated in equation below:

Chemical equation 6:

$$[Mg_2Ti_4(O)_2(OH)_4(TFA)_8(THF)_6]\cdot THF \xrightarrow{500\ ^oC} 2MgTi_2O_5 + \text{Volatiles}$$

4.3.3 XRD Analysis of $MgTi_2O_5$ thin film

Magnesium dititanate films via AACVD were grown at three different temperatures of 500, 550 and 600 °C from ethanolic solution of precursor (**3**) using air as a carrier gas. XRD analysis was carried out to obtain information on chemical formula and purity of the deposited phase and diffraction patterns as function of substrate temperature are depicted in Figure 4.29. Apparently, all the XRD patterns look similar in terms of their peak positions and 2θ values however the diffraction peak intensities displayed a notable increase with the rise in deposition temperature. Each XRD pattern, in Figure 4.29 was carefully matched with the standard Inorganic Crystal Structure Database which reveals the formation of "Armalcolite (Fe-free) $MgTi_2O_5$" ICSD = [98-003-7232] as a crystalline product in each case. The as-synthesized $MgTi_2O_5$ crystallizes in the orthorhombic crystal system with a = 3.7450, b = 9.7280, c = 9.9900 Å and α = β = γ = 90˚. As shown in Fig. 4, each peak related to $MgTi_2O_5$ have been indexed by its standard reflection plane and peaks labelled by (*) correspond to the SnO_2 layer of the FTO substrate. No obvious impurity peaks of TiO_2, $MgTiO_3$ or Mg_2TiO_4 phases appeared in these XRD patterns. This clearly indicates that the precursor (**3**) decomposes cleanly at all temperatures of 500, 550, 600 °C to yield the pure crystalline orthorhombic phase of $MgTi_2O_5$. This formation temperature is considerably lower than the temperature reported (1000-1200 °C) in recent works for $MgTi_2O_5$ powder synthesis through solid state techniques. Although the synthesis of $MgTi_2O_5$ nano powders had been achieved even at the lower temperature of 600 ˚C by various wet processes. The formation of phase pure $MgTi_2O_5$ thin films via SMP based AACVD route coincides well with previous investigations (N. Zhang et al., 2015; N. Zhang, Qu, Pan, Wang, & Li, 2015).

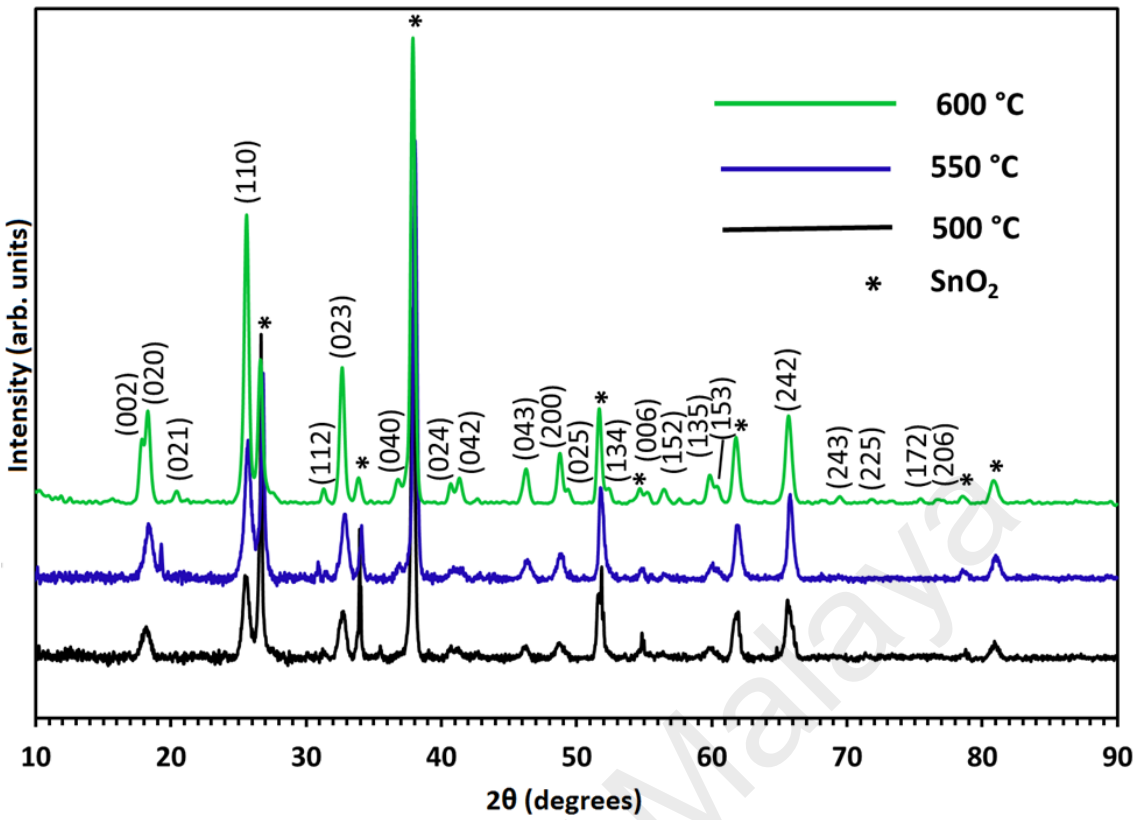

Figure 4.29: XRD patterns of $MgTi_2O_5$ ICSD = [98-003-7232] films deposited on FTO glass substrate at different temperatures of 500 (black line), 550 (blue line) and 600 ˚C (green line) from ethanolic solution of precursor (**3**).

4.3.4 Surface Morphologies and Compositions of $MgTi_2O_5$ Thin Film

Figure 4.30 shows FESEM micrographs of the surface microstructure of $MgTi_2O_5$ thin films developed at different temperatures of 500, 550 and 600 ˚C from ethanol solution of the precursor (**3**) on FTO glass substrates. At 500 ˚C, an obvious growth of spherical objects can be observed by low resolution SEM image (Figure. 4.30a), although the substrate surface is not fully covered by these objects. An increase in the deposition temperature to 550 ˚C, intensified the thin film growth rates and the substrate surface is completely decorated with these spherical objects. The nucleation and growth of spherical objects further increases with increase in deposition temperature to 600 ˚C which results in formation of compact and uniform spherical features of $MgTi_2O_5$. High resolution images, Figure 4.30 (b, d and f) indicate that the shape and design of these microspheres

remain unaffected by rise in deposition temperature and porous $MgTi_2O_5$ microspheres in size range of 0.3- 1.8μm have been observed at all temperatures.

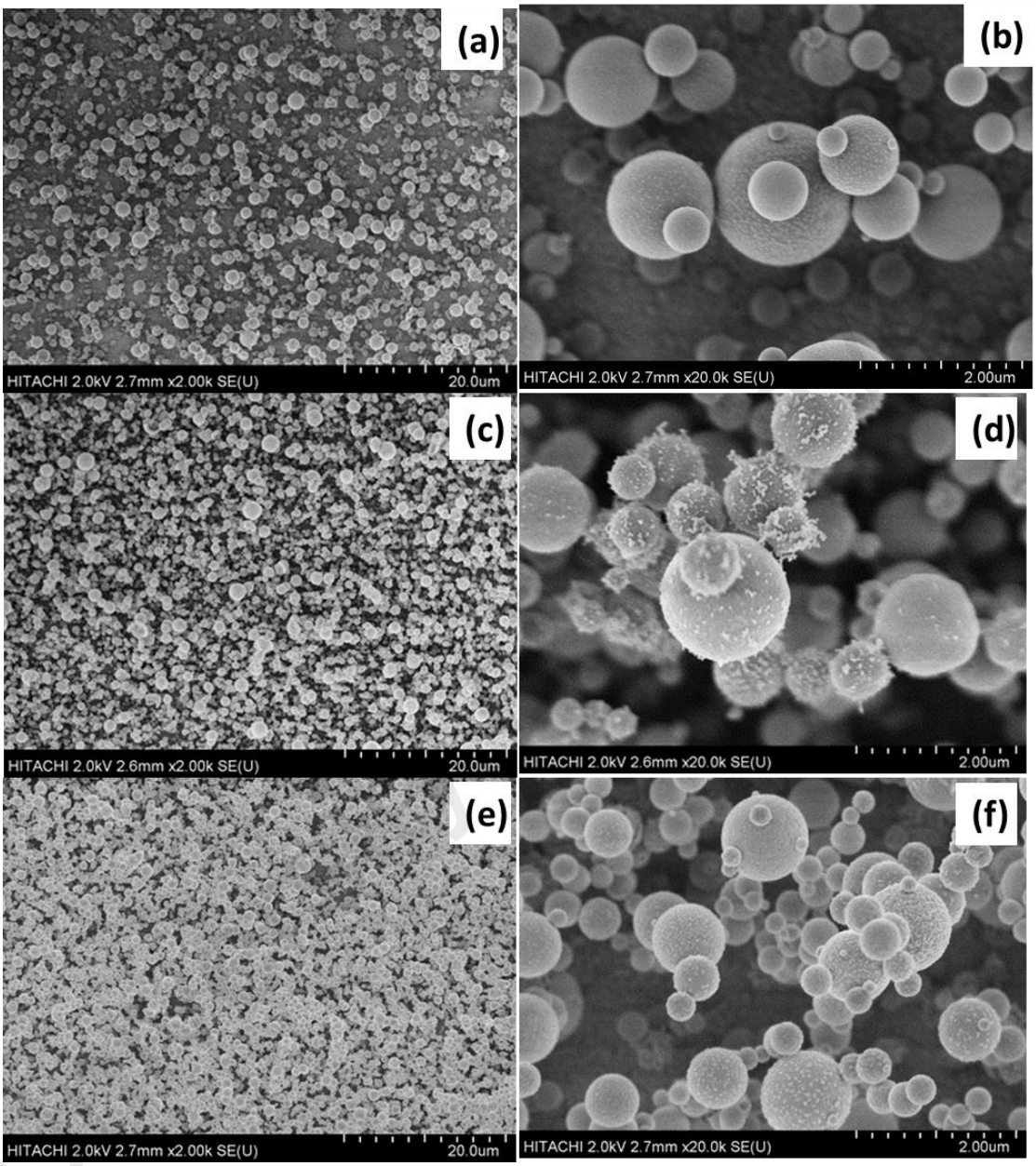

Figure 4.30: (a,c, e) low resolution (2KX) and (b, d, f) high resolution(20KX) FESEM images of $MgTi_2O_5$ thin films deposited on FTO glass substrate from ethanolic solution of precursor (3) at temperatures (a, b) 500 ˚C (c, d) 550 ˚C and (e, f) 600 ˚C, respectively.

The FESEM images display the regularly interconnected porous spherical microstructure of the film prepared at 600 ˚C; this is highly suitable for PEC applications where liquid electrolytes can penetrate in the interior of the film to provide the required large area of solid/electrolyte interfaces for charge transfer reactions (Malengreaux et al., 2014).

The elemental stoichiometry of all the films were probed by energy dispersive X-ray (EDX) analysis and spectra are shown in Appendix 4 (i, ii and iii) which indicates that the metallic ratios of Mg and Ti is about 1:2, that matches well with the expected elemental ratio present in the precursor complex (**3**) and $MgTi_2O_5$ formula identified from XRD results. The various peaks originating from substrate elements (Sn, Si, Ca, Na, F) were not omitted from EDX spectra.

4.3.5 XPS Analysis of $MgTi_2O_5$ Thin Film

$MgTi_2O_5$ film obtained at 600 ˚C was employed to XPS analysis for the investigation of chemical and valence states of the constituent elements and results are depicted in Figure 4.31. The survey scan spectrum in Figure 4.31a confirms that Mg, Ti and O are major components at the surface of the film. The high resolution spectrum (Figure 4.31b) indicates that strong peak at 49.6 eV is indicative of Mg^{2+} ion and is in good agreement with the reported data for Mg 2p3/2 (N. Zhang, Y. Qu, et al., 2015; N. Zhang, K. Zhang, et al., 2015). The binding energies of 458.66 and 464.37 eV are indicative of Ti 2p3/2 and Ti 2p1/2 respectively which correspond to Ti^{4+} and matches well with the published data for TiO_2. (Figure 4.31c) Meanwhile, the peak at 529.94 eV, in Figure 4.31(d) is accredited to Ti–O and Mg–O in $MgTi_2O_5$. Two small peaks at 531.13 and 532.15 eV are assigned to the atmospheric oxygen and hydroxyl oxygen, respectively.

Taken together, the XRD, EDX and XPS data confirm that pure orthorhombic phase $MgTi_2O_5$ films have been successfully prepared from precursor (**3**).

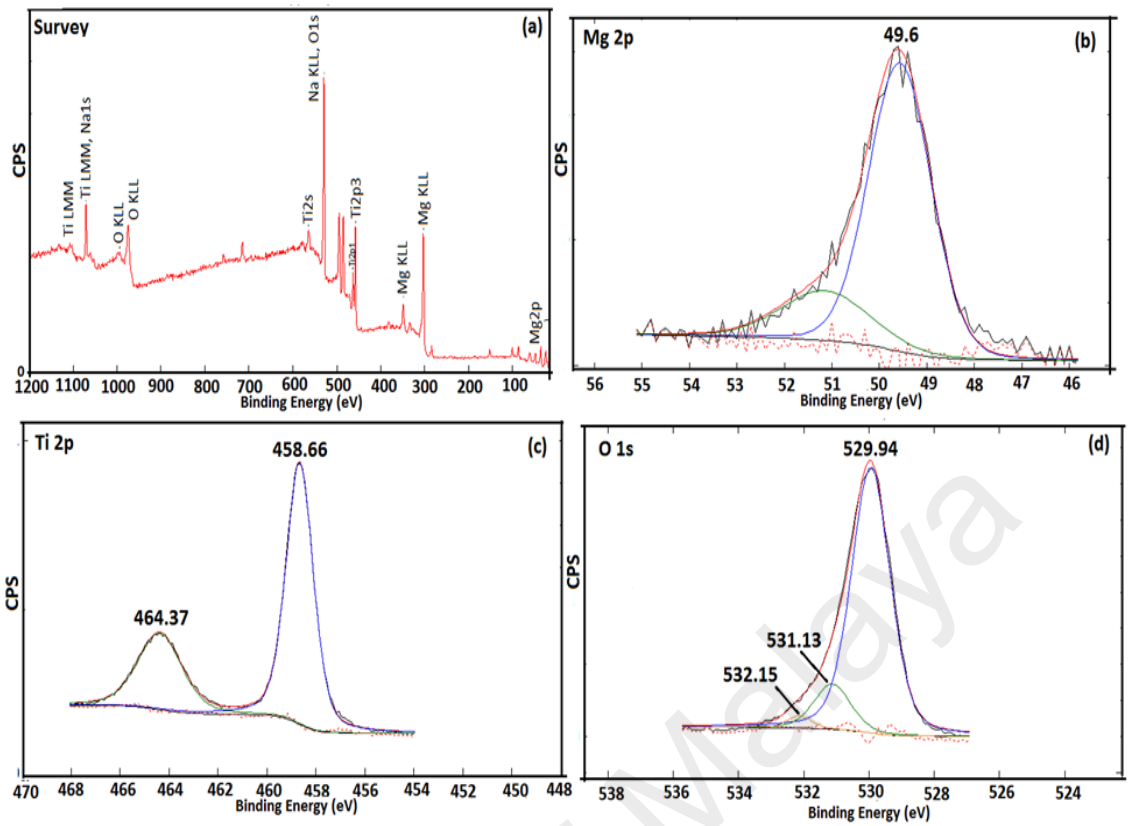

Figure 4.31: (a) XPS spectra of $MgTi_2O_5$ film prepared at 600 ˚C from precursor (3) ; High resolution spectra of $MgTi_2O_5$ for (b) Mg 2p, **(c)** Ti 2p **(d)** O 1s.

4.3.6 Optical Band Gap of $MgTi_2O_5$ Thin Film

The optical properties of $MgTi_2O_5$ film deposited at 600 °C were investigated using UV–vis spectrophotometry; the absorption spectrum shown in Figure 4.32 reveals that no significant absorbance occurs in visible region and $MgTi_2O_5$ film exhibits steep photoabsorption features in wavelength range from 350-390 with absorption tail at 450nm. The Tauc's formula, $\alpha h\nu = A(h\nu - E_g)^{\gamma}$, for the optical band gap determination was employed, where, α is the linear absorption coefficient of the material, $h\nu$ is the photon energy, A is a proportionality constant. Among these, γ determines the characteristics of the transition in a semiconductor, a value $\gamma = ½$ signifies allowed direct band gap and $\gamma = 2$ stands for indirect band gap. The inset Tauc plot in Figure 4.32 demonstrates a direct band gap of 3.4 eV for $MgTi_2O_5$ film which is in good agreement with the literature reported value for phase pure magnesium dititanate (Suzuki & Shinoda, 2016). This

observation suggests that the impurity free $MgTi_2O_5$ film developed in this work acts as a photocatalyst under UV light irradiation.

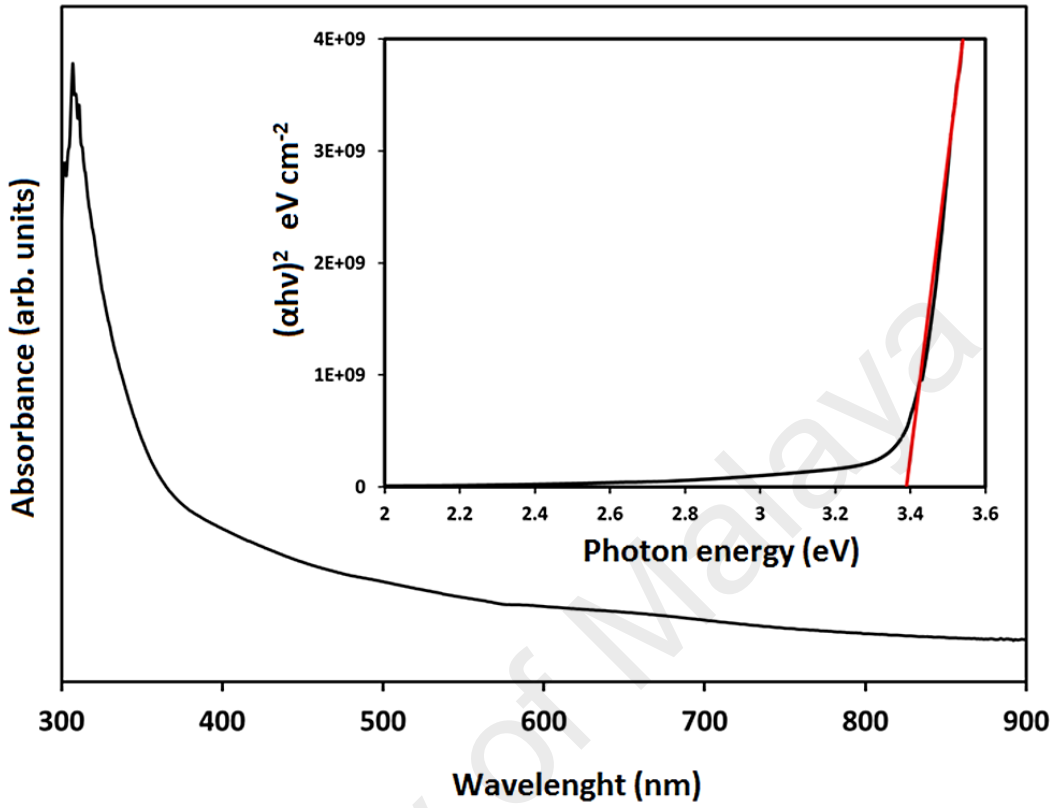

Figure 4.32: (a) UV-visible spectrum of $MgTi_2O_5$ film deposited from precursor (**3**) at 600 °C on the FTO substrate. The inset shows the Tauc's plot of $(\alpha h\nu)^2$ vs photon energy (eV) obtained for the $MgTi_2O_5$ film.

4.3.7 Photoelectrochemical Performance of $MgTi_2O_5$ thin film

The $MgTi_2O_5$ (MT) film electrodes developed at three different temperatures were further investigated for photoelectrochemical water splitting for H_2 production. The PEC performance of the microspherical electrodes, MT-500, MT-550 and MT-600 designed at 500, 550 and 600 ^oC respectively, were investigated in presence of 1 M NaOH under dark (D) and simulated solar irradiation (L) of AM 1.5G (100mW/cm^2) (Saremi-Yarahmadi, Tahir, Vaidhyanathan, & Wijayantha, 2009) and their corresponding Linear Scanning Voltammograms (LSVs) are shown in Figure 4.33a. The dark current from -0.6 V to +0.7 V(vs. Ag/AgCl) of all $MgTi_2O_5$ electrodes was almost zero due to inactivation of electron-holes phenomenon. Interestingly, when $MgTi_2O_5$ electrodes are exposed to

light, they exhibit significantly enhanced photocurrent response due to the triggering of photo-induced electro-hole pair separation. It has been observed that MT-600 electrode produces maximum photocurrent density of 400 μA cm^{-2} at 0.7 V as compared to the film electrodes MT-500 and MT-550 that produce photocurrent density of 148 and 226 μA cm^{-2} respectively. This difference in the PEC performances of these electrodes can be explained on the basis of different thin film deposition temperatures that significantly affect the thickness, crystallinity and porosity of $MgTi_2O_5$ electrodes (Figure 4.30). The more thick and compact microspherical architecture of $MgTi_2O_5$ electrode developed at 600 ˚C (Figure 4.30c to c2) is found more attractive for unidirectional charge transport while its regularly connected porous structure allows the electrolyte to penetrate *via* the pinholes thereby enhancing the PEC efficiency as compared to the films fabricated at 500 and 550 ˚C. Although the MT-500 and MT-550 electrodes are also comprised of crystalline porous microspherical entities but they are loosely bonded and their lower film thicknesses are responsible for the decrease in their photocurrent densities. The maximum photocurrent density of 400 μA cm^{-2} measured for MT-600 electrode is significantly improved than the previously reported photocurrent densities for $MgTi_2O_5$ (102 μA cm^{-2}) and $Mg_{1.2}Ti_{1.8}O_5$ (61 μA cm^{-2}) nanocrystals electrodes (N. Zhang, K. Zhang, et al., 2015; N. Zhang, Y. Qu, et al., 2015).

To authenticate the PEC performances of $MgTi_2O_5$ photoanodes, amperometric I–t studies were performed at 0.7 V vs. Ag/AgCl under on–off illumination conditions. Figure 4.33 (b) shows that all $MgTi_2O_5$ photoanodes exhibit steady and reproducible photocurrent responses and no significant decrease in the photocurrents was observed during various on-off illumination cycles for 1 hour which indicate the higher efficiency and good stabilities of all photoelectrodes prepared at different temperature. Moreover, the transient photocurrents recoded for MT-500 (148 μA cm^{-2}), MT 550 (226 μA cm^{-2}) and MT-600 (400 μA cm^{-2}) agree well with their LSV results and strengthened the PEC

performance of the $MgTi_2O_5$ electrodes. Again, the amperometric photocurrent response is found to be better and durable than those observed previously for $MgTi_2O_5$ and $Mg_{1.2}Ti_{1.8}O_5$ nanocrystal electrodes (N. Zhang, Qu, Pan, Wang, & Li, 2016; N. Zhang et al., 2015).

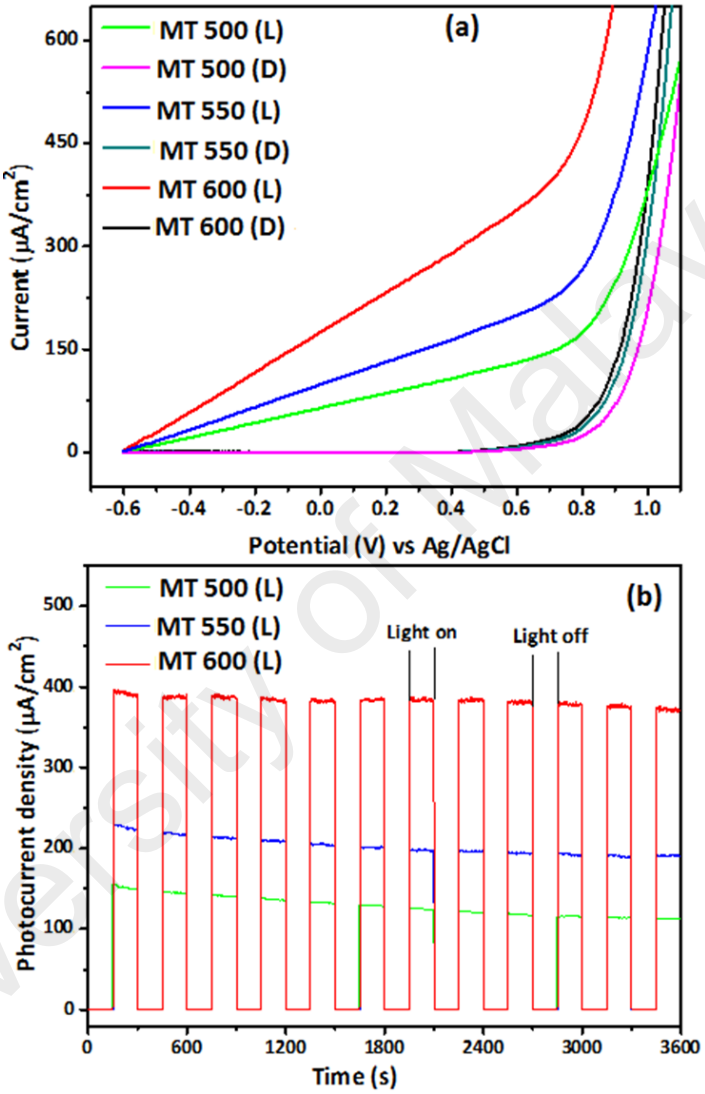

Figure 4.33: (a) Linear Sweep Voltammograms and (b) transient photocurrent response recorded for $MgTi_2O_5$ film electrode in 1M NaOH under simulated AM 1.5 illumination of 100 $mWcm^{-2}$

The charge separation and transportation are key factors in establishing the photocatalytic performances of a semiconductor material; therefore, electrochemical impedance measurements (EIS) were conducted to demonstrate the charge separation and transfer dynamics in $MgTi_2O_5$ photoelectrodes. The Nyquist plots obtained from the EIS

measurements under light and dark conditions for the $MgTi_2O_5$ films deposited at 500, 550 and 600 ˚C in the presence of 1 M NaOH in the frequency range of 0.1 Hz-10 kHz are displayed in Figure 4.33 (a) and (b), respectively.

Under dark condition each MT-500, MT-550 and MT-600 electrodes exhibited a semicircle like Nyquist plot (Figure 4.34a) with higher the electron transfer resistance (R_{ct}) values (Table 4.6) which suggests hindrance to the electron-transfer kinetics at the electrode surface (Figure 4.34a). While under illumination, the electron transfer resistance (R_{ct}) values in all the film electrodes is decreased as compared to the dark indicating better charge electron transfer with low charge resistance (Figure. 4.34b, and Table 4.6). Moreover, under illumination, MT-600 electrode produced lowest R_{ct} value as compared to MT-550 and MT-500 electrodes, indicating the efficient charge separation and transfer across the electrode-electrolyte interface as well as reducing the possibility of charge recombination at the surface of the film fabricated 600 ˚C than those prepared at 500 and 550 ˚C. These results indicate that the formation of tightly packed mesoporous microspherical design of MT-600 plays a vital role in charge transfer mechanism under light which are in good agreement with LSV results.

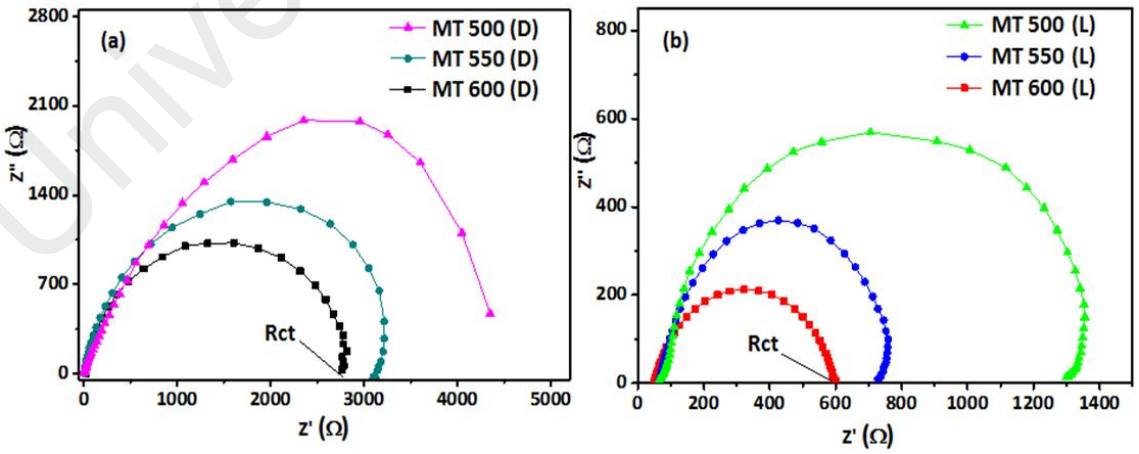

Figure 4.34: EIS Nyquist plots obtained for the $MgTi_2O_5$ films fabricated at 500, 550 and 600 ˚C at frequency range of 0.1 Hz-10 kHz in (a) dark and (b) light conditions

Table 4.6: Charge transfer resistance, maximum frequency and recombination lifetime calculated for $MgTi_2O_5$ film electrodes fabricated at 500, 550 and 600 ˚C via AACVD.

Film electrode	R_{ct} (ohm)	f_{max} (Hz)	τ_n (msec)
MT 500 (D)	4603	48.8	3.27
MT 500 (L)	1301	0.85	187
MT 550 (D)	3128	23.2	6.89
MT 550 (L)	730	0.44	363
MT 600 (D)	2775	11.06	14.4
MT 600 (L)	600	0.19	842

R_{ct} – Charge transfer resistance; f_{max} – Maximum frequency; τ_n – recombination lifetime.

The frequency dependence phase angle plots (Bode plot) were recorded for detailed understanding of the charge-transfer resistance phenomenon in $MgTi_2O_5$ electrodes. The Bode phase plots obtained for the $MgTi_2O_5$ electrodes under dark and light conditions are shown in Figure 4.35 (a) and (b) respectively. It has been observed that the characteristic frequency peaks are shifted under dark and light conditions for the $MgTi_2O_5$ electrodes fabricated at different temperatures. Figure 4.35 (a) shows that MT-500, MT-550 and MT 600 electrodes showed the frequency peak maximum (f_{max}) at 48.8, 23.2 and 11.06 respectively in dark condition. However, the shifting of peaks toward the low frequency region below 0.1 Hz in presence of light indicates (Figure 4.35b) the rapid electron-transfer behavior of all MT electrodes. The conducting nature of MT-600 under light facilitates the peak shift in the Bode plot. The phase angle of the plot under illumination is less than 90˚ at higher frequency and there is lesser log z value in low frequency range of 1-100 Hz which suggests that electrode does not behave like ideal capacitor (M. M. Shahid et al., 2015). These characteristic frequencies can be used to calculate the electron recombination lifetime (τ_n) of the material with following relationship (Lim et al., 2014):

$$\tau_n = {}^{1}/_{2\pi f_{max}}$$

Where f_{max} is the frequency peak maximum. The calculated recombination life time (τ_n) for MT-500, MT-550 and MT-600 in absence and presence of light are listed in Table 4.6 which indicates that the lifetime of charge carriers in $MgTi_2O_5$ electrodes is prolonged effectively under light compared to dark conditions. The highest τ_n is calculated for MT-600 (L) confirming the production of highest current density in $MgTi_2O_5$ film fabricated at 600 ˚C.

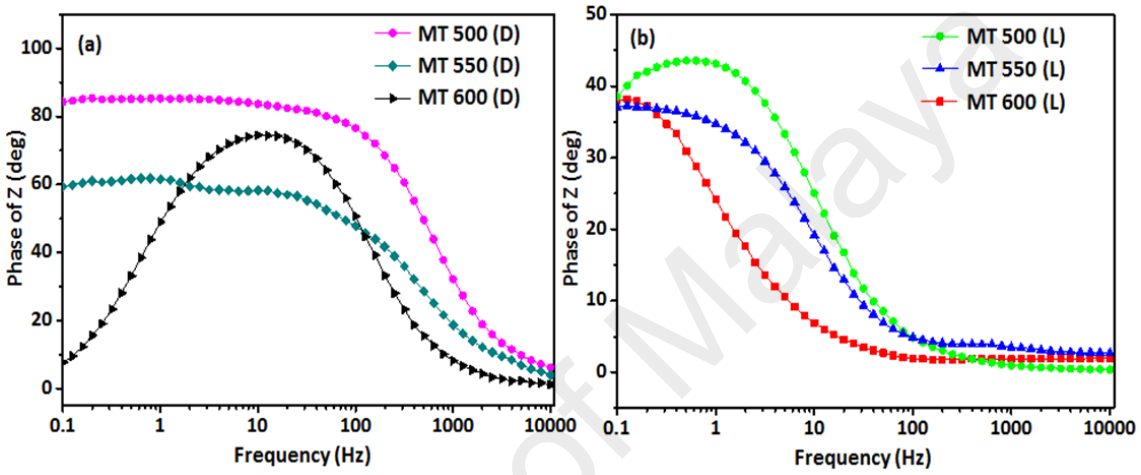

Figure 4.35: Bode phase plots obtained for the $MgTi_2O_5$ films fabricated at 500, 550 and 600 ˚C at frequency range of 0.1 Hz-10 kHz in (a) dark and (b) light conditions.

The Mott–Schottky (MS) approach is a usual way to obtain information about flat band potential and the charge density values and type of semiconductor material. Figure 4.36 shows the MS plot of $MgTi_2O_5$ film measured as a function of applied potential at a frequency of 1 kHz using 1M NaOH in dark condition which indicates that $MgTi_2O_5$ is a n-type semiconductor due to the positive slope in MS plot, as expected for n-type materials. The flat band potential values measured from the slope and intercept of the MS curve were found to be -1.35V. It is well-known that the materials with a more negative flat band potential have a better ability to facilitate charge transport in PEC applications.

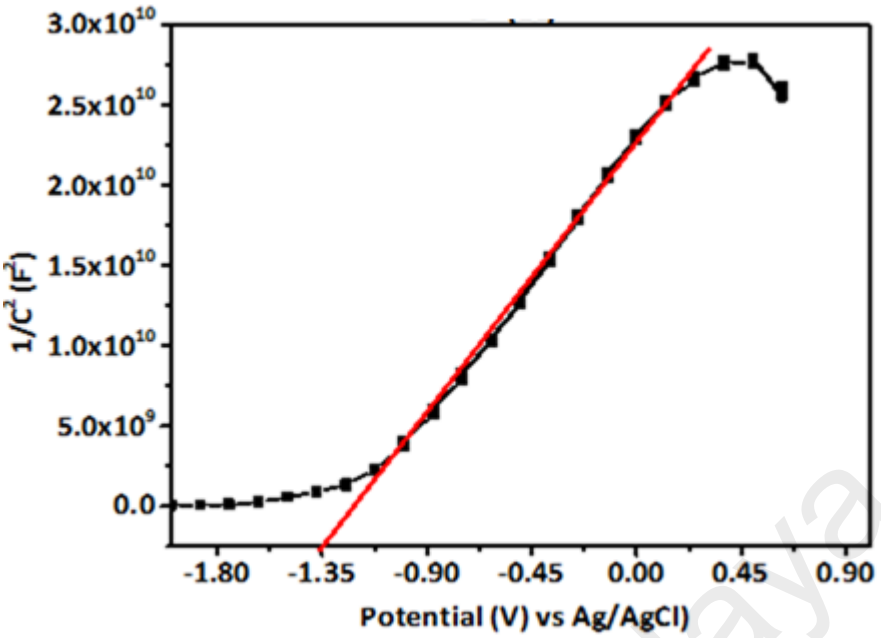

Figure 4.36: Mott –Schottky plot of $MgTi_2O_5$ film obtained at frequency of 1kHz in 1M NaOH.

Thus, the porous spherical designed $MgTi_2O_5$ photoelectrode developed from precursor (**3**) displays higher photocurrent density, smaller interface impedance and higher charge density. These results indicate that the PEC response is very auspicious and competitive as compare to the outcomes of other well established magnesium titanate nanocrystal materials (N. Zhang, Qu, Pan, Wang, & Li, 2016; N. Zhang et al., 2015).

We tentatively attribute this enhancement to the higher purity achieved in the $MgTi_2O_5$ phase through SSP (**3**) which, because of its exact metallic ratio (Mg/Ti 1:2), eliminates the growth of impurity phases of TiO_2, $MgTiO_3$ and Mg_2TiO_4. Another key factor is the formation of porous and well-connected microspherical architecture in $MgTi_2O_5$ which gives the film a large effective surface area, amplified photo absorption ability and an increased electrode electrolyte interfacial area, leading to a reduction in electron-hole recombination as the photogenerated hole travels through fewer material before being collected at the electrode/electrolyte interface and hence increasing cell efficiency (T. W. Kim & Choi, 2014).

4.4 Synthesis and Characterization of Complex $[Mn(dmae)_2(TFA)_4]$ (4)

A mononuclear Mn-complex $[Mn(dmae)_2(TFA)_4]$ (**4**) (TFA = triforoacetato, dmae = N, N-dimethylaminoethanolato) was prepared by the replacement of the acetate ligands by the more strongly chelating TFA and dmae moieties in stoichiometric quantities of manganese(II) acetate dehydrate and trifuoroacetic acid in THF solution as shown in the following chemical equation.

Chemical equation 7:

$$Mn(CH_3COO)_2\,4H_2O + 4CF_3COOH + 2(CH_3)_2NCH_2CH_2OH \xrightarrow{THF} [Mn((CF_3COO)_4(O(CH_2)_2N(CH_3)_2] + 2\,CH_3COOH + 4H_2O$$

The above reaction produced complex (**4**) in 75 % yield in form of transparent white crystals that are stable in air and moisture and soluble in common organic solvents such as methanol, ethanol and THF. The stoichiometric composition of the complex was first ascertained by single crystal X-ray diffraction analysis and was supported by elemental analysis, FT-IR and thermogravimetry. Elemental analysis: % calculated (found) for $[Mn(dmae)_2(TFA)_4]$ C, 21.11 (20.83), H, 1.77 (1.69), N, 2.05 (1.95). The FT-IR spectrum of complex (**4**) clearly indicates the presence of the asymmetric and symmetric ν(C=O) vibrations of trifluoroacetato ligand have been located at 1635 and 1444 cm^{-1} respectively. The difference of 191 cm^{-1} between asymmetric and symmetric ν(C=O) vibrations designates the bidentate nature of the carboxylate groups of trifuoroacetato ligands that are bonded to different Mn centre (Mansoor, Mazhar, McKee, & Arifin, 2014; Mansoor et al., 2016). Similarly, the peak at 1177 cm^{-1} confirms the presence of C–F bonds in

complex (**4**). The absorption at low frequency of 502 cm^{-1} is due to stretching vibration mode of (M-O).

4.4.1 Single Crystal Analysis of Complex $[Mn(dmae)_2(TFA)_4]$ (4)

The molecular structure of complex (**4**) is presented in Figure 4.37 while geometric parameters and structure refinement details are provided in Table 4.7 and 4.8, respectively. $[Mn(dmae)_2(TFA)_4]$ is a monomeric coordination complex in which "Mn (IV)" cation lies at the center of symmetry. Mn (IV) is coordinated to four oxygen donor atoms from four independent TFA anions and two oxygen atoms from two different dmae molecules which occupy the equatorial position, thus, completing the approximate coordination sphere around the metal center. The co-ordination behavior of each TFA anion is monodentate and four oxygen atoms are coordinated with both syn and anti-geometry. Similarly, each dameH molecules also act as a monodentate ligand. No distortion from linearity is observed at the Mn(IV) center and there are not any notable interactions found in the crystal structure.

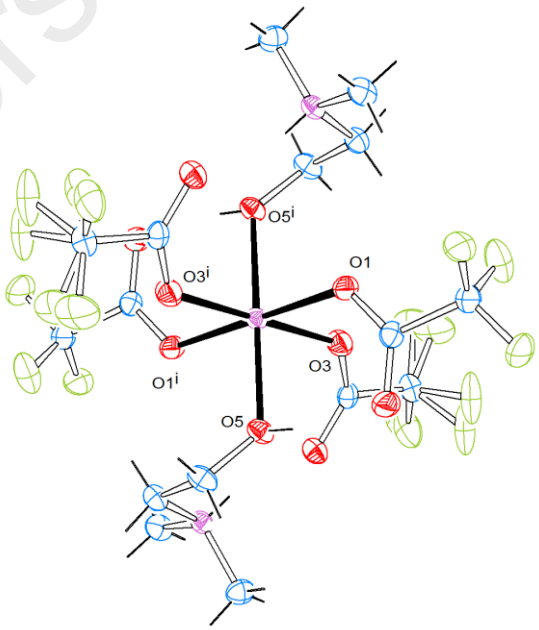

Figure 4.37: ORTEP diagram of complex (**4**) at the 50 % probability level.

Table 4.7: Crystal data and structure refinement.

Identification code	
Empirical formula	C16 H24 F12 Mn N2 O10
Formula weight	687.31
Temperature	114(2) K
Wavelength	0.71073 Å
Crystal system	Orthorhombic
Space group	P b c a
Unit cell dimensions	a = 9.0076(6) Å
α= 90°.	
	b = 16.6072(12) Å
β= 90°.	
	c = 18.0267(11) Å
γ = 90°.	
Volume	2696.6(3) $Å^3$
Z	4
Density (calculated)	1.693 Mg/m^3
Absorption coefficient	0.623 mm^{-1}
F(000)	1388
Crystal size	0.500 x 0.300 x 0.300 mm^3
Theta range for data collection	3.197 to 28.694°.
Index ranges	-8<=h<=11, -22<=k<=21, -20<=l<=24
Reflections collected	13593
Independent reflections	3427 [R(int) = 0.0350]
Completeness to theta = 25.242°	99.8 %
Absorption correction	"multi-scan"
Max. and min. transmission	0.4329 and 0.3934
Refinement method	Full-matrix least-squares on F^2
Data / restraints / parameters	3427 / 51 / 207
Goodness-of-fit on F^2	1.108
Final R indices [I>2sigma(I)]	R1 = 0.0458, wR2 = 0.1153
R indices (all data)	R1 = 0.0538, wR2 = 0.1211
Extinction coefficient	n/a
Largest diff. peak and hole	0.805 and -0.549 $e.Å^{-3}$

Table 4.8: Selected Bond lengths [Å]

Mn(1)-O(3)#1	2.1065(15)	Mn(1)-O(3)	2.1065(15)
Mn(1)-O(5)	2.2005(14)	Mn(1)-O(5)#1	2.2005(14)
Mn(1)-O(1)#1	2.2175(14)	Mn(1)-O(1)	2.2175(14)

4.4.2 Thermogravimetric Analysis of Complex [Mn(dmae)$_2$(TFA)$_4$] (4)

The thermal degradation of (**4**) has been examined by thermogravimetric (TGA) and differential thermogravimetric (DTG) analyses performed under flowing nitrogen ambient at a flow rate of 25 cm^3/min with a heating rate of 10 ˚C/min (Figure 4.38).

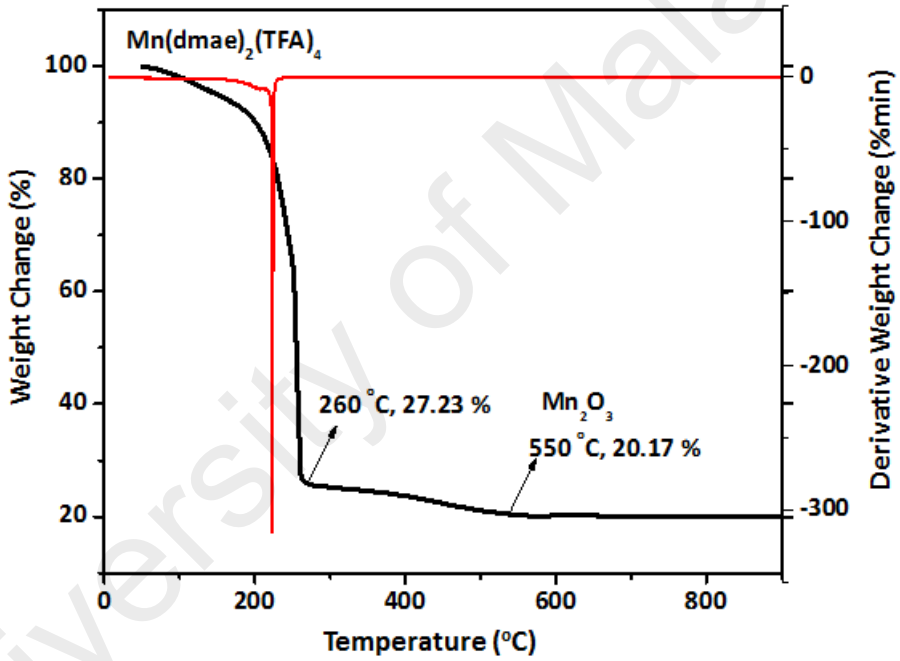

Figure 4.38: TGA (black line) and DTG (red line) plot of complex (4) under nitrogen flow rate of 25 cm^3 min^{-1} and heating rate of 10 ^{o}Cmin^{-1}

The thermogram shows that the decay process in complex (**4**) occurs in two successive stages and the first major and rapid decomposition occurs in the temperature range of 179 to 260 ^{o}C with weight loss of 72.77 %. The second pyrolysis step is relatively slower and befalls in a wide temperature range of 260 to 550 ^{o}C giving a weight loss of 7.06%. The residual mass of 20.17 % observe at 550 ˚C indicates the formation of expected Mn_2O_3 oxide material from complex (**4**) as shown in following equation.

Chemical equation 8:

$$2[Mn((CF_3COO)_4(O(CH_2)_2N(CH_3)_2)] \xrightarrow{550\ ^oC} Mn_2O_3 + \text{Volatile}$$

4.4.3 XRD Analysis of Pristine Mn_2O_3 and Ag-Mn_2O_3

Methanol solution of precursor (**4**) and its mixture with $Ag(CH_3COO)$ were employed in AACVD for the formation of pristine Mn_2O_3 and Ag-Mn_2O_3 composite films, respectively, on FTO glass substrate at a temperature of 450 ˚C. The resultant films were examined by XRD analysis to identify the crystalline and chemical nature of the deposit and both the difrractograms are overlaid in Figure 4.39. In both the cases, the common Mn_2O_3 phase is in good agreement with standard ICDD card No [98-000-9091] (Appendix 5(i)) and belongs to cubic crystal system. The characteristics peaks of Mn_2O_3 indicated by (♦) at 2θ = 23.0˚, 33.1˚, 38.3˚, 45.0˚ and 55.2˚ are originated from their Miller indices (012), (112), (222), (004) and (044) respectively. In Ag-Mn_2O_3 composite XRD pattern (Figure 4.39b), the metallic Ag is identified from its peaks at 2θ = 38.1 (111), 44.2 (002), 64.5 (022), 77.6 (113) and 81.9˚ (222) denoted by symbol (●) and corresponds well to standard ICDD pattern number [01-071-6549] (Appendix 5(ii)). Peaks indicated by (*) are obtained from crystalline F:SnO_2 of the FTO substrate. These XRD patterns do not show any probable crystalline impurities such as MnO, MnO_2 and Mn_3O_4, Ag_2O or AgO. Therefore, we can infer that methanol solution of precursor (**4**) and its mixture with silver acetate are capable of generating phase pure Mn_2O_3 and Ag-Mn_2O_3 composite films, respectively, at 450 ˚C through AACVD method.

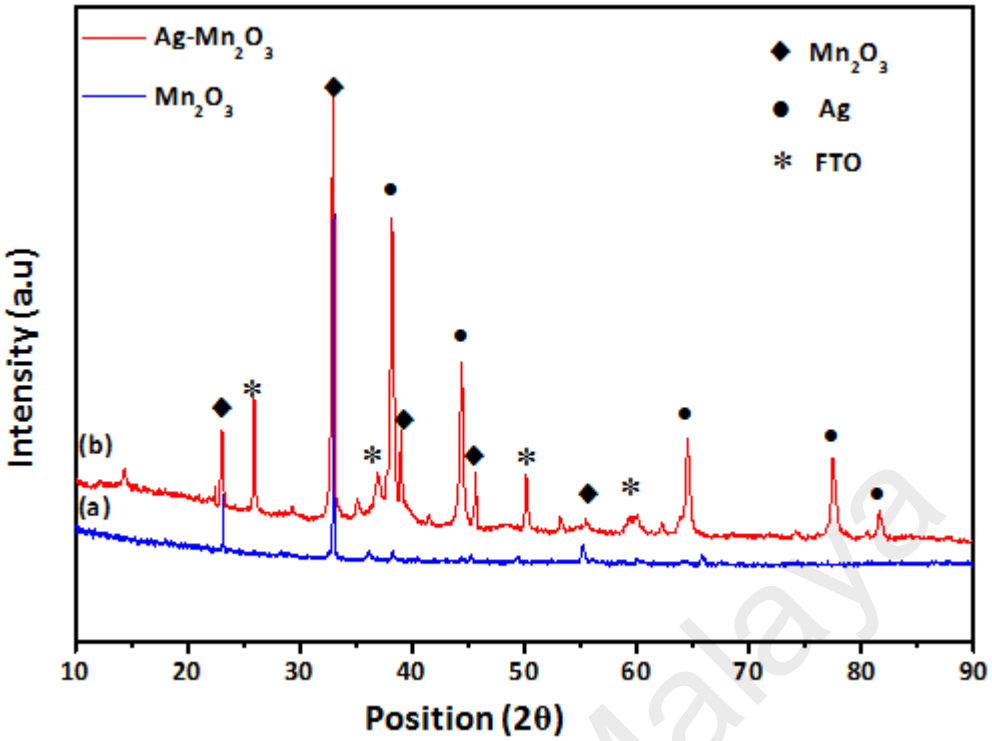

Figure 4.39: XRD patterns of pristine **(a)** Mn_2O_3 and **(b)** Ag- Mn_2O_3 composite thin films grown on FTO at 450 ^oC via AACVD

4.4.4 Raman Spectroscopy of Pristine Mn_2O_3 and Ag-Mn_2O_3

Pristine Mn_2O_3 and Ag-Mn_2O_3 composite films were further examined are comparatively shown in Figure 4.40. Figure 4.40 showed four Raman active modes at 195, 309, 644 and 691 cm^{-1} in pristine Mn_2O_3 as reported in the literature (Han et al., 2007; Javed et al., 2012). These vibrational modes appeared to be out of plane band, asymmetric and symmetric bridging oxygen species Mn-O-Mn. On Ag-Mn_2O_3 composite formation scattering mode at 196 cm^{-1} disappears and band at 309 cm^{-1} remains at its place. The other two modes at 644 and 691 cm^{-1} are shifted to lower wave numbers of 601 and 641cm^{-1}. This is perhaps the Mn-O band is effected by the presence of Ag metal. No characteristic peak for metallic Ag has been observed due to as pure metals do not exhibit raman scattering (Lewis & Edwards, 2001).

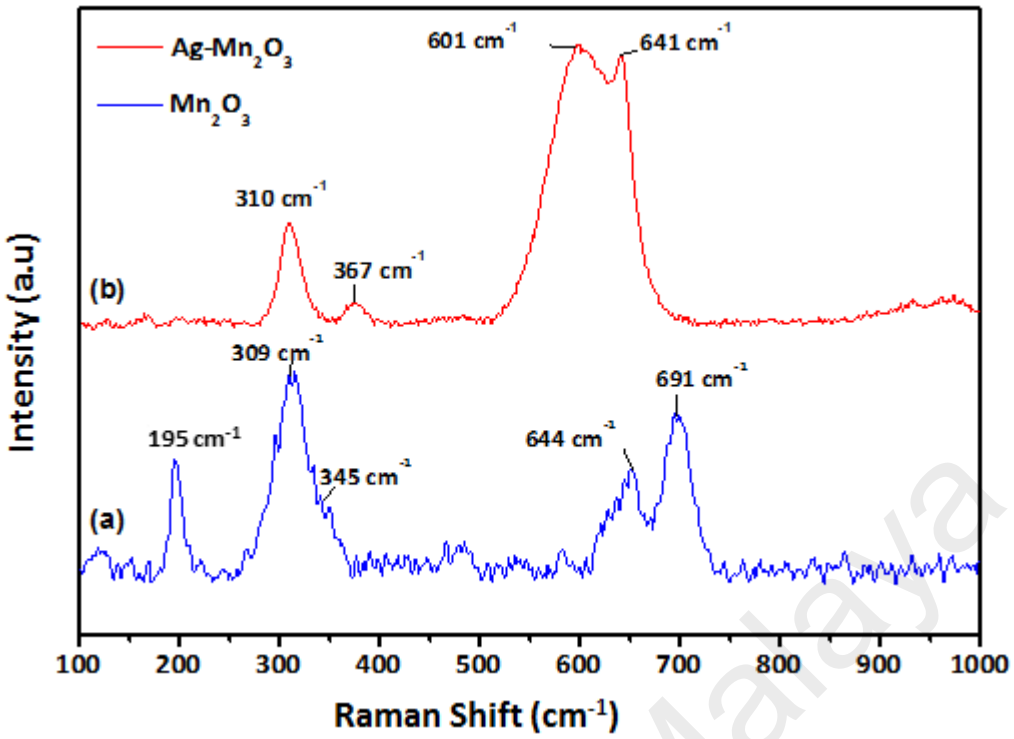

Figure 4.40: FT-Raman spectra of **(a)** pristine Mn_2O_3 and **(b)** Ag- Mn_2O_3 composite thin film deposited on FTO substrate by AACVD at 450 ^oC.

4.4.5 Surface Morphology of Pristine Mn_2O_3 and Ag-Mn_2O_3

The surface morphologies and microarchitectures of pristine Mn_2O_3 and Ag-Mn_2O_3 composite films developed at 450 °C via AACVD were examined by FESEM analysis and images are presented in Figure 4.41. The surface morphology of pristine Mn_2O_3 is consist of cubical shaped particles with sharp edges which are regularly grown on FTO substrate and making the film compact in nature. However Ag-Mn_2O_3 composite film grown at 450 ˚C exhibits a different kind of surface topography and various multi-shaped particles including triangular, octahedral, rod like objects in size range 200-400nm with clear grains boundary can be observed on FTO substrate Figure 4.41b. The composite nature of Ag-Mn_2O_3 was established by EDX map analysis (Figure 4.42) and results show that Ag, Mn and O atoms are uniformly dispersed throughout the film matrix.

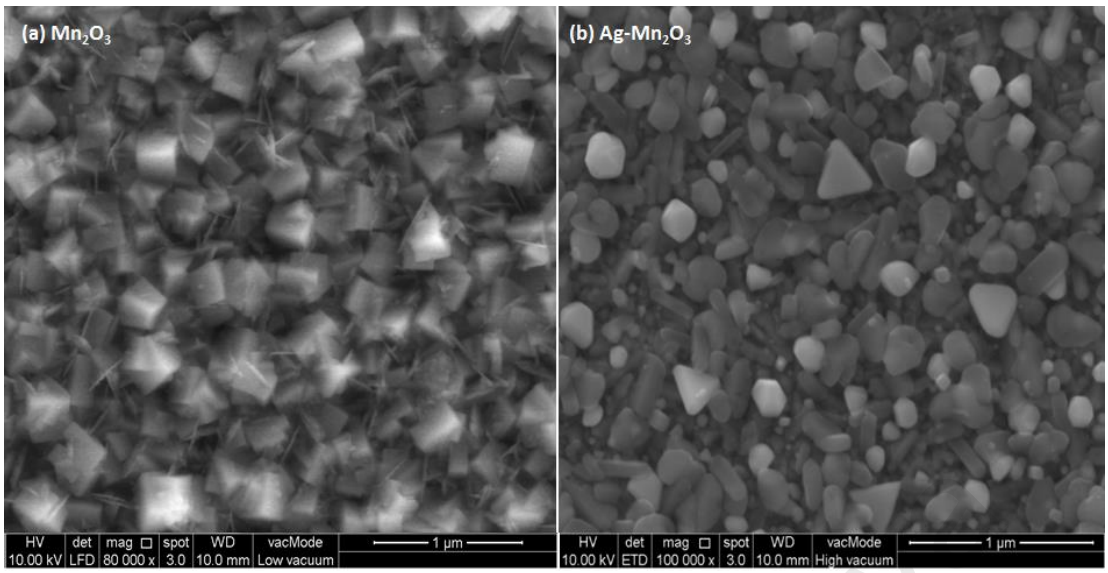

Figure 4.41: FESEM images **(a)** pristine Mn_2O_3 **(b)** Ag-Mn_2O_3 composite thin films grown at 450 ˚C on FTO substrate.

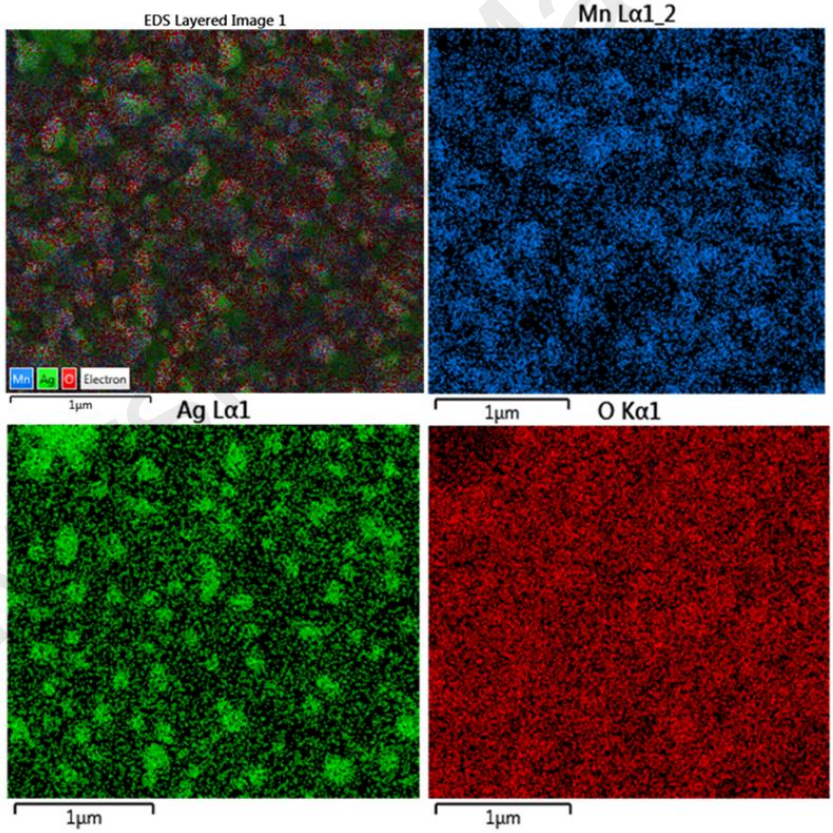

Figure 4.42: Elemental map showing the distribution of Ag, Mn and O elements in Ag-Mn_2O_3 composite thin film.

The surface compositions of both types of films were analyzed by energy dispersive analysis (EDX) analysis. EDX spectra recorded at various arbitrary large areas (Appendix 6(i and ii)) revealed that the pristine manganese oxide films contains only Mn

atoms throughout the film matrix. While the metallic ratio of Ag: Mn in composite films is found to be 1:2 which exactly matches with the formula of target Ag-Mn_2O_3 material.

4.4.6 XPS Analysis of Pristine Mn_2O_3 and Ag-Mn_2O_3

The pristine Mn_2O_3 and Ag-Mn_2O_3 composite films were employed to X-ray photoelectron spectroscopy (XPS) to investigate the composition, oxidation states and electronic structure of the involved atoms and results are presented in Figure 4.43. The survey scan spectra (Figure 4.43a) reveals that, except for the O 1s (530 eV) and Mn 2p (640 eV) peaks, the Ag 3d peaks emerged with strong relative intensities, showing that the Mn_2O_3 was mainly coated with Ag nanoparticles. In high resolution Mn 2p spectrum, Figure 4.42c, two main peaks at binding energies of 641.10 eV and 653.12 eV correspond to Mn $2p_{3/2}$ and Mn $2p_{1/2}$. The difference (Δ) between Mn $2p_{3/2}$ and Mn $2p_{1/2}$ is 12 eV which implies a typical value for Mn^{3+} and is very similar to those reported earlier for Mn_2O_3 (Chigane & Ishikawa, 2000). The higher resolution XPS spectrum of the Ag 3d was fitted to two peaks at 368.43 and 374.43 eV for $Ag3d_{3/2}$ and $Ag3d_{5/2}$, respectively (Sun et al., 2009; D. Wang et al., 2012) (Figure 4.42b). The difference (Δ) between $Ag3d_{3/2}$ and $Ag3d_{5/2}$ peaks is about the ~6eV indicating that Ag mainly exists in the Ag^0 state on the Mn_2O_3 surface.

Meanwhile, the high resolution XPS spectrum of O1s, Figure 4.42d, exhibits asymmetric contours at about 530 eV, attributed with Mn–O in Mn_2O_3. The small peaks at 531 and 532 eV are assigned to the adsorbed oxygen and hydroxyl oxygen, respectively (Sekhar, Babu, & Kalaiselvi, 2015; Smith Stegen, 2015). The identical electronic structure (Mn 2p, O1s) confirms the formation of analogues Mn_2O_3 phases in both pristine Mn_2O_3 and Ag-Mn_2O_3 composite films. On the basis of XRD, EDX and XPS results, we infer that pristine Mn_2O_3 and Ag-Mn_2O_3 composite were successfully fabricated by AACVD in this work.

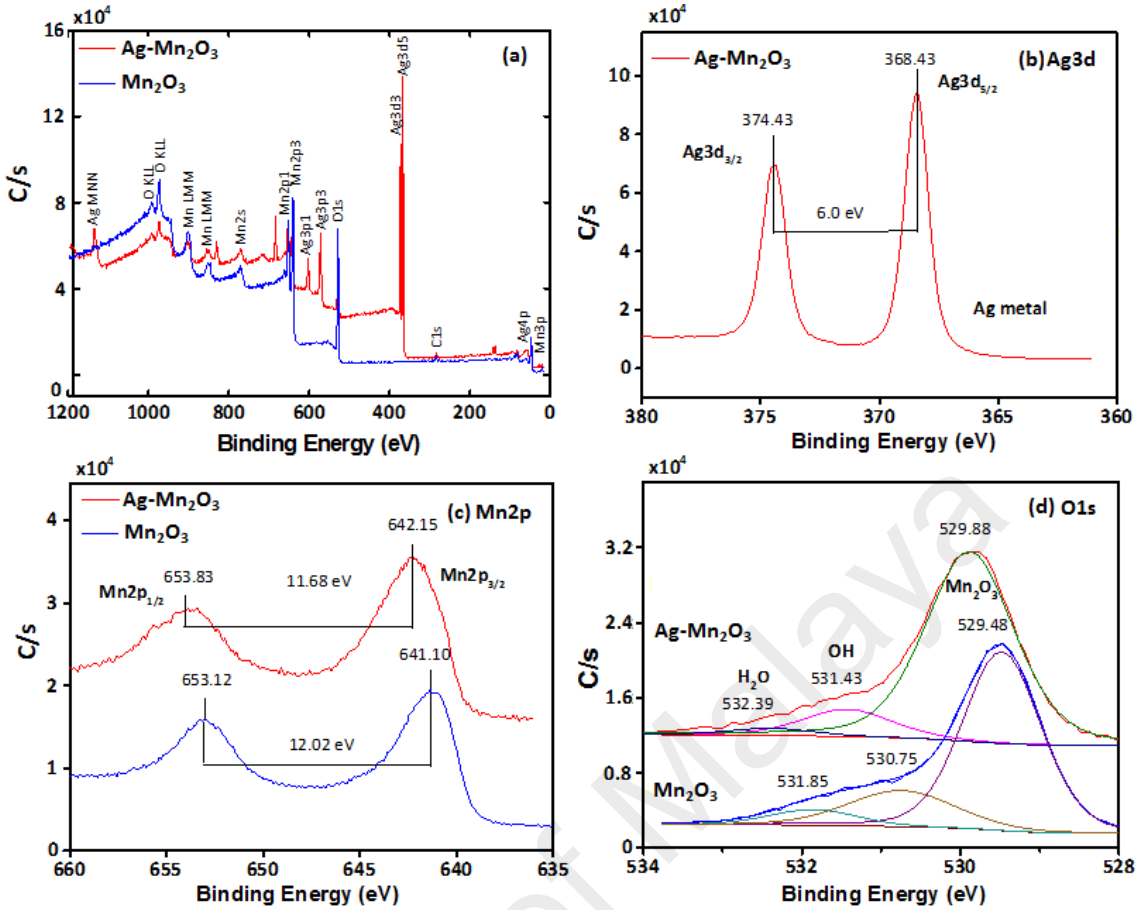

Figure 4.43: (a) Survey scan XPS spectra of pristine Mn_2O_3 (blue line) and Ag-Mn_2O_3 (red line). High resolution spectra for (b) Ag 3d, (c) Mn 2p (d) O 1s.

4.4.7 Optical Band gap of pristine Mn_2O_3 and Ag-Mn_2O_3

The optical band gap of as-synthesized pristine Mn_2O_3 and Ag-Mn_2O_3 composite thin films were recorded in UV-visible region of 350-800 nm and is shown in Figure 4.44 (a and b) respectively. It is obvious from the spectra that both the films continuously absorb in visible region from 400-750nm. The UV-vis data were applied to Tauc's formula and direct bandgaps E_g of 2.0 and 1.8 eV were measured for pristine Mn_2O_3 and Ag-Mn_2O_3 composite films, and from their respective Tauc's plots (Insets Figure). The bandgap of 2.0 eV is in good agreement with previous reported values for pure Mn_2O_3 prepared by different method (Naeem et al., 2015).

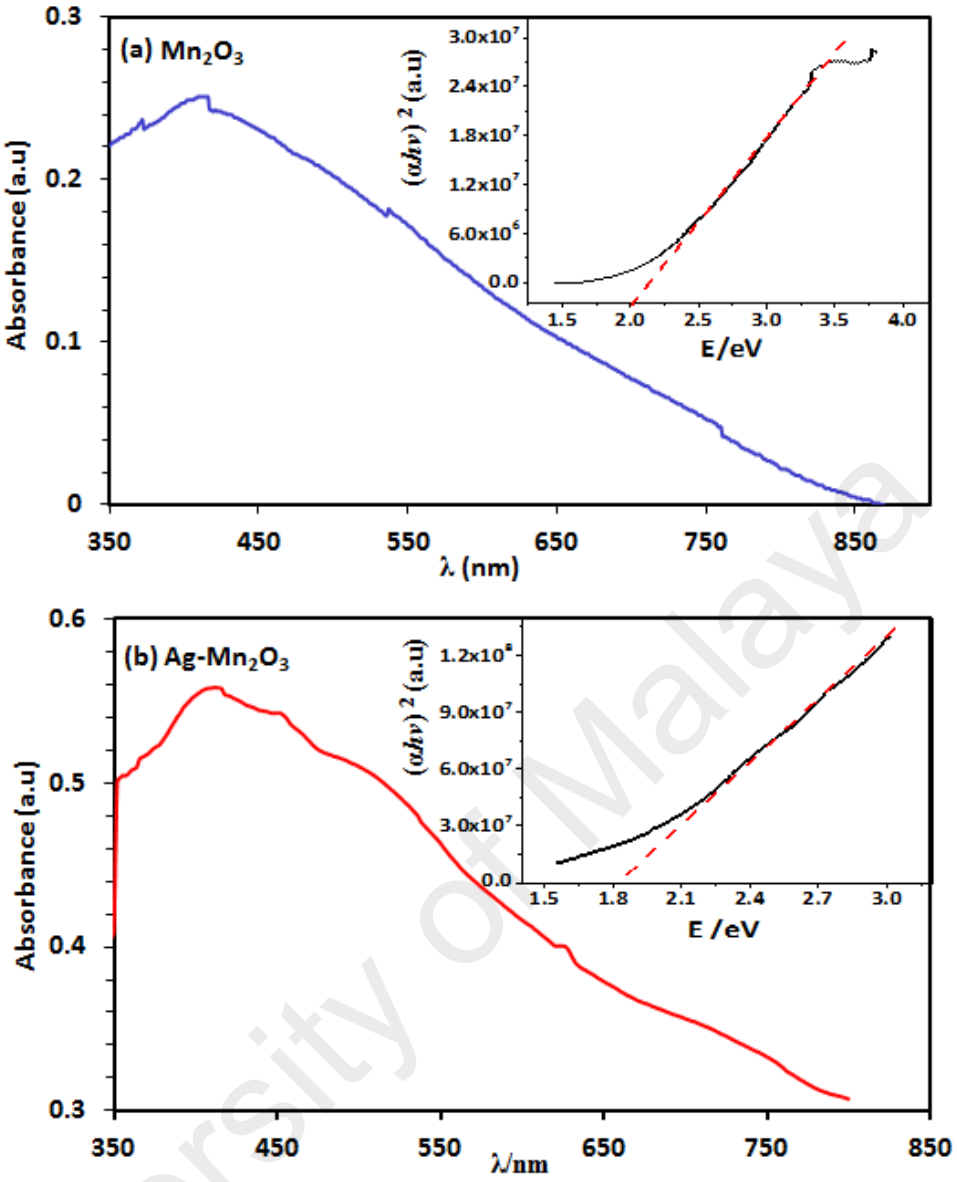

Figure 4.44: UV-Vis spectra of absorbance as function of wavelength and inset Tauc plot ($(\alpha hv)^2$ Vs E/eV) of **(a)** Mn_2O_3 and **(b)** Ag-Mn_2O_3 thin films deposited at 450 ºC on FTO substrate by AACVD.

The lowering of bandgap in case of Ag-Mn_2O_3 composite film is attributed with the plasmonic effect of metallic Ag on Mn_2O_3 oxide. The plasmonic effect of Ag on Mn_2O_3 is also evident from Raman scattering where two bands at 644 and 691 cm^{-1} are shifted to lower frequency region. Similar plasmonic effect imparted by silver in attaining low band gap with better absorbance in the visible region of light have been reported in metal integrated metal oxide composites (Kharade et al., 2013; Lim, Pandikumar, Huang, & Lim, 2014).

4.4.8 Photoelectrochemical Studies of Pristine Mn_2O_3 and Ag-Mn_2O_3

The PEC properties of pristine Mn_2O_3 and Ag-Mn_2O_3 composite electrodes were evaluated using a three electrode system having Pt wire and standard Ag/AgCl as counter and reference electrodes, respectively. The Mn_2O_3 and Ag-Mn_2O_3 thin films were used as the working electrode. 0.1M Na_2SO_4 aqueous solution was used as an electrolyte. The separation of the photo generated electron-hole pairs was evaluated by measuring photocurrents and Figure 4.45a shows a comparative study of Linear Scanning voltammograms (LSVs) of both pristine Mn_2O_3 and Ag-Mn_2O_3 composite films at scan rate of 50mV/s. The dark current from -0.2 V to 1.0 V (*vs.* Ag/AgCl) of each sample was very low. Upon illumination, the Ag-Mn_2O_3 electrode showed a significant enhancement in photocurrent density (3.0 mA cm^{-2}) as compare to pure Mn_2O_3 (1.8 $mAcm^{-2}$) at a potential of 0.7 V *versus* Ag/AgCl. This pronounced photocurrent could be ascribed to the decoration of Ag on Mn_2O_3, resulting in a higher separation efficiency of the generated electron–hole pairs and enhanced visible light absorption due to the surface plasmon resonance (SPR) effect (Linic, Christopher, & Ingram, 2011; Warren & Thimsen, 2012).

The Mn_2O_3 and Ag-Mn_2O_3 photoelectrodes were further tested under on–off cycle illumination conditions to determine whether the measured photocurrents were associated with the absorption of light (Figure 4.45b).

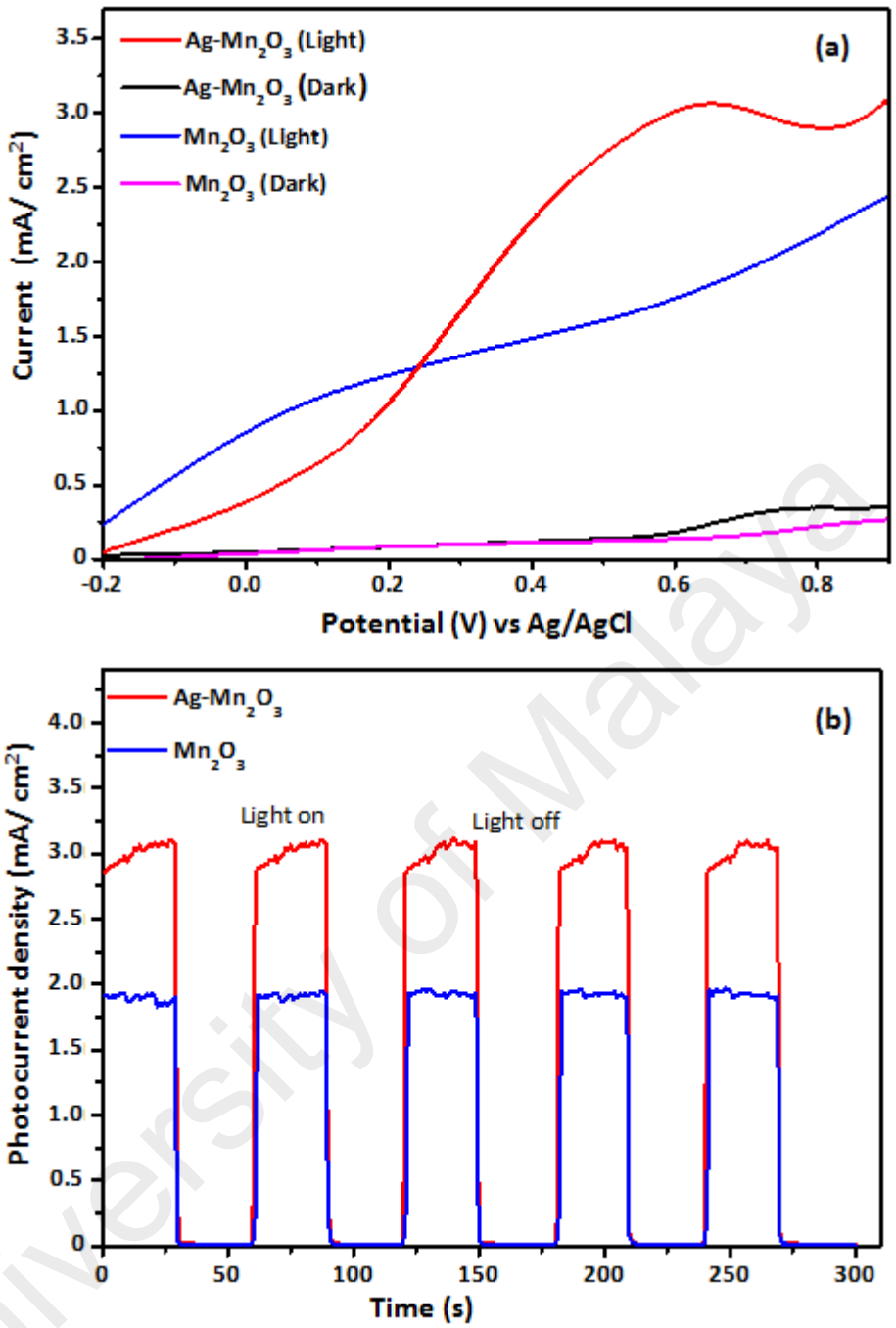

Figure 4.45: (a) Linear sweep Voltammetry (LSV) of pristine Mn_2O_3 and Ag-Mn_2O_3 composite thin films in dark and light **(b)** Chronoamperometry (I–t) profiles (on-off cycles) of pristine Mn_2O_3 and Ag-Mn_2O_3 composite thin films at an applied potential of +0.7 V versus Ag/AgCl under 100 mW cm^{-2} illumination (AM 1.5) in 0.1 M Na_2SO_4 aqueous solution.

Figure 4.45b shows the photocurrent generated under visible light irradiation of Mn_2O_3 and Ag-Mn_2O_3 electrodes. A steady and stable photo response of 1.8 and 3.0 mA cm^{-2} within 5 on-off cycles could be observed over a 5 min period (Figure 4.45b) revealing the

higher efficiencies and good stabilities of Mn_2O_3 and Ag-Mn_2O_3 photoelectrodes. Moreover, the transient photocurrents agrees well with LSV results and strengthened the PEC performance in the visible light region, as well as indicating the existence of the SPR effect of Ag nanoparticles on Mn_2O_3.

Electrochemical impedance spectroscopy (EIS) was performed to scrutinize the conductivity of electrode material, charge transport in the electrode–electrolyte interface and mechanistic analysis of interfacial processes. Figure 4.46a displays the Nyquist plots of both pristine Mn_2O_3 and Ag-Mn_2O_3 composite films in the frequency range of 0.1 Hz to 10 kHz in 0.1M Na_2SO_4 electrolyte under dark and visible light illumination. As shown in Figure 4.46a, the diameter of the pristine Mn_2O_3 was much larger than that of Ag-Mn_2O_3 composite in the dark as well as under visible light irradiation. The diameter of the semicircle in the Nyquist plots at high frequency represents the charge transfer resistance (R_{ct}), which is associated with the electronic properties of the electrode. Under illumination, the R_{ct} of Ag- Mn_2O_3 (~127 Ω) is considerably lower than R_{ct} of Mn_2O_3 (~195 Ω). The decrease of the charge transfer resistance of Ag- Mn_2O_3 is attributed to the larger number of charge carriers in the electrode sample. It is believed that these charge carriers are produced only because of the presence of Ag inside the Mn_2O_3 which facilitates fastest electron transport and shortest ion-diffusion path inside the Ag- Mn_2O_3 electrode. Normally, the smaller arc radius on the EIS Nyquist plot indicates an effective separation of photo-generated electron– hole pairs and a fast interfacial charge transfer process (Ge et al., 2016). This implies that Ag decoration significantly facilitated the electron mobility by reducing the recombination of electron–hole pairs and contributing to the enhanced PEC performance induced by Ag- Mn_2O_3 .

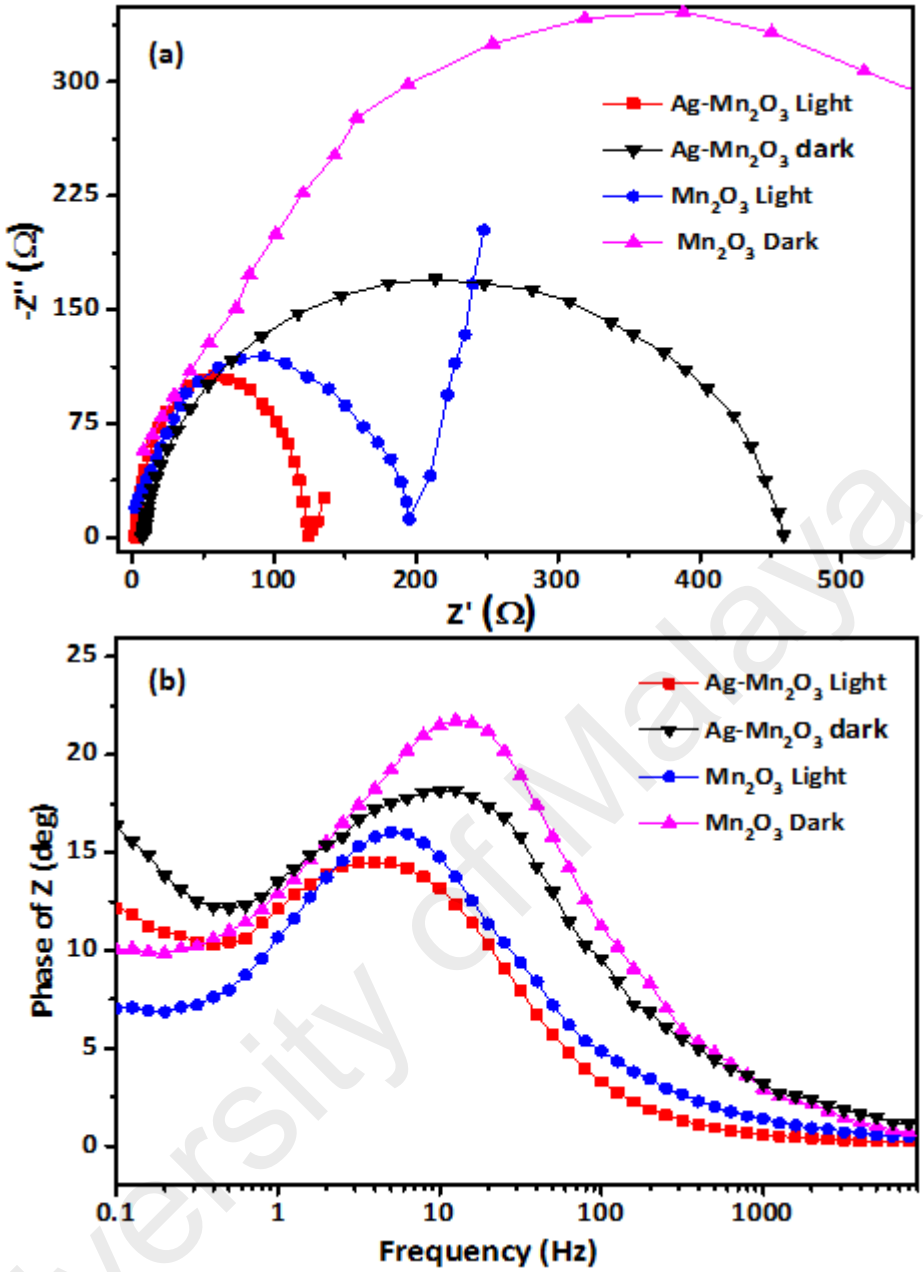

Figure 4.46: (a) EIS in the Nyquist plots of pristine Mn_2O_3 and Ag-Mn_2O_3 composite thin films in 0.1 M Na_2SO_4 aqueous solution. **(b)** Bode angle phase plots of the Mn_2O_3 and Ag-Mn_2O_3 composite thin films.

The frequency dependence phase angle plot (Bode plot) of both pristine Mn_2O_3 and Ag-Mn_2O_3 composite electrodes were recorded for the detailed understanding of the charge-transfer resistance phenomenon in these materials. The Bode phase plots found for the Mn_2O_3 and Ag-Mn_2O_3 thin films are shown in Figure 4.46b where the characteristic frequency peaks were affected under dark and light conditions. In dark environment, the Mn_2O_3 and Ag-Mn_2O_3 films showed the frequency peak maxima (f_{max}) at 13.7 and 9.79

Hz respectively, suggesting larger charge-transfer resistance at the electrode/electrolyte interface due to a lack of availability for electroactive species. However the f_{max} is observed to shift toward the low frequency region (~1 Hz) in presence of light indicating the rapid electron-transfer (conductive) behavior of the Mn_2O_3 and Ag-Mn_2O_3 films. It is worth noticing that the phase angle values of Mn_2O_3 and Ag-Mn_2O_3 are increased in dark, revealing the conducting nature of the films. Approaching the phase angle to towards -90° signifies the ideal capacitor behavior of the electrode (Sheng, Sun, Li, Yuan, & Shi, 2012). In the present case, still the phase angle of the pristine Mn_2O_3 and Ag-Mn_2O_3 in dark and under illumination is much less than 90˚ suggests that the electrode does not behave like an ideal capacitor. These characteristic frequencies can be used to calculate the electron recombination lifetime (τ_n) of the corresponding material with following relationship (Lim, Pandikumar, et al., 2014):

$$\tau_n = {}^{1}/_{2\pi f_{max}}$$

Where f_{max} is the frequency peak maximum. The recombination life time (τ_n) values for the pristine Mn_2O_3 and Ag-Mn_2O_3 composite films are calculated to be are 11.6 and 16.2 ms, respectively in the absence of light. It is well known that when Ag nanoparticles are deposited on metal oxide surface, the plasmon resonance energy transfer (PRET) from Ag to metal oxide would occur (Jana et al., 2009). This PRET process would establish an oscillating electric field which would reduce the recombination of photo-generated electron–hole pairs. Therefore, the lifetime of charge carriers in Ag-Mn_2O_3 is prolonged effectively compared to pristine Mn_2O_3.

Further Mott–Schottky (MS) experiments for pristine Mn_2O_3 and Ag- Mn_2O_3 composites were conducted to deduce information about the type of semiconductor, flat band potential and the charge density values (Figure 4.47).

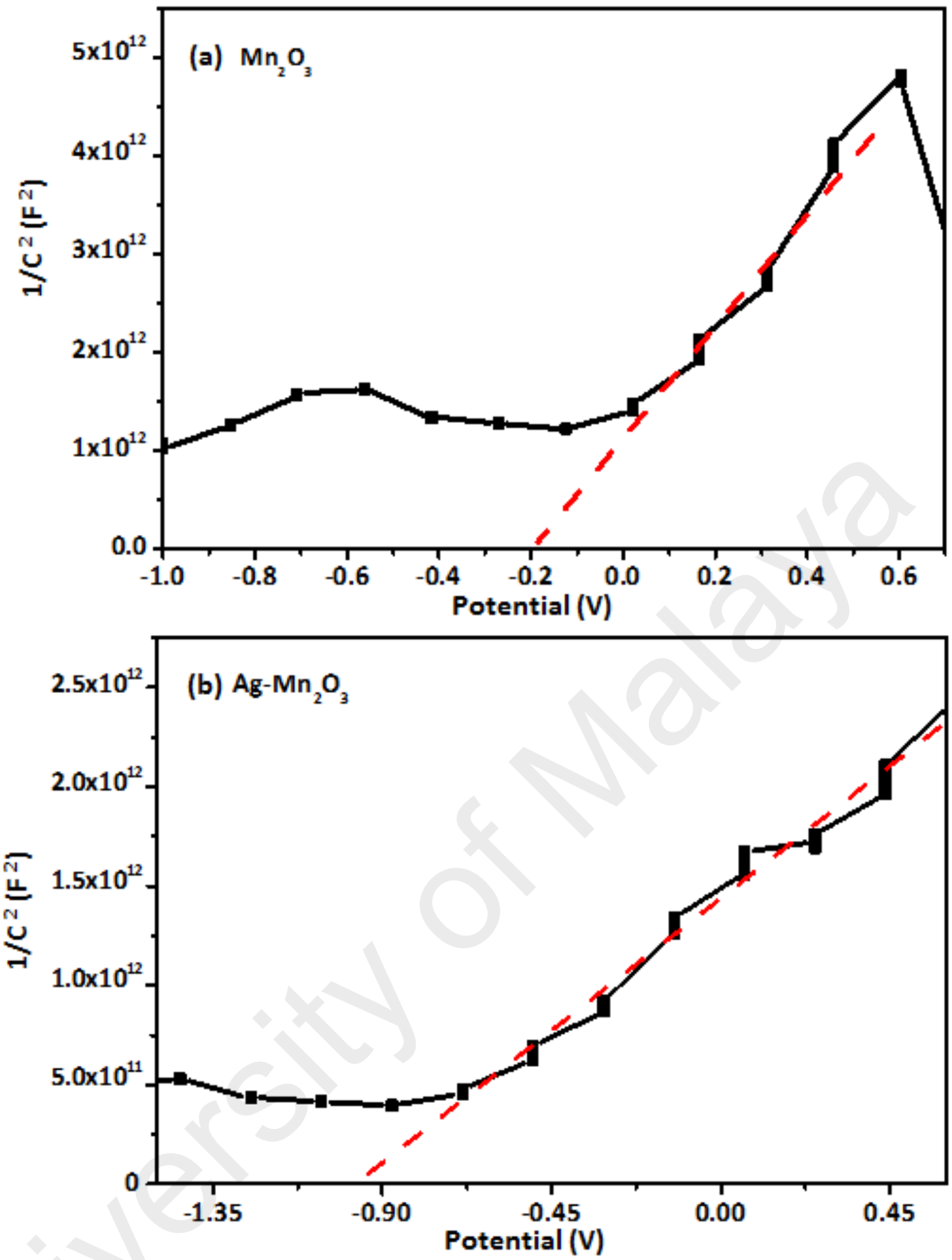

Figure 4.47: Mott–Schottky curves for (a) pristine Mn_2O_3 and (b) Ag-Mn_2O_3 composite thin films.

Figure 4.47 shows that both the Mn_2O_3 and Ag- Mn_2O_3 show a positive slope in the MS plots, as expected for the n-type semiconductor. Importantly, the considerably smaller slope of Ag- Mn_2O_3 composite in MS plot represents higher carrier concentration compare to pure Mn_2O_3. The flat band potential of Ag- Mn_2O_3 composite, −0.91 V/SCE, is observed to be lower than −0.22 V/SCE of pristine Mn_2O_3 , indicating better transportation of the photogenerated carriers in the Ag- Mn_2O_3 composite case. Also the

carrier densities of both pristine and composite films were calculated to be 1.62×10^{13} and 3.09×10^{13} cm^{-3} respectively. In Ag-Mn_2O_3 composite thin film, Ag is the source of extra charge carriers. A higher charge carrier concentration in the composite film has an influence on changing the work function of the material which enhances the charge transfer at the electrode electrolyte interface and an improved PEC performance.

The markedly enhanced photocurrent of Ag- Mn_2O_3 film electrode is a direct consequence of the synergetic effects of the uniformly dispersed Ag on to Mn_2O_3 structure. On the basis of PEC results, we have proposed a mechanism of electrons transportation from Ag to Mn_2O_3 as shown in Figure 4.48.

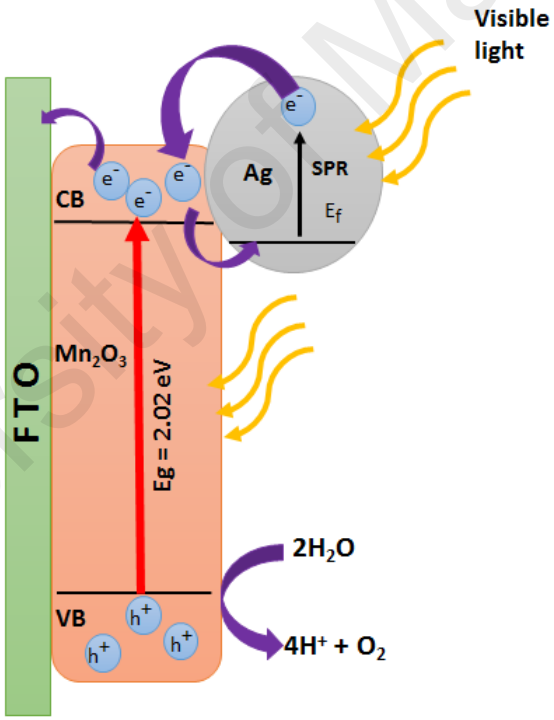

Figure 4.48: Charge transfer mechanism between Ag particles and Mn_2O_3 in visible light.

Under visible light irradiation, Ag nanoparticles could be photo-excited and generate hot electrons on its surface due to the surface plasmon resonance. Electrons are excited from valence band to conduction band by illumination with visible light and then migrate to Ag metal. The plasmon-induced hot electrons are introduced into the conduction band of

Mn_2O_3, and then to the FTO substrate through the Mn_2O_3 backbone. Finally, the electrons were transferred to the Pt electrode to reduce water and generate hydrogen. As a result, Ag nanoparticles attached on Mn_2O_3 could increase the photocurrent intensity under illumination of the entire solar spectrum.

4.5 Synthesis of Complex $[Sn(dmae)(OAc)]_2$ (5)

The new single source dimeric complex (**5**) was readily prepared by ligand exchange reaction of equimolar quantities of bis(dimethylaminoethanolato)tin(II), $Sn(dmae)_2$ (Wakeshima & Kijima, 1972; Hollingsworth et al., 2006; Nawar & Hosny, 2000; M. Veith, Haas, & Huch, 2004; B.-H. Ye, Li, Williams, & Chen, 2002) and $Y(OAc)_3\ xH_2O$ in (10 mL) of dry toluene. The complex is soluble in toluene and has a melting point of 147 ^oC. The overall reaction for the formation of (**5**) is shown below in equation 6

Chemical Equation 9

$$SnCl_2 + 2(C_2H_5)_3N \xrightarrow{CH_3OH} Sn(OCH_3)_2 + 2(C_2H_5)_3NHCl$$
$$Sn(OCH_3)_2 + (CH_3)_2NCH_2CH_2OH \longrightarrow Sn(OCH_2CH_2N(CH_3)_2$$
$$Sn(OCH_2CH_2N(CH_3)_2 + Y(CH_3COOH) \xrightarrow{Toluene} Sn(OCH_2CH_2NCH_3)(OOCCH_3)$$

The single crystal analysis indicated that precursor 5 is stabilized by the establishment of an intramolecular coordinate Sn←N bond and the orthorhombic crystal system with space group Pna2(1).

4.5.1 Crystal Structure of Complex $[Sn(dmae)(OAc)]_2$ (5)

The X-ray crystal and structure refinement data for $[Sn\ (OAc)(dmae)]_2$ (**5**), selected bond lengths, bond angles and crystal parameters are listed in Table 4.9 and 4.10 respectively.

Table 4.9: X-ray crystal and structure refinement data for [Sn (dmae) (OAc)]$_2$ (**5**)

Empirical Formula	C_{12} H_{26} N_2 O_6 Sn_2	**Limiting indices**	-19<=h<=19, -7<=k<=7, -24<=l<=24
Formula weight	531.73	**Reflections collected / unique**	15567 / 3889 [R(int) = 0.0266]
Temperature	100(2) K	**Completeness to theta = 26.50**	100.0 %
Crystal system, space group	Orthorhombic, *Pna2(1)*	**Max. and min. transmission**	0.9003 and 0.3474
Unit cell dimensions	α = 15.6753(4) Å alpha = 90°. β = 6.1527(2) Å beta = 90° γ = 19.5022(6) Å gamma = 90°	**Refinement method**	Full-matrix least-squares on F^2
Volume	1880.90(10) $Å^3$	**Data / restraints / parameters**	3889 / 1 / 205
Z, Calculated density	4, 1.878 Mg/m^3	**Goodness-of-fit on F^2**	1.040
Absorption coefficient	2.681 mm^{-1}	**Final R indices [I>2sigma(I)]**	R1 = 0.0137, wR2 = 0.0327
F(000)	1040	**R indices (all data)**	R1 = 0.0140, wR2 = 0.0329
Crystal size	0.50 x 0.04 x 0.04 mm	**Absolute structure parameter**	10(10)
Theta range for data collection	2.09 to 26.50 deg.	**Gest diff. peak and hole**	0.605 and -0.255 e.$Å^{-3}$

Table 4.10: Bond lengths [Å] and angles [o] for complex [Sn(oAc)(dmae)]$_2$ (**5**)

Sn1-O1	2.1190(17**)**	O6-C11	1.225(3)
Sn1-O2	2.1530(17)	O1-Sn1-O2	89.13(7)
Sn1-O4	2.2339(16)	O1-Sn1-O4	68.52(6)
Sn2-O1	2.2282(17)	O2-Sn1-O4	85.28(6)
Sn2-O4	2.1179(17)	O1-Sn1-N1	72.41(7)
Sn2-O5	2.1482(18)	O2-Sn1-N1	80.21(7)
Sn1-N1	2.497(2)	O4-Sn1-N1	138.35(7)
Sn2-N2	2.513(2)	O4-Sn2-O5	89.82(7)
O1-C1	1.419(3)	O4-Sn2-O1	68.64(6)
O2-C5	1.297(3)	O5-Sn2-O1	85.28(7)
O3-C5	1.227(3)	O4-Sn2-N2	72.47(7)
O4-C7	1.415(3)	O5-Sn2-N2	79.71(6)
O5-C11	1.302(3)	O1-Sn2-N2	138.17(6)

The molecular structure (Figure 4.49) indicates that the centre of inversion lies at the centre of a Sn2O2 four-membered ring. Each tin(II) atom adopts a distorted trigonal bipyramidal geometry with the lone pair of electrons situated at the equatorial position. The stronger interactions between the lone pair of electrons and the bonding pairs of electrons push the other two bonding pairs at the equatorial positions towards the axial positions, thus giving rise to a distorted trigonal pyramidal geometry at the two tin sites as can be evidenced from the axial N2-Sn2-O1 and N1-Sn1-O4 bond angles of 138.17(6)^{o} and 138.35(7)^{o}, respectively.

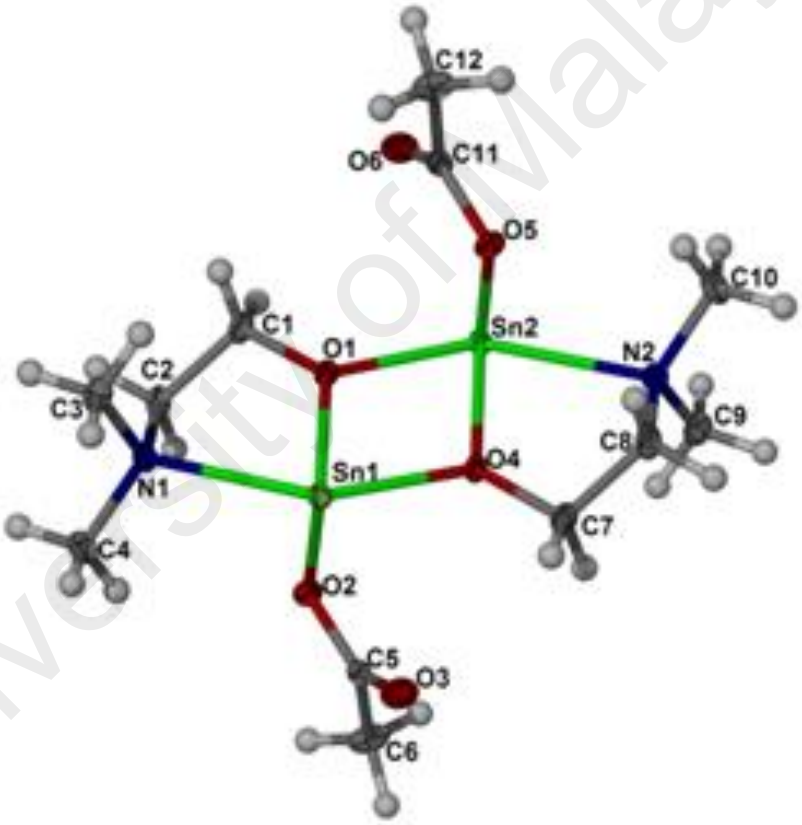

Figure 4.49: The Ortep plot of complex [Sn (OAc)(dmae)]$_2$ (**5**) showing 30% probability displacement ellipsoids and the atom numbering. Hydrogen atoms are drawn as spheres of arbitrary radii.

The two covalent Sn-O bond distances are at Sn1-O1 and Sn2-O4 are 2.119(2) and 2.118(2) Å respectively while the other two bridging oxygen coordinate bonds, Sn1-O4 and Sn2-O1 bond distances are longer at, 2.339(2) and 2.282(2) Å respectively, to form

a four-membered Sn_2O_2 ring. The terminal Sn-O bonds are somewhat longer than the bridging Sn-O bonds. The Sn1-N1 and Sn2-N2 bond distances are 2.497(2) and 2.513(2) Å, respectively. The four membered Sn_2O_2 ring is planar (RMS deviation from planarity = 0.0294Å) whereas the chelate rings formed by Sn1 O1 C1 C2 N1 and Sn2 O4 C7 C8 N2 are puckered with RMS deviation from planarity of 0.1814 and 0.1856Å, respectively. These two chelate rings make an angle of 22.40(8)^o and 19.99(9)^o, respectively with the four-membered ring. The long separation of 3.5922(2) Å between the two tin atoms in the dimeric unit shows that there is no significant bond interaction between the two tin atoms. The marked difference in the C-O bond distances of the 153arboxylate group (O6-C11= 1.225(3), O5-C11= 1.302(3) Å and O2-C5= 1.297(3), O3-C5 = 1.227(3) Å) indicates that there is no intramolecular interaction between the carbonyl oxygen of the carboxylate and the tin atom.

4.5.2 Thermogravimetric Analysis of Complex $[Sn(dmae)(OAc)]_2$ (5)

The thermal decomposition pattern of complex (**5**) was examined by thermogravimetric/derivative thermogravimetric (TG/DTG) analysis, performed under a flow of N_2 (25 mL/min) at a heating rate of 10 ^{o}C/min. The (TG/DTG) (Figure 4.50) shows two stages of weight loss. The first minor weight loss of 5.33 % regime exists at 177 ^{o}C. Immediately after the first weight loss, the second major pyrolysis step begins at 178^{o}C and is completed at 258.19 ^{o}C to yield 51.46 % of the solid residue. This decomposition step involves a total weight loss of 48.54 %. The weight of the residue agrees very well with the theoretically expected yield (51.15 %) of tin(IV) oxide from the precursor (**5**). Further heating of the residue to 900 ^{o}C did not bring any change in weight indicating complete decomposition of precursor 1 to furnish a residual mass of SnO_2 as expected from the complete decomposition of $[Sn(OAc)(dmae)]_2$. The FTIR study of the residue obtained from TG studies showed strong absorption at 588.6 cm^{-1} that agrees well

with the reported value for SnO_2 (Hollingsworth, et al., 2006; M. Veith, et al., 2004; B.-H. Ye, et al., 2002). Further no C-H vibrations were recorded indicating absence of any carbonaceous impurity in the residue. The residual mass of 51.47 % observe at 258 ˚C indicates the formation of expected SnO_2 oxide material from complex (**5**) as shown in following equation.

Chemical equation 10:

$$[Sn(dmae)(OAc)] \xrightarrow{260^{o}C} SnO_2 + Volatiles$$

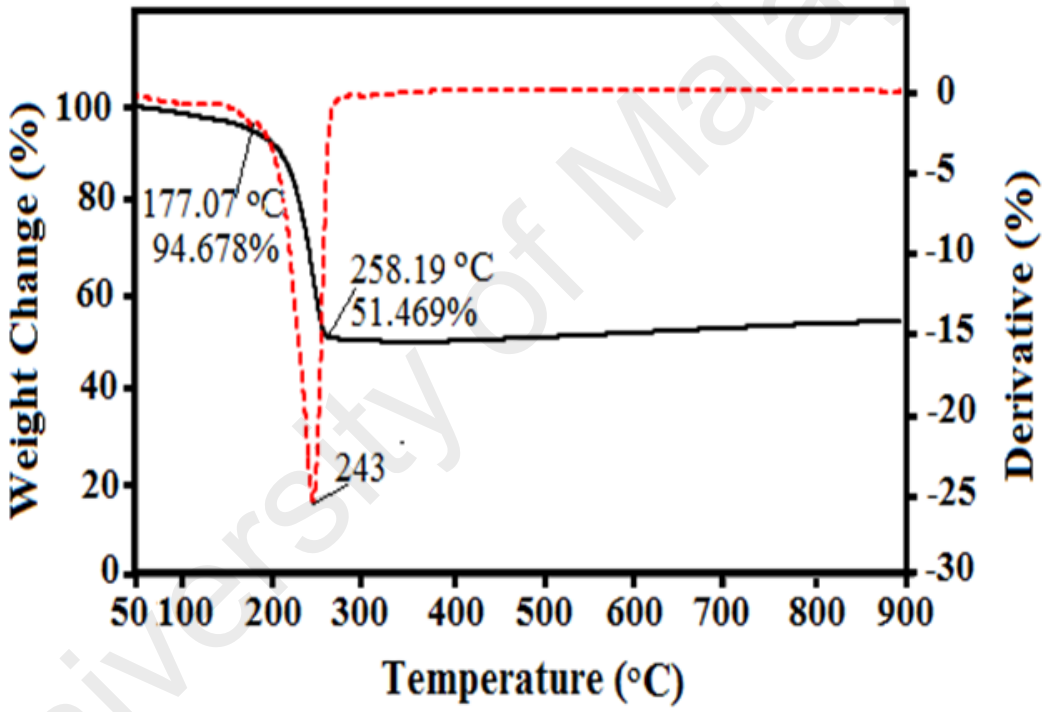

Figure 4.50: The TG and DTG plots of precursor (**5**) recorded under an inert atmosphere of nitrogen gas with constant flow of 25cm^3/min and heating rate of 20 ^{o}C/min.

4.5.3 XRD Analysis of SnO_2

The XRD pattern displayed in Figure 4.51 confirms the formation of crystalline SnO_2 mesoporous micro balls. The weak diffraction peaks at 2θ values of 26.7^{o}, 34.0^{o}, 38.2^{o}, 52.1^{o}, 54.6^{o} and 65.0^{o} are associated with (110), (101), (200), (211), (220) and (301) planes and are in complete match with the literature values reported in (JCPDPS card no.

41-1445) for tetragonal structure (Patil GE, Kajale DD, Gaikwad VB, & GH, 2012; Z. Wang, Luan, Boey, & Lou, 2011). Further sintering of the sample at 500 ^{o}C for two hours did not bring any change in the XRD pattern indicating ability of the micro balls to retain their morphology and structure at high temperature. The FTIR of the micro balls showed only one stretching absorption band at 588.67 cm^{-1} due to Sn-O vibration confirming carbonaceous impurity-free SnO_2.

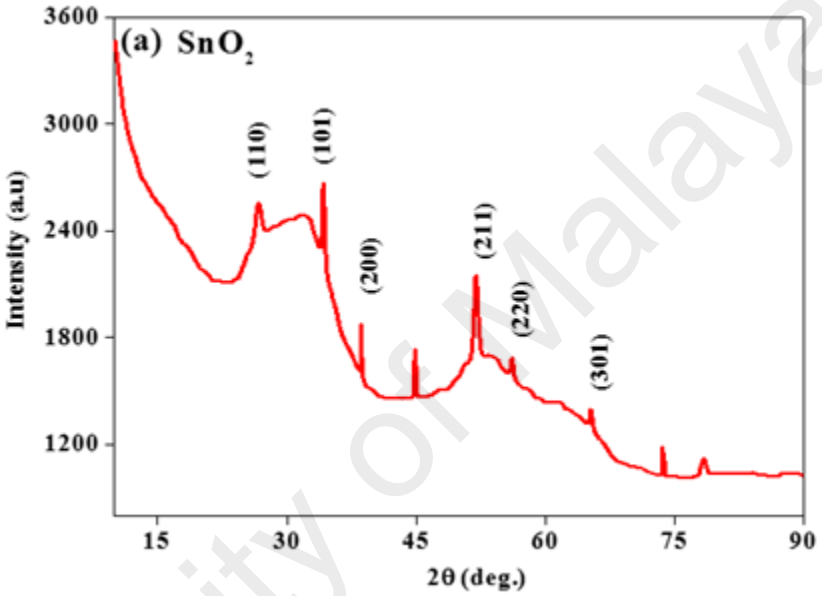

Figure 4.51: The XRPD pattern of the SnO_2 micro balls thin film on plain glass substrate deposited from a toluene solution of precursor (**5**) and sintered at 450 ^{o}C for 6 hours in air atmosphere

4.5.4 XPS Analysis of SnO_2

The XPS is appreciated technique to study the surface and sub surface chemical states of the prepared samples as the binding energy values of core levels are, to a certain extent dependent on the molecular environment. The 3d core of Sn splits in to 3d 5/2 (486.6 eV) and 3d 3/2 (495.0 eV) which are consistent with the reported values of 486.4(3d5/2) and 494.8 eV (3d3/2) for SnO_2 as shown in Figure 4.52(a). Also the binding energies found for O 1s core level from Si oxide (532.8eV) is clearly distinguishable from O1s of Sn oxide (530.7 eV) and are in good agreement with the previously reported values. The XPS data clearly shows the micro balls consist of only SnO_2.

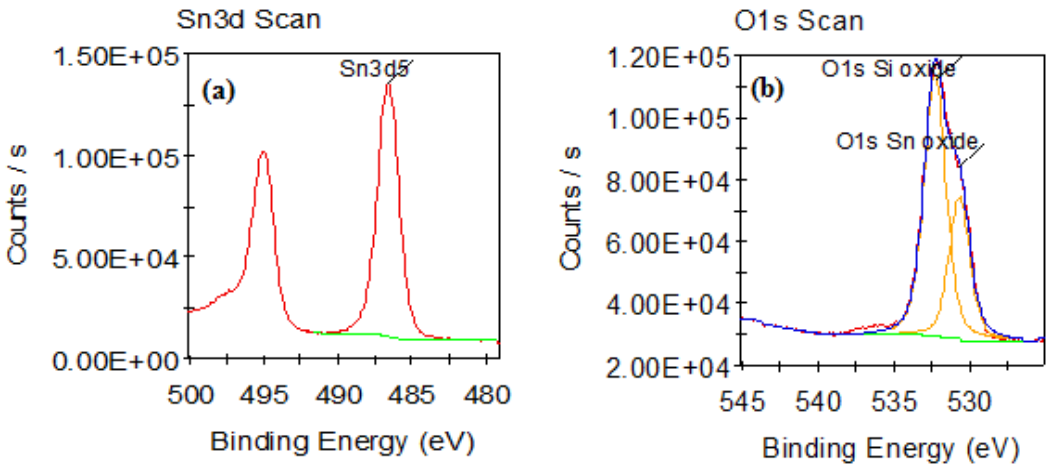

Figure 4.52: The XPS spectra of SnO_2 micro ball thin films deposited on glass substrate **(a)** Sn 3d **(b)** O 1s.

4.5.5 Surface Morphology of SnO_2

The FESEM results indicate that the aerosol generated from toluene solution of Sn (IV) precursor and deposited onto plain and FTO coated glass substrates under the influence of electric fields and then annealed at 450 ^oC for 6 hours, led to the growth of amorphous mesoporous SnO_2 micro balls (Figures 4.53b) of uniform lateral dimensions in the range of 195-632 nm. The exterior porosity is visible in the form of small holes with pore sizes from 56-66 nm in Figure 4.53c. The interior surface of the particles seems to be rough, having pores of various sizes ranging from 8-160 nm as revealed by FESEM image of the milled balls by Focussed Ion Beam (FIB) at an ion acceleration of 30 keV with a milling and cleaning cross section current of 2 nA and 10 pA, respectively Figure 4.53d.The deposited films, as observed from the outer surface are highly homogenous and possess smooth features. The FESEM image of the films deposited by AACVD, without application of an electric field, on FTO substrate show formation of non-porous smooth surface micro balls as shown in (Appendix 7). When aerosol generated particles experience an electric field, these charged particles move in certain orientations. When deposited on the substrate certain orientations make the material porous as observed in Figure 4.53. While for AACVD without an electric field did not experience these

orientations show smooth spherical morphology. Further the EDAX analysis (Appendix 8) confirmed that only tin and oxygen are present in the nanoball thin films.

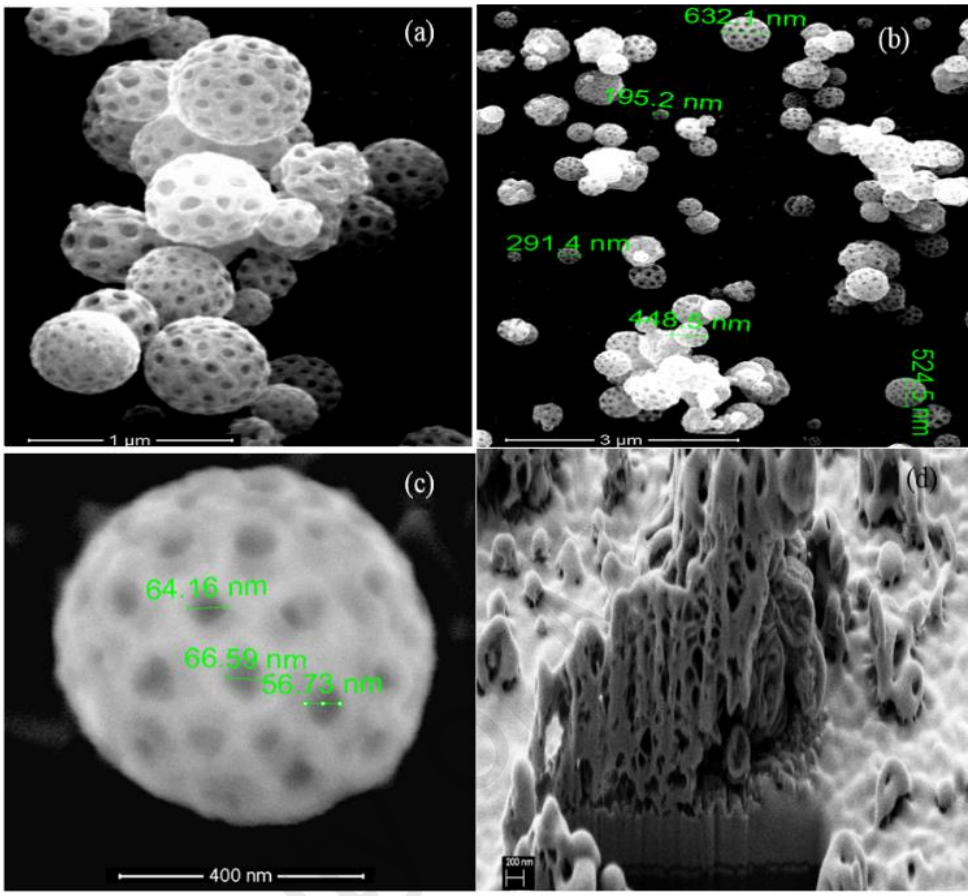

Figure 4.53: Illustrate SEM images of SnO_2 micro balls thin films deposited on FTO glass substrates and (a) agglomerization of micro balls , (b) lateral dimensions, (c) pores of the exterior and (d) the interior surfaces of the micro balls.

4.5.6 Optical Band gap of SnO_2

The optical absorption spectrum of SnO_2 micro-ball thin films deposited at 400^oC using toluene and having a thickness of 310 nm was recorded on a Lambda 35 Perkin-Elmer UV-Vis spectrophotometer in the wavelength range of 310-710 nm using FTO. The UV-Vis spectrum of SnO_2 micro ball thin films shows an absorption edge at 360 nm and the band gap was calculated by plotting Tauc plot of energy versus $(\alpha h\upsilon)^2$ to give a value of 3.8eV (Figure 4.54).

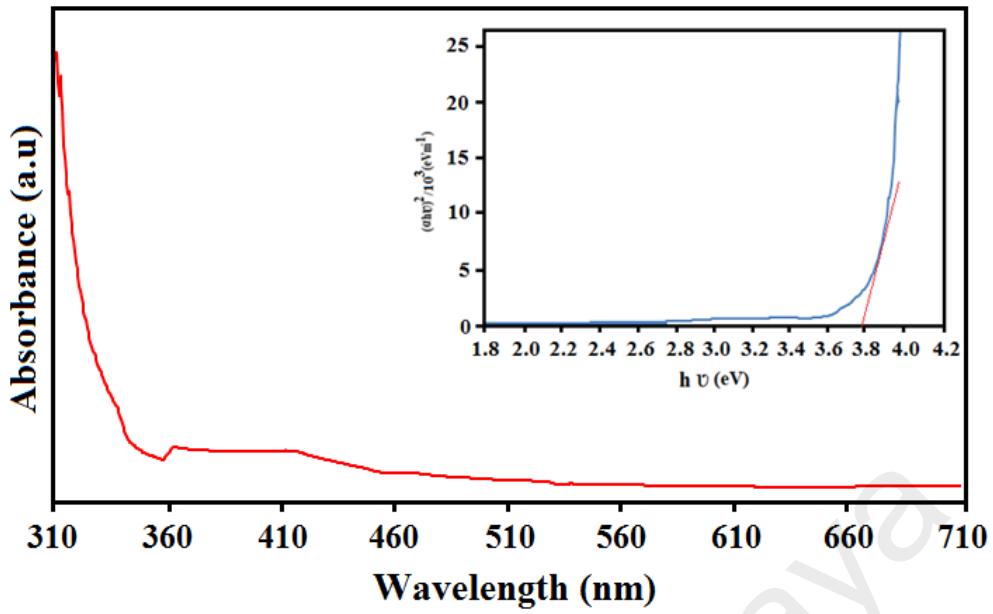

Figure 4.54: UV-Vis absorption spectrum of wavelength versus absorption and inset Tauc plot of energy versus $(\alpha h\upsilon)^2$ of SnO_2 microball thin films deposited from precursor using EFDAACVD showing a sharp absorption edge at 360 nm.

4.5.7 BET Analysis of SnO_2

The surface area of 136m^2/g and 191.6m^2/g of the tin oxide micro balls powder scratched from FTO substrate deposited by EFDAACVD was estimated by Brunauer-Emmett-Teller (BET) and Langmuir methods, respectively. The adsorption-desorption isotherm was shown in Figure 4.55a indicating hysteric loop characteristic of mesoporous materials. The pore volume and pore size determined by Barret-Joyner-Halenda (BJH) adsorption-desorption method is about 0.05 ml/g and 45A^o respectively Figure 4.55b. The high surface area is due to high porosity in the interior and exterior surfaces and is about two and a half times more than the previously reported values for SnO_2.

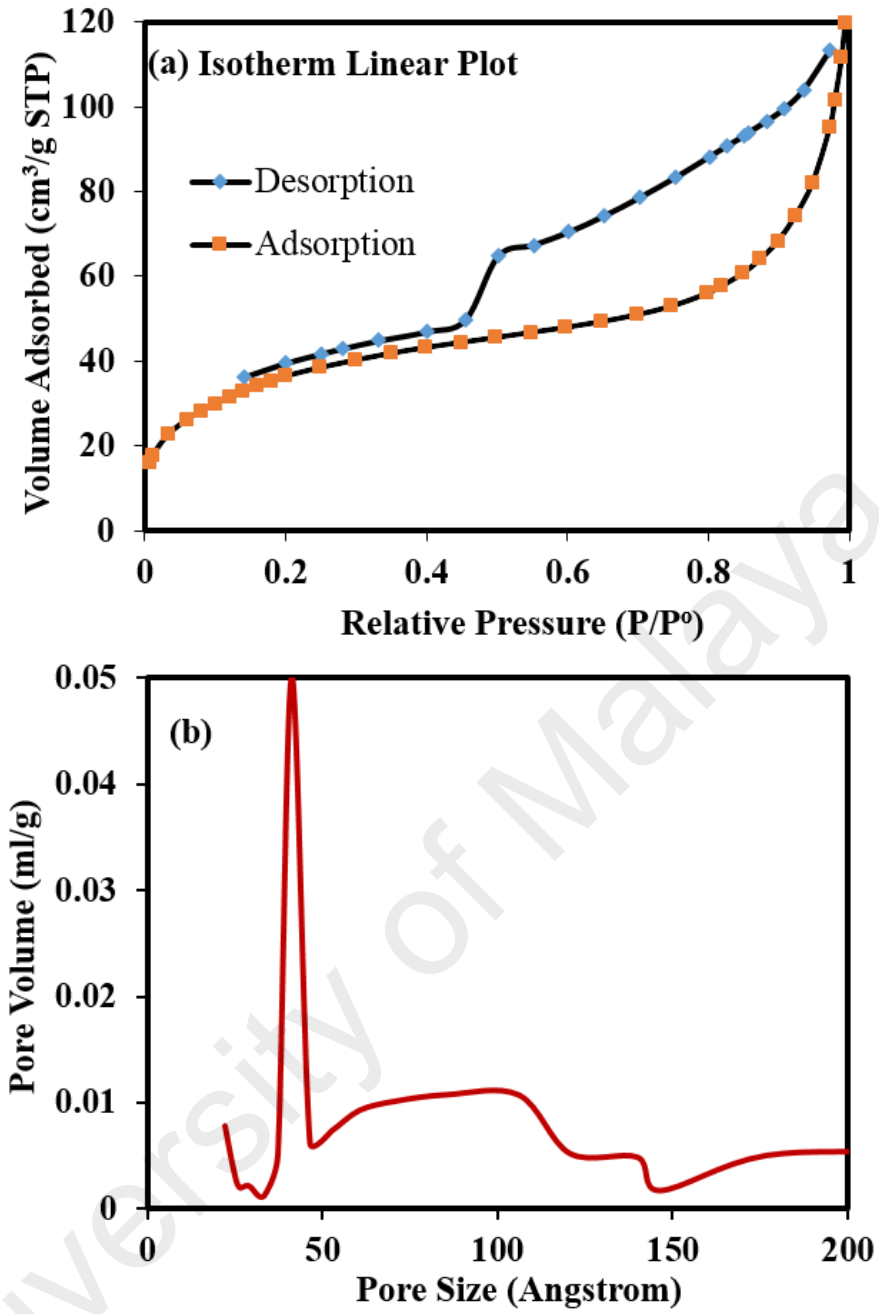

Figure 4.55: (a) Nitrogen adsorption-desorption isotherm and **(b)** BJH pore size distribution for mesoporous SnO_2 micro balls.

4.5.8 Electrochemical Studies of SnO_2

Electrochemical impedance measurements of the SnO_2 microball coated FTO electrodes were conducted in a three electrode electrochemical cell in order to determine the resistance of the electrode/electrolyte interface. The resistance of the electrode/electrolyte interface can be determined from the high frequency x-axis intercept from the Nyquist

plot, shown in Figure 4.56. The resistance was found to be 80 Ω which indicates that the SnO_2 microballs have suitable conductivity for application in batteries.

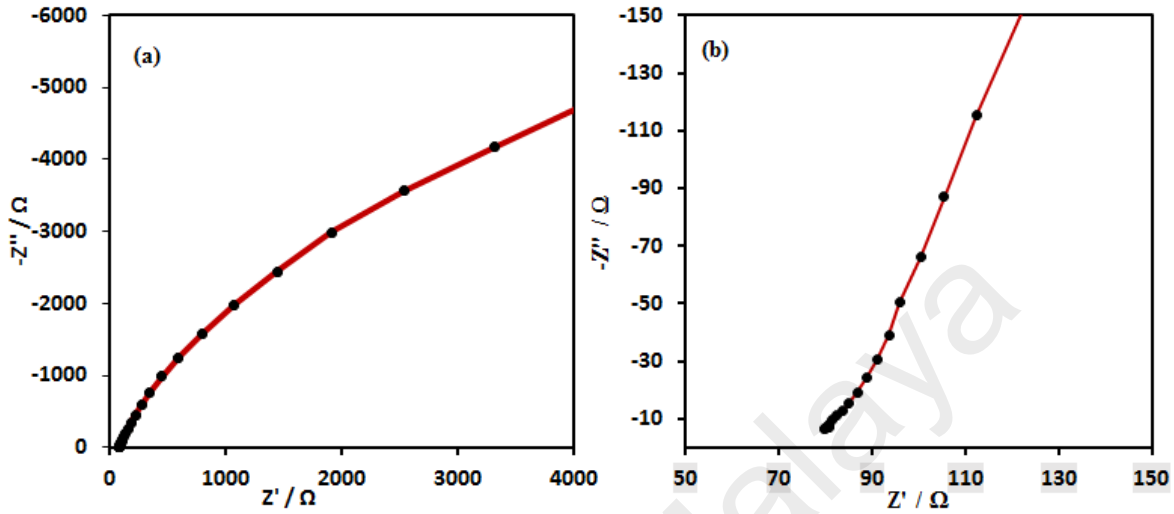

Figure 4.56: Impedance measurement **(a)** Nyquist Plot of the SnO_2 microball electrode conducted in a 3-electrode electrochemical cell, using an Ag/AgCl reference electrode and a Pt counter electrode in a 1 M LiPF6-EC:DMC (1:2 by volume) electrolyte at open circuit potential. **(b)** Expanded plot of showing the high frequency region of the Nyquist plot.

Tin (Sn)-based and tin oxide (SnO_2)-based anodes in **Li-ion batteries** typically show enhanced performance and improved cycle life only when incorporated with nanoscale or composite particles. The reaction mechanism of SnO_2 with lithium has been proposed to take place as indicated in the following two steps:

$$SnO_2 + 4Li^+ + 4e^- \rightarrow Sn + 2Li_2O \qquad (4.1)$$

$$Sn + xLi^+ + 4e^- \rightarrow Li_xSn\,(0 \leq x \leq 4.4) \qquad (4.2)$$

In the first reaction, SnO_2 is reduced to metallic Sn, which is partially irreversible. The second reaction is the Sn alloying/de-alloying reaction with lithium, which is usually reversible in most cases.

However, SnO_2 nanowires covered with Sn nanoclusters have exhibited an exceptional capacity of > 800 $mAhg^{-1}$ over hundred cycles. The reaction of SnO_2 with Li ions,

electrolyte decomposition, and solid electrolyte interface formation are believed to be some of the reasons for large irreversible capacity during the first cycle. This involves an additional step of formation of SnO which subsequently reduces to Sn.

$$SnO_2 + 2Li^+ \rightarrow SnO + Li_2O \qquad (4.3)$$

$$SnO + 2Li^+ + 2e^- \rightarrow Sn + Li_2O \qquad (4.4)$$

$$Sn + xLi^+ + xe^- \rightarrow Li_xSn\,(0 \leq x \leq 4.4) \qquad (4.5)$$

In addition to the pulverization of SnO_2 particles due to large volume expansion during cycling, agglomeration of the primary particle can drastically reduce the surface-to-volume ratio causing diminishing of the electrochemical activity. Several strategies have been utilized to mitigate the pulverization and particle agglomeration. In the past decade, great efforts have been devoted to synthesizing SnO_2 nanostructures with varying morphologies. Nanocrystalline SnO_2 with various crystallite sizes (Z. Wang, et al., 2011), SnO_2 nanomaterials with a hollow structures (Lou, Wang, Yuan, Lee, & Archer, 2006) uniform SnO_2 nanoboxes have been synthesized and tested for the anode material in Li-ion batteries.

Recent studies have shown that even 1-d SnO_2 nanostructures show low capacities ranging from 300 to ~ 620 mAhg-1 after 50 cycles (D.-W. Kim et al., 2007). SnO_2 nanowires and hetero-structured SnO_2/In_2O_3 nanowires retain a capacity of ~700 mAhg-1 up to 15 cycles, but quickly fade to ~ 300 mAhg-1 after 50 cycles. Similarly, SnO_2 nanorods have been shown to retain a capacity of only ~400 mAhg-1 after 60 cycles (Yong Wang & Lee, 2004).

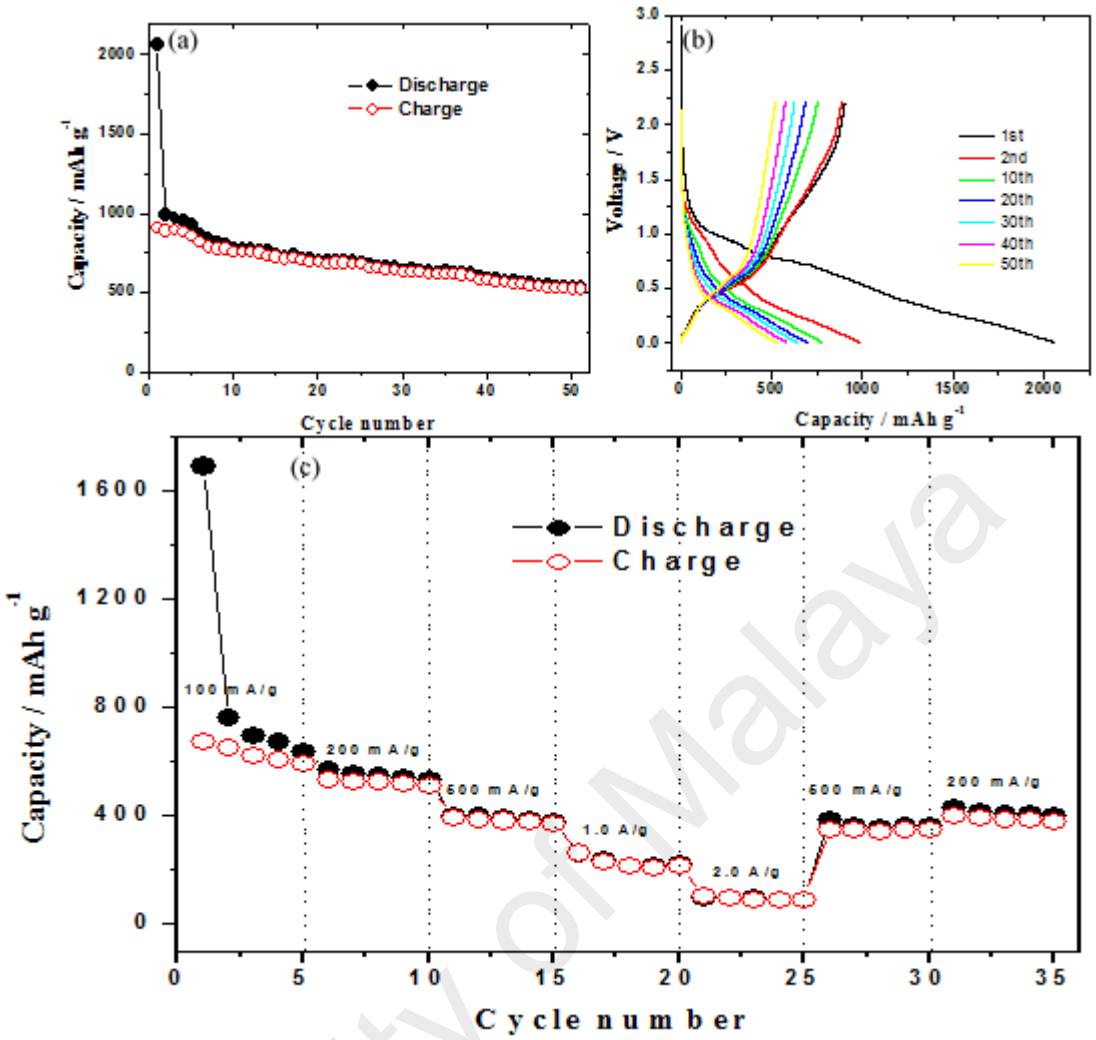

Figure 4.57: (a) Charge-discharge curves of SnO_2 micro ball electrode measured in coin cell configuration in the voltage range of 2.2-0.005 V with a current of 100 mA/g. **(b)** Charge-discharge capacities vs. cycle number of SnO_2 electrode SnO_2 micro ball electrode measured in coin cell configuration in the voltage range of 2.2-0.005 V with a current of 100 mA/g. (c) Charge-discharge capacities vs. cycle number of SnO_2 micro ball electrode in the voltage range of 2.2 V-0.005V at varying current densities of 100, 200, 500 mA/g, 1.0A/g, and 2.0 A/g.

Therefore, the significantly enhanced performance of stand-alone SnO_2 micro-ball nanostructures without incorporating any supporting materials/strategies to increase the stability with high capacity retention is a useful information for the community who work in the energy storage area.

The charge-discharge curves of SnO_2 micro ball anode electrodes at the voltage range of 2.2-0.005 V using a current density of 100 mA/g are shown in Figure 4.57a. It has an

initial large discharge capacity of 2066 mAh g^{-1} during the first cycle. The high initial discharge capacity is believed to be due to the reduction of tin oxide to tin and the intercalation of Li into SnO_2. The initial capacity loss is mainly due to the solid-electrolyte-interface formation and the reduction of SnO_2 to Sn. During subsequent charge-discharge processes, SnO_2 micro ball anode shows the discharge capacities of 997, 788, 704, 649, 593, 542 $mAhg^{-1}$ after 2^{nd}, 10^{th}, 20^{th}, 30^{th}, 40^{th} and 50^{th} cycles, respectively.

Figure 4.57b summarizes the charge-discharge capacities vs. cycle number of SnO_2 micro ball electrode in the voltage range of 2.2-0.005 V with a current of 100 mAg^{-1}. The initial discharge capacity of 2066 mAh g^{-1} during the first cycle is seen to fade away, but remains over 540 mAh g^{-1} after 50 cycles.

Figure 4.57c shows the rate capability of SnO_2 micro ball electrodes at varying current densities of 100, 200, 500, 1000, and 2000 mAh g^{-1}. The discharge capacity decreased with increasing current density as expected. The initial discharge capacity of the SnO_2 micro ball electrodes at current density of 100 mAg^{-1} remains 1691 $mAhg^{-1}$ and at 200, 500, 1000 and 2000 mA g^{-1} current densities it shows an initial discharge capacities of 569, 399, 258, and 100 $mAhg^{-1}$, respectively. When the current density is reduced to 500 and 200 mAg^{-1} after the initial rate performance testing, the SnO_2 micro balls can still provide discharge capacity close to formerly measured value of 382, and 430 $mAhg^{-1}$, indicating its good reversibility and high rate capability. The reversibility, high rate capacity and relative stability shown by SnO_2 micro-ball based anodic materials appeared to be strongly related to the specific morphology and texture of the materials we prepared and used in our study. Further work is currently underway to understand this phenomena.

4.6 Deposition of Mn_2O_3, Fe_2O_3, CuO, NiO, ZnO, CdO and PbO Thin Film by EFDAACVD Method

Metal carboxylates because of their distinct characteristics of high volatility, solubility, stability and suitable decomposition temperature during transport in gas phase make them favorable CVD precursor for the deposition of thin layers of metal oxides for photoelectrochemical applications. The different coordination modes of the carboxylate ligands force the metal into strict molecular regime that improves their potential to perform as CVD precursor. Metal oxide center enclosed by organic environment making the precursor soluble in suitable organic solvents like toluene, THF, methanol, ethanol and acetonitrile etc. We therefore selected carboxylates of Manganese, Iron, Copper, Nickle, zinc, cadmium and lead for the fabrication of thin films of Mn_2O_3, Fe_2O_3, CuO, NiO, ZnO, CdO and PbO and by using unique EFDAACVD method. The motive behind use EFDAACVD was to obtain films of well-defined uniform morphology, stoichiometry and structure that is reproducible in a single step with the instantaneous reduction in CVD parameters. The thin films produced by EFDAACVD were analyzed by XRD, XPS, Raman scattering, Uv-visible spectroscopy, FESEM and EDX and investigated for their photo electrochemical behavior.

4.6.1 XRD Analysis of Mn_2O_3, Fe_2O_3, CuO, NiO, ZnO, CdO and PbO Thin Films

Figure 4.58 shows the XRD patterns of Mn_2O_3, α-Fe_2O_3, NiO, CuO, ZnO, CdO and PbO thin films fabricated on the FTO by the EFDAACVD technique. The peaks indexed by the symbol (♦) correspond to the SnO_2 in the FTO substrate (A. Chen et al., 2009; Klahr, Martinson, & Hamann, 2010; Mansoor, Mazhar, McKee, & Arifin, 2014; Sialvi et al., 2013; A. A. Tahir, Mazhar, Hamid, Zeller, & Hunter, 2009; A. A. Tahir, Wijayantha, Saremi-Yarahmadi, Mazhar, & McKee, 2009). The XRD pattern of cubic Mn_2O_3 with (211), (400) and (622) diffraction planes observed at 2θ values of 22.5°, 37.8° and 65.6°

respectively matched well with the JCPDS card No. 00-002-0896 (Dakhel, 2006). Figure 4.58 shows three strong peaks, namely, (012), (104) and (110), which are the reflections of α-Fe_2O_3 (hematite) as indicated in JCPDS card No. 86-0550 (A. A. Tahir, Wijayantha, et al., 2009). The X-ray diffraction data have been recorded for NiO thin films as shown in Figure 4.58 displaying distinct peaks at 2θ values of 37.1°, 43.1° and 62.6°. These peaks have been assigned to cubic NiO crystallites with various diffracting planes (111), (200) and (220) respectively revealing the formation of the NiO cubic phase (JCPDS card No. 47-1049) (Johan, Suan, Hawari, & Ching, 2011). The two broad peaks at 2θ values of 35.5° and 38.7° match the reflections from the (111) and (200) planes respectively, which is attributed to the structure of cubic CuO (JCPDS card No. 01–085–1326) (Necmi, Tülay, Şeyda, & Yasemin, 2005; M. Shahid, Mazhar, Tahir, Rauf, & Raftery, 2014). The XRD pattern of well-crystallized stoichiometric ZnO were observed at the 2θ values of 31.7°, 34.3°, 36.2°, 47.5°, 56.5° and 62.7° with *hkl* lattice planes (100), (002), (101), (102), (110) and (103) and are in good agreement with those given in the standard data (JCPDS: 98-002-6170) for hexagonal ZnO (Cheng, Zhao, Huo, Gao, & Zhao, 2004). For comparing observed peaks of CdO thin film the (JCPDS: 96-101-1004) card was referred.

The main peaks for (111), (200), (220), (311) and (222) reflections originated at the 2θ values of 33.1°, 38.5°, 55.3°, 66.5° and 69.4° which indicated the cubic phase of CdO (Maity & Chattopadhyay, 2006; R. S. Mane, Pathan, Lokhande, & Han, 2006). PbO thin film examined by XRD was identified by (JCPDS card No. 96-900-5762) for diffraction planes (111), (020), (200) and (111) at the 2θ values of 29.2°, 30.1°, 32.4° and 53.7° shows the tetragonal structure of PbO (Madsen & Weaver, 1998).

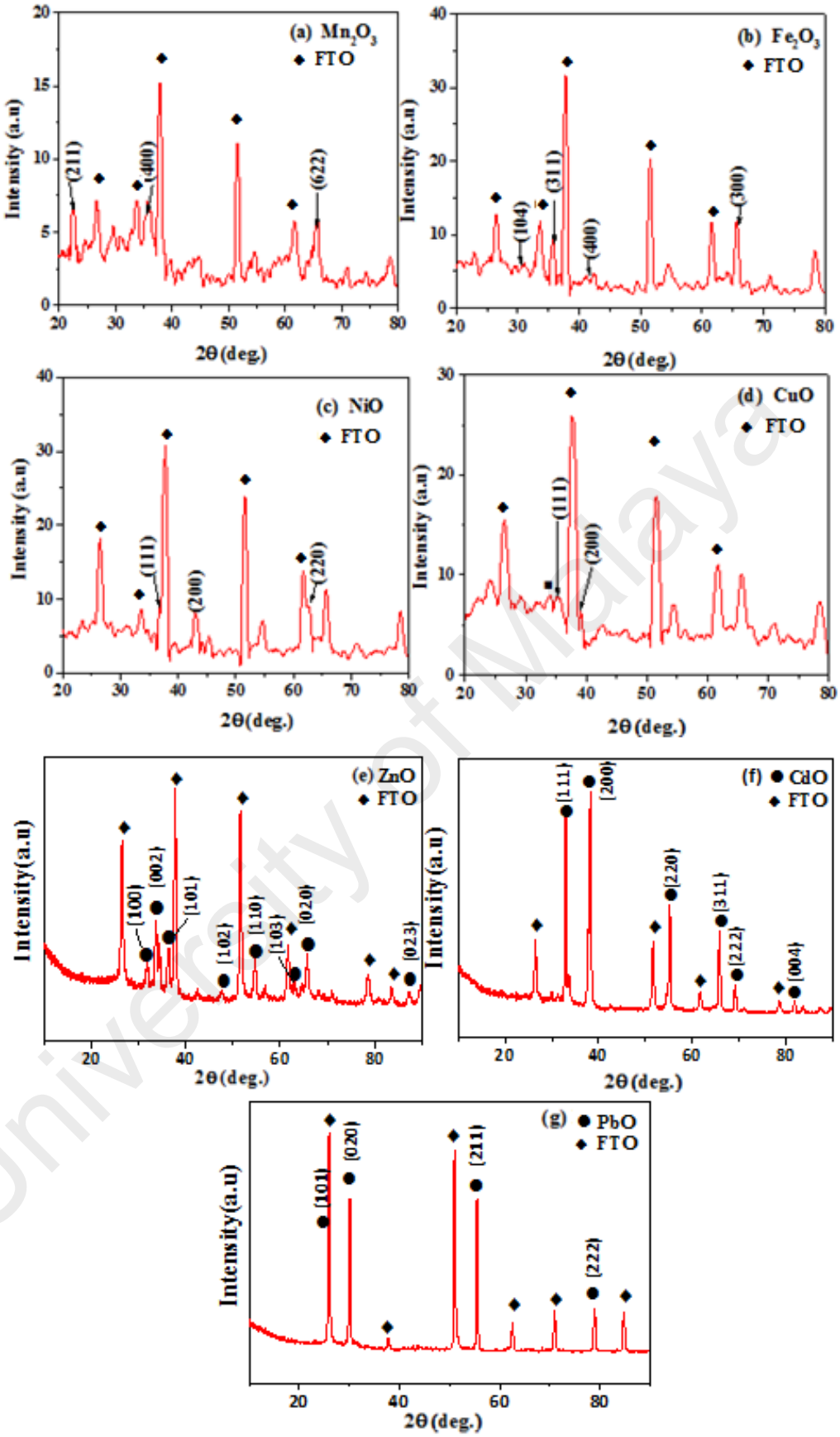

Figure 4.58: XRD pattern of EFDAACVD-deposited thin films of Mn_2O_3, α-Fe_2O_3, NiO, CuO, ZnO, CdO and PbO on an FTO glass substrate at 400 °C.

4.6.2 Raman Analysis of Mn_2O_3, Fe_2O_3, CuO, NiO, ZnO, CdO and PbO Thin Films

Raman scattering is a sensitive means to reveal the crystallinity and phase purity of a material. The Raman spectra of synthesized nanoballs of Mn_2O_3, α-Fe_2O_3, NiO and CuO recorded in the range of 200 to 1000 cm^{-1} as shown in Figure. 4.59 are indicated by a strong peak at 620 cm^{-1} with a left shoulder at 580 cm^{-1} which is associated with a symmetric Mn-O stretching vibration as reported earlier (Dokko, Mohamedi, Anzue, Itoh, & Uchida, 2002). Iron oxide exists in several forms such as magnetite (Fe_3O_4), hematite (α-Fe_2O_3), maghematite (γ-Fe_2O_3) and wustite (FeO). Raman spectroscopy can identify each of these forms better than any other tool. The Raman spectrum of iron oxide Figure 4.59 shows the entire three strong bands at 222, 288, 401 cm^{-1} and one peak of medium-strong intensity at 659 cm^{-1} as reported in the literature that are characteristic for α-Fe_2O_3. However, the Raman band for the magnetite (Fe_3O_4), maghematite (γ-Fe_2O_3) and wustite (FeO) also fall at 663 cm^{-1} (Bersani, Lottici, & Montenero, 1999). The possibility of the existence of FeO is excluded because of the absence of its characteristic peak at 655 cm^{-1} while the existence of maghematite is eliminated because its phase is formed only at temperatures above 400 ^oC. It can therefore be safely concluded that the thin film consists of mainly hematite (α-Fe_2O_3) with a minor impurity of magnetite. The Raman spectrum of NiO, Figure 4.59, shows a characteristic strong peak at 505 cm^{-1} with a shoulder at 407 cm^{-1} and a weak signal at 706 cm^{-1} (S.-H. Lee et al., 2001). It is reported in the literature that the Raman spectrum, Figure 4.58, of CuO has three Raman active modes at 297, 337 and 558 cm^{-1} (A. Chen, et al., 2009). All these modes of vibration have been identified in the spectrum and assigned to CuO with no extra peak due to Cu_2O found. Therefore, it can be inferred that CuO nanoball thin film is free from Cu_2O impurity.

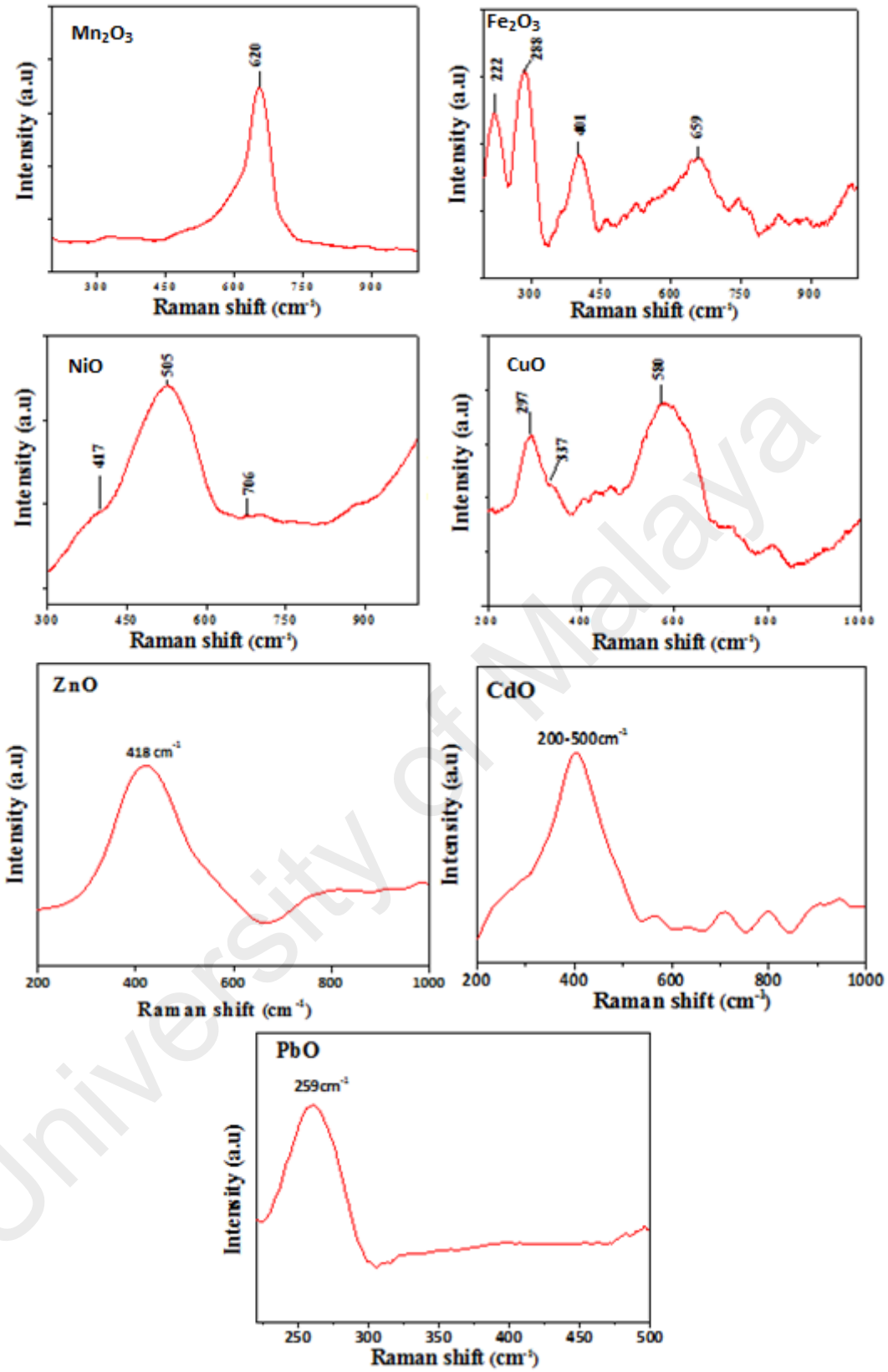

Figure 4.59: Raman spectra of EFDAACVD-deposited thin films of Mn_2O_3, α-Fe_2O_3, NiO and CuO, ZnO, CdO and PbO on FTO glass substrate at 400 ^oC in THF.

A broad band that corresponds to symmetry mode of ZnO is observed at ~418 cm^{-1}. The onset and offset of this peak are at 320 and 518 cm^{-1} respectively. Immediately after the offset a shoulder appears at 533 cm^{-1} which ends at 625 cm^{-1} (Saw, Ibrahim, Lim, & Chai, 2007; X. Q. Wei et al., 2007). The Raman spectra of CdO contain one broad intense feature spanning from 200 to 500 cm^{-1} and a weaker band located at ~960 cm^{-1}.The weak broad band at 561 and 960 cm^{-1} are in good agreement with the experimental values (Cuscó et al., 2010; S. Kumar, Ojha, & Singh, 2014). The Raman shift at 259cm^{-1} is attributed to the litharge modification of PbO. (Madsen & Weaver, 1998). It is concluded form the Raman spectrum Mn_2O_3, α-Fe_2O_3, NiO and CuO ZnO, CdO and PbO thin films deposited by EFDAACVD have hexagonal, cubic and litharge tetragonal structures respectively and agree very well with the XRD findings.

4.6.3 Surface Morphology of Mn_2O_3, Fe_2O_3, CuO, NiO, ZnO, CdO and PbO

The field emission scanning electron micrographs of metal oxide thin films at magnification 100,000 are presented in Figure 4.59.The surface morphology of the thin films deposited on FTO by EFDAACVD affects the surface morphology of the films as compared with AACVD (Warwick, Smith, Furlan, Crane, & Binions, 2010). The application of electric field is one of the key process parameters to control the morphology of the deposited film by chemical vapour deposition. The effect of electric field on the morphology of the films was studied by depositing films using air as a carrier gas at 400 °C substrate temperature. In the presence of an electric field, the morphology of the thin films showed particles caked as nanoballs onto the substrate surface. The smooth surface spherical shaped nanoballs of α-Fe_2O_3, NiO and CuO appeared on the FTO surface while the surface morphology of the Mn_2O_3 films turned into independent nanoballs sticking on the rough surface of the bulk. The precursor was assumed to be completely deposited on

the substrate in the presence of an electric field of 9.5 kV. The distance of needle from the substrate, deposition time, and strength of the electric field play an important part in the morphology control of metal oxides thin films. The Mn_2O_3 aggregated rough-surfaced nanoballs and the spherical shaped smooth-surfaced α-Fe_2O_3 nanoball thin films have average sizes ranging from 396 to 898 and 325 to 529 nm respectively. The NiO films by AACVD adopted a columnar structure with flower-like surface morphology (Mat-Teridi et al., 2014), while with EFDAACVD method nanoballs with average sizes of 273 to 471 nm were formed. The morphology of the thin films of CuO fabricated by simple AACVD gave densely packed globular aggregates (Barreca et al., 2009) with particle sizes of 600 to 800 nm while the film deposited in the presence of the electric field yielded nanoballs of CuO with sizes ranging from 195 to 401 nm. The architecture of thin films fabricated by EFDAACVD process is influenced by the deposition conditions such as presence of electric field, physical properties of solvent (boiling point, heat of combustion viscosity, specific heat capacity and coordination ability), as well as the growth temperature and nature of the substrate. When films were deposited in the presence of electric field using THF solution, different morphologies of ZnO, CdO and PbO were detected on FTO substrate by using argon as a carrier gas at 400 °C are presented in Figure 4.59. The center of the thin film of ZnO consists of urchin like structure surrounded by okra like particles. (Deng et al., 2004). While the CdO thin film consist of agglomerates of particle (R. S. Mane, et al., 2006) and PbO thin films have compact slate like morphology. All these observations indicate that the morphology and size of the thin films can be controlled by the application of an electric field of appropriate strength independent of the nature of the metal precursors.

The EDX analysis of large areas of Mn_2O_3, α-Fe_2O_3 , NiO, CuO, ZnO, CdO and PbO thin films confirms the presence of only Mn, Fe, Ni, Cu, Zn, Cd, Pb and O elements respectively and is shown in (Appendix 9). The tin and fluorine signals appear from the

FTO substrate. The EDX analysis recorded at randomly different places confirms the uniform distribution of all the components of the metal oxide in the respective thin films.

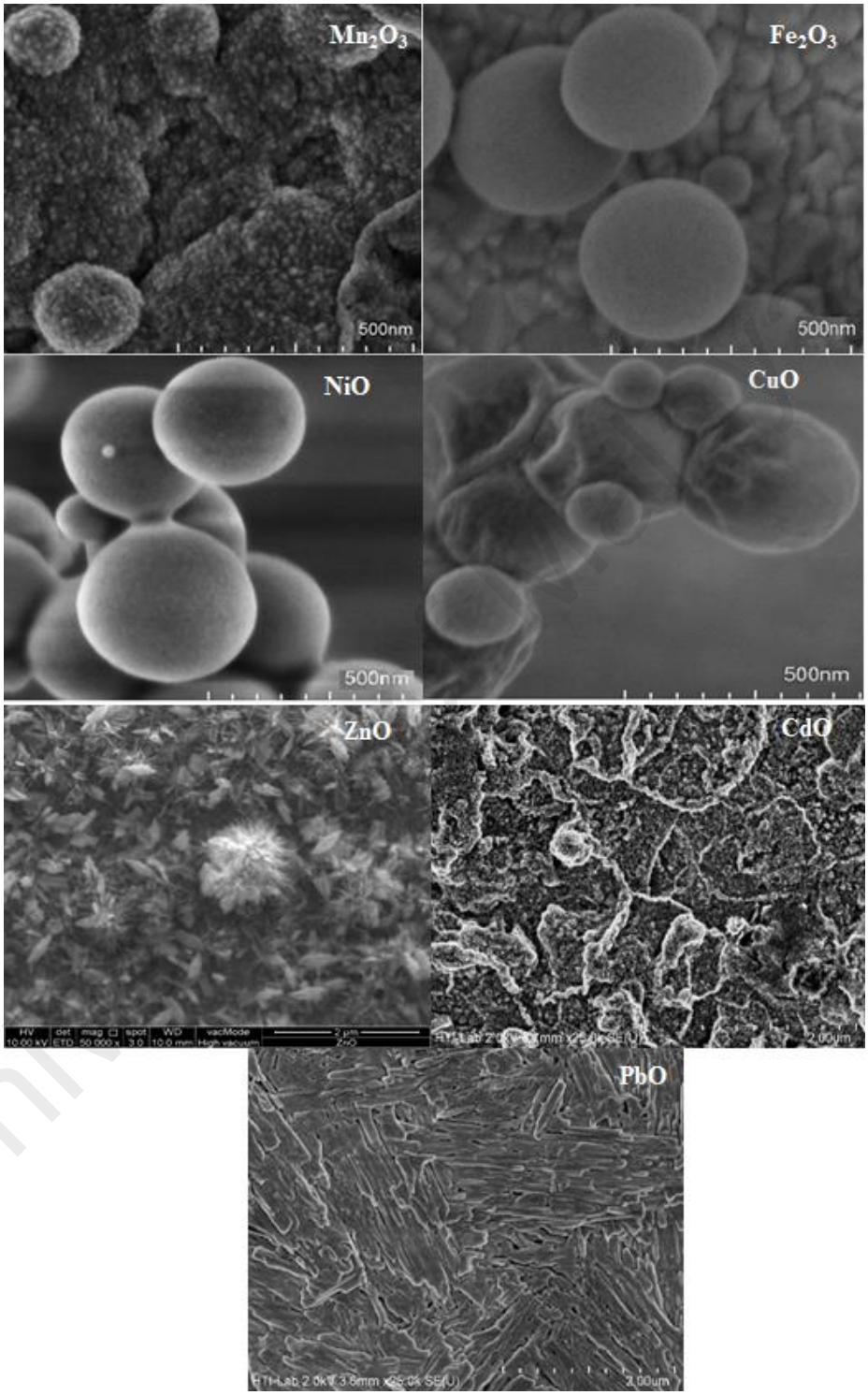

Figure 4.60: FESEM images of Mn_2O_3, α-Fe_2O_3, NiO, CuO, ZnO, CdO and PbO thin films deposited at 400 °C from THF solution of metal acetates on FTO glass substrates deposited by EFDAACVD.

4.6.4 Optical Studies of Mn_2O_3, Fe_2O_3, CuO, NiO, ZnO, CdO and PbO Thin Films

The optical absorption spectra of EFDAACVD-deposited thin films were recorded in the wavelength range of 300 − 900 nm using a similar FTO coated glass substrate as a reference to exclude substrate contribution in the spectrum. The UV−visible spectra of the Mn_2O_3, α-Fe_2O_3 , NiO, CuO, ZnO, CdO and PbO nanoball thin films were used to calculate the band gaps by means of Tauc's plot of $(\alpha h\nu)^2$ versus energy, Tauc's plot (Dolgonos, Mason, & Poeppelmeier, 2016) method by using the following equation given below.

$$\alpha = A(h\nu - E_g)^{1/2}/h\nu$$

where α, E_g, and A are the absorption coefficient, band-gap energy and a constant, respectively. Figure 4.61, to give the values of 1.2, 2.2, 1.9 and 0.9 eV respectively for the direct band gaps. The band gap values for Mn_2O_3 and α-Fe_2O_3 are in good agreement with the corresponding values of 1.2 and 2.2 eV (Mansoor, et al., 2014a; A. A. Tahir, Wijayantha, et al., 2009), while the band gap values for NiO and CuO films showed lower band gap energies of 1.9 and 0.9 eV respectively as compared to the reported values of 3.2 and 1.7 eV (Mat-Teridi, et al., 2014; Johan, et al., 2011). This lower band gap energy may be due to absorption involving defect states. 3.1, 2.2 and 1.8 eV were obtained by extrapolation of the linear region in the plots of $(\alpha h\nu)^2$ versus *E/eV* for the ZnO, CdO and PbO thin films respectively as depicted in Figure 4.61. The band gap energy values for all the three oxides are in good agreement with the reported values of 3.2, 2.3 and 1.9 eV for ZnO, CdO and PbO respectively (Aly, Kaid, & El-Sayed, 2013; Carballeda-Galicia et al., 2000; Ilician*, Caglar, & Caglar, 2008).

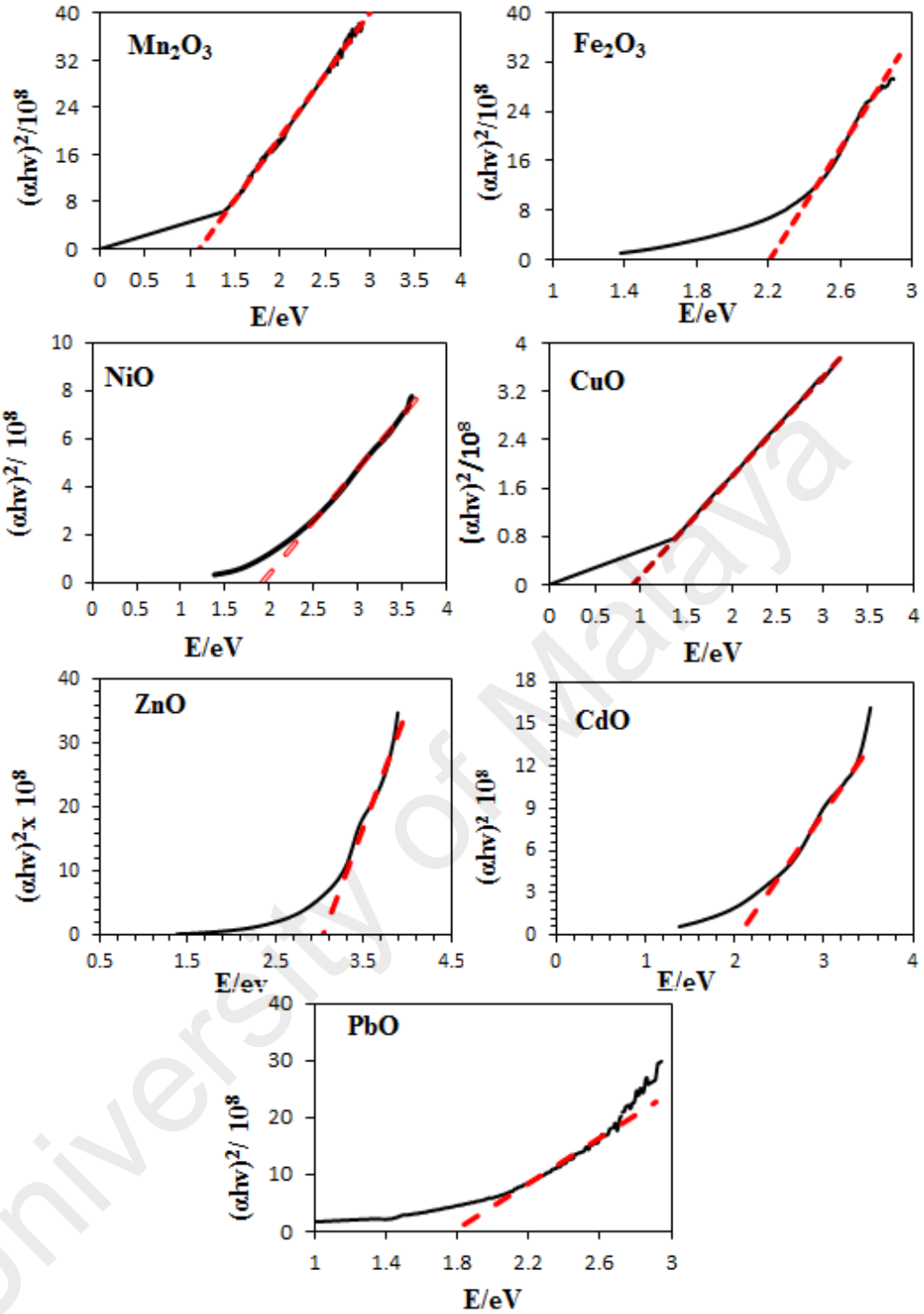

Figure 4.61: UV-vis spectrum shows Tauc's plot of energy versus $(\alpha h\upsilon)^2$ for Mn_2O_3, α-Fe_2O_3, NiO, CuO, ZnO, CdO and PbO thin films deposited at 400 °C from THF solution of metal acetates on FTO glass substrates by EFDAACVD.

This scatter in reported values may be attributed to two factors. First, the optical properties depend critically on the physical properties of the films, which are subsequently affected by the deposition and post-deposition conditions. Secondly, different models have been used to extract the optical properties from measured quantities. For example, α, α^2, $(\alpha E)^2$,

$(\alpha E)^{2/3}$, and $(\alpha E)^{1/2}$ were all plotted against the photon energy to determine the band gap. This not only affects the value of the band gap but also affects the interpretation of the nature of the gap i.e. direct or indirect.

4.6.5 Photoelectrochemical Studies of Metal Oxide Thin Films

The photoelectrochemical behavior of the EFDAACVD-produced metal oxide (Mn_2O_3, α-Fe_2O_3, NiO and CuO) thin films were investigated for water oxidation using linear sweep voltammetry (LSV) technique under simulated solar AM 1.5G irradiation in the presence of 0.1 M Na_2SO_4 at a scan rate of 50 mV/s. Under applied bias, the metal oxide thin films undergo photo-induced charge separation thereby promoting the valence band electrons to the conduction band resulting in the formation of holes at the valence band. The holes produced at the valence band can be readily scavenged through water oxidation that produces O_2 and H^+ ions. The electron present in the conduction band can be collected as a photocurrent generated by this EFDAACVD-produced metal oxide thin films. These overall photo-induced charge separation obtained for the metal oxide thin films in the photoelectrochemical cells are schematically shown in Figure 2.17. The photocurrent density-applied voltage responses observed for the various metal oxide thin films indicate that with increasing applied potential, the photocurrent density increases as depicted in Figure 4.62. It can be seen that among the various thin films, the Mn_2O_3 thin film showed a higher photocurrent density than the α-Fe_2O_3, NiO and CuO thin films due to its hierarchical and roughened morphology. The lowest photocurrent density was generated by the α-Fe_2O_3 thin film (120 $\mu A/cm^2$), whereas the maximum photocurrent density of 1.132 mA/cm^2 at 0.70 V potential versus Ag/AgCl (~1.23 V versus RHE) was found for the manganese dioxide (Mn_2O_3) thin film. In the case of CuO and NiO thin films, photocurrent densities of 129 and 226 $\mu A/cm^2$ respectively, were obtained.

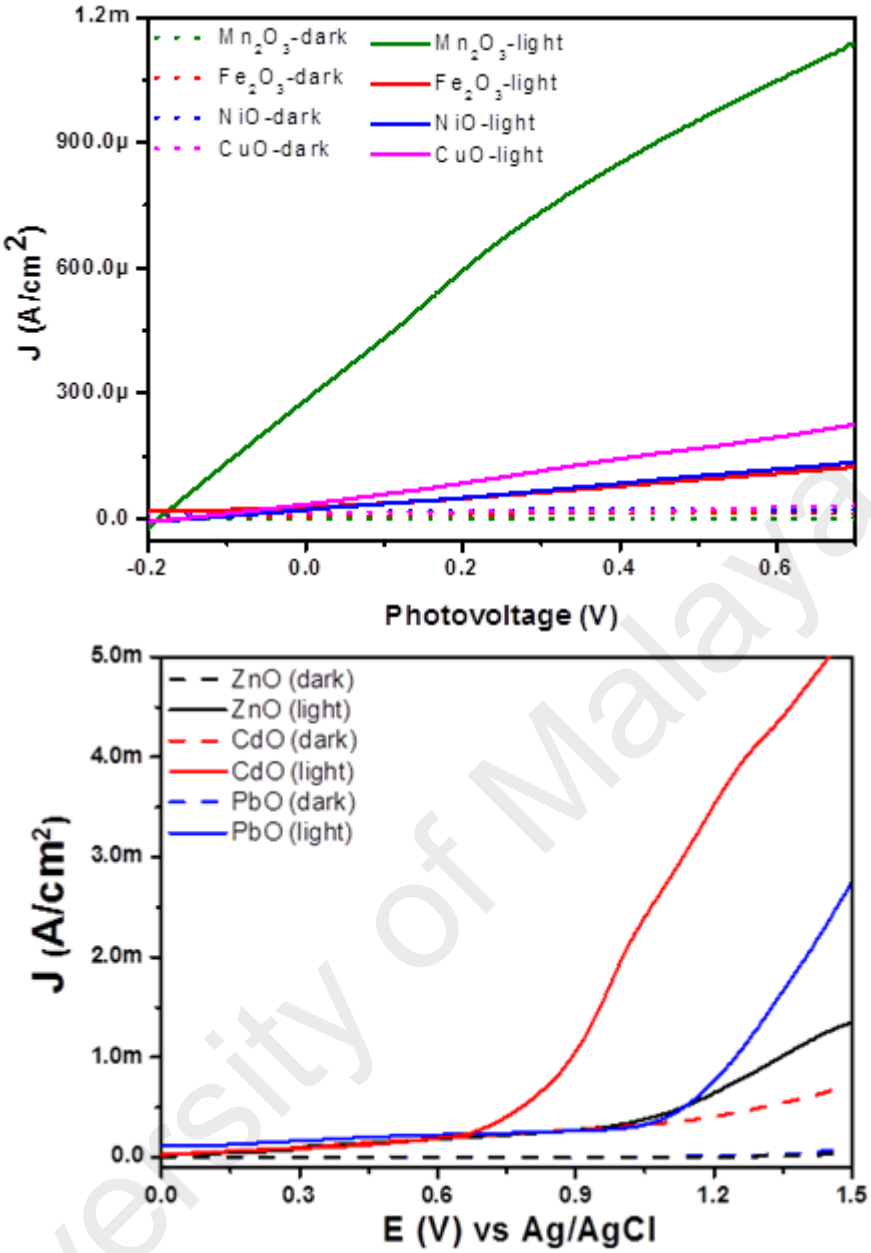

Figure 4.62: LSV plot obtained for the EFDAACVD- produced metal oxide (a) Mn_2O_3, α-Fe_2O_3, NiO, CuO and (b) ZnO, CdO, PbO thin films were dipped in to a solution containing 0.1 M Na_2SO_4 at a scan rate of 50 mV/s under dark and simulated solar AM 1.5G irradiation

The photocurrent LSV responses (Figure 4.62) observed for all the three metal oxide thin films shows that with increase in the applied potential, the photocurrent density increases. It can be seen that among the three oxides, CdO which has band-gap value of 2.2 eV and granular morphology, shows higher photocurrent density as compared with the ZnO and PbO thin films. Although band gap of PbO is lower than CdO yet the photocurrent

produced by it is lesser than CdO. This observation suggests that in addition to band gap energy of the photocatalyst, other parameters such as microstructure, morphology, particle size and shape etc of the thin film play important role in photoelectrochemical events and hence these parameters need to be controlled during the deposition of thin films. These two factors significantly accelerated photocurrent generation in terms of light absorption, charge recombination and charge transport.

The variations in the photocurrent responses of the thin films were further understood by recording the electrochemical impedance spectroscopy (EIS) measurements in the frequency range of 0.01 Hz to 10 kHz. The Nyquist plots obtained from the EIS measurements in the presence of 0.1 M Na_2SO_4 are displayed in Figure 4.63.

It can be seen that the Mn_2O_3, NiO and CuO thin films show a well-defined semicircle due to the charge transfer resistance of the thin films, whereas the α-Fe_2O_3 thin film exhibits a straight oblique line, which shows better conductivity and an increase in charge carriers due to low interfacial charge transfer resistance. Moreover, the Mn_2O_3 thin film shows a semicircle with a small diameter, which reveals a lower charge transfer resistance between the electrode and the electrolyte. It is known from the literature (Yusoff et al., 2015) that the corresponding value of the intercept on the X-axis at high frequency represents the ohmic resistance of the electrolyte and the internal resistance of the electrode (R_s). The lower values of R_s and R_{ct} for the Mn_2O_3 thin films result in an efficient charge transfer across the electrode-electrolyte interface, thereby minimizing charge recombination and enhancing the photocurrent response. The Nyquist plots obtained from the EIS measurements for the ZnO, CdO and PbO thin films are displayed in Figure 4.63. The ZnO thin film showed a semi-circle like oblique straight line due to the high charge transfer resistance (R_{ct}) value of 5225 Ω. In the case of CdO thin film, it showed well defined semicircle with the (R_{ct}) value of 3570 Ω. Interestingly, the PbO thin film showed

a very small semi-circle with a straight-line and it showed the (R_{ct}) value of 6.5 Ω (Inset of Figure. 4.63) along with the residual phase element. The smaller in the R_{ct} causes better conductivity and an increase in charge carriers due to low interfacial charge transfer resistance and also lower charge transfer resistance between the electrode and the electrolyte interfaces.

The Bode phase plots obtained for the EFDAACVD-deposited metal oxide thin films are depicted in Figure 4.64. The characteristic frequency peak for different metal oxide thin films are as follows: Mn_2O_3 (794.3 Hz), α-Fe_2O_3 (5.851 Hz), NiO (5.011 Hz),CuO (7.943 Hz), ZnO (15.851 Hz), CdO (24.99 Hz) and PbO (1995 Hz). These obtained characteristic frequencies can be related to the electron recombination lifetime (τ_n) of the corresponding metal oxide thin films by referring to the equation below (Lim et al., 2014):

$$\tau_n = {}^{1}/_{2\pi f_{max}}$$

Where f_{max} is the frequency peak maximum. Among different metal oxide thin films, Mn_2O_3 showed a very low recombination life time (τ_n) value (0.0002 sec) compared to other metal oxide thin films (α-Fe_2O_3, NiO and CuO). Hence variations in τ_n values make a difference in the photocurrent values for different metal oxide thin films (Table 4.11).

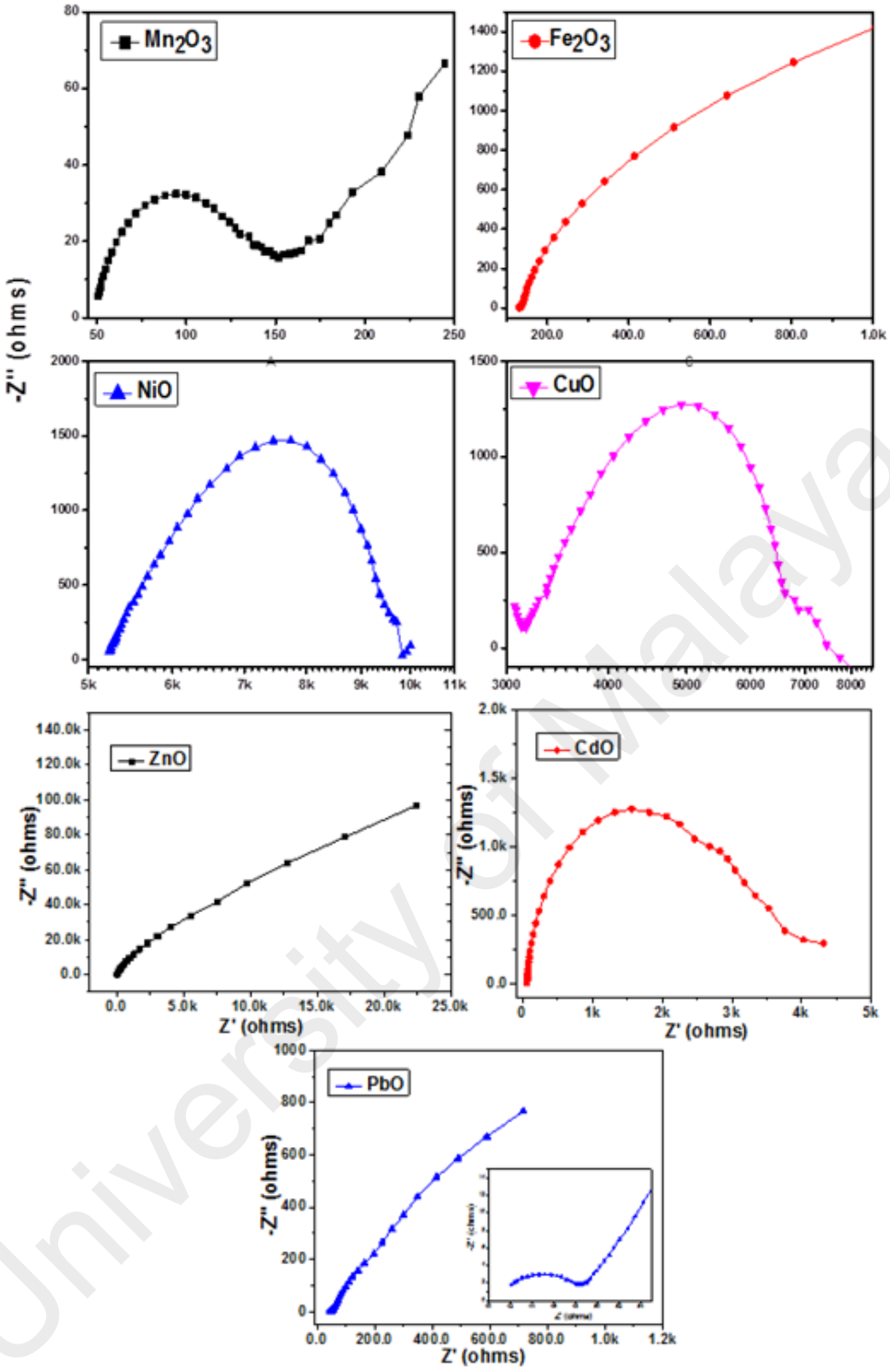

Figure 4.63: Nyquist phase plots obtained for the Mn_2O_3, α-Fe_2O_3, NiO, CuO, ZnO, CdO and PbO thin films in the presence of 0.1 M Na_2SO_4 at frequencies ranges of 0.1 Hz to 10 kHz.

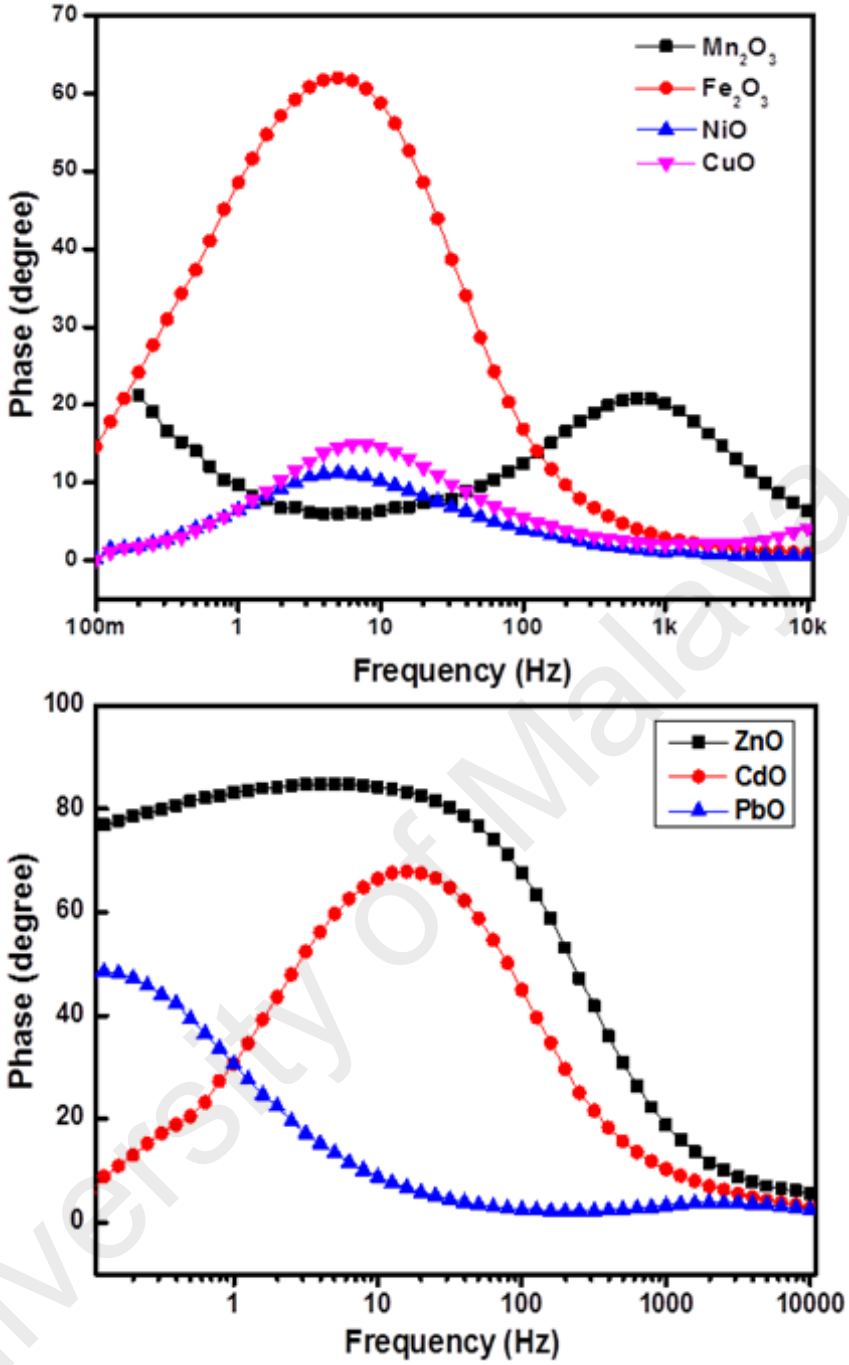

Figure 4.64: Bode phase plots obtained for the Mn_2O_3, α-Fe_2O_3, NiO, CuO, ZnO, CdO and PbO thin films in the presence of 0.1 M Na_2SO_4 at frequencies ranges of 0.1 Hz to 10 kHz.

Table 4.11: Charge transfer resistance, maximum frequency and recombination lifetime calculated for the EFDAACVD deposited metal oxide thin films.

Thin films	R_{ct} (ohm)	f_{max} (Hz)	τ_n (sec)
Mn_2O_3	102	794.3	0.0002
Fe_2O_3	750	5.851	0.0271
NiO	4600	5.011	0.0317
CuO	3800	7.943	0.0200
ZnO	5225	15.85	167.44×10^{-5}
CdO	3570	24.99	637.19×10^{-5}
PbO	6.5	1995	7.98×10^{-5}

Footnote: R_{ct} – Charge transfer resistance; f_{max} – Maximum frequency; τ_n – recombination lifetime.

Contribution of various morphology and band-gap causes difference in the recombination life time and thus significantly influence the photoelectrochemical performance.

4.7 Copper Lead Iodide ($CuPbI_3$)

The solid state synthesis of $CuPbI_3$ was carried out by using a precipitated mixture of copper(I) iodide and lead(II) iodide from an aqueous solution. Lead(II) iodide is soluble in dimethylformamide (DMF) while copper(I) iodide is insoluble. Therefore, we precipitated lead(II) iodide in slight excess over copper(I) iodide to ensure complete utilization of the latter in solid state reaction, while excess of the former was removed from the product by washing with DMF. Henceforth a dry mixture of co-precipitated copper(I) iodide- lead(II) iodide (1.65 g) was charged in a 5 mL pyrex glass ampule, then evacuated and sealed under vacuum. The charged ampule was placed in a horizontal tube furnace and heated at 620 ^oC for 72 hours before it was cooled to room temperature. The

mustard coloured final product was mechanically removed from the ampule, ground to a fine powder in an agate pestle and mortar and washed with several 5 mL portions of DMF to ensure complete removal of unreacted PbI_2 to yield 99.9% pure $CuPbI_3$ m.p. 307 ^oC. The synthesized $CuPbI_3$ is stable in air and is insoluble in common polar and non-polar solvents.

4.7.1 Thermal Studies of $CuPbI_3$

The thermal decomposition pattern of $CuPbI_3$ was examined by thermogravimetric/derivative thermogravimetric (TG/DTG) analyses, performed in the temperature range of 50- 900 ^oC, under a flow of dinitrogen (20 cm^3min^{-1}) at a heating rate of 20 $^oCmin^{-1}$ (Figure 4.65). The (TG/DTG) plot (Figure 4.65) shows no appreciable loss in weight till the temperature reaches to 432 ^oC where its pyrolysis begins. This pyrolysis step is sharp and is completed at 693 ^oC with a mass loss of 53.31% of the original weight of the sample. TG/DTG curves also indicate that there is no mentionable loss in weight at the start in the temperature range of 50 to 400 ^oC, which indicates that $CuPbI_3$ is thermally stable from room temperature to above its melting point of 307 ^oC. Further heating to 900 °C yields a stable residual mass of 41.53% of the original weight of the sample indicating formation of Cu-Pb (1: 1) alloy with liberation of iodine as indicated in the following chemical equation.

Chemical equation 11:

$$\mathbf{CuPbI_3} \xrightarrow{\triangle} \mathbf{Cu\text{-}Pb_{(alloy)} + 1.5\ I_2}$$

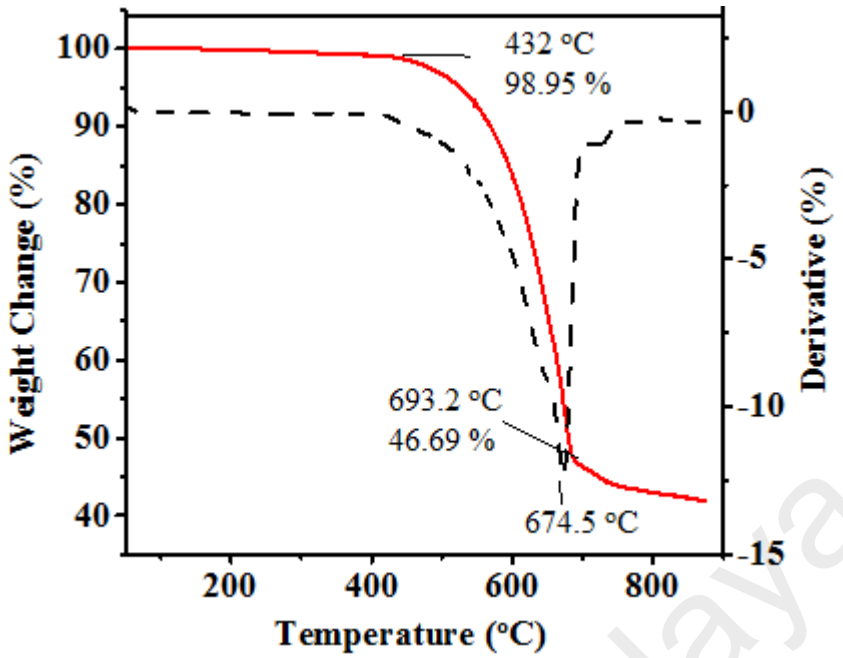

Figure 4.65: The simultaneous TG and DTG plots of $CuPbI_3$ recorded under an inert atmosphere of nitrogen gas with constant flow of 20 cm^3min^{-1} and heating rate of 20 $^oCmin^{-1}$.

DSC trace of $CuPbI_3$ recorded under an inert atmosphere of nitrogen gas with constant flow of 20 cm^3min^{-1} and heating rate of 20 $^oC\ min^{-1}$ is shown in Figure 4.66. The DSC curve displays two endothermic peaks at 240 ^oC and 307 ^oC. The well-defined sharp endotherm at 307 ^oC indicates melting point of $CuPbI_3$. The onset melting begins at 294.51 °C and melting process is completed at 315^oC with maximum heat flow at 307 ^oC.

The sharp and well-defined endotherm at 307 ^oC indicates that material is highly crystalline in nature needing enthalpy of -19.00 $J.g^{-1}$ for melting. A weak endotherm with small enthalpy value of -2.79 $J.g^{-1}$ in DSC plot further suggests that $CuPbI_3$ passes through a phase change process at 240 ^oC before melting.

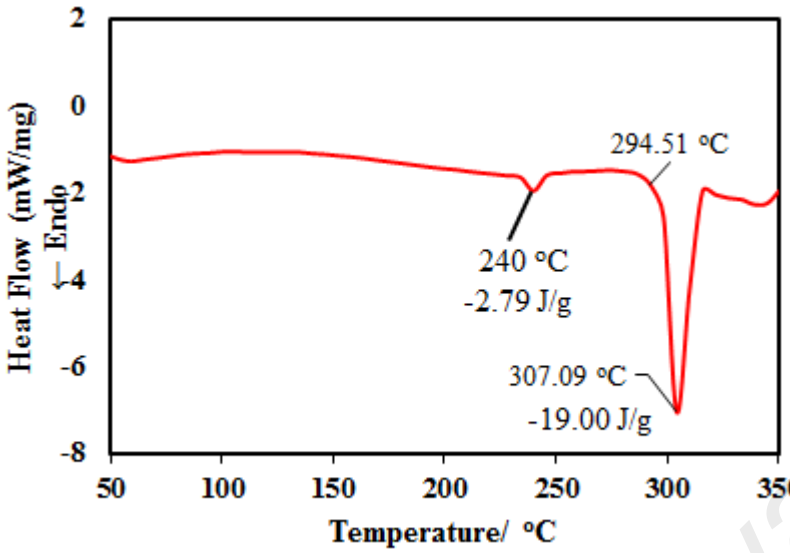

Figure 4.66: The DSC trace of $CuPbI_3$ recorded under an inert atmosphere of nitrogen gas with constant flow of 20 cm^3min^{-1} and heating rate of 20 $^oCmin^{-1}$.

4.7.2 XRD Analysis of $CuPbI_3$

X-ray diffraction patterns of the powder and electrophoretically deposited film of $CuPbI_3$ are displayed in Figure 4.67 and (Appendix 10) respectively. The XRD pattern of powdered $CuPbI_3$ agrees well with the pattern obtained for the films of $CuPbI_3$. This observation suggests that FTO does not chemically interfere during electrophoretic fabrication of $CuPbI_3$ film. The diffraction peaks at 2θ values of 12.9, 25.7, 39.7 and 52.5 corresponds to (002), (004), (302) and (312) planes of the hexagonal $CuPbI_3$ lattice is in good agreement with literature data (T. A. Kuku, 1998; Titilayo A. Kuku & Salau, 1987). The crystallite size of the $CuPbI_3$ film is obtained by Debye Scherer formula $L = k\lambda/\beta\cos\theta$ whereas k represents the Scherer constant, λ is the wavelength and θ the Braggs angle .The estimated crystallite size of $CuPbI_3$ is L = 62.5 nm which agrees well with the literature value (T. A. Kuku, 1998).

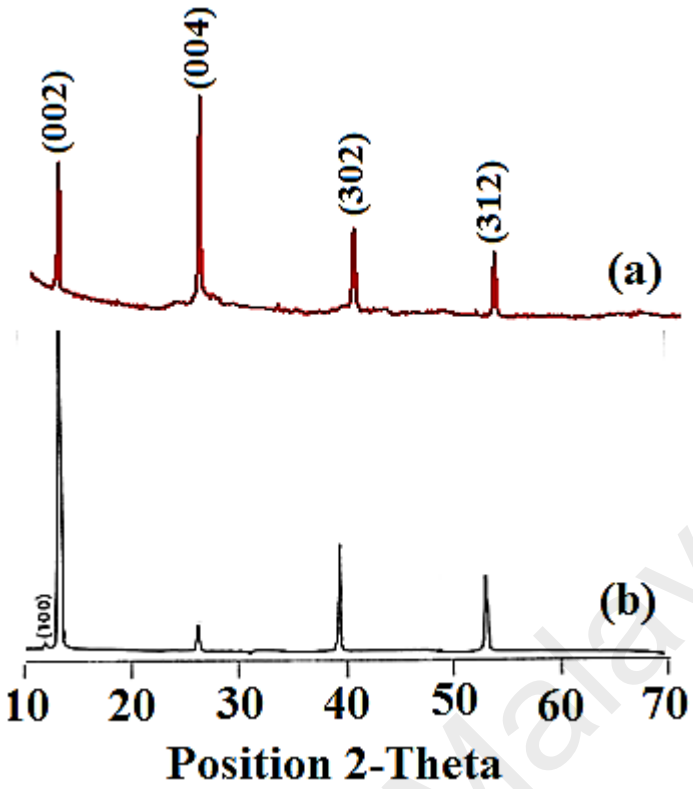

Figure 4.67: A comparison of powder XRD diffraction pattern of (a) as-synthesized $CuPbI_3$ powder with (b) reported in the literature (T. A. Kuku, 1998).

The XRD pattern of powdered $CuPbI_3$ agrees well with the pattern obtained for the films of $CuPbI_3$. This observation suggests that FTO does not chemically interfere during electrophoretic fabrication of $CuPbI_3$ film. The diffraction peaks at 2θ values of 12.9, 25.7, 39.7 and 52.5 corresponds to (002), (004), (302) and (312) planes of the hexagonal $CuPbI_3$ lattice is in good agreement with literature data (T. A. Kuku, 1998; Titilayo A. Kuku & Salau, 1987). The crystallite size of the $CuPbI_3$ film is obtained by Debye Scherer formula $L = k\lambda/\beta\cos\theta$ whereas k represents the Scherer constant, λ is the wavelength and θ the Braggs angle .The estimated crystallite size of $CuPbI_3$ is L = 62.5 nm which agrees well with the literature value (T. A. Kuku, 1998).

4.7.3 Raman Spectroscopy of $CuPbI_3$

Raman spectroscopy with polarized laser beams (λ = 514 nm) at dissimilar geometries with respect to the crystal orientation should be used to investigate the distinguish Raman

active modes of different symmetries. The Raman scattering of as-synthesized $CuPbI_3$ film was recorded in the range of 100 – 1000 cm^{-1} and is shown in Figure 4.68.

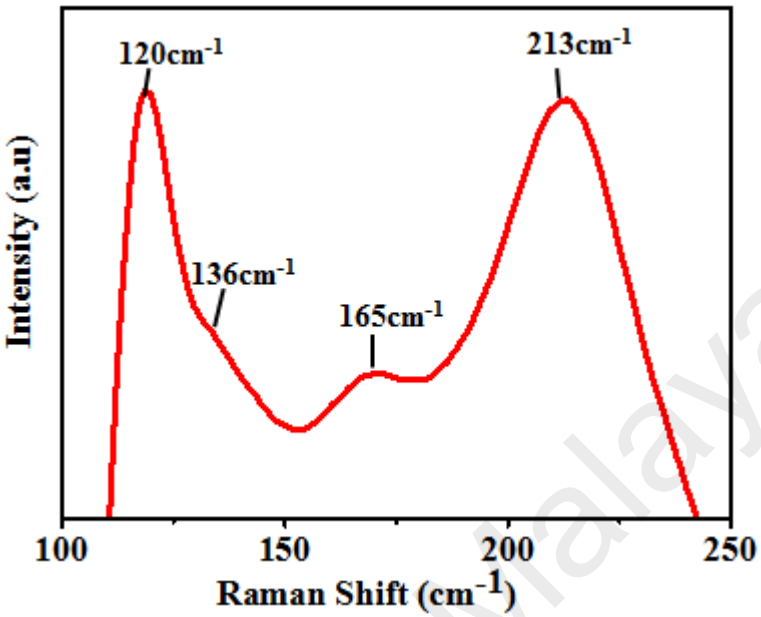

Figure 4.68: Raman spectrum of $CuPbI_3$ film

It is reported in the literature that pure CuI show Raman scattering mode at 140 cm^{-1} (Irish, Stolberg, & Shoesmith, 1985), while an intense peak was observed at 120 cm^{-1} which is attributable to the Pb-I bond vibration (Quarti et al., 2014) further PbI_2 modes are observed at 112 and 164 cm^{-1} (Baibarac et al., 2015; Preda et al., 2008). It is found that Raman active modes related to CuI in $CuPbI_3$ fall at lower wave number with a difference of 4 cm^{-1} and detected at 136 cm^{-1} (Safdari, Fischer, Xu, Kloo, & Gardner, 2015). The broad band at 165 cm^{-1} characteristic of PbI_2 has been found at its place as reported (Preda, et al., 2008). A new broad and intense Raman scattering mode that appeared at 213 cm^{-1} is considered as characteristic mode for $CuPbI_3$ (Quarti, et al., 2014).

4.7.4 Surface Morphology of $CuPbI_3$

The surface morphology of the EPD deposited films have been investigated by FE-SEM and are shown in Figure 4.69(a). The $CuPbI_3$ films consist of compact grain structure with better surface coverage in the form of strips.

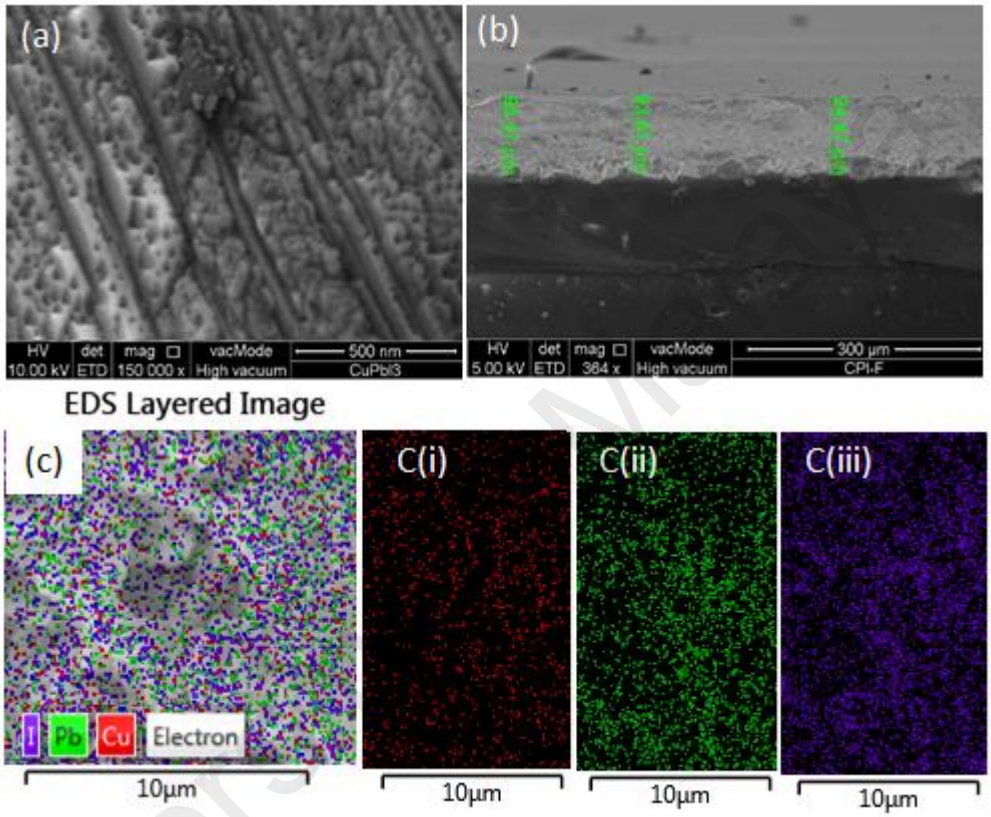

Figure 4.69: (a) Illustrates FESEM image of $CuPbI_3$ film deposited by Electrophoresis on FTO substrate, c(i) red, c(ii) green and c(iii) violet colour represent EDX mapping of Cu, Pb and I respectively

Films prepared by electrophoresis tend to grow with small grains grouped together in clusters of different sizes and show smooth uniform surfaces with presence of some randomly scattered voids in layers. This uniform, compact and granular morphology shows better performance for photocatalytic applications. The cross sectional view of $CuPbI_3$ film prepared by EPD is displayed in (Figure 4.69b).The growth of small grains on the boundary layer of the FTO substrate can be seen and the average film thickness was measured to be 96 µm. The results of FE-SEM examination combined with EDX mapping for the elements Cu, Pb and I are shown in Figure 4.69c (i, ii and iii). The bright

regions with different colors correspond to the presence of the elements Cu, Pb and I, respectively, and indicate all these elements are distributed uniformly maintaining stoichiometric proportion of 1:1:3 throughout the whole area as indicated in (Appendix 11). The atomic concentration of Cu, Pb and I elements were also determined by XPS and compared with EDX results.

4.7.5 XPS Analysis of $CuPbI_3$

The surface and sub surface chemical states were investigated by high resolution narrow scan XPS spectra in the Cu2p, Pb4f and I3d region of $CuPbI_3$ film and is recorded as Figures 4.70(a, b and c). Figure 4.70a shows the binding energy of Cu $2p_{3/2}$ as 931.5 eV which is closer to the 931.9 eV that was found in CuI (M. Yang, Xu, Xu, Zhu, & Chen, 2004). The binding energies of Pb $4f_{7/2}$ and Pb $4f_{5/2}$ (Figure 4.70b) are 137.3 eV and 142.1eV respectively, indicating a spin orbital splitting of 4.8eV. These values are in good agreement for the reported energy values for Pb in $Cs_{0.2}FA_{0.8}PbI_3$ and PbI_2 (Morgan & Van Wazer, 1973; Yi et al., 2016; J. Zhang et al., 2015). The binding energies of the peaks $I3d_{5/2}$ and $I3d_{3/2}$ (Figure 4.69c) are 618.0 eV and 629.3 eV respectively which are in close agreement to the I3d values reported for I in CuI, $Cs_{0.2}FA_{0.8}PbI_3$ and PbI_2 (M. Yang, et al., 2004; Yi, et al., 2016; J. Zhang, et al., 2015).

For the precise measurement of the valance band maximum (VBM) energy position, 200 measurement scan cycles were carried out. A plot of normalized intensity and binding energy ranging from -6 to 8 eV is shown in Figure 4.71 (d). The valance band maximum was determined by linear extrapolation method and was found to be at 1.20 eV vs NHE. The position of conduction band minimum (CBM) was estimated on the basis of band gap energy determined by UV-vis spectrophotometry and VBM energy determined by XPS. The value obtained for CBM of $CuPbI_3$ was found to be -0.62 eV vs NHE as shown in Figure 4.72.

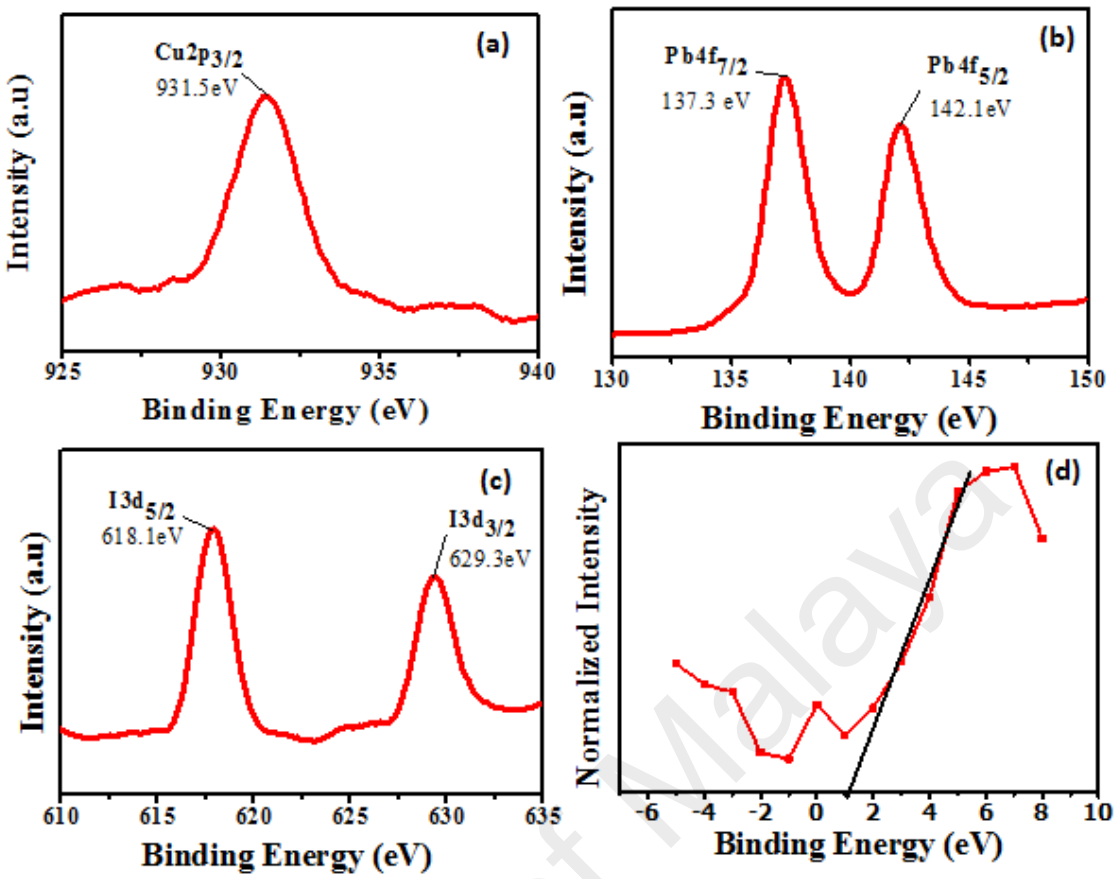

Figure 4.70: The XPS spectra of (a) Cu $2p_{3/2}$ (b) Pb $4f_{7/2}$, $4f_{5/2}$ (c) I $3d_{5/2}$, $I3d_{3/2}$ and (d) plot of normalized intensity and binding energy ranging from -6 to 8 eV of $CuPbI_3$ film.

4.7.6 Optical Band Gap of $CuPbI_3$

The optical band gap of $CuPbI_3$ film was studied by measuring the UV- visible absorption spectra recorded in the wavelength range of 300 - 900 nm using a similar FTO substrate as reference to minimize the contribution from the substrate. It can be seen that the Uv-vis spectrum (Figure 4.71) of the $CuPbI_3$ thin film shows wide range absorption which gradually increases towards lower wavelengths and shows the maximum absorption in the range of 330 - 790 nm. The Tauc's plot of energy versus $(\alpha hv)^2$ (Figure 4.71 inset) shows direct optical band gap energy of 1.82 eV.

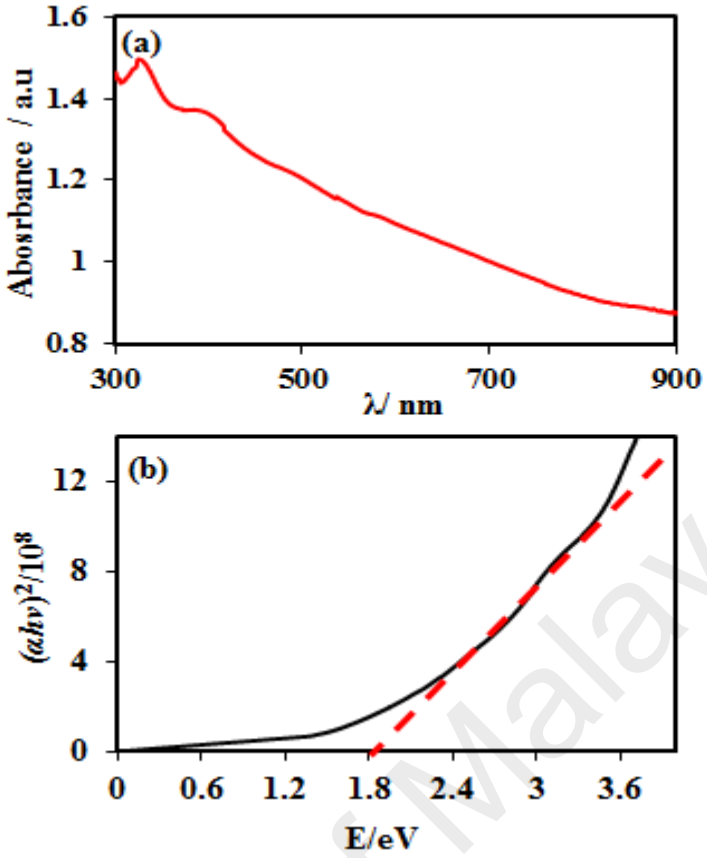

Figure 4.71: (a) UV-vis spectra of wavelength versus absorbance and (b) shows Tauc's plot of energy versus $(\alpha h\upsilon)^2$ $CuPbI_3$ film deposited by electrophoretic technique.

This optical band gap value agrees well with the band gap value calculated for $CH_3NH_3PbI_3$ by Uv-visible spectroscopy (Y. Zhao & Zhu, 2016). It is also reported that presence of methylammonium cation or Cs^+ does not affect the band gap region and it is the inorganic component of metal halide perovskites that plays dominant role in ascertaining the band gap energy. (Brivio, Walker, & Walsh, 2013; Yin, Shi, & Yan, 2014) In case of $CuPbI_3$ the band gap energy value remains unchanged inferring that replacement of $CH_3NH_3^+$ or Cs^+ by a univalent transition d^{10} metal ion e.g Cu^+ did not affect the band gap. After successful deposition of high purity film of $CuPbI_3$ and evaluation of its thermal properties, structure, stoichiometric composition, surface morphology and optical band gap, we investigated its photoelectrochemical (PEC) behavior.

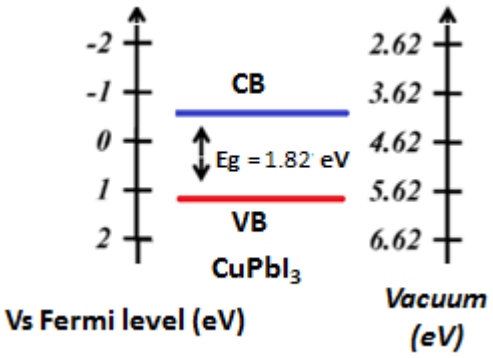

Figure 4.72: Shows energy of conduction band minimum calculated from XPS determined valence band maximum and Uv-visible band gap of $CuPbI_3$ film.

4.7.7 Photoelectrochemical Studies of $CuPbI_3$

The photoelectrochemical behavior of the $CuPbI_3$ film was investigated to evaluate its ability to perform water oxidation using linear sweep voltammetry (LSV) technique under simulated solar AM 1.5G irradiation in the presence of 0.1 M Na_2SO_4 at a scan rate of 50 mV/s. Under applied bias, the film undergoes photo-induced charge separation thereby promoting the valence band electrons to the conduction band resulting in the formation of holes at the valence band. The holes produced at the valence band can be readily scavenged through water oxidation that produces O_2 and H^+ ions. The electron present in the conduction band can be readily collected as a photocurrent generated by the film. The H^+ ions are transported through the electrolyte towards the counter electrode where they react with photo generated electrons to produce hydrogen. Further enhancement in photocurrent can be brought about by improving film thickness, morphology, surface roughness, structure and geometry. The photoelectrode shows active response under illumination and represents an anodic photocurrent pattern. The onset of photocurrent begins at -0.1 V under illumination and increases with increasing applied potential as depicted in Figure 9a. In the dark, however, no current can be observed until a bias of 0.1 V and after that small currents appear before it increases sharply beyond 0.8 V (vs.

Ag/AgCl). Moreover, the most important and notable point in this case is that the $CuPbI_3$ requires an over-potential of +0.62 V vs Ag/AgCl, pH 7, which is similar to 1.23 V vs RHE i.e. the thermodynamic potential required for water oxidation according to the equation given below :(Yourey & Bartlett, 2011).

$$E_{RHE} = E_{Ag/AgCl} + 0.059\,V.pH + 0.199\,V \qquad (4.6)$$

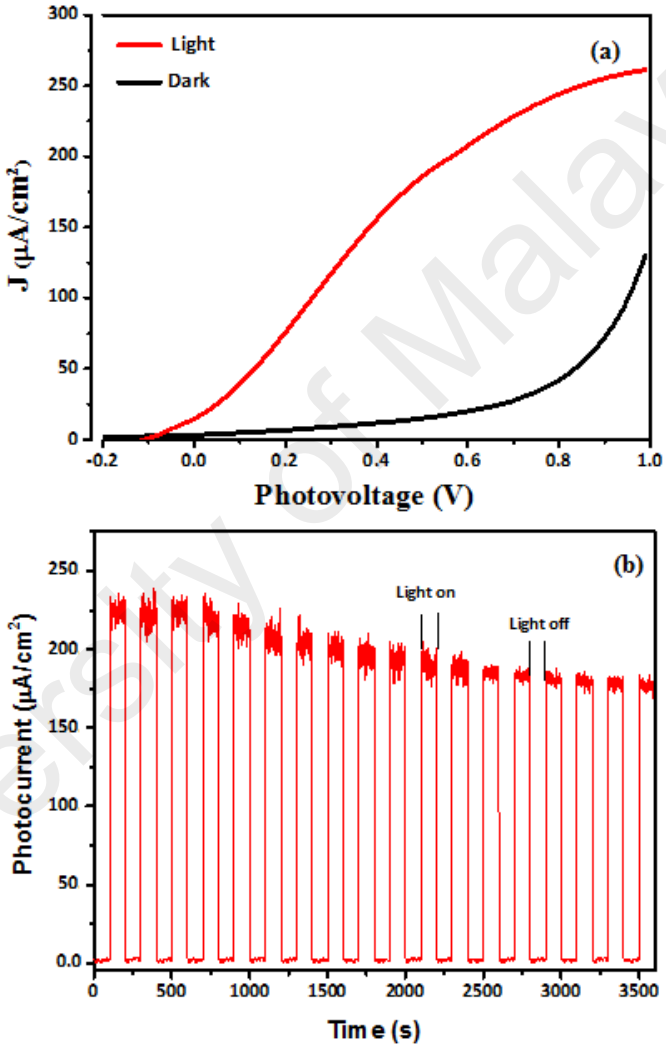

Figure 4.73: (a) Photocurrent density – applied voltage (J-V) plots obtained for the electrophoretic produced $CuPbI_3$ films dipped in 0.1M Na_2SO_4 at a scan rate of 50mV/s in light and dark. (b) Chronoamperometry (I–t) profiles (on-off cycles) of $CuPbI_3$ films at an applied potential of +0.65 V versus Ag/AgCl under 100 mW cm^{-2} illumination (AM 1.5) in 0.1 M Na_2SO_4 aqueous solution.

Under illumination, a photocurrent density of 220 μA/cm^2 can be observed at the thermodynamic potential of +0.62 V vs Ag/AgCl, pH 7. However, the dark current for the $CuPbI_3$ film has slightly increased probably due to the leakage of electrons from the

electrolyte to the FTO due to the pin hole effect. Nevertheless, many of the pin holes already have been cover by the compact thin film as seen in high resolution SEM picture shown in the Figure 5(a). We assume that the low band gap and compact morphology facilitates better electronic flow under illumination that enhances photocurrent density.

The role of Cu^{+} with d^{10} configuration is just to balance the charge, it does not have any important contribution for the conduction and valence band states except for donating one electron to the Pb–I framework as is reported for $CH_3NH_3^{+}$ and Cs^{+} ion in $CH_3NH_3PbI_3$ and $CsPbI_3$ respectively(Y. Zhao & Zhu, 2016) (Umebayashi, Asai, Kondo, & Nakao, 2003). The molecular orbital diagram of $[PbI_3]^{-1}$ ion (Appendix 13) depicts that I, (EN: 2.5) atomic orbitals (AO) are at low energy and Pb, (EN: 2.0) AO are at high energy. After linear combination of atomic orbitals these orbitals split into two sets of valence band and conduction band orbitals. The valence band orbitals are further divided into two, lowest and middle order energy state orbitals while, conduction band orbitals are highest energy orbitals. Hence σ Pb 6p – I 5s and σ Pb 6p – I $5p_z$ are in the lowest energy state of the valence orbitals while nonbonding Pb 6s, I $5p_x$ and $5p_y$ orbitals that are of intermediate energy remain as nonbonding orbitals. Pb 6s nonbonding orbital is at slightly high energy state than I $5p_x$ and $5p_y$. After crossing fermi level there begins a region where empty conduction band orbitals σ* Pb 6p – I $5p_z$ and σ* Pb 6p – I 5s are located. The process of photoelectrochemical water splitting begins with the photo activation of VBM Pb 6s nonbonding electron that on solar activation cross fermi level (E_f) and fall into σ* Pb 6p – I $5p_z$ conduction band orbitals from where they are removed by the applied bias. The hole generated by the photo activation reacts with water to split water into oxygen and H^{+} ions. It is believed that mostly Pb electrons are being used in photocatalytic process (Brivio, et al., 2013; Filippetti & Mattoni, 2014; Q. Liu et al., 2014; Umebayashi, et al., 2003; Yin, et al., 2014; Kang et al., 2015; Mansoor, Ehsan, et al., 2013).

The $CuPbI_3$ photoelectrode was further tested under on–off cycle illumination conditions to determine the stability of material. Figure 4.73b shows the photocurrent generated under visible light irradiation of $CuPbI_3$ electrode. A photo response of $CuPbI_3$ within 18 on-off cycles could be observed over a 60 min period (Figure 4.73b) revealing the efficiency and stability of $CuPbI_3$ photoelectrode. Initially the film is stable at 224 μA cm^{-2} for 15 min the current is dropped to 190 μAcm^{-2}. Moreover, the transient photocurrents agree well with LSV results and strengthened the PEC performance in the visible light region, as well as indicating the stability of $CuPbI_3$ films after 40 minutes.

The $CuPbI_3$ has distinct advantages of its environmental stability, wide light absorption range due to its appropriate band gap and efficient charge transport due to structural defects. The combination of these unique properties enables this class of halide materials to adopt solar cell structure in which high efficiencies could be possible to achieve.

CHAPTER 5: CONCLUSION

It is concluded that reproducible and robust CuO-TiO_2, $CoTiO_3$-TiO_2 and $MgTi_2O_5$ composites and SnO_2 thin films can easily be designed from single source precursors $[Cu_2Ti_4(O)_2(OH)_4(TFA)_8(THF)_6]\cdot THF$ (**1**)., $[Co_2Ti_4(\mu\text{-}O)_6(TFA)_8(THF)_6]\cdot THF$ **(2)**, $[Mg_2Ti_4(O)_2(OH)_4(TFA)_8(THF)_6]\cdot THF$ (**3**) and $[Sn(dmae)(OAc)]_2$ **(5)** respectively, While the Ag-Mn_2O_3 semiconducting thin films can be deposited from dual sources of $[Mn(dmae)_2(TFA)_4]$ (**4**) and Ag(I) acetate by AACVD method.

All the precursors **(1-5)** are prepared viably in a quantitative yield by simple chemical reactions of their respective metal alkoxides in the presence of TFAH/dmaeH using THF or toluene as solvent. The stoichiometry of all the complexes are determined by elemental analyses, FT-IR, ^1H NMR, thermogravimetry and single crystal X-ray diffraction analysis. All complexes have adaptable physical and chemical characteristics are stable in air or moisture, highly soluble in many organic solvents and decompose at relatively low to normal temperatures making them suitable precursors for CVD to deposit metal oxide composite thin films in temperature range of 450 to 630 ^oC.

Thin films of SnO_2, Mn_2O_3, Fe_2O_3, NiO, CuO, ZnO, CdO and PbO prepared under EFDAACVD indicate that morphology of the films can be controlled precisely by this technique but the PEC studies indicate a little improvement in photocurrent as compared to the films prepared in absence of electric field. UV-visible studies of thin films of Ag-Mn_2O_3 and $MgTi_2O_5$ indicate the band gap values of 1.8 and 3.4 respectively. While thin films of SnO_2, Mn_2O_3, Fe_2O_3, NiO, CuO, ZnO, CdO and PbO prepared under EFDAACVD depict band gap values of 3.8, 1.2, 2.2, 1.9, 0.9, 3.2, 2.2 and 1.9eV respectively. Thin film of $CuPbI_3$ prepared by electrophoretic technique indicate a band gap of 1.82eV. The electrochemical measurement of all fabricated thin films conducted

in conventional three-electrode electrochemical set-up employing an Ag/AgCl/ 3M KCl as the reference electrode and a platinum wire as the counter electrode studied by cyclic voltammetry, linear sweep voltammentry, chronoamperometery, electrochemical impedance spectroscopy and Mott schotty plot. These investigations that the thin films of $CuO\text{-}2TiO_2$ and $CoTiO_3–TiO_2$ are provides an attractive for the sensitive and selective detection of nitrite ion and dopamine, respectively. The reversibility, high rate capacity and relative stability shown by SnO_2 micro-ball based anodic materials in lithium ion batteries. The good photoelectrochemical behavior of Ag-Mn_2O_3, $MgTi_2O_5$, Mn_2O_3, Fe_2O_3, NiO, CuO, ZnO, CdO, PbO and $CuPbI_3$ thin films shows that these films could be a potentially valuable tool for photoelectrochemical water splitting.

Future Research Plan

The improvement of clean energy has become a main interest among recent research work. However, many routes to generate hydrogen have been introduced include both reforming and non-reforming hydrogen production. Further work is to develop trimetallic photocatalyst thin films electrodes by AACVD is under investigation to achieve high performance cells. In future effort is being carried out towards establishing stacked solar cells by connecting the photoelectrodes in series. Further improvement in photocurrent of the synthesized materials can be determined by producing dye sensitizes solar cells (DSSC). In future we will further expand the applications of ceramic-based nanostructures in fuel cells, supercapacitors, sensors, batteries and PEC to meet the environment- and energy-related demands.

REFERENCES

Adekunle, A. S., Agboola, B. O., Pillay, J., & Ozoemena, K. I. (2010). Electrocatalytic detection of dopamine at single-walled carbon nanotubes–iron (III) oxide nanoparticles platform. *Sensors and Actuators B: Chemical, 148*(1), 93-102.

Affatato, S., Ruggiero, A., & Merola, M. (2015). Advanced biomaterials in hip joint arthroplasty. A review on polymer and ceramics composites as alternative bearings. *Composites Part B: Engineering, 83*, 276-283.

Alothman, Z. A., Bukhari, N., Wabaidur, S. M., & Haider, S. (2010). Simultaneous electrochemical determination of dopamine and acetaminophen using multiwall carbon nanotubes modified glassy carbon electrode. *Sensors and Actuators B: Chemical, 146*(1), 314-320.

Aly, S. A., Kaid, M. A., & El-Sayed, N. Z. (2013). Some Optical Aspects of Thermally Evaporated Lead Oxide Thin Films. *Acta Physica Polonica A, 124*, 713-716.

Amadelli, R., De Battisti, A., Girenko, D. V., Kovalyov, S. V., & Velichenko, A. B. (2000). Electrochemical oxidation of trans-3,4-dihydroxycinnamic acid at PbO2 electrodes: direct electrolysis and ozone mediated reactions compared. *Electrochimica Acta, 46*(2–3), 341-347.

Arredondo Valdez, H. C., García Jiménez, G., Gutiérrez Granados, S., & Ponce de León, C. (2012). Degradation of paracetamol by advance oxidation processes using modified reticulated vitreous carbon electrodes with TiO_2 and $CuO/TiO_2/Al_2O_3$. *Chemosphere, 89*(10), 1195-1201.

Åsbrink, S., & Norrby, L.-J. (1970). A refinement of the crystal structure of copper (II) oxide with a discussion of some exceptional esd's. *Acta Crystallographica Section B: Structural Crystallography and Crystal Chemistry, 26*(1), 8-15.

Askeland, D., & Wright, W. (2015). *The Science and Engineering of Materials*: Cengage Learning, United states.

Atta, N. F., El-Kady, M. F., & Galal, A. (2010). Simultaneous determination of catecholamines, uric acid and ascorbic acid at physiological levels using poly (N-methylpyrrole)/Pd-nanoclusters sensor. *Analytical biochemistry, 400*(1), 78-88.

Aytug, T., Bogorin, D. F., Paranthaman, P. M., Mathis, J. E., Simpson, J. T., & Christen, D. K. (2014). Superhydrophobic ceramic coatings enabled by phase-separated nanostructured composite TiO_2–Cu_2O thin films. *Nanotechnology, 25*(24), 245601.

Azaceta, E., Chavhan, S., Rossi, P., Paderi, M., Fantini, S., Ungureanu, M., Oscar, M., Grande, H.G., Tena-Zaera, R. (2012). NiO cathodic electrochemical deposition from an aprotic ionic liquid: Building metal oxide n–p heterojunctions. *Electrochimica Acta, 71*, 39-43.

AzadáMalik, M. (1994). Growth of ZnO by MOCVD using alkylzinc alkoxides as single-source precursors. *Journal of Materials Chemistry, 4*(8), 1249-1253.

Babuji, B., Balasubramanian, C., Radhakrishnan, N., & Kasilingam, A. R. (1980). DC conduction studies in ion plated titanium oxide thin films. *Physica Status Solidi (A), 60*(1), K39-K42.

Baibarac, M., Smaranda, I., Scocioreanu, M., Mitran, R. A., Enculescu, M., Galatanu, M., & Baltog, I. (2015). Exciton-phonon interaction in PbI_2 revealed by Raman and photoluminescence studies using excitation light overlapping the fundamental absorption edge. *Materials Research Bulletin, 70*, 762-772.

Baker, D. R., & Kamat, P. V. (2009). Photosensitization of TiO_2 nanostructures with CdS quantum dots: particulate versus tubular support architectures. *Advanced Functional Materials, 19*(5), 805-811.

Barreca, D., Comini, E., Gasparotto, A., Maccato, C., Sada, C., Sberveglieri, G., & Tondello, E. (2009). Chemical vapor deposition of copper oxide films and entangled quasi-1D nanoarchitectures as innovative gas sensors. *Sensors and Actuators B: Chemical, 141*(1), 270-275.

Bates, J., Gruzalski, G., Dudney, N., Luck, C., Yu, X., & Jones, S. (1993). Rechargeable thin-film lithium microbatteries. *Solid state technology, 36*(7), 59-64.

Beckel, D., Bieberle-Hütter, A., Harvey, A., Infortuna, A., Muecke, U., Prestat, M., Gauckler, L. (2007). Thin films for micro solid oxide fuel cells. *Journal of Power Sources, 173*(1), 325-345.

Bersani, D., Lottici, P. P., & Montenero, A. (1999). Micro-Raman investigation of iron oxide films and powders produced by sol–gel syntheses. *Journal of Raman Spectroscopy, 30*(5), 355-360.

Besra, L., Compson, C., & Liu, M. (2006). Electrophoretic Deposition of YSZ Particles on Non- Conducting Porous NiO–YSZ Substrates for Solid Oxide Fuel Cell Applications. *Journal of the American Ceramic Society, 89*(10), 3003-3009.

Besra, L., & Liu, M. (2007). A review on fundamentals and applications of electrophoretic deposition (EPD). *Progress in Materials Science, 52*(1), 1-61.

Besra, L., Zha, S., & Liu, M. (2006). Preparation of NiO-YSZ/YSZ bi-layers for solid oxide fuel cells by electrophoretic deposition. *Journal of Power Sources, 160*(1), 207-214.

Boccaccini, A. R., Cho, J., Roether, J. A., Thomas, B. J. C., Jane Minay, E., & Shaffer, M. S. P. (2006). Electrophoretic deposition of carbon nanotubes. *Carbon, 44*(15), 3149-3160.

Boccaccini, A. R., Kaya, C., & Chawla, K. K. (2001). Use of electrophoretic deposition in the processing of fibre reinforced ceramic and glass matrix composites: a review. *Composites Part A: Applied Science and Manufacturing, 32*(8), 997-1006.

Booth, F., Garrido, L., Aglietti, E., Silva, A., Pena, P., & Baudín, C. (2016). $CaZrO_3$–MgO structural ceramics obtained by reaction sintering of dolomite-zirconia mixtures. *Journal of the European Ceramic Society, 36*(10), 2611-2626.

Brivio, F., Walker, A. B., & Walsh, A. (2013). Structural and electronic properties of hybrid perovskites for high-efficiency thin-film photovoltaics from first-principles. *APL Mater., 1*(4), 042111.

Cahill, D. G., Goodson, K., & Majumdar, A. (2002). Thermometry and thermal transport in micro/nanoscale solid-state devices and structures. *Journal of Heat Transfer, 124*(2), 223-241.

Cao. (2004). Growth of Oxide Nanorod Arrays through Sol Electrophoretic Deposition. *The Journal of Physical Chemistry B, 108*(52), 19921-19931.

Cao, A. M., Hu, J. S., Liang, H. P., & Wan, L. J. (2005). Self- assembled vanadium pentoxide (V2O5) hollow microspheres from nanorods and their application in lithium- Ion batteries. *Angewandte Chemie International Edition, 44*(28), 4391-4395.

Carballeda-Galicia, D. M., Castanedo-Pérez, R., Jiménez-Sandoval, O., Jiménez-Sandoval, S., Torres-Delgado, G., & Zúñiga-Romero, C. I. (2000). High transmittance CdO thin films obtained by the sol-gel method. *Thin Solid Films, 371*(1–2), 105-108.

Chandler, C. D., Roger, C., & Hampden-Smith, M. J. (1993). Chemical aspects of solution routes to perovskite-phase mixed-metal oxides from metal-organic precursors. *Chemical Reviews, 93*(3), 1205-1241.

Chang, H., Su, H.-T., Chen, W.-A., David Huang, K., Chien, S.-H., Chen, S.-L., & Chen, C.-C. (2010). Fabrication of multilayer TiO2 thin films for dye-sensitized solar cells with high conversion efficiency by electrophoresis deposition. *Solar Energy, 84*(1), 130-136.

Chen, A., Yang, G., Long, H., Li, F., Li, Y., & Lu, P. (2009). Nonlinear optical properties of laser deposited CuO thin films. *Thin Solid Films, 517*(15), 4277-4280.

Chen, F., & Liu, M. (2001). Preparation of yttria-stabilized zirconia (YSZ) films on La 0.85 Sr 0.15 MnO 3 (LSM) and LSM–YSZ substrates using an electrophoretic deposition (EPD) process. *Journal of the European Ceramic Society, 21*(2), 127-134.

Chen, J., Xu, L., Li, W., & Gou, X.-l. (2005). α- Fe2O3 nanotubes in gas sensor and lithium- ion battery applications. *Advanced Materials, 17*(5), 582-586.

Chen, J. S., & Lou, X. W. D. (2013). SnO2- Based Nanomaterials: Synthesis and Application in Lithium- Ion Batteries. *small, 9*(11), 1877-1893.

Chen, W., Cai, S., Ren, Q.-Q., Wen, W., & Zhao, Y.-D. (2012). Recent advances in electrochemical sensing for hydrogen peroxide: a review. *Analyst, 137*(1), 49-58.

Chen, Y., Bagnall, D. M., Zhu, Z., Sekiuchi, T., Park, K.-t., Hiraga, K., Goto, T. (1997). Growth of ZnO single crystal thin films on c-plane (0 0 0 1) sapphire by plasma enhanced molecular beam epitaxy. *Journal of Crystal Growth, 181*(1), 165-169.

Cheng, X. L., Zhao, H., Huo, L. H., Gao, S., & Zhao, J. G. (2004). ZnO nanoparticulate thin film: preparation, characterization and gas-sensing property. *Sensors and Actuators B: Chemical, 102*(2), 248-252.

Chigane, M., & Ishikawa, M. (2000). Manganese oxide thin film preparation by potentiostatic electrolyses and electrochromism. *Journal of The Electrochemical Society, 147*(6), 2246-2251.

Chopra, K., Paulson, P., & Dutta, V. (2004). Thin- film solar cells: an overview. *Progress in photovoltaics: research and applications, 12*(2- 3), 69-92.

Choudhary, N., & Kaur, D. (2016). Shape memory alloy thin films and heterostructures for MEMS applications: A review. *Sensors and Actuators A: Physical, 242*, 162-181.

Choudhary, S., Upadhyay, S., Kumar, P., Singh, N., Satsangi, V. R., Shrivastav, R., & Dass, S. (2012). Nanostructured bilayered thin films in photoelectrochemical water splitting–A review. *International Journal of Hydrogen Energy, 37*(24), 18713-18730.

Chuang, S. H., Gao, R. H., Wang, D. Y., Liu, H. P., Chen, L. M., & Chiang, M. Y. (2010). Synthesis and Characterization of Ilmenite- Type Cobalt Titanate Powder. *Journal of the Chinese Chemical Society, 57*(4B), 932-937.

Clavero, C. (2014). Plasmon-induced hot-electron generation at nanoparticle/metal-oxide interfaces for photovoltaic and photocatalytic devices. *Nature Photonics, 8*(2), 95-103.

Corneille, J. S., He, J.-W., & Goodman, D. W. (1995). Preparation and characterization of ultra-thin iron oxide films on a Mo(100) surface. *Surface Science, 338*(1–3), 211-224.

Crane, J., Warwick, M., Smith, R., Furlan, N., & Binions, R. (2011). The application of electric fields to aerosol assisted chemical vapor deposition reactions. *Journal of The Electrochemical Society, 158*(2), D62-D67.

Cuscó, R., Ibáñez, J., Domenech-Amador, N., Artús, L., Zúñiga-Pérez, J., & Muñoz-Sanjosé, V. (2010). Raman scattering of cadmium oxide epilayers grown by metal-organic vapor phase epitaxy. *Journal of Applied Physics, 107*(6), 063519.

da Silva, M. G. F. (2016). Optical properties and crystallization behaviour of some MnO and/or Fe_2O_3-containing silicate glasses and glass-ceramics. *Journal of Non-Crystalline Solids, 447*, 223-232.

Dakhel, A. A. (2006). Correlated structural and electrical properties of thin manganese oxide films. *Thin Solid Films, 496*(2), 353-359.

Damjanovic, D. (1998). Ferroelectric, dielectric and piezoelectric properties of ferroelectric thin films and ceramics. *Reports on Progress in Physics, 61*(9), 1267.

Dar, M. A., Nam, S. H., Kim, Y. S., & Kim, W. B. (2010). Synthesis, characterization, and electrochemical properties of self-assembled leaf-like CuO nanostructures. *Journal of Solid State Electrochemistry, 14*(9), 1719-1726.

Deng, H., Russell, J. J., Lamb, R. N., Jiang, B., Li, Y., & Zhou, X. Y. (2004). Microstructure control of ZnO thin films prepared by single source chemical vapor deposition. *Thin Solid Films, 458*(1–2), 43-46.

Dhanalakshmi, R., Pandikumar, A., Sujatha, K., & Gunasekaran, P. (2013). Photocatalytic and antimicrobial activities of functionalized silicate sol–gel embedded ZnO-TiO_2 nanocomposite materials. *Materials Express, 3*(4), 291-300.

Djurisic, A. B., Leung, Y. H., & Ching Ng, A. M. (2014). Strategies for improving the efficiency of semiconductor metal oxide photocatalysis. [10.1039/C4MH00031E]. *Materials Horizons, 1*(4), 400-410.

Dokko, K., Mohamedi, M., Anzue, N., Itoh, T., & Uchida, I. (2002). In situ Raman spectroscopic studies of LiNixMn2 - xO4 thin film cathode materials for lithium ion secondary batteries. [10.1039/B206764A]. *Journal of Materials Chemistry, 12*(12), 3688-3693.

Dolgonos, A., Mason, T. O., & Poeppelmeier, K. R. (2016). Direct optical band gap measurement in polycrystalline semiconductors: A critical look at the Tauc method. *Journal of Solid State Chemistry, 240*, 43-48.

Dudney, N. J. (2005). Solid-state thin-film rechargeable batteries. *Materials Science and Engineering: B, 116*(3), 245-249.

E.P. Meagher, C. F. S., M. Horn, , Wroclaw, . (2002). *Golden Book of Phase Transitions, 1*, 1 - 123.

Edusi, C., Sankar, G., & Parkin, I. P. (2012). The Effect of Solvent on the Phase of Titanium Dioxide Deposited by Aerosol- assisted CVD. *Chemical Vapor Deposition, 18*(4- 6), 126-132.

Ehsan, M. A., Khaledi, H., Pandikumar, A., Huang, N. M., Arifin, Z., & Mazhar, M. (2015). Dye sensitized solar cell applications of $CdTiO_3$–TiO_2 composite thin films deposited from single molecular complex. *Journal of Solid State Chemistry, 230*, 155-162.

Ehsan, M. A., Khaledi, H., Pandikumar, A., Rameshkumar, P., Huang, N. M., Arifin, Z., & Mazhar, M. (2015). Nitrite ion sensing properties of $ZnTiO_3$–TiO_2 composite thin films deposited from a zinc–titanium molecular complex. *New Journal of Chemistry, 39*(9), 7442-7452.

Ehsan, M. A., Naeem, R., Khaledi, H., Sohail, M., Saeed, A. H., & Mazhar, M. (2016). Fabrication of $CoTiO_3$–TiO_2 composite films from a heterobimetallic single source precursor for electrochemical sensing of dopamine. *Dalton Transactions*.

Ehsan, M. A., Naeem, R., McKee, V., Saeed, A. H., Pandikumar, A., Huang, N. M., & Mazhar, M. (2016a). Electrochemical sensing of nitrite using a copper-titanium

oxide composite derived from a hexanuclear complex. *RSC Advances, 6*(33), 27852-27861.

Ehsan, M. A., Tahir, A. A., Hamid, M., Mazhar, M., Wijayantha, K. U., & Zeller, M. (2011). Deposition of iron titanate/titania ceramic composite thin films from a single molecular precursor. *Inorganica Chimica Acta, 376*(1), 189-194.

El Khatib, K. M., & Abdel Hameed, R. M. (2011). Development of Cu_2O/Carbon Vulcan XC-72 as non-enzymatic sensor for glucose determination. *Biosensors and Bioelectronics, 26*(8), 3542-3548.

Feng, J., Johnson, D. C., Lowery, S. N., & Carey, J. J. (1994). Electrocatalysis of Anodic Oxygen- Transfer Reactions Evolution of Ozone. *Journal of The Electrochemical Society, 141*(10), 2708-2711.

Filippetti, A., & Mattoni, A. (2014). Hybrid perovskites for photovoltaics: Insights from first principles. *Phys. Rev. B, 89*, 125203-125208.

Fujimoto, D., Kuwata, N., Matsuda, Y., Kawamura, J., & Kang, F. (2015). Fabrication of solid-state thin-film batteries using $LiMnPO_4$ thin films deposited by pulsed laser deposition. *Thin Solid Films, 579*, 81-88.

Fujishima, A., Zhang, X., & Tryk, D. A. (2008). TiO_2 photocatalysis and related surface phenomena. *Surface Science Reports, 63*(12), 515-582.

Fulay, P., & Lee, J. K. (2013). *Electronic, Magnetic, and Optical Materials*: CRC Press.

Gao, P., Grätzel, M., & Nazeeruddin, M. K. (2014). Organohalide lead perovskites for photovoltaic applications. *Energy & Environmental Science, 7*(8), 2448-2463.

Gao, P., & Liu, D. (2015). Facile synthesis of copper oxide nanostructures and their application in non-enzymatic hydrogen peroxide sensing. *Sensors and Actuators B: Chemical, 208*, 346-354.

Ge, M.-Z., Cao, C.-Y., Li, S.-H., Tang, Y.-X., Wang, L.-N., Qi, N., Lai, Y.-K. (2016). In situ plasmonic Ag nanoparticle anchored TiO_2 nanotube arrays as visible-light-driven photocatalysts for enhanced water splitting. *Nanoscale, 8*(9), 5226-5234.

Gonçalves, R. H., Leite, L. D., & Leite, E. R. (2012). Colloidal WO_3 nanowires as a versatile route to prepare a photoanode for solar water splitting. *ChemSusChem, 5*(12), 2341-2347.

Graf, P., Mantion, A., Haase, A., Thünemann, A. F., Mašić, A., Meier, W., M. Admir, M., Wolfgang, M., Taubert, A. (2011). Silicification of Peptide-Coated Silver Nanoparticles A Biomimetic Soft Chemistry Approach toward Chiral Hybrid Core− Shell Materials. *ACS Nano, 5*(2), 820-833.

Grimm, J., Bessarabov, D., Maier, W., Storck, S., & Sanderson, R. D. (1998). Papers presented at the Water Institute of Southern Africa Membrane Technology DivisionSol-gel film-preparation of novel electrodes for the electrocatalytic oxidation of organic pollutants in water. *Desalination, 115*(3), 295-302.

Gryshkov, O., Klyui, N. I., Temchenko, V. P., Kyselov, V. S., Chatterjee, A., M., Ahmad, F., Molloy, Belyaev, A. E., Iarmolenko, D., Glasmacher, B. (2016). Porous biomorphic silicon carbide ceramics coated with hydroxyapatite as prospective materials for bone implants. *Materials Science and Engineering: C, 68*, 143-152.

Guidelli, R., Pergola, F., & Raspi, G. (1972). Voltammetric behavior of nitrite ion on platinum in neutral and weakly acidic media. *Analytical chemistry, 44*(4), 745-755.

Guo, S., Liu, J., Qiu, S., Liu, W., Wang, Y., Wu, N., Guo, Z. (2015). Porous ternary TiO 2/$MnTiO_3$@C hybrid microspheres as anode materials with enhanced electrochemical performances. *Journal of Materials Chemistry A, 3*(47), 23895-23904.

Guo, Y., Zheng, Y., & Huang, M. (2008). Enhanced activity of PtSn/C anodic electrocatalyst prepared by formic acid reduction for direct ethanol fuel cells. *Electrochimica Acta, 53*(7), 3102-3108.

Hamid, M., Tahir, A. A., Mazhar, M., Ahmad, F., Molloy, K. C., & Kociok-Kohn, G. (2008). Deposition and characterization of ZnO thin films from a novel hexanuclear zinc precursor. *Inorganica Chimica Acta, 361*(1), 188-194.

Han, Y.-F., Ramesh, K., Chen, L., Widjaja, E., Chilukoti, S., & Chen, F. (2007). Observation of the reversible phase-transformation of α-Mn_2O_3 nanocrystals during the catalytic combustion of methane by in situ Raman spectroscopy. *The Journal of Physical Chemistry C, 111*(7), 2830-2833.

Hanaor, D., Michelazzi, M., Veronesi, P., Leonelli, C., Romagnoli, M., & Sorrell, C. (2011). Anodic aqueous electrophoretic deposition of titanium dioxide using carboxylic acids as dispersing agents. *Journal of the European Ceramic Society, 31*(6), 1041-1047.

Handoko, A. D., & Goh, G. K. L. (2013). Hydrothermal growth of piezoelectrically active lead-free (Na,K)NbO3-LiTaO3 thin films. *CrystEngComm, 15*(4), 672-678.

Hannon, J., Kodambaka, S., Ross, F., & Tromp, R. (2006). The influence of the surface migration of gold on the growth of silicon nanowires. *Nature, 440*(7080), 69-71.

Hardcastle, F. (2011). Raman spectroscopy of titania (TiO_2) nanotubular water-splitting catalysts. *J Ark Acad Sci, 65*, 43-48.

Harrison, K., Levene, J., Rajeshwar, K., McConnell, R., & Licht, S. (2008). Solar hydrogen generation: toward a renewable energy future. *Electrolysis of water. New York: Springer Inc*, 41-64.

Hartnagel, H., Dawar, A., Jain, A., & Jagadish, C. (1995). *Semiconducting transparent thin films*: Institute of Physics Bristol.

Hasenkox, U., Hoffmann, S., & Waser, R. (1998). Influence of precursor chemistry on the formation of $MTiO_3$ (M= Ba, Sr) ceramic thin films. *Journal of sol-gel science and technology, 12*(2), 67-79.

Hass, G., Francombe, M. H., & Hoffman, R. W. (2013). *Physics of Thin Films: Advances in Research and Development*: Elsevier.

Hensel, F., Slocombe, D. R., & Edwards, P. P. (2015). On the occurrence of metallic character in the periodic table of the chemical elements. *Phil. Trans. R. Soc. A, 373*(2037), 20140477.

Herman, I. P. (1989). Laser-assisted deposition of thin films from gas-phase and surface-adsorbed molecules. *Chemical Reviews, 89*(6), 1323-1357.

Hisatomi, T., Kubota, J., & Domen, K. (2014). Recent advances in semiconductors for photocatalytic and photoelectrochemical water splitting. *Chemical Society Reviews, 43*(22), 7520-7535.

Ho, J. C. K., Filho, G. T., Simpraga, R., & Conway, B. E. (1994). Structure influence on electrocatalysis and adsorption of intermediates in the anodic O_2 evolution at dimorphic α- and β-PbO_2. *Journal of Electroanalytical Chemistry, 366*(1), 147-162.

Hollingsworth, N., Horley, G. A., Mazhar, M., Mahon, M. F., Molloy, K. C., Haycock, P. W., . . . Critchlow, G. W. (2006). Tin(II) aminoalkoxides and heterobimetallic derivatives: the structures of $Sn_6(O)_4(dmae)_4$, $Sn_6(O)_4(OEt)_4$ and $[Sn(dmae)_2Cd(acac)_2]_2$. *Appl. Organomet. Chem, 20*(10), 687-695.

Hossein-Babaei, F., & Taghibakhsh, F. (2000). Electrophoretically deposited zinc oxide thick film gas sensor. *Electronics Letters, 36*(21), 1815-1816.

Hotovy, I., Huran, J., Spiess, L., Hascik, S., & Rehacek, V. (1999). Preparation of nickel oxide thin films for gas sensors applications. *Sensors and Actuators B: Chemical, 57*(1), 147-152.

Hozumi, A., & Takai, O. (1997). Preparation of ultra water-repellent films by microwave plasma-enhanced CVD. *Thin Solid Films, 303*(1), 222-225.

Huang, C.-L., Wang, S.-Y., Chen, Y.-B., Li, B.-J., & Lin, Y.-H. (2012). Investigation of the electrical properties of metal–oxide–metal structures formed from RF magnetron sputtering deposited $MgTiO_3$ films. *Current Applied Physics, 12*(3), 935-939.

Huang, Y., Huang, H., Gao, Q., Gan, C., Liu, Y., & Fang, Y. (2014). Electroless synthesis of two-dimensional sandwich-like Pt/Mn_3O_4/reduced-graphene-oxide nanocomposites with enhanced electrochemical performance for methanol oxidation. *Electrochimica Acta, 149*, 34-41.

Hubert- Pfalzgraf, L. (1992). Metal alkoxides and β- diketonates as precursors for oxide and non- oxide thin films. *Applied Organometallic Chemistry, 6*(8), 627-643.

Humphreys, R., Satchell, J., Chew, N., Edwards, J., Goodyear, S., Blenkinsop, S., Cullis, A. (1990). Physical vapour deposition techniques for the growth of $YBa_2Cu_3O_7$ thin films. *Superconductor Science and Technology, 3*(1), 38.

Hyde, M. E., Jacobs, R. M. J., & Compton, R. G. (2004). An AFM Study of the Correlation of Lead Dioxide Electrocatalytic Activity with Observed Morphology. *The Journal of Physical Chemistry B, 108*(20), 6381-6390.

Ikhsan, N. I., Rameshkumar, P., Pandikumar, A., Shahid, M. M., Huang, N. M., Kumar, S. V., & Lim, H. N. (2015). Facile synthesis of graphene oxide–silver nanocomposite and its modified electrode for enhanced electrochemical detection of nitrite ions. *Talanta, 144*, 908-914.

Ilician, S., Caglar, Y., & Caglar, M. (2008). Preparation and characterization of ZnO thin films deposited by sol-gel spin coating method. *Journal of optoelectronics and advanced materials, 10*(10), 2578 - 2583.

Ioroi, T., Akita, T., Yamazaki, S.-i., Siroma, Z., Fujiwara, N., & Yasuda, K. (2006). Comparative study of carbon-supported Pt/Mo-oxide and PtRu for use as CO-tolerant anode catalysts. *Electrochimica Acta, 52*(2), 491-498.

Irish, D. E., Stolberg, L., & Shoesmith, D. W. (1985). Surface enhanced Raman spectroscopy and electrochemistry at the copper/iodide, water interface. *Surface Science, 158*(1–3), 238-253.

Ito, S., Chen, P., Comte, P., Nazeeruddin, M. K., Liska, P., Pechy, P., & Grätzel, M. (2007). Fabrication of screen- printing pastes from TiO_2 powders for dye-sensitised solar cells. *Progress in photovoltaics: research and applications, 15*(7), 603-612.

Izaki, M., Shinagawa, T., Mizuno, K.-T., Ida, Y., Inaba, M., & Tasaka, A. (2007). Electrochemically constructed p-Cu_2O/n-ZnO heterojunction diode for photovoltaic device. *Journal of Physics D: Applied Physics, 40*(11), 3326.

Izyumskaya, N., Alivov, Y.-I., Cho, S.-J., Morkoç, H., Lee, H., & Kang, Y.-S. (2007). Processing, structure, properties, and applications of PZT thin films. *Critical Reviews in Solid State and Materials Sciences, 32*(3-4), 111-202.

Jagadish, C., & Pearton, S. J. (2011). *Zinc oxide bulk, thin films and nanostructures: processing, properties, and applications*: Elsevier.

Jana, S., Pande, S., Sinha, A. K., Sarkar, S., Pradhan, M., Basu, M., Pal, T. (2009). A green chemistry approach for the synthesis of flower-like Ag-doped MnO_2 nanostructures probed by surface-enhanced Raman spectroscopy. *The Journal of Physical Chemistry C, 113*(4), 1386-1392.

Javed, Q., Wang, F., Rafique, M., Toufiq, A., Li, Q., Mahmood, H., & Khan, W. (2012). Diameter-controlled synthesis of α-Mn_2O_3 nanorods and nanowires with enhanced surface morphology and optical properties. *Nanotechnology, 23*(41), 415603.

Jia, L., Lü, Z., Huang, X., Liu, Z., Chen, K., Sha, X., Su, W. (2006). Preparation of YSZ film by EPD and its application in SOFCs. *Journal of Alloys and Compounds, 424*(1–2), 299-303.

Jiao, Z., Chen, T., Xiong, J., Wang, T., Lu, G., Ye, J., & Bi, Y. (2013). Visible-light-driven photoelectrochemical and photocatalytic performances of Cr-doped $SrTiO_3/TiO_2$ heterostructured nanotube arrays. *Scientific reports, 3*.

Johan, M. R., Suan, M. S., Hawari, M. N. L., & Ching, H. A. (2011). Annealing Effects on the Properties of Copper Oxide Thin Films Prepared by Chemical Deposition. *Int. J. Electrochem. Sci., 6*, 6094 - 6104.

Jones, A. C., Leedham, T. J., Wright, P. J., Crosbie, M. J., Lane, P. A., Williams, D. J., Otway, D. J. (1998). MOCVD of zirconia thin films by direct liquid injection using a new class of zirconium precursor. *Chemical Vapor Deposition, 4*(2), 46-49.

Joshi, P., & Cole, M. (2000). Mg-doped Ba0. 6Sr0. 4TiO3 thin films for tunable microwave applications. *Applied Physics Letters, 77*, 289.

Kang, Z., Yan, X., Wang, Y., Bai, Z., Liu, Y., Zhang, Z., Zhang, Y. (2015). Electronic Structure Engineering of Cu2O Film/ZnO Nanorods Array All-Oxide p-n Heterostructure for Enhanced Photoelectrochemical Property and Self-powered Biosensing Application. [Article]. *Scientific Reports, 5*, 7882.

Kapoor, P., Uma, S., Rodriguez, S., & Klabunde, K. (2005). Aerogel processing of MTi_2O_5 (M= Mg, Mn, Fe, Co, Zn, Sn) compositions using single source precursors: synthesis, characterization and photocatalytic behavior. *Journal of Molecular Catalysis A: Chemical, 229*(1), 145-150.

Kawachi, M., Sato, N., Suzuki, E., Ogawa, S., Noto, K., & Yoshizawa, M. (2001). Fabrication of $YBa_2Cu_4O_8$ films by electrophoretic deposition technique. *Physica C: Superconductivity, 357*, 1023-1026.

Kern, W. (2012). *Thin film processes II* (Vol. 2): Academic press, New York.

Kessler, V. G. (2003). Molecular structure design and synthetic approaches to the heterometallic alkoxide complexes (soft chemistry approach to inorganic materials by the eyes of a crystallographer). *Chemical Communications*(11), 1213-1222.

Kharade, R. R., Mali, S. S., Patil, S. P., Patil, K. R., Gang, M. G., Patil, P. S., Bhosale, P. N. (2013). Enhanced electrochromic coloration in Ag nanoparticle decorated WO 3 thin films. *Electrochimica Acta, 102*, 358-368.

Kim, D.-W., Hwang, I.-S., Kwon, S. J., Kang, H.-Y., Park, K.-S., Choi, Y.-J., Park, J.-G. (2007). Highly Conductive Coaxial SnO_2−In_2O_3 Heterostructured Nanowires for Li Ion Battery Electrodes. *Nano Lett, 7*(10), 3041-3045.

Kim, G.-S., Shin, D. H., Seo, Y. I., & Do Kim, Y. (2008). Microstructure and mechanical properties of a ZnS–SiO_2 composite prepared by ball-milling and spark plasma sintering. *Materials Characterization, 59*(9), 1201-1205.

Kim, K. J., & Heo, J. W. (2012). Electronic structure and optical properties of inverse-spinel $MnCo_2O_4$ thin films. *Journal of the Korean Physical Society, 60*(9), 1376-1380.

Kim, T. W., & Choi, K.-S. (2014). Nanoporous $BiVO_4$ photoanodes with dual-layer oxygen evolution catalysts for solar water splitting. *Science, 343*(6174), 990-994.

Kim, Y. J., Gao, B., Han, S. Y., Jung, M. H., Chakraborty, A. K., Ko, T., Lee, W. I. (2009). Heterojunction of $FeTiO_3$ nanodisc and TiO_2 nanoparticle for a novel visible light photocatalyst. *The Journal of Physical Chemistry C, 113*(44), 19179-19184.

Klahr, B. M., Martinson, A. B. F., & Hamann, T. W. (2010). Photoelectrochemical Investigation of Ultrathin Film Iron Oxide Solar Cells Prepared by Atomic Layer Deposition. *Langmuir, 27*(1), 461-468.

Koper, M. T. M., Lukkien, J. J., Jansen, A. P. J., & van Santen, R. A. (1999). Lattice Gas Model for CO Electrooxidation on Pt−Ru Bimetallic Surfaces. *The Journal of Physical Chemistry B, 103*(26), 5522-5529.

Korotcenkov, G., Brinzari, V., Schwank, J., DiBattista, M., & Vasiliev, A. (2001). Peculiarities of SnO_2 thin film deposition by spray pyrolysis for gas sensor application. *Sensors and Actuators B: Chemical, 77*(1–2), 244-252.

Kose, N., Çaylak, R., Pekşen, C., Kiremitçi, A., Burukoglu, D., Koparal, S., & Doğan, A. (2016). Silver ion doped ceramic nano-powder coated nails prevent infection in open fractures: In vivo study. *Injury, 47*(2), 320-324.

Krause, L., Herbst-Irmer, R., Sheldrick, G. M., & Stalke, D. (2015). Comparison of silver and molybdenum microfocus X-ray sources for single-crystal structure determination. *Applied Crystallography, 48*(1).

Krause, L., Herbst-Irmer, R., Sheldrick, G. M., & Stalke, D. (2015). Comparison of silver and molybdenum microfocus X-ray sources for single-crystal structure determination. *Journal of applied crystallography, 48*(1), 3-10.

Kud, I., Ieremenko, L., Likhoded, L., Uvarova, I., & Zyatkevich, D. (2012). Features of the Solid Solution (Mo 0. 9, Cr 0. 1) Si 2 Formation Depending on the State of Initial Mixture. *American Journal of Materials Science, 2*(6), 202-209.

Kuku, T. A. (1998). Ionic transport and galvanic cell discharge characteristics of $CuPbI_3$ thin films. *Thin Solid Films, 325*(1–2), 246-250.

Kuku, T. A., & Salau, A. M. (1987). Electrical conductivity of $CuSnI_3$, $CuPbI_3$ and $KPbI_3$. *Solid State Ionics, 25*(1), 1-7.

Kumar, S., Ojha, A. K., & Singh, R. K. (2014). Synthesis and Raman signature for the formation of CdO/MnO_2 (core/shell) nanostructures. *Journal of Raman Spectroscopy, 45*(9), 717-722.

Kumar, S. A., Tang, C.-F., & Chen, S.-M. (2008). Electroanalytical determination of acetaminophen using nano-TiO_2/polymer coated electrode in the presence of dopamine. *Talanta, 76*(5), 997-1005.

Lahcen, D., Hicham, E. E., Latifa, S., Abderrahmane, A., Jamal, B., Mohamed, W., Nathalie, F. (2014). Characteristics and ceramic properties of clayey materials

from Amezmiz region (Western High Atlas, Morocco). *Applied Clay Science, 102*, 139-147.

Lang, X., Hirata, A., Fujita, T., & Chen, M. (2011). Nanoporous metal/oxide hybrid electrodes for electrochemical supercapacitors. *Nature Nanotechnology, 6*(4), 232-236.

Langley, C. E., ŠLJUKIC, B., Banks, C. E., & Compton, R. G. (2007). Manganese dioxide graphite composite electrodes: application to the electroanalysis of hydrogen peroxide, ascorbic acid and nitrite. *Analytical sciences, 23*(2), 165-170.

Lazar, M. A., & Daoud, W. A. (2013). Achieving selectivity in TiO2-based photocatalysis. [10.1039/C2RA22665K]. *RSC Advances, 3*(13), 4130-4140.

Le Formal, F., Grätzel, M., & Sivula, K. (2010). Controlling Photoactivity in Ultrathin Hematite Films for Solar Water- Splitting. *Advanced Functional Materials, 20*(7), 1099-1107.

Lee, S.-H., Cheong, H. M., Park, N.-G., Tracy, C. E., Mascarenhas, A., Benson, D. K., & Deb, S. K. (2001). Raman spectroscopic studies of Ni–W oxide thin films. *Solid State Ionics, 140*(1–2), 135-139.

Lee, S. S., Bai, H., Liu, Z., & Sun, D. D. (2013). Optimization and an insightful properties—Activity study of electrospun TiO_2/CuO composite nanofibers for efficient photocatalytic H 2 generation. *Applied Catalysis B: Environmental, 140*, 68-81.

Lepage, D., Michot, C., Liang, G., Gauthier, M., & Schougaard, S. B. (2011). A soft chemistry approach to coating of $LiFePO_4$ with a conducting polymer. *Angewandte Chemie International Edition, 50*(30), 6884-6887.

Leung, D. Y., Fu, X., Wang, C., Ni, M., Leung, M. K., Wang, X., & Fu, X. (2010). Hydrogen Production over Titania- Based Photocatalysts. *ChemSusChem, 3*(6), 681-694.

Lewis, I. R., & Edwards, H. (2001). *Handbook of Raman spectroscopy: from the research laboratory to the process line*: CRC Press, New York.

Li, G., Wu, L., Li, F., Xu, P., Zhang, D., & Li, H. (2013). Photoelectrocatalytic degradation of organic pollutants via a CdS quantum dots enhanced TiO_2 nanotube array electrode under visible light irradiation. *Nanoscale, 5*(5), 2118-2125.

Li, J., Yang, J., Yang, Z., Li, Y., Yu, S., Xu, Q., & Hu, X. (2012). Graphene–Au nanoparticles nanocomposite film for selective electrochemical determination of dopamine. *Analytical Methods, 4*(6), 1725-1728.

Li, X., Magnuson, C. W., Venugopal, A., Tromp, R. M., Hannon, J. B., Vogel, E. M., Ruoff, R. S. (2011). Large-area graphene single crystals grown by low-pressure chemical vapor deposition of methane on copper. *Journal of the American Chemical Society, 133*(9), 2816-2819.

Li, Y., Tan, B., & Wu, Y. (2008). Mesoporous Co_3O_4 Nanowire Arrays for Lithium Ion Batteries with High Capacity and Rate Capability. *Nano Letters, 8*(1), 265-270.

Liang, Y.-C., Wang, C.-C., & Lo, Y.-J. Photoactivity enhancement of zinc sulfide ceramics thin films through ultrathin buffering engineering. *Ceramics International*. doi: http://dx.doi.org/10.1016/j.ceramint.2016.07.054.

Liang, Y., Cui, Z., Zhu, S., Li, Z., Yang, X., Chen, Y., & Ma, J. (2013). Design of a highly sensitive ethanol sensor using a nano-coaxial p-Co_3O_4/n-TiO_2 heterojunction synthesized at low temperature. *Nanoscale, 5*(22), 10916-10926.

Lim, S. P., Pandikumar, A., Huang, N. M., & Lim, H. N. (2014). Enhanced photovoltaic performance of silver@ titania plasmonic photoanode in dye-sensitized solar cells. *RSC Advances, 4*(72), 38111-38118.

Lim, S. P., Pandikumar, A., Huang, N. M., Lim, H. N., Gu, G., & Ma, T. L. (2014a). Promotional effect of silver nanoparticles on the performance of N-doped TiO2 photoanode-based dye-sensitized solar cells. [10.1039/C4RA09775K]. *RSC Advances, 4*(89), 48236-48244.

Lim, S. P., Pandikumar, A., Huang, N. M., Lim, H. N., Gu, G., & Ma, T. L. (2014b). Promotional effect of silver nanoparticles on the performance of N-doped TiO_2 photoanode-based dye-sensitized solar cells. *RSC Advances, 4*(89), 48236-48244.

Lin, K.-C., Lin, Y.-C., & Chen, S.-M. (2013). A highly sensitive nonenzymatic glucose sensor based on multi-walled carbon nanotubes decorated with nickel and copper nanoparticles. *Electrochimica Acta, 96*, 164-172.

Linic, S., Christopher, P., & Ingram, D. B. (2011). Plasmonic-metal nanostructures for efficient conversion of solar to chemical energy. *Nature materials, 10*(12), 911-921.

Liu, B., Ouyang, X., Ding, Y., Luo, L., Xu, D., & Ning, Y. (2016). Electrochemical preparation of nickel and copper oxides-decorated graphene composite for simultaneous determination of dopamine, acetaminophen and tryptophan. *Talanta, 146*, 114-121.

Liu, Q., Lu, H., Shi, Z., Wu, F., Guo, J., Deng, K., & Li, L. (2014). 2D $ZnIn_2S_4$ Nanosheet/1D TiO_2 Nanorod Heterostructure Arrays for Improved Photoelectrochemical Water Splitting. *ACS Applied Materials & Interfaces, 6*(19), 17200-17207.

Liu, Y., She, P., Gong, J., Wu, W., Xu, S., Li, J., Deng, A. (2015). A novel sensor based on electrodeposited Au–Pt bimetallic nano-clusters decorated on graphene oxide (GO)–electrochemically reduced GO for sensitive detection of dopamine and uric acid. *Sensors and Actuators B: Chemical, 221*, 1542-1553.

Liu, Z., Sun, Y., Yuan, J., Wei, H., Huang, X., Han, L., Ma, W. (2013). High- Efficiency Hybrid Solar Cells Based on Polymer/PbSxSe1- x Nanocrystals Benefiting from Vertical Phase Segregation. *Advanced Materials, 25*(40), 5772-5778.

Lokhande, C., Dubal, D., & Joo, O.-S. (2011). Metal oxide thin film based supercapacitors. *Current Applied Physics, 11*(3), 255-270.

Lokhande, C. D., Dubal, D. P., & Joo, O.-S. (2011). Metal oxide thin film based supercapacitors. *Current Applied Physics, 11*(3), 255-270.

Lou, X. W., Wang, Y., Yuan, C., Lee, J. Y., & Archer, L. A. (2006). Template-Free Synthesis of SnO_2 Hollow Nanostructures with High Lithium Storage Capacity. *Adv. Mater, 18*(17), 2325-2329.

Lu, H.-H., & Chen, C.-Y. (2016). Investigation of nano-silicon nitride ceramics containing an yttria sintering additive and the carbon thermal reduction reaction. *Ceramics International, 42*(10), 12452-12459.

Lu, Q., Yang, B., Zhuang, L., & Lu, J. (2005). Anodic Activation of PtRu/C Catalysts for Methanol Oxidation. *The Journal of Physical Chemistry B, 109*(5), 1715-1722.

M. Nirmala, A. A. (2010). Structural and optical properties of an undoped and Mn doped ZnO nanocrysatlline thin film. *Photonics letters of poland, 2*(4), 3.

Ma, Y., Wang, X., Jia, Y., Chen, X., Han, H., & Li, C. (2014). Titanium dioxide-based nanomaterials for photocatalytic fuel generations. *Chemical Reviews, 114*(19), 9987-10043.

Macrae, C. F., Edgington, P. R., McCabe, P., Pidcock, E., Shields, G. P., Taylor, R., Streek, J. v. d. (2006). Mercury: visualization and analysis of crystal structures. *Journal of applied crystallography, 39*(3), 453-457.

Madsen, L. D., & Weaver, L. (1998). Characterization of Lead Oxide Thin Films Produced by Chemical Vapor Deposition. *Journal of the American Ceramic Society, 81*(4), 988-996.

Maglia, F., Tredici, I. G., & Anselmi-Tamburini, U. (2013). Densification and properties of bulk nanocrystalline functional ceramics with grain size below 50 nm. *Journal of the European Ceramic Society, 33*(6), 1045-1066.

Mahan, J. E. (2000). Physical vapor deposition of thin films. *Physical Vapor Deposition of Thin Films, by John E. Mahan, pp. 336. ISBN 0-471-33001-9. Wiley-VCH, January 2000.*, 336.

Maity, R., & Chattopadhyay, K. K. (2006). Synthesis and characterization of aluminum-doped CdO thin films by sol–gel process. *Solar Energy Materials and Solar Cells, 90*(5), 597-606.

Malengreaux, C. M., Léonard, G. M.-L., Pirard, S. L., Cimieri, I., Lambert, S. D., Bartlett, J. R., & Heinrichs, B. (2014). How to modify the photocatalytic activity of TiO_2 thin films through their roughness by using additives. a relation between kinetics, morphology and synthesis. *Chemical engineering journal, 243*, 537-548.

Mane, R., & Lokhande, C. (2000). Chemical deposition method for metal chalcogenide thin films. *Materials Chemistry and Physics, 65*(1), 1-31.

Mane, R. S., Pathan, H. M., Lokhande, C. D., & Han, S.-H. (2006). An effective use of nanocrystalline CdO thin films in dye-sensitized solar cells. *Solar Energy, 80*(2), 185-190.

Manning, T. D., Parkin, I. P., Pemble, M. E., Sheel, D., & Vernardou, D. (2004). Intelligent Window Coatings: Atmospheric Pressure Chemical Vapor Deposition of Tungsten-Doped Vanadium Dioxide. *Chemistry of Materials, 16*(4), 744-749.

Mansoor, M. A., Ehsan, M. A., McKee, V., Huang, N.-M., Ebadi, M., Arifin, Z., Mazhar, M. (2013). Hexagonal structured Zn(1-x)CdxO solid solution thin films: synthesis, characterization and applications in photoelectrochemical water splitting. [10.1039/C3TA10558J]. *Journal of Materials Chemistry A, 1*(17), 5284-5292.

Mansoor, M. A., Ismail, A., Yahya, R., Arifin, Z., Tiekink, E. R. T., Weng, N. S., Esmaeili, A. R. (2013). Perovskite-Structured PbTiO3 Thin Films Grown from a Single-Source Precursor. *Inorganic Chemistry, 52*(10), 5624-5626.

Mansoor, M. A., Mazhar, M., McKee, V., & Arifin, Z. (2014). Mn_2O_3–$4TiO_2$ semiconducting composite thin films for photo-electrochemical water splitting. *Polyhedron, 75*, 135-140.

Mansoor, M. A., Mazhar, M., Pandikumar, A., Khaledi, H., Ming, H. N., & Arifin, Z. (2016). Photoelectrocatalytic activity of Mn_2O_3–TiO_2 composite thin films engendered from a trinuclear molecular complex. *International Journal of Hydrogen Energy*.

Marchand, P., Hassan, I. A., Parkin, I. P., & Carmalt, C. J. (2013). Aerosol-assisted delivery of precursors for chemical vapour deposition: expanding the scope of CVD for materials fabrication. *Dalton Transactions, 42*(26), 9406-9422.

Martin, D. J., Liu, G., Moniz, S. J., Bi, Y., Beale, A. M., Ye, J., & Tang, J. (2015). Efficient visible driven photocatalyst, silver phosphate: performance, understanding and perspective. *Chemical Society Reviews, 44*(21), 7808-7828.

Mat-Teridi, M. A., Tahir, A. A., Senthilarasu, S., Wijayantha, K. G. U., Sulaiman, M. Y., Ahmad-Ludin, N., . . . Sopian, K. (2014). Fabrication of NiO photoelectrodes by aerosol-assisted chemical vapour deposition (AACVD). *physica status solidi (RRL) – Rapid Research Letters, 8*(12), 982-986.

Minegishi, K., Koiwai, Y., Kikuchi, Y., Yano, K., Kasuga, M., & Shimizu, A. (1997). Growth of p-type zinc oxide films by chemical vapor deposition. *Japanese Journal of Applied Physics, 36*(11A), L1453.

Minh, N. Q. (1993). Ceramic fuel cells. *Journal of the American Ceramic Society, 76*(3), 563-588.

Momeni, M. M., Ghayeb, Y., & Davarzadeh, M. (2015). Single-step electrochemical anodization for synthesis of hierarchical WO_3–TiO_2 nanotube arrays on titanium foil as a good photoanode for water splitting with visible light. *Journal of Electroanalytical Chemistry, 739*, 149-155.

Mondal, S., Bhattacharyya, S. R., & Mitra, P. (2013). Preparation of manganese-doped ZnO thin films and their characterization. *Bulletin of Materials Science, 36*(2), 223-229.

Mor, G. K., Shankar, K., Paulose, M., Varghese, O. K., & Grimes, C. A. (2006). Use of highly-ordered TiO_2 nanotube arrays in dye-sensitized solar cells. *Nano Letters, 6*(2), 215-218.

Moreno, B., Chinarro, E., Pérez, J. C., & Jurado, J. R. (2007). Combustion synthesis and electrochemical characterisation of Pt–Ru–Ni anode electrocatalyst for PEMFC. *Applied Catalysis B: Environmental, 76*(3–4), 368-374.

Morgan, W. E., & Van Wazer, J. R. (1973). Binding energy shifts in the x-ray photoelectron spectra of a series of related Group IVa compounds. *The Journal of Physical Chemistry, 77*(7), 964-969.

Mumme, W., Cranswick, L., & Chakoumakos, B. (2002). Golden Book of Phase Transitions. *Wroclaw, 1*, 1-123.

Muralt, P. (2000). Ferroelectric thin films for micro-sensors and actuators: a review. *Journal of Micromechanics and Microengineering, 10*(2), 136.

Myung, J.-H., Ko, H.-J., Lee, J.-J., Lee, J.-H., & Hyun, S.-H. (2012). Synthesis and characterization of NiO/GDC–GDC dual nano-composite powders for high-performance methane fueled solid oxide fuel cells. *International Journal of Hydrogen Energy, 37*(15), 11351-11359.

Naeem, R., Yahya, R., Pandikumar, A., Huang, N. M., Misran, M., Arifin, Z., & Mazhar, M. (2015). Materials Today Communications. *Materials Today, 4*, 141-148.

Naeem, R., Yahya, R., Pandikumar, A., Huang, N. M., Misran, M., Arifin, Z., & Mazhar, M. (2015). Photoelectrochemical properties of morphology controlled manganese, iron, nickel and copper oxides nanoball thin films deposited by electric field directed aerosol assisted chemical vapour deposition. *Materials Today Communications, 4*, 141-148.

Naik, A. J. T., Warwick, M. E. A., Moniz, S. J. A., Blackman, C. S., Parkin, I. P., & Binions, R. (2013). Nanostructured tungsten oxide gas sensors prepared by electric field assisted aerosol assisted chemical vapour deposition. [10.1039/C2TA01126C]. *Journal of Materials Chemistry A, 1*(5), 1827-1833.

Nair, M., & Nair, P. (1991). Simplified chemical deposition technique for good quality SnS thin films. *Semiconductor Science and Technology, 6*(2), 132.

Nakata, K., & Fujishima, A. (2012). TiO_2 photocatalysis: Design and applications. *Journal of Photochemistry and Photobiology C: Photochemistry Reviews, 13*(3), 169-189.

Nawar, N., & Hosny, N. (2000). Synthesis, spectral and antimicrobial activity studies of o-aminoacetophenone o-hydroxybenzoylhydrazone complexes. *Transition Met. Chem, 25*(1), 1-8.

Necmi, S., Tülay, S., Şeyda, H., & Yasemin, Ç. (2005). Annealing effects on the properties of copper oxide thin films prepared by chemical deposition. *Semiconductor Science and Technology, 20*(5), 398.

Newnham, R., Fang, J., & Santoro, R. (1964). Crystal structure and magnetic properties of $CoTiO_3$. *Acta Crystallographica, 17*(3), 240-242.

Nguyen, T. H., Nguyen, T. L., Ung, T. D. T., & Nguyen, Q. L. (2013). Synthesis and characterization of nano-CuO and CuO/TiO_2 photocatalysts. *Advances in Natural Sciences: Nanoscience and Nanotechnology, 4*(2), 025002.

Nicholas, R. J., & Tuley, R. S. (2012). 4 - Thermophotovoltaic (TPV) devices: introduction and modelling. In J. A. Kilner, S. J. Skinner, S. J. C. Irvine & P. P. Edwards (Eds.), *Functional Materials for Sustainable Energy Applications* (pp. 67-90): Woodhead Publishing.

Niederberger, M., & Pinna, N. (2009). *Metal oxide nanoparticles in organic solvents: synthesis, formation, assembly and application*: Springer Science & Business Media.

Niederberger, M., Pinna, N., Polleux, J., & Antonietti, M. (2004). A General Soft-Chemistry Route to Perovskites and Related Materials: Synthesis of $BaTiO_3$, $BaZrO_3$, and $LiNbO_3$ Nanoparticles. *Angewandte Chemie International Edition, 43*(17), 2270-2273.

Niesen, T. P., & De Guire, M. R. (2001). Review: deposition of ceramic thin films at low temperatures from aqueous solutions. *Journal of Electroceramics, 6*(3), 169-207.

Nolan, N. T., Seery, M. K., & Pillai, S. C. (2011). Crystallization and phase-transition characteristics of sol− gel-synthesized zinc titanates. *Chemistry of Materials, 23*(6), 1496-1504.

Norman, J. A., Perez, M., Schulz, S. E., & Waechtler, T. (2008). New precursors for CVD copper metallization. *Microelectronic Engineering, 85*(10), 2159-2163.

Noro, H., Sato, K., & Kagechika, H. (1993). The thermoelectric properties and crystallography of Bi- Sb- Te- Se thin films grown by ion beam sputtering. *Journal of Applied Physics, 73*(3), 1252-1260.

Nowotny, J., Bak, T., Nowotny, M., & Sheppard, L. (2007). Titanium dioxide for solar-hydrogen I. Functional properties. *International Journal of Hydrogen Energy, 32*(14), 2609-2629.

Ohring, M. (2001). *Materials science of thin films*: Academic press, New York.

Ozegowski, M., Meteva, K., Metev, S., & Sepold, G. (1999). Pulsed laser deposition of multicomponent metal and oxide films. *Applied Surface Science, 138–139*(0), 68-74.

Özgür, Ü., Alivov, Y. I., Liu, C., Teke, A., Reshchikov, M. A., Doğan, S., Morkoç, H. (2005). A comprehensive review of ZnO materials and devices. *Journal of Applied Physics, 98*(4), 041301.

Palgrave, R. G., & Parkin, I. P. (2007). Aerosol assisted chemical vapor deposition of gold and nanocomposite thin films from hydrogen tetrachloroaurate (III). *Chemistry of Materials, 19*(19), 4639-4647.

Pandikumar, A., Murugesan, S., & Ramaraj, R. (2010). Functionalized Silicate Sol−Gel-Supported TiO2−Au Core−Shell Nanomaterials and Their Photoelectrocatalytic Activity. *ACS Applied Materials & Interfaces, 2*(7), 1912-1917.

Pandikumar, A., Yusoff, N., Huang, N. M., & Lim, H. N. (2014). Electrochemical sensing of nitrite using a glassy carbon electrode modified with reduced functionalized graphene oxide decorated with flower-like zinc oxide. *Microchimica Acta, 182*(5-6), 1113-1122.

Pang, X., & Zhitomirsky, I. (2005). Electrodeposition of composite hydroxyapatite–chitosan films. *Materials Chemistry and Physics, 94*(2–3), 245-251.

Panjawi, N., Naik, A., Warwick, M. E., Hyett, G., & Binions, R. (2012a). The preparation of titanium dioxide gas sensors by the electric field assisted aerosol CVD reaction of titanium isopropoxide in toluene. *Chemical Vapor Deposition, 18*(4- 6), 102-106.

Panjawi, N., Naik, A., Warwick, M. E. A., Hyett, G., & Binions, R. (2012b). The Preparation of Titanium Dioxide Gas Sensors by the Electric Field Assisted Aerosol CVD Reaction of Titanium Isopropoxide in Toluene. *Chemical Vapor Deposition, 18*(4-6), 102-106.

Park, H., Park, Y., Kim, W., & Choi, W. (2013). Surface modification of TiO_2 photocatalyst for environmental applications. *Journal of Photochemistry and Photobiology C: Photochemistry Reviews, 15*(0), 1-20.

Patil GE, Kajale DD, Gaikwad VB, & GH, J. (2012). Effect of thickness on nanostructured SnO_2 thin films by spray pyrolysis as highly sensitive H_2S gas sensor. *J Nanosci Nanotechnol., 12(8)*(6), 192-201.

Peng, Z., & Liu, M. (2001). Preparation of Dense Platinum- Yttria Stabilized Zirconia and Yttria Stabilized Zirconia Films on Porous La0. 9Sr0. 1MnO3 (LSM) Substrates. *Journal of the American Ceramic Society, 84*(2), 283-288.

Pierson, H. O. (1999). *Handbook of chemical vapor deposition: principles, technology and applications*: William Andrew.

Ping, J., Wu, J., Wang, Y., & Ying, Y. (2012). Simultaneous determination of ascorbic acid, dopamine and uric acid using high-performance screen-printed graphene electrode. *Biosensors and Bioelectronics, 34*(1), 70-76.

Poortmans, J., & Arkhipov, V. (2006). *Thin film solar cells: fabrication, characterization and applications* (Vol. 5): John Wiley & Sons.

Preda, N., Mihut, L., Baibarac, M., Husanu, M., Bucur, C., & Baltog, I. (2008). Raman and photoluminescence studies on intercalated

lead iodide with pyridine and iodine. *Journal of optoelectronics and advanced materials, Vol. 10, No. 2, ,* 319-322.

Prellier, W., Singh, M., & Murugavel, P. (2005). The single-phase multiferroic oxides: from bulk to thin film. *Journal of Physics: Condensed Matter, 17*(30), R803.

Quarti, C., Grancini, G., Mosconi, E., Bruno, P., Ball, J. M., Lee, M. M., Angelis, F. D. (2014). The Raman Spectrum of the $CH_3NH_3PbI_3$ Hybrid Perovskite: Interplay of Theory and Experiment. *The Journal of Physical Chemistry Letters, 5*(2), 279-284.

Rafiee, B., & Fakhari, A. R. (2013). Electrocatalytic oxidation and determination of insulin at nickel oxide nanoparticles-multiwalled carbon nanotube modified screen printed electrode. *Biosensors and Bioelectronics, 46*, 130-135.

Rahman, M., Haider, J., Akter, T., & Hashmi, M. S. J. (2014). 1.02 - Techniques for Assessing the Properties of Advanced Ceramic Materials *Comprehensive Materials Processing* (pp. 3-34). Oxford: Elsevier.

Rahman, M. M., Ahammad, A., Jin, J.-H., Ahn, S. J., & Lee, J.-J. (2010). A comprehensive review of glucose biosensors based on nanostructured metal-oxides. *Sensors, 10*(5), 4855-4886.

Raviprakash, Y., Bangera, K. V., & Shivakumar, G. (2009). Preparation and characterization of $Cd_xZn_{1-x}S$ thin films by spray pyrolysis technique for photovoltaic applications. *Solar Energy, 83*(9), 1645-1651.

Rehman, S., Ullah, R., Butt, A. M., & Gohar, N. D. (2009). Strategies of making TiO_2 and ZnO visible light active. *Journal of Hazardous Materials, 170*(2–3), 560-569.

Ribeiro, N. F. P., Mendes, F. M. T., Perez, C. A. C., Souza, M. M. V. M., & Schmal, M. (2008). Selective CO oxidation with nano gold particles-based catalysts over Al_2O_3 and ZrO_2. *Applied Catalysis A: General, 347*(1), 62-71.

Ripolles-Sanchis, T., Guerrero, A., Azaceta, E., Tena-Zaera, R., & Garcia-Belmonte, G. (2013). Electrodeposited NiO anode interlayers: Enhancement of the charge carrier selectivity in organic solar cells. *Solar Energy Materials and Solar Cells, 117*, 564-568.

Rolison, D. R., Hagans, P. L., Swider, K. E., & Long, J. W. (1999). Role of Hydrous Ruthenium Oxide in Pt−Ru Direct Methanol Fuel Cell Anode Electrocatalysts: The Importance of Mixed Electron/Proton Conductivity. *Langmuir, 15*(3), 774-779.

Romero, L., & Binions, R. (2013). Effect of AC electric fields on the aerosol assisted chemical vapour deposition growth of titanium dioxide thin films. *Surface and Coatings Technology, 230*, 196-201.

Romero, L., & Binions, R. (2013). On the Influence of DC Electric Fields on the Aerosol Assisted Chemical Vapor Deposition Growth of Photoactive Titanium Dioxide Thin Films. *Langmuir, 29*(44), 13542-13550.

Romero, L., Piccirillo, C., Castro, P. M. L., Bowman, C., Warwick, M. E. A., & Binions, R. (2015). Titanium Dioxide Thin Films Deposited by Electric Field-Assisted CVD: Effect on Antimicrobial and Photocatalytic Properties. *Chemical Vapor Deposition, 21*(1-2-3), 63-70.

Rossetti, I. (2013). Advanced Oxides In Catalysis. *Current Inorganic Chemistry, 3*(1), 50-69.

Russell, A. E., Ball, S. C., Maniguet, S., & Thompsett, D. (2007). Unravelling the complexities of CO2 tolerance at PtRu/C and PtMo/C. *Journal of Power Sources, 171*(1), 72-78.

Safdari, M., Fischer, A., Xu, B., Kloo, L., & Gardner, J. M. (2015). Structure and function relationships in alkylammonium lead(ii) iodide solar cells. [10.1039/C4TA06174H]. *Journal of Materials Chemistry A, 3*(17), 9201-9207.

Saji, K. J., Venkata Subbaiah, Y. P., Tian, K., & Tiwari, A. (2016). P-type SnO thin films and SnO/ZnO heterostructures for all-oxide electronic and optoelectronic device applications. *Thin Solid Films, 605*, 193-201.

Salimi, A., Hallaj, R., Mamkhezri, H., & Hosaini, S. M. T. (2008). Electrochemical properties and electrocatalytic activity of FAD immobilized onto cobalt oxide nanoparticles: Application to nitrite detection. *Journal of Electroanalytical Chemistry, 619–620*, 31-38.

Santos, L., Neto, J., Crespo, A., Baião, P., Barquinha, P., Pereira, L., Fortunato, E. (2015). Electrodeposition of WO3 Nanoparticles for Sensing Applications.

Saremi-Yarahmadi, S., Tahir, A. A., Vaidhyanathan, B., & Wijayantha, K. (2009). Fabrication of nanostructured α-Fe 2 O 3 electrodes using ferrocene for solar hydrogen generation. *Materials Letters, 63*(5), 523-526.

Saterlay, A. J., Wilkins, S. J., Holt, K. B., Foord, J. S., Compton, R. G., & Marken, F. (2001). Lead dioxide deposition and electrocatalysis at highly boron-doped diamond electrodes in the presence of ultrasound. *Journal of The Electrochemical Society, 148*(2), E66-E72.

Saw, K. G., Ibrahim, K., Lim, Y. T., & Chai, M. K. (2007). Self-compensation in ZnO thin films: An insight from X-ray photoelectron spectroscopy, Raman spectroscopy and time-of-flight secondary ion mass spectroscopy analyses. *Thin Solid Films, 515*(5), 2879-2884.

Scott, A. C. (2008). Molecular beam epitaxial growth of doped oxide semiconductors. *Journal of Physics: Condensed Matter, 20*(26), 264004.

Secu, M., Secu, C. E., & Bartha, C. (2016). Crystallization and luminescence properties of a new Eu3+-doped LaOCl nano-glass-ceramic. *Journal of the European Ceramic Society, 36*(1), 203-207.

Sekhar, B. C., Babu, G., & Kalaiselvi, N. (2015). Nanoflake driven Mn_2O_3 microcubes modified with cooked rice derived carbon for improved electrochemical behavior. *RSC Advances, 5*(6), 4568-4577.

Seo, D.-K., & Hoffmann, R. (1999). Direct and indirect band gap types in one-dimensional conjugated or stacked organic materials. *Theoretical Chemistry Accounts, 102*(1-6), 23-32.

Serpone, N., & Emeline, A. (2012). Semiconductor Photocatalysis Past, Present, and Future Outlook. *The Journal of Physical Chemistry Letters, 3*(5), 673-677.

Shahid, M., Hamid, M., Tahir, A. A., Mazhar, M., Malik, M. A., & Helliwell, M. (2012). Nanostructured ZnO thin films for optical, electrical, and photoelectrochemical applications from a new Zn complex. *Industrial & Engineering Chemistry Research, 51*(50), 16361-16368.

Shahid, M., Mazhar, M., Tahir, A. A., Rauf, M. K., & Raftery, J. (2014). Temperature-controlled Deposition of Copper(i) Oxide and Metallic Copper Nanostructures from Single-source Molecular Precursor. *Australian Journal of Chemistry, 67*(5), 757-762.

Shahid, M. M., Rameshkumar, P., Pandikumar, A., Lim, H. N., Ng, Y. H., & Huang, N. M. (2015). An electrochemical sensing platform based on a reduced graphene oxide–cobalt oxide nanocube@ platinum nanocomposite for nitric oxide detection. *Journal of Materials Chemistry A, 3*(27), 14458-14468.

Shan, W., Zhang, Y., Yang, W., Ke, C., Gao, Z., Ye, Y., & Tang, Y. (2004). Electrophoretic deposition of nanosized zeolites in non-aqueous medium and its application in fabricating thin zeolite membranes. *Microporous and Mesoporous Materials, 69*(1–2), 35-42.

Shaw, G., Parkin, I. P., Pratt, K. F. E., & Williams, D. E. (2005). Control of semiconducting oxide gas-sensor microstructure by application of an electric field during aerosol-assisted chemical vapour deposition. [10.1039/B411680A]. *Journal of Materials Chemistry, 15*(1), 149-154.

Sheldrick, G. M. (2008). A short history of SHELX. *Acta Crystallographica Section A: Foundations of Crystallography, 64*(1), 112-122.

Sheldrick, G. M. (2015). Crystal structure refinement with SHELXL. *Acta Crystallographica Section C: Structural Chemistry, 71*(1), 3-8.

Sheldrick, G. M. (2015). SHELXT-Integrated space-group and crystal-structure determination. *Acta Crystallographica Section A: Foundations and Advances, 71*(1), 3-8.

Sheng, K., Sun, Y., Li, C., Yuan, W., & Shi, G. (2012). Ultrahigh-rate supercapacitors based on eletrochemically reduced graphene oxide for ac line-filtering. *Scientific reports, 2*.

Shi, Z., Wen, X., Guan, Z., Cao, D., Luo, W., & Zou, Z. (2015). Recent progress in photoelectrochemical water splitting for solar hydrogen production. *Annals of Physics, 358*, 236-247.

Shilpy, M., Ehsan, M. A., Ali, T. H., Hamid, S. B. A., & Ali, M. E. (2015). Performance of cobalt titanate towards H_2O_2 based catalytic oxidation of lignin model compound. *RSC Advances, 5*(97), 79644-79653.

Shinde, S. S., Bhosale, C. H., & Rajpure, K. Y. (2013). Kinetic Analysis of Heterogeneous Photocatalysis: Role of Hydroxyl Radicals. *Catalysis Reviews, 55*(1), 79-133.

Sialvi, M. Z., Mortimer, R. J., Wilcox, G. D., Teridi, A. M., Varley, T. S., Wijayantha, K. G. U., & Kirk, C. A. (2013). Electrochromic and Colorimetric Properties of Nickel(II) Oxide Thin Films Prepared by Aerosol-Assisted Chemical Vapor Deposition. *ACS Applied Materials & Interfaces, 5*(12), 5675-5682.

Sivula, K., Zboril, R., Le Formal, F., Robert, R., Weidenkaff, A., Tucek, J., Gratzel, M. (2010). Photoelectrochemical water splitting with mesoporous hematite prepared by a solution-based colloidal approach. *Journal of the American Chemical Society, 132*(21), 7436-7444.

Šljukić, B., Banks, C. E., Crossley, A., & Compton, R. G. (2007a). Copper oxide–graphite composite electrodes: application to nitrite sensing. *Electroanalysis, 19*(1), 79-84.

Šljukić, B., Banks, C. E., Crossley, A., & Compton, R. G. (2007). Lead (IV) oxide–graphite composite electrodes: application to sensing of ammonia, nitrite and phenols. *Analytica chimica acta, 587*(2), 240-246.

Šljukić, B., Banks, C. E., Crossley, A., & Compton, R. G. (2007). Lead(IV) oxide–graphite composite electrodes: Application to sensing of ammonia, nitrite and phenols. *Analytica Chimica Acta, 587*(2), 240-246.

Smith Stegen, K. (2015). Heavy rare earths, permanent magnets, and renewable energies: An imminent crisis. *Energy Policy, 79*(0), 1-8.

Sommers, A., Wang, Q., Han, X., T'Joen, C., Park, Y., & Jacobi, A. (2010). Ceramics and ceramic matrix composites for heat exchangers in advanced thermal systems—A review. *Applied Thermal Engineering, 30*(11–12), 1277-1291.

Song, H., Qiu, X., Guo, D., & Li, F. (2008). Role of structural H_2O in TiO_2 nanotubes in enhancing Pt/C direct ethanol fuel cell anode electro-catalysts. *Journal of Power Sources, 178*(1), 97-102.

Su, F., Wang, T., Lv, R., Zhang, J., Zhang, P., Lu, J., & Gong, J. (2013). Dendritic Au/TiO_2 nanorod arrays for visible-light driven photoelectrochemical water splitting. *Nanoscale, 5*(19), 9001-9009.

Su, J., Feng, X., Sloppy, J. D., Guo, L., & Grimes, C. A. (2010). Vertically aligned WO_3 nanowire arrays grown directly on transparent conducting oxide coated glass: synthesis and photoelectrochemical properties. *Nano letters, 11*(1), 203-208.

Suchea, M., Christoulakis, S., Moschovis, K., Katsarakis, N., & Kiriakidis, G. (2006). ZnO transparent thin films for gas sensor applications. *Thin Solid Films, 515*(2), 551-554.

Sun, L., Li, J., Wang, C., Li, S., Lai, Y., Chen, H., & Lin, C. (2009). Ultrasound aided photochemical synthesis of Ag loaded TiO_2 nanotube arrays to enhance photocatalytic activity. *Journal of hazardous materials, 171*(1), 1045-1050.

Suresh, S. (2013). Semiconductor nanomaterials, methods and applications: a review. *Nanoscience and Nanotechnology, 3*(3), 62-74.

Suzuki, Y., & Shinoda, Y. (2016). Magnesium dititanate ($MgTi_2O_5$) with pseudobrookite structure: a review. *Science and Technology of Advanced Materials*.

Taberna, P.-L., Mitra, S., Poizot, P., Simon, P., & Tarascon, J.-M. (2006). High rate capabilities Fe3O4-based Cu nano-architectured electrodes for lithium-ion battery applications. *Nature materials, 5*(7), 567-573.

Tahir, A. A., Mazhar, M., Hamid, M., Zeller, M., & Hunter, A. D. (2009). Heterobimetallic copper-barium complexes for deposition of composite oxide thin films. *New Journal of Chemistry, 33*(7), 1535-1541.

Tahir, A. A., Wijayantha, K. G. U., Saremi-Yarahmadi, S., Mazhar, M., & McKee, V. (2009). Nanostructured α-Fe_2O_3 Thin Films for Photoelectrochemical Hydrogen Generation. *Chemistry of Materials, 21*(16), 3763-3772.

Tahir, D., & Tougaard, S. (2012). Electronic and optical properties of Cu, CuO and Cu_2O studied by electron spectroscopy. *Journal of Physics: Condensed Matter, 24*(17), 175002.

Tajabadi, M. T., Basirun, W. J., Lorestani, F., Zakaria, R., Baradaran, S., Amin, Y. M., Sookhakian, M. (2015). Nitrogen-doped graphene-silver nanodendrites for the non-enzymatic detection of hydrogen peroxide. *Electrochimica Acta, 151*, 126-133.

Tomaszewski, P. (2002). Golden book of phase transitions. *Wroclaw, 1*, 1-123.

Traversa, E., Gnappi, G., Montenero, A., & Gusmano, G. (1996). Ceramic thin films by sol-gel processing as novel materials for integrated humidity sensors. *Sensors and Actuators B: Chemical, 31*(1), 59-70.

Treccani, L., Yvonne Klein, T., Meder, F., Pardun, K., & Rezwan, K. (2013). Functionalized ceramics for biomedical, biotechnological and environmental applications. *Acta Biomaterialia, 9*(7), 7115-7150.

Treimer, S. E., Feng, J., Scholten, M. D., Johnson, D. C., & Davenport, A. J. (2001). Comparison of Voltammetric Responses of Toluene and Xylenes at Iron (III)-Doped, Bismuth (V)-Doped, and Undoped β-Lead Dioxide Film Electrodes in 0.50 M H 2 SO 4. *Journal of The Electrochemical Society, 148*(12), E459-E463.

Umebayashi, T., Asai, K., Kondo, T., & Nakao, A. (2003). Electronic structures of lead iodide based low-dimensional crystals. *Phys. Rev. B, 65*, 155405-155401-155405-155406.

Uusi-Esko, K., Rautama, E.-L., Laitinen, M., Sajavaara, T., & Karppinen, M. (2010). Control of oxygen nonstoichiometry and magnetic property of $MnCo_2O_4$ thin

films grown by atomic layer deposition. *Chemistry of Materials, 22*(23), 6297-6300.

Veith, M., Haas, M., & Huch, V. (2004a). Single Source Precursor Approach for the Sol−Gel Synthesis of Nanocrystalline $ZnFe_2O_4$ and Zinc−Iron Oxide Composites. *Chem. Mater, 17*(1), 95-101.

Veith, M., Haas, M., & Huch, V. (2004b). Single Source Precursor Approach for the Sol−Gel Synthesis of Nanocrystalline $ZnFe_2O_4$ and Zinc−Iron Oxide Composites. *Chemistry of Materials, 17*(1), 95-101.

Veith, M., Mathur, S., Lecerf, N., Huch, V., Decker, T., Beck, H. P., Haberkorn, R. (2000). Sol-Gel Synthesis of Nano-Scaled $BaTiO_3$, $BaZrO_3$ and BaTi0.5Zr0.5O3 Oxides via Single-Source Alkoxide Precursors and Semi-Alkoxide Routes. [journal article]. *Journal of sol-gel science and technology, 17*(2), 145-158.

Voitsekhovskii, A. V., Drobyazko, V. P., & Mityurev, V. K. (1995). Solid Solutions of Indium Arsenide with AII BVI Compounds and Some of Their Properties. In A. N. Sirota (Ed.), *Chemical Bonds in Solids* (pp. 104-107): Springer US.

Wakeshima, I., & Kijima, I. (1972). Synthesis of stannous chelate compounds. *Chem. Lett, 1972*(4), 325-326.

Walter, M. G., Warren, E. L., McKone, J. R., Boettcher, S. W., Mi, Q., Santori, E. A., & Lewis, N. S. (2010). Solar water splitting cells. *Chemical Reviews, 110*(11), 6446-6473.

Walters, G., & Parkin, I. (2009). Aerosol assisted chemical vapour deposition of ZnO films on glass with noble metal and p-type dopants; use of dopants to influence preferred orientation. *Applied Surface Science, 255*(13), 6555-6560.

Wang, D., Zhou, Z.-H., Yang, H., Shen, K.-B., Huang, Y., & Shen, S. (2012). Preparation of TiO_2 loaded with crystalline nano Ag by a one-step low-temperature hydrothermal method. *Journal of Materials Chemistry, 22*(32), 16306-16311.

Wang, H., Cui, L.-F., Yang, Y., Sanchez Casalongue, H., Robinson, J. T., Liang, Y., Dai, H. (2010). Mn3O4− graphene hybrid as a high-capacity anode material for lithium ion batteries. *Journal of the American Chemical Society, 132*(40), 13978-13980.

Wang, H., Kalytchuk, S., Yang, H., He, L., Hu, C., Teoh, W. Y., & Rogach, A. L. (2014). Hierarchical growth of SnO_2 nanostructured films on FTO substrates: structural defects induced by Sn (II) self-doping and their effects on optical and photoelectrochemical properties. *Nanoscale, 6*(11), 6084-6091.

Wang, M., Sun, L., Lin, Z., Cai, J., Xie, K., & Lin, C. (2013). p–n Heterojunction photoelectrodes composed of Cu_2O-loaded TiO_2 nanotube arrays with enhanced photoelectrochemical and photoelectrocatalytic activities. *Energy & Environmental Science, 6*(4), 1211-1220.

Wang, X., Liu, E., & Zhang, X. (2014). Non-enzymatic glucose biosensor based on copper oxide-reduced graphene oxide nanocomposites synthesized from water-isopropanol solution. *Electrochimica Acta, 130*, 253-260.

Wang, Y., & Lee, J. Y. (2004). Molten Salt Synthesis of Tin Oxide Nanorods: Morphological and Electrochemical Features. *Journal Physical Chemistry B, 108*(46), 17832-17837. doi: 10.1021/jp046744.

Wang, Y., Li, Y., Zhou, Z., Zu, X., & Deng, Y. (2011). Evolution of the zinc compound nanostructures in zinc acetate single-source solution. *Journal of Nanoparticle Research, 13*(10), 5193-5202.

Wang, Z., Luan, D., Boey, F. Y. C., & Lou, X. W. (2011). Fast Formation of SnO_2 Nanoboxes with Enhanced Lithium Storage Capability. *J. Amer. Chem. Soc, 133*(13), 4738-4741.

Warren, S. C., & Thimsen, E. (2012). Plasmonic solar water splitting. *Energy & Environmental Science, 5*(1), 5133-5146.

Warwick, M., Smith, R., Furlan, N., Crane, J., & Binions, R. (2010). Electric Fields And Chemical Vapor Deposition. *ECS Transactions,, 28 (15)*, 1-13.

Wei, J., Xu, Z., Liu, P., Su, W., Lin, H., Zheng, P., Qin, H. (2016). Ba9Y2Si6O24: A new silicate dielectric ceramic for microwave communication application. *Materials Letters, 178*, 144-146.

Wei, X. Q., Man, B. Y., Liu, M., Xue, C. S., Zhuang, H. Z., & Yang, C. (2007). Blue luminescent centers and microstructural evaluation by XPS and Raman in ZnO thin films annealed in vacuum, N_2 and O_2. *Physica B: Condensed Matter, 388*(1–2), 145-152.

Windischmann, H. (1987). An intrinsic stress scaling law for polycrystalline thin films prepared by ion beam sputtering. *Journal of Applied Physics, 62*(5), 1800-1807.

Wong, E. M., & Searson, P. C. (1999). ZnO quantum particle thin films fabricated by electrophoretic deposition. *Applied Physics Letters, 74*(20), 2939-2941.

Wu, D., Li, H., Xue, X., Fan, H., Xin, Q., & Wei, Q. (2013). Sensitive and selective determination of dopamine by electrochemical sensor based on molecularly imprinted electropolymerization of o-phenylenediamine. *Analytical Methods, 5*(6), 1469-1473.

Wu, L., Feng, L., Ren, J., & Qu, X. (2012). Electrochemical detection of dopamine using porphyrin-functionalized graphene. *Biosensors and Bioelectronics, 34*(1), 57-62.

Xia, C., Wang, N., Wang, L., & Guo, L. (2010). Synthesis of nanochain-assembled ZnO flowers and their application to dopamine sensing. *Sensors and Actuators B: Chemical, 147*(2), 629-634.

Xiaoxin, L., Zhengguo, J., Shaojing, B., & Tao, Y. (2005). Influences of solvent on properties of TiO_2 porous films prepared by a sol-gel method from the system containing PEG. *Journal of sol-gel science and technology, 36*(1), 103-11.

Yan, J., Ye, Q., Wang, X., Yu, B., & Zhou, F. (2012). CdS/CdSe quantum dot co-sensitized graphene nanocomposites via polymer brush templated synthesis for potential photovoltaic applications. *Nanoscale, 4*(6), 2109-2116.

Yang, J. L., An, S. J., Park, W. I., Yi, G. C., & Choi, W. (2004). Photocatalysis using ZnO thin films and nanoneedles grown by metal–organic chemical vapor deposition. *Advanced Materials, 16*(18), 1661-1664.

Yang, M., Xu, J.-Z., Xu, S., Zhu, J.-J., & Chen, H.-Y. (2004). Preparation of porous spherical CuI nanoparticles. *Inorganic Chemistry Communications, 7*(5), 628-630.

Yang, Y., Li, B., Zhang, C., Wang, S., Liu, K., & Yang, B. (2015). Fabrication and properties of graphene reinforced silicon nitride composite materials. *Materials Science and Engineering: A, 644*, 90-95.

Yao, K., Chen, S., Rahimabady, M., Mirshekarloo, M. S., Yu, S., Tay, F. E. H., Lu, L. (2011). Nonlinear dielectric thin films for high-power electric storage with energy density comparable with electrochemical supercapacitors. *IEEE transactions on ultrasonics, ferroelectrics, and frequency control, 58*(9), 1968-1974.

Ye, B.-H., Li, X.-Y., Williams, I. D., & Chen, X.-M. (2002). Synthesis and Structural Characterization of Di- and Tetranuclear Zinc Complexes with Phenolate and Carboxylate Bridges. Correlations between 13C NMR Chemical Shifts and Carboxylate Binding Modes. *Inorg. Chem, 41*(24), 6426-6431.

Ye, F., Feng, C., Fu, N., Wu, H., Jiang, J., & Han, S. (2015). Application of graphene oxide/lanthanum-modified carbon paste electrode for the selective determination of dopamine. *Applied Surface Science, 357, Part A*, 1251-1259.

Yeh, M.-H., Lin, L.-Y., Lee, C.-P., Chou, C.-Y., Tsai, K.-W., Lin, J.-T. s., & Ho, K.-C. (2013). High performance CdS quantum-dot-sensitized solar cells with Ti-based ceramic materials as catalysts on the counter electrode. *Journal of Power Sources, 237*, 141-148.

Yi, C., Luo, J., Meloni, S., Boziki, A., Ashari-Astani, N., Gratzel, C., Gratzel, M. (2016). Entropic stabilization of mixed A-cation ABX3 metal halide perovskites for high performance perovskite solar cells. *Energy & Environmental Science, 9*(2), 656-662.

Yin, W.-J., Shi, T., & Yan, Y. (2014). Unusual defect physics in $CH_3NH_3PbI_3$ perovskite solar cell absorber. *Applied Physics Letters, 104*(6), 063903.

Yourey, J. E., & Bartlett, B. M. (2011). Electrochemical deposition and photoelectrochemistry of $CuWO_4$, a promising photoanode for water oxidation. *Journal of Materials Chemistry, 21*(21), 7651-7660.

Yuan, H., Guo, D., Qiu, X., Zhu, W., & Chen, L. (2009). Influence of metal oxides on Pt catalysts for methanol electrooxidation using electrochemical impedance spectroscopy. *Journal of Power Sources, 188*(1), 8-13.

Yusoff, N., Kumar, S. V., Pandikumar, A., Huang, N. M., Marlinda, A. R., & An'amt, M. N. (2015). Core-shell Fe_3O_4-ZnO nanoparticles decorated on reduced graphene oxide for enhanced photoelectrochemical water splitting. *Ceramics International, 41*(3, Part B), 5117-5128.

Zeng, Y., Zhou, Y., Kong, L., Zhou, T., & Shi, G. (2013). A novel composite of SiO_2-coated graphene oxide and molecularly imprinted polymers for electrochemical sensing dopamine. *Biosensors and Bioelectronics, 45*, 25-33.

Zhang, J., Bang, J. H., Tang, C., & Kamat, P. V. (2009). Tailored TiO_2− $SrTiO_3$ heterostructure nanotube arrays for improved photoelectrochemical performance. *ACS nano, 4*(1), 387-395.

Zhang, J., Song, T., Zhang, Z., Ding, K., Huang, F., & Sun, B. (2015). Layered ultrathin PbI2 single crystals for high sensitivity flexible photodetectors. [10.1039/C4TC02712D]. *Journal of Materials Chemistry C, 3*(17), 4402-4406.

Zhang, J., Wu, Y., Xing, M., Leghari, S. A. K., & Sajjad, S. (2010). Development of modified N doped TiO_2 photocatalyst with metals, nonmetals and metal oxides. [10.1039/B927575D]. *Energy & Environmental Science, 3*(6), 715-726.

Zhang, N., Qu, Y., Pan, K., Wang, G., & Li, Y. (2015). Synthesis of pure phase Mg1. 2Ti1. 8O5 and MgTiO3 nanocrystals for photocatalytic hydrogen production. *Nano Research*, 1-9.

Zhang, N., Qu, Y., Pan, K., Wang, G., & Li, Y. (2016). Synthesis of pure phase $Mg_{1.2}Ti_{1.8}O_5$ and MgTiO3 nanocrystals for photocatalytic hydrogen production. [journal article]. *Nano Research, 9*(3), 726-734.

Zhang, N., Zhang, K., Zhou, W., Jiang, B., Pan, K., Qu, Y., & Wang, G. (2015). Pure phase orthorhombic $MgTi_2O_5$ photocatalyst for H_2 production. [10.1039/C5RA20992G]. *RSC Advances, 5*(128), 106151-106155.

Zhang, N., Zhang, K., Zhou, W., Jiang, B., Pan, K., Qu, Y., & Wang, G. (2015). Pure phase orthorhombic MgTi 2 O 5 photocatalyst for H 2 production. *RSC Advances, 5*(128), 106151-106155.

Zhang, S., Li, F., Jiang, X., Kim, J., Luo, J., & Geng, X. (2015). Advantages and challenges of relaxor-$PbTiO_3$ ferroelectric crystals for electroacoustic transducers – A review. *Progress in Materials Science, 68*, 1-66.

Zhao, Q., Ma, L., Zhang, Q., Wang, C., & Xu, X. (2015). SnO_2-based nanomaterials: synthesis and application in lithium-ion batteries and supercapacitors. *Journal of Nanomaterials, 2015*, 6.

Zhao, Y., & Zhu, K. (2016). Organic-inorganic hybrid lead halide perovskites for optoelectronic and electronic applications. *Chemical Society Reviews, 45*(3), 655-689.

Zhitomirsky, I. (1998). Cathodic electrophoretic deposition of diamond particles. *Materials Letters, 37*(1), 72-78.

Zhou, G., Lee, D. K., Kim, Y. H., Kim, C. W., & Kang, Y. S. (2006). Preparation and Spectroscopic Characterization of Ilmenite-Type $CoTiO_3$ Nanoparticles. *BULLETIN-KOREAN CHEMICAL SOCIETY, 27*(3), 368.

Zhou, G., Wang, D.-W., Li, F., Zhang, L., Li, N., Wu, Z.-S., Cheng, H.-M. (2010). Graphene-wrapped Fe_3O_4 anode material with improved reversible capacity and cyclic stability for lithium ion batteries. *Chemistry of Materials, 22*(18), 5306-5313.

Zhou, S., Wei, D., Shi, H., Feng, X., Xue, K., Zhang, F., & Song, W. (2013). Sodium dodecyl benzene sulfonate functionalized graphene for confined electrochemical growth of metal/oxide nanocomposites for sensing application. *Talanta, 107*, 349-355.

Zhu, L., Hong, M., & Ho, G. W. (2015). Fabrication of wheat grain textured TiO_2/CuO composite nanofibers for enhanced solar H_2 generation and degradation performance. *Nano Energy, 11*, 28-37.

Zhu, X., Zhu, Y., Murali, S., Stoller, M. D., & Ruoff, R. S. (2011). Nanostructured reduced graphene oxide/Fe_2O_3 composite as a high-performance anode material for lithium ion batteries. *ACS Nano, 5*(4), 3333-3338.

LIST OF PUBLICATIONS

1. **Naeem, R.**, Yahya, R., Pandikumar, A., Huang, & Mazhar, M. (2016). Optical and Optoelectronic properties of morphology and structure controlled ZnO, CdO and PbO by electric field directed aerosol assisted chemical vapour deposition. *Journal of Materials science: materials in Electronics,* DOI: 10.1007/s10854-016-5601-3 (Published). (IF: 1.79)
2. **Naeem, R**., Ehsan, M. A., Yahya, R., Sohail, M., Khaledi, H., & Mazhar, M. (2016). Fabrication of pristine Mn_2O_3 and Ag-Mn_2O_3 composite thin films by AACVD for photoelectrochemical water splitting. *Dalton Transactions*. DOI: 10.1039/C6DT02656G. (Published).(IF: 4.17)
3. Ehsan, M. A., **Naeem, R**., Khaledi, H., Sohail, M., Saeed, A. H., & Mazhar, M. (2016). Fabrication of $CoTiO_3$–TiO_2 composite films from a heterobimetallic single source precursor for electrochemical sensing of dopamine. *Dalton Transactions*. *45, 10222-10232*. DOI: 10.1039/C6DT01016D (Published). (IF: 4.17)
4. Ehsan, M. A., **Naeem, R**., McKee, V., Saeed, A. H., Pandikumar, A., Huang, N. M., & Mazhar, M. (2016). Electrochemical sensing of nitrite using a copper–titanium oxide composite derived from a hexanuclear complex. *RSC Advances, 6*(33), 27852-27861. DOI: 10.1039/C6RA00104A (Published). (IF: 3.28)
5. **Naeem, R.**, Ahmed, S., Lo, K. M., Basirun, W. J., Yahya, R., Misran, M., . . . Thapa, A. K. (2015). Electric- Field Aerosol- Assisted CVD: Synthesis, Characterization, and Properties of Tin Oxide Microballs Prepared from a Single Source Precursor. *Chemical Vapor Deposition, 21*(10-11-12), 360-368. DOI: 10.1002/cvde.201507178. (Published). (IF: 1.70)
6. **Naeem, R.**, Yahya, R., Pandikumar, A., Huang, N. M., Misran, M., Arifin, Z., & Mazhar, M. (2015). Photoelectrochemical properties of morphology controlled

manganese, iron, nickel and copper oxides nanoball thin films deposited by electric field directed aerosol assisted chemical vapour deposition. *Materials Today Communications, 4,* 141-148.doi.org/10.1016/j.mtcomm.2015.06.004 (Published).

7. **Naeem, R**., Yahya, R., Mansoor, M.A., Teridi, M. A. M., Sookhakian, M. & Mazhar, M. (2016). Photoelectrochemical water splitting over mesoporous CuPbI3 films prepared by electrophoretic technique.*Monatshfefte fur Chemie-Chemical Monthly,* (Accepted) (IF: 1.13)
8. Ehsan, M. A., **Naeem, R**., Khaledi, H., Sohail, M., Saeed, A. H., & Mazhar, M. (2017). $MgTi_2O_5$ Thin Films from Single Molecular Precursor for Photoelectrochemical Water Splitting. *Solar Energy Materials and Solar Cells*. *161*, 328-337 (Published) (IF: 4.73).